Interfaces between Metal Anodes and Solid Electrolytes in Solid-State Batteries



Dominic Spencer Jolly

Department of Materials, University of Oxford

A thesis submitted for the degree of

Doctor of Philosophy

Michaelmas 2021

Supervised by Prof. Peter Bruce

Declaration of Originality

I, Dominic Spencer Jolly, declare that this thesis is my own work and has not been submitted to another institution for any other degree or qualification. All contributions from collaborators have been appropriately referenced throughout the work.

This thesis is approximately 39,950 words in length, and so complies with the Departmental word limit for doctoral theses.

Acknowledgments

I would first like to express my unreserved gratitude to my supervisor, Prof. Peter Bruce, who has been a constant source of guidance and mentorship throughout this degree, and without whom this work would not have been possible. I feel extremely privileged to have had the opportunity to work under such a knowledgeable and dedicated scientific leader on the timely topic of solid-state batteries.

I would also like to extend my sincere thanks to the EPSRC for funding my studies, and to the Henry Royce Institute and the Faraday Institution for providing funding for research and equipment.

I would like to thank members of the Bruce group, past and present, for their friendship and support over the last four years. In particular, I would like to thank Dr. Jitti Kasemchainan for his help and guidance over the first 18 months of this degree. His mentorship laid the foundations upon which much of this thesis is built. I would also especially like to thank Ziyang Ning, both for the friendship we forged over long meetings and even longer days at various synchrotrons, and for his invaluable scientific contributions to this thesis. My thanks also go to Dr. Paul Adamson for his help in steering my research, and in preparing this thesis for submission. Finally, I would also like to specifically thank all other members of the solid-state sub-group over the last four years; Dr. Gareth Hartley, Dr. Stefanie Zekoll, Dr. Zhaoxin Yu, Dr. Boyang Liu, Dr. Xiangwen Gao, Dr. Peiyu Chen, Dominic Melvin, Varnika Agarwal, Johann Perera, Shengming Zhang and Bingkun Hu.

I would like to thank collaborators from outside the Bruce solid-state sub-group who have made important contributions to this thesis. My thanks go to Prof. James Marrow for the support he has offered Ziyang Ning in carrying out XCT, to Dr. Ed Darnbrough and Prof. Dave Armstrong for help with accurate pressure application to cells and for helpful

discussions on mechanics of materials, to Dr. Robert House for helping to carry out *operando* XRD, and to Chris Doerrer and Prof. Patrick Grant for spray deposition of carbon-based interlayers. I want to thank Dr. Phil Holdway of the Oxford Materials Characterisation Service for carrying out XPS, the staff of the David Cockayne Centre for Electron Microscopy and in particular Jenny Holter for training and maintenance of the electron microscopy facilities, and to Stephen Turrell and Marco Siniscalchi for offering support for PVD. I would also like to take this opportunity to thank Prof. Mauro Pasta for his leadership within the SOLBAT Faraday project, Nadia Abdul-Karim for keeping the Rex Richard's facilities running, and Zsofia Lazar, Miki Bennett and Dr. Erez Cohen for their management of the Bruce group.

From the bottom of my heart I'd like to express enormous gratitude to all the members of the Bruce group who have made my DPhil such an enjoyable experience. In particular, I'd like to thank Stef, Conrad, Alex, Rob, Greg, Gareth, Dom and Johann. All the lunches and coffees have been some of the best parts of the last four years. You've all helped to shape me as a scientist and I'm honoured to call you my friends.

Finally, I'd like to thank my family and friends who've given me so much support over the years. I'd especially like to thank my parents, Chris and Kate. I couldn't have done this without you.

Abstract

Solid-state batteries promise to revolutionise battery safety and energy density. However, there remain significant challenges to be overcome before their potential can be realised. This thesis focuses on the difficulties of interfacing a metal anode with a solid electrolyte. Perhaps the most limiting problem is that the metal anode/solid electrolyte interface is morphologically unstable at high rates of charge/discharge, with dendrites penetrating through the solid electrolyte on plating, and voids forming at the interface during stripping.

In **Chapter 3**, the formation of interfacial voids during stripping is investigated for a Na metal anode. The Na anode enables the use of X-ray computed micro-tomography to follow the dynamics of voiding at the interface during cycling, revealing how voiding worsens with each successive stripping until failure of the cell. The Na anode also offers an interesting contrast to previous work on Li anodes, with lower stack-pressures required to suppress voiding, due to its greater propensity to creep under pressure.

Chapter 4 describes investigation of the temperature dependence of voiding at the Li anode/solid electrolyte interface, finding that moderately elevated temperatures enable higher rates of morphologically stable stripping by increasing self-diffusion and creep in the Li metal. Stable cycling at a high current density of 2.5 mA/cm^2 is demonstrated under 5 MPa stack-pressure at a moderately elevated temperature of 80 °C.

Finally, **Chapter 5** investigates the use of carbon-based interlayers to protect the solid electrolyte from dendrite penetration. A number of interlayers are investigated, with their effectiveness determined to be dependent on the Li diffusivity. Addition of silver to graphite interlayers is also studied, finding that formation of a Ag-Li alloy significantly improves the homogeneity of Li deposition during charging.

List of Publications

1. Spencer Jolly, D., Ning, Z., Darnbrough, J. E., Kasemchainan, J., Hartley, G. O., Adamson, P., Armstrong, D. E. J., Marrow, T. J. & Bruce, P. G. Sodium/Na β'' Alumina Interface: Effect of Pressure on Voids. *ACS Appl. Mater. Interfaces*, 12, 1, 678-685 (2020).
2. Spencer Jolly, D., Ning, Z., Hartley, G. O., Liu, B., Melvin, D. L. R., Adamson, P., Marrow, T. J. & Bruce, P. G. Temperature Dependence of Voiding in Argyrodite Solid-State Batteries. *ACS Appl. Mater. Interfaces*, 13, 19, 22708-22716 (2021).
3. Ning, Z., Spencer Jolly, D., Li, G., De Meyere, R., Pu, S. D., Chen, Y., Kasemchainan, J., Ihli, J., Gong, C., Liu, B., Melvin, D. L. R., Bonnin, A., Magdysyuk, O., Adamson, P., Hartley, G. O., Monroe, C. W., Marrow, T. J. & Bruce, P. G. Visualising Plating-Induced Cracking in Lithium-Anode Solid Electrolyte Cells. *Nat. Mater.*, 20, 1121-1129 (2021).
4. Rees, G. J., Spencer Jolly, D., Ning, Z., Marrow, T. J., Pavlovskaya, G. E. & Bruce, P. G. Imaging Sodium Dendrite Growth in All-Solid-State Sodium Batteries Using ^{23}Na T_2-Weighted Magnetic Resonance Imagining. *Angew. Chem. Int. Ed.*, 60, 2110-2115 (2021).
5. Kasemchainan, J., Zekoll, S., Spencer Jolly, D., Ning, Z., Hartley, G. O., Marrow, T. J. & Bruce, P. G. Critical Stripping Current Leads to Dendrite Formation on Plating in 3-Electrode Lithium Anode Solid Electrolyte Cells. *Nat. Mater.* 18, 1105-1111 (2019).
6. Hartley, G. O., Jin, L., Bergner, B. J., Spencer Jolly, D., Rees, G. J., Zekoll, S., Ning, Z., Pateman, A. T. R., Holc, C., Adamson, P. & Bruce, P. G. Is Nitrogen Present in $Li_3N{\cdot}P_2S_5$ Solid Electrolytes Produced by Ball Milling? *Chem. Mater.*, 31, 24, 9993-10001 (2019).
7. Pasta, M., Armstrong, D., Brown, Z. L., Bu, J., Castell, M. R., Chen, P., Cocks, A., Corr, S. A., Cussen, E. J., Darnbrough, E., Deshpande, V., Doerrer, C., Dyer, M. S., El-Shinawi, H., Fleck, N., Grant, P., Gregory, G. L., Grovenor, C., Hardwick, L. J., Irvine, J. T. S., Lee, H. J., Li, G., Liberti, E., McClelland, I., Monroe, C., Nellist, P. D., Shearing, P. R., Shoko, E., Song, W., Spencer Jolly, D., Thomas, C. I., Turrell, S. J., Vestli, M., Williams, C. K., Zhou, Y. & Bruce, P. G. 2020 Roadmap on Solid-State Batteries. *J. Phys. Energy*, 2, 032008 (2020).

List of Abbreviations

2D	Two dimensional
3D	Three dimensional
ASSBs	All-solid-state batteries
BSE	Back-scattered electron
CCD	Critical current density
CE	Counter electrode
CT	Charge transfer
E_A	Activation energy
EDX/EDS	Energy-dispersive X-ray Spectroscopy
EIS	Electrochemical impedance spectroscopy
EV	Electric vehicles
FIB	Focussed ion beam
GB	Grain-boundary
HAXPES	Hard X-ray photoelectron spectroscopy
LAGP	$Li_{1-x}Al_xGe_{2-x}(PO_4)_3$
LLTO	$Li_{3x}La_{2/(3-x)}TiO_3$
LLZO	$Li_7La_3Zr_2O_{12}$
MCIs	Mixed conducting interphases
NMR	Nuclear magnetic resonance
PAA	Polyacrylic acid
PEEK	Polyether ether ketone
PEIS	Potentiostatic electrochemical impedance spectroscopy
PEO	Polyethylene oxide
PTFE	Polytetrafluoroethylene
PVD	Physical vapour deposition
PVdF	Polyvinylidene fluoride
PXRD	Powder X-ray diffraction
R/C element	Resistor/Capacitor element
RE (or Ref)	Reference electrode
SE	Solid electrolyte
SEI	Solid electrolyte interphase
SEM	Scanning electron microscope/microscopy
SHE	Standard hydrogen electrode
SIMS	Secondary ion mass spectrometry
SSBs	Solid-state batteries
WE	Working electrode
XCT	X-ray computed tomography
XPS	X-ray photoelectron spectroscopy
XRD	X-ray diffraction
ZEBRA	Zeolite Battery Research Africa Project

Table of Contents

1 Chapter 1: Introduction 1

1.1 Introduction 1

1.2 Towards Lithium Anode Solid-State Batteries 2

1.2.1 The Li-ion battery 2
1.2.2 Lithium metal anodes 4
1.2.3 The solid-state battery 5

1.3 Solid Electrolytes 7

1.3.1 Properties of solid electrolytes 8
1.3.2 Solid electrolytes in this thesis 16

1.4 Metal Anodes 21

1.4.1 Lithium anodes 21
1.4.2 Comparison with sodium 24
1.4.3 Comparison with lithium alloys 26

1.5 Lithium Anode/Solid Electrolyte Interfaces 26

1.5.1 Chemical and electrochemical stability 26
1.5.2 Voiding when stripping the Li anode 28
1.5.3 Dendrite growth when plating the Li anode 34

1.6 Thesis Aims 45

2 Chapter 2: Experimental Techniques 47

2.1 Aim 47

2.2 Characterisation 47

2.2.1 X-ray Diffraction (XRD) 47
2.2.2 X-ray Photoelectron Spectroscopy (XPS) 50
2.2.3 Scanning Electron Microscopy (SEM) 51
2.2.4 Energy-dispersive X-ray Spectroscopy (EDX) 54
2.2.5 X-ray Computed Tomography (XCT) 56

2.3 Electrochemical Testing 58

2.3.1 Potentiostatic Electrochemical Impedance Spectroscopy (PEIS) 58
2.3.2 Galvanostatic Cycling and Critical Current Determination 64

3 Chapter 3: Voiding at the Na/Na-β”-Alumina Interface during Anode Stripping and the Effect of Stack-Pressure 68

3.1 Aim 68

3.2 Introduction 68

3.3 Experimental 73

3.3.1 Cell Preparation 73
3.3.2 Electrochemistry 75
3.3.3 Characterisation 76

3.4 Results and Discussion 78

3.4.1 Optimisation of Na-β”-Alumina and the Na/Na-β”-Alumina Interface 78
3.4.2 3- Electrode Cycling under 4 MPa of Pressure 86
3.4.3 Cycling 3-Electrode Cells under 7 MPa of Pressure 97
3.4.4 Counter Electrode *versus* Reference Electrode 99

3.4.5 Critical Pressure with Current Density 100
3.5 Conclusions 106
4 Chapter 4: Temperature Dependence of Lithium Anode Voiding in Argyrodite Solid-State Batteries 108
4.1 Aim 108
4.2 Introduction 108
4.3 Experimental 110
4.3.1 Preparation of Cells 110
4.3.2 Electrochemistry 112
4.3.3 Characterisation 113
4.4 Results and Discussion 115
4.4.1 Characterisation of Li_6PS_5Cl and the Li/Li_6PS_5Cl Interface 115
4.4.2 Influence of Temperature and Pressure on Charge Transfer Resistance 125
4.4.3 Effect of Temperature on the Critical Current for Voiding 127
4.4.4 High Critical Current for Voiding with Moderate Temperature and Pressure 133
4.4.5 Importance of Continuous Stack-Pressure 136
4.5 Conclusions 137
5 Chapter 5: Graphite and Graphite-Silver Anode Protective Interlayers for Lithium Solid-State Batteries 139
5.1 Aim 139
5.2 Introduction 139
5.3 Experimental Methods 142
5.3.1 Cell Fabrication 142
5.3.2 Electrochemical Testing 147
5.3.3 Characterisation 147
5.4 Results and Discussion 148
5.4.1 Cell Fabrication 148
5.4.2 First Charge Voltage Profiles 150
5.4.3 Charging Graphite and Carbon Black Interlayers 151
5.4.4 Charging Silver Interlayers 165
5.4.5 Charging Silver-Carbon Interlayers 171
5.5 Conclusions 186
5.6 Future Direction of Interlayer Research 187
6 Chapter 6: Conclusions and Outlook 191
7 References 195
8 Appendices 224

1 Introduction

1.1 Introduction

Electrochemical energy storage has become a ubiquitous part of modern life; most of us own several devices such as phones and laptops that are powered by rechargeable (secondary) batteries. However, with climate change now "a code red for humanity",[1] the role of batteries in our everyday lives is broadening. As we shift to a world in which we burn fewer fossil fuels, electrochemical energy storage will play a role in enabling greener energy production and consumption. One area of particular interest is automotive vehicles. Governments of several major nations have announced policies towards phasing out the sale of internal combustion engine powered vehicles, with electric vehicles (EVs) powered by batteries offering an attractive alternative.[2,3] In addition, further applications for electrochemical energy storage continue to emerge, including grid-level energy storage as well as for rail, shipping and aviation.[4–7]

As demand for batteries broadens beyond consumer electronics into these new sectors, so too do the demands made of battery performance. For example, in the EV market consumers want increased vehicle range, decreased charging times, longer battery lifetimes, higher safety and lower costs.[8] Meeting these demands will require innovation and invention and will potentially necessitate moving away from today's 'conventional' lithium-ion (Li-ion) battery, to beyond Li-ion solutions such as lithium metal anode cells and solid-state batteries. However, many of these next-generation battery technologies face fundamental challenges that must be overcome by research before successful commercialisation can be realised.[9,10]

This thesis reports the results of research on the interfaces between metal anodes and solid electrolytes in solid-state batteries. Common interfacial failures such as dendrites and voids

are studied, and potential solutions for overcoming these problems are explored. As an introduction to these topics, this chapter aims to summarise the relevant key areas of literature. First, the lithium anode solid-state battery is introduced, leading into detailed discussions of the solid electrolyte and metal anode components. Finally, literature on the lithium anode/solid electrolyte interface and potential solutions to common interfacial failures are explored in detail.

1.2 Towards Lithium Anode Solid-State Batteries

1.2.1 The Li-ion battery

"Li-ion battery" can be a somewhat misleading term, as it can refer to any number of battery technologies in which electrochemical energy is stored by the movement of Li-ions. However, in this thesis "Li-ion battery" will be used as a term to describe cells of the type developed by Goodenough, Whittingham and Yoshino, in which energy is stored in an electrochemical cell composed of a cathode (commonly a layered transition metal oxide)

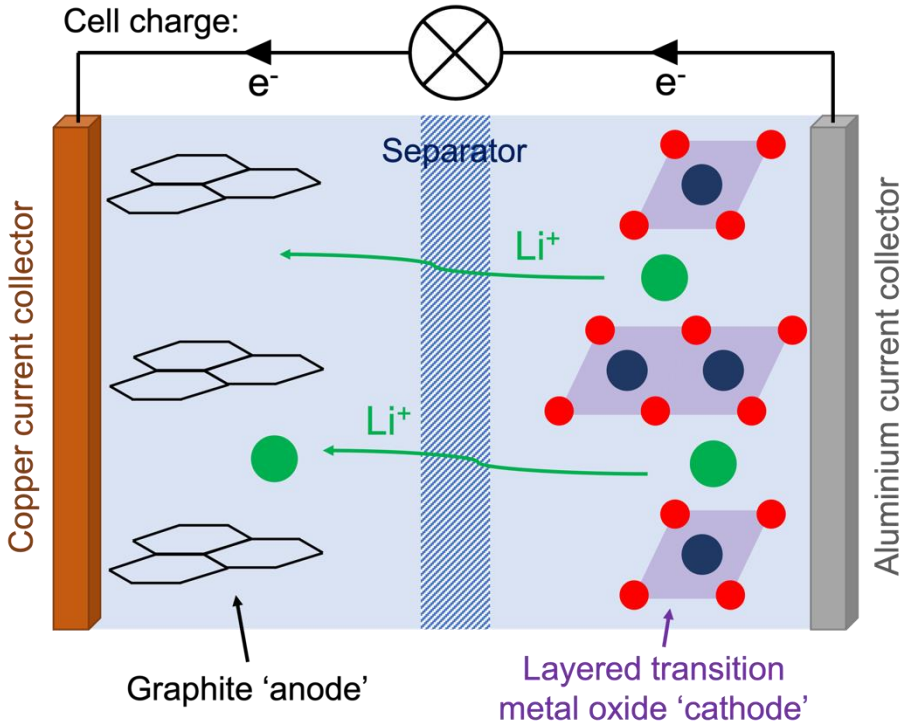


Figure 1.1: Schematic showing charging of a conventional Li-ion battery with a graphite anode, liquid electrolyte and layered transition metal oxide cathode.

and a graphite anode, separated by a Li-ion conducting organic liquid electrolyte.[11–13] A schematic of a Li-ion battery is shown in Figure 1.1.

As a Li-ion cell is charged, the cathode active material is oxidised and Li-ions migrate across the organic liquid electrolyte, reducing as they are intercalated into the graphite anode. During discharge, the reverse process takes place, with Li-ions deintercalating from the lithiated graphite anode and intercalating back into the layered transition metal oxide active material. For example, when $LiCoO_2$ is used as the cathode active material, the underlying reactions at each electrode are:

$$Cathode: LiCoO_2 \rightleftharpoons Li_{1-x}CoO_2 + xLi^+ + xe^-$$

$$Anode: 6C + xLi^+ + xe^- \rightleftharpoons Li_xC_6$$

$$Full\ cell: LiCoO_2 + 6C \rightleftharpoons Li_{1-x}CoO_2 + Li_xC_6$$

These "rocking chair" type batteries, in which Li-ions move reversibly between layered cathode and anode materials have proved highly effective, dominating the secondary battery market for years.[12] However, Li-ion batteries face a number of challenges which place an upper limit of their performance:

- Solid electrolyte interphase (SEI) formation at the graphite/liquid electrolyte interface. Degradation at the anode interface can form a passivating layer of inactive, resistive SEI phase composed of Li_2CO_3, LiF, Li_2O and alkyl carbonates. It is necessary to add additives to the electrolyte to mitigate this, and even so formation of SEI results in loss of active Li and capacity fade. The resistive SEI can reduce the charge rate capability of the cell, leading to plating of mossy lithium metal on the graphite anode. This poses serious safety concerns as short-circuiting of the cell can lead to thermal run-away and explosion.[14–16]

- Li-ion batteries also pose some application specific safety concerns. Damage to a battery module, for example in the event of a road traffic accident, can cause critical cell failure with risk of fire, explosion and release of toxic gases.
- At elevated temperatures, when the cathode has a high state of charge, degradation will occur at the cathode interface, leading to Li loss and capacity fade.[14]
- The energy density of Li-ion batteries has a lower theoretical limit than alterative cell chemistries. Increases in cell energy density have been driven by discovery of new high capacity, high voltage cathode materials. However, continued increase may be reliant on increasing the anodic capacity of cells beyond the limits of graphite.[17]

1.2.2 Lithium metal anodes

Li metal anodes have greater anodic capacity than graphite (3860 mA·h/g compared to 372 mA·h/g) and so promise to deliver a step-change in battery energy densities.[18] However, simply exchanging a graphite anode for Li metal in a conventional cell is not possible for a number of reasons, most notably; 1) reactions between the Li and the liquid electrolyte form a solid electrolyte interphase (SEI) that is renewed each cycle, unlike graphite, depleting the Li metal over multiple cycles and leading to capacity fade and 2) due to inhomogeneous plating, growths of Li metal (dendrites and mossy Li) gradually transverse the liquid electrolyte, resulting in catastrophic failure and posing a severe safety risk, Figure 1.2.[19] This risk is considerably greater than for graphite anode cells, because whereas in graphite cells Li only plates at the anode when the cell is charged at too high a rate, in lithium metal anode cells dendrites can form simply as a result of anodic roughening caused by multiple cycles of stripping and plating. Historic cases of lithium anode cells include batteries by Moli Energy and Exxon in the early 1990s, the safety performance of which

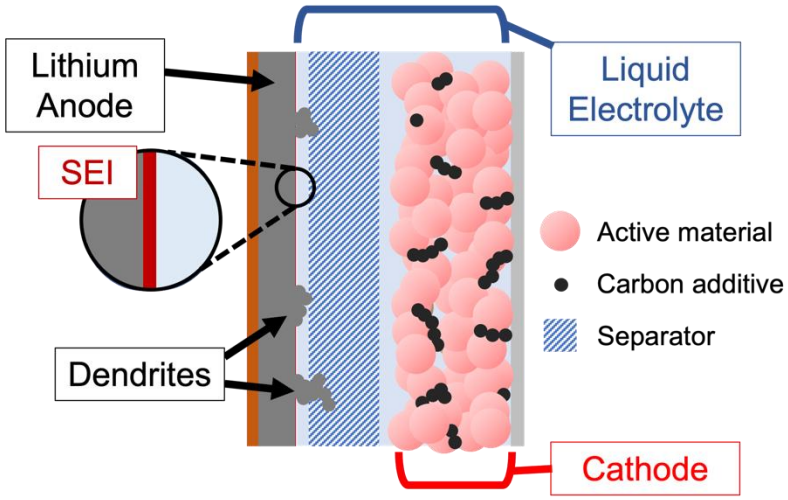


Figure 1.2: Schematic showing the common failures of utilising a Li metal anode with a liquid electrolyte, including growth of Li dendrites across the cell and formation of a resistive solid electrolyte interphase (SEI).

saw commercial pursuit of lithium metal anodes put on hold in favour of safer graphite anodes.[17,20]

Strategies to minimise Li loss to SEI formation and to inhibit dendrite/mossy Li growth (which results in loss of electrochemically active Li) commonly involve use of high salt concentrations[21–24] and introduction of additives to the liquid electrolyte.[25–28] This being said, whilst such strategies can be effective at modest cycling rates, at high rates of charge efforts have fallen short and cells are still susceptible to unacceptable dendritic growth and short cycle lives. It should be noted that electrolyte salts are high-cost battery materials and so high salt concentrations have an associated expense. What is more, the safety concerns of these batteries necessitate additional packaging and other non-active components, adding expense and decreasing the pack-level energy density.

1.2.3 The solid-state battery

Batteries utilising solid Li-ion conducting electrolytes rather than liquid electrolytes provide possible solutions to the aforementioned problems of Li loss to SEI formation and safety risks posed due to dendrite growth, Figure 1.3. A well-chosen solid electrolyte gives limited or even no reactivity against a Li metal anode, almost eliminating capacity fade as

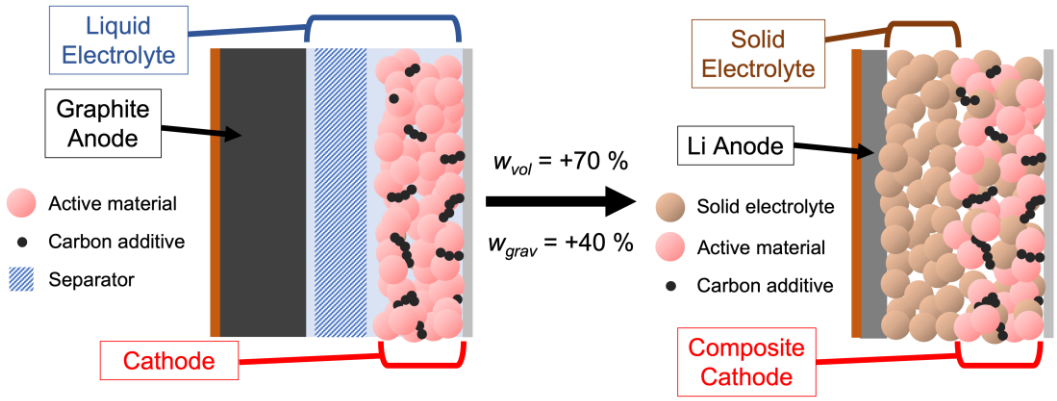


Figure 1.3: Schematic showing the potential gravimetric and volumetric energy density advantages of a Li anode solid-state battery over a conventional Li-ion battery with a liquid electrolyte. Adapted from Janek, J.; Zeier, W. G. *Nat. Energy* 2016, *1* (9), 16141.[29]

a result of Li consumption in side-reactions.[29,30] In addition, solid electrolytes can act as a physical barrier against dendritic growth.[31,32] However, solid electrolytes have a "critical current density" below which cells can charge free of dendrites, but above which dendrites penetrate the solid electrolyte, leading to cell failure, in the case of ceramic electrolytes even when > 95 % dense.[10,33] This limits the rate at which they can charge, although best-in-class materials are now reaching practical charging rates as high as 8.6 mA/cm^2.[34]

Solid electrolytes come with their own challenges, including for ceramic electrolytes the difficulty of producing highly dense, highly conductive thin films and the difficulties of interfacing these with the anode and cathode respectively.[10,35–37] Interfacing a solid electrolyte with a cathode is highly challenging and necessitates a wholesale change in the cathode architecture.[29] Active materials require both ionically conducting pathways across the cell and electronically conducting pathways to the current collector to enable redox to occur. In a liquid electrolyte cell, the electrolyte soaks into the pores of the cathode, giving Li-ion pathways, and carbon additives to the cathode material provide electronic conductivity throughout the cathode. In a solid electrolyte cathode this is more challenging. To give ionically conducting pathways throughout, solid electrolyte particles must be added to form a composite cathode.[38] This poses a number of challenges:

- Addition of solid electrolyte to the composite cathode increases the mass and the volume of the cathode.
- Solid electrolyte particles are electronically insulating and so have the potential to disrupt electronically conductive pathways.
- Some solid electrolyte materials require densification by high-temperature sintering to be effective ionic conductors. Co-sintering can lead to degradation of the active material or reactivity between the active material and solid electrolyte.[39–41]
- Intimate contact at the solid-solid interfaces between active material and solid electrolyte particles must be maintained throughout cycling despite the volume contractions and expansions of the cathode active material particles during the process of Li-ion intercalation/deintercalation.[42,43]

Whilst the problems to be overcome at the cathode interface demand intense research effort, this thesis instead focusses on the challenges of forming and maintaining a stable metal anode/solid electrolyte interface. To this end, the next two sections of this introduction discuss properties of solid electrolytes (Section 1.3) and metal anodes (Section 1.4), before discussing theory and key literature relating to the metal anode/solid electrolyte interface in Section 1.5.

1.3 Solid Electrolytes

This section aims to summarise the properties of common ionically conductive solid electrolytes, before delving in greater detail into the solid electrolytes used in this thesis. Properties that will be discussed include ionic conductivity, anodic and cathodic stability, mechanical properties and processability.

1.3.1 Properties of solid electrolytes

To be considered as potential candidates for solid-state battery application, solid electrolytes must satisfy a number of stringent criteria[31,44,45]:

- High room-temperature ionic conductivity. Common liquid electrolytes have conductivities of approximately 10^{-2} S/cm. Solid electrolyte separators require conductivities of > 10^{-3} S/cm and it has even been suggested that conductivities of > 10^{-2} S/cm are necessary for the solid electrolyte component of the composite cathode if high charge/discharge rates are going to be achieved.[46,47]
- Negligible electronic conductivity to prevent self-discharge and dendrite growth.
- Acceptable chemical stability against the Li metal anode and common cathode materials. Whilst few materials are truly stable across the voltage range of cell operation, it is important that any interphases formed are self-passivating and have some ionic conductivity.[30,33,48,49]
- High critical current above which dendrites grow (more details are given in Section 1.5.3). The solid separator must be able to resist the penetration of dendrites at high rates of charge.[50] This is sometimes considered to be related to the mechanical properties of the electrolyte.[51–54]
- Ease of processability of the solid electrolyte.[35]

Whilst there is some heterogeneity in each, properties of solid electrolytes will be discussed by class for the purpose of brevity. First, inorganic solid electrolytes are discussed, primarily focussing on oxides and sulphides, but concluding with a brief discussion of other inorganic solid electrolytes such as nitrides, boranes, carboranes and halides. Next, a very brief discussion of solid polymer electrolytes is made. Finally, the most common Na-ion conducting solid electrolytes are discussed and comparisons to Li-ion conducting analogues are drawn.

1.3.1.1 Oxide solid electrolytes

Perhaps the most commonly used oxide solid electrolytes are the garnets, such as $Li_7La_3Zr_2O_{12}$ and its dopants.[55] The specific advantages and disadvantages of LLZO-type solid electrolytes will be discussed first, as most are general to all oxide solid electrolytes. Some differences from other oxide-type solid electrolytes will be discussed at the end of the section.

Advantages:

- Kinetic stability against the Li anode means that no Li is lost to formation of a resistive SEI, (Figure 1.4).[48,56–59]
- Oxides have reasonable oxidative stability against high voltage cathodes. Indeed, stability is much improved compared to organic liquid electrolytes and so should lead to reduced degradation.[48,55,57,58]
- LLZO-type electrolytes are relatively stable in air, making them more easily processable. This being said, they are not stable in moist air, forming a resistive surface layer composed of Li_2CO_3 and LiOH.[60,61]

Disadvantages:

- Oxide ceramics require sintering at high temperatures (often > 1000 °C) in order to create low resistance pathways for Li-ion diffusion between grains.[62] In the composite cathode, the oxide solid electrolyte requires high temperature sintering, but at high temperatures there will be degradation of, or reaction with, the cathode active material.[63,64] Due to this challenge, oxide solid electrolytes are more commonly deployed as solid separators in hybrid batteries than in truly all-solid-state batteries. What is more, high temperature sintering is an expensive, energy intensive process.

- Common oxide solid electrolytes have fairly low ionic conductivities (~ 10^{-4} S/cm).[55] Provided the separator (layer of electrolyte between the anode and cathode) can be manufactured sufficiently thin (10s of microns) then this conductivity is sufficient for the separator. However, the cathode needs to be much thicker and the ionic conductivity in the composite cathode needs to be higher than oxides can currently deliver, which can be limiting to the achievable rates of charge and discharge.
- Mechanically, oxides are stiff and brittle,[65] for example LLZO has a high elastic modulus of approximately 150 GPa and a fracture toughness of 0.9-2.4 MPa·$m^{0.5}$.[33,66–68] As a result, good interfacial contact is a challenge, especially within the cathode where volume changes can lead to fractures in the solid electrolyte and cathode particles.

In summary, LLZO-type electrolytes have excellent stability against both Li anodes and high-voltage cathodes, but are disadvantaged by their relatively low ionic conductivities and the necessity of sintering them at high temperatures. Other common oxides include NASICON-structured $Li_{1-x}Al_xGe_{2-x}(PO_4)_3$ (LAGP) and perovskite-structured $Li_{3x}La_{2/(3-x)}TiO_3$ (LLTO). However, these materials have the severe disadvantage that they are unacceptably unstable against a Li metal, forming mixed conducting interphases (MCIs) which do not self-passivate and continue to grow, leading to unworkably high cell resistance.[69–73] These materials therefore cannot be used in conjunction with a Li metal anode, removing one of the key advantages of the solid-state battery.

1.3.1.2 Sulphide solid electrolytes

Sulphide solid electrolytes, such as Li_3PS_4 and argyrodite-structured Li_6PS_5Cl, have quite contrasting strengths and weaknesses compared to the oxides:

Advantages:

- Sulphide electrolytes are "softer" than their oxide counterparts and can be effectively densified under moderate conditions, without requiring high sintering temperatures.[74] This is in part due to their relatively low elastic modulus of approximately 15-30 GPa.[74,75] Their deformation enables better contact with the cathode particles under pressure, enabling their use in truly all-solid-state batteries.
- Sulphides have the highest ionic conductivities of common solid electrolyte materials, often in the order of 10^{-3} S/cm,[44] with some such as $Li_{10}GePS_{12}$ (LGPS) and $Li_7P_3S_{11}$ achieving conductivities of > 10^{-2} S/cm.[76,77] These high conductivities are sufficient to enable enough ion transport in the composite cathode to permit at least moderately high current densities compared with oxides.

Disadvantages:

- Unlike oxides, sulphides are not stable against Li metal and react to form resistive SEI layers, Figure 1.4.[57,58,78] This being said, whilst these reactions will consume active Li on the first formation of the SEI, for electrolytes such as Li_3PS_4 and Li_6PS_5Cl this is a "one-time-cost" in contrast to liquid electrolytes in which each cycle leads to reformation of new SEI, consumption of active Li and resultant capacity fade.[79–81] This is not the case for more conductive LGPS as, like LLTO and LAGP, the interphase formed against Li metal does not passivate and continues to consume the solid electrolyte, resulting in cell death.[82,83]
- Sulphides also have poor oxidative stability against high voltage cathode materials, Figure 1.4.[30,58,78,84] As a result, it is necessary to coat cathode active material particles with ceramic coatings to prevent severe degradation.[85–87] This adds an additional highly resistive barrier to Li-ion conduction into the cell, with associated overpotential.

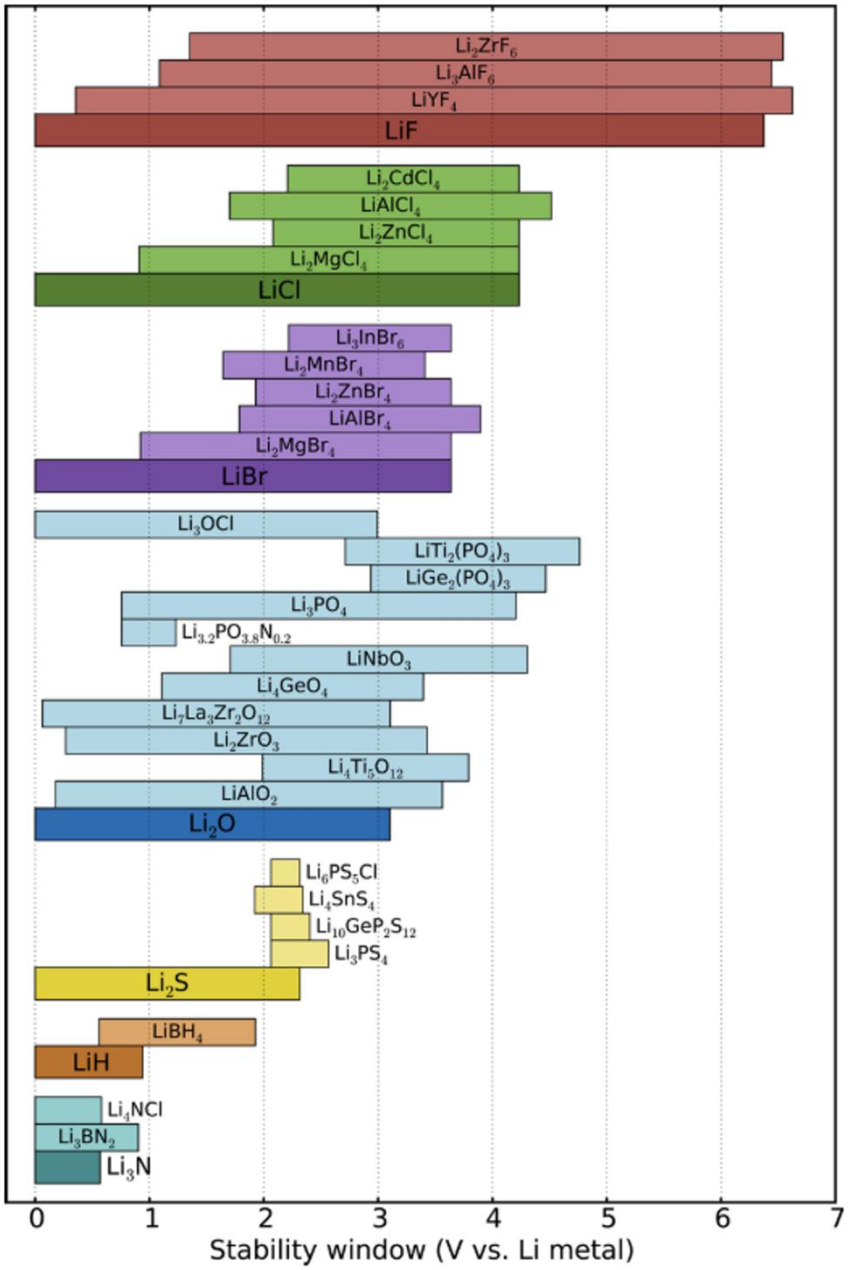


Figure 1.4: Figure showing the computationally predicted electrochemical stability windows of solid electrolyte materials. Reprinted with permission from Richards, W. D.; Miara, L. J.; Wang, Y.; Kim, J. C.; Ceder, G. *Chem. Mater.* 2015, *28*, 266–273.[48] Copyright 2015 *American Chemical Society*.

- Sulphide electrolytes are air and moisture sensitive, making manufacture more challenging.[44,88,89]

In summary, whilst sulphides have challenges related to their stability against Li metal anodes and high voltage cathodes, these problems are surmountable. Their favourable

mechanical properties and high ionic conductivities make them attractive candidates for commercial all-solid-state batteries, which is why companies are pursuing this cell chemistry (e.g. Solid Power).

1.3.1.3 Other inorganic solid electrolytes

Whilst they receive the most research interest, sulphides and oxides are not the only classes of inorganic solid electrolytes. The nitride solid electrolyte Li_3N can reach a conductivity of approximately 1 mS/cm with H^+ doping,[90] and displays excellent stability against a Li metal anode. However, the material is very highly reducing and so has a poor oxidative stability, degrading above approximately 0.44 V vs. Li^+/Li.[78,91] The reducing nature of Li_3N makes it very difficult to process, reacting with air and violently with water. In addition, achieving high conductivities requires the ceramic to be sintered, making processing more challenging.[91]

Boron-based chemistries such as the borohydride $LiBH_4$, boranes such as $Li_2B_2H_{12}$ and carboranes such as $Li_2(CB_9H_{10})_{0.7}(CB_{11}H_{12})_{0.3}$ have recently shown promise,[92–95] with best-in-class materials showing high room-temperature conductivities approaching 10^{-2} S/cm and appearing to show excellent stability against a Li metal anode.[96] However, poor stability against high voltage cathodes has been observed[97] and the synthesis of the best performing materials such as $Li_2(CB_9H_{10})_{0.7}(CB_{11}H_{12})_{0.3}$ is highly challenging and scalability has not been proven.[96] As such, despite their promise, boron-based chemistries lag behind their oxide and sulphide counterparts in both material development and understanding.

Finally, Li halides show promise as solid electrolyte materials.[98,99] These materials show many advantages, in particular high oxidative stability windows of > 4 V vs Li^+/Li.[100–102] What is more, halide electrolytes show acceptable ionic conductivities without the need for

high temperature sintering, making them more easily deployable in composite cathodes than common oxide solid electrolytes. However, a significant drawback is the stability of the halides against lithium metal anodes, with Li_3YCl_6 reported to form a continuously growing mixed conducting interphase, and Li_3InCl_6 reported to form a highly resistive SEI against Li metal.[103] Although halides are not utilisable in contact with the Li anode, a recent study showing low resistance against Li_6PS_5Cl raises the intriguing possibility of using halides such as Li_3InCl_6 as the solid electrolyte component of the composite cathode and using a different solid electrolyte such as Li_6PS_5Cl as the separator.[103]

1.3.1.4 Solid polymer electrolytes

Solid polymer electrolytes consist of Li-ion conducting salts (such as LiTFSI and $LiPF_6$) dissolved in a polymer (most commonly a PEO-based polymer). The conductivity of polymer electrolytes is based on covalent bonding between the polymer chain and the salt which facilitates ionic separation and Li-ion hopping. Whilst polymer electrolytes have found commercial application (e.g. by Bolloré),[104] they too have significant drawbacks as well as advantages.[105,106]

Advantages:

- It is much more facile to fabricate thin films of polymer electrolytes compared with making thin films of inorganic solid electrolytes. Solution-based casting methods are well established and the flexibility of the cast films (elastic moduli on the order of 1 MPa) makes them more easily handleable.[107]
- Whilst Li-ion conductive salts are costly, overall, solid polymer electrolytes are lower-cost alternatives than their inorganic solid electrolyte competitors, in a large part due to their manufacturability.[105,106]

Disadvantages:

- Solid polymer electrolytes often have poor room-temperature conductivity (typically $\leq 10^{-5}$ S/cm). This is charge/discharge rate limiting and necessitates operation of polymer electrolyte solid-state batteries at elevated temperatures, typically as high as 80 to 120 ºC.[105,106,108]
- Just as with liquid electrolytes, Li metal reacts with polymer electrolytes. It is commonly observed that Li reacts with trace solvents remaining in the electrolyte, forming highly resistive interlayers.[106,109]
- The transference number (the ratio of electrical current carried in the electrolyte by the cation) of Li-ion conduction in a polymer electrolyte is < 1 and therefore salt depletion at the Li anode interface will lead to dendrite growth by the same mechanism as for liquid electrolytes. Greater detail on this mechanism is given in Section 1.5.3.1. There is some evidence that polymer electrolytes can help to reduce dendrite growth to some extent compared with liquids, but the charging currents are limited by dendrite growth at high rates.[110,111]

A key advantage of polymer electrolytes is their processability, however they are strongly disadvantaged by their low ionic conductivities and their inability to prevent Li dendrite penetration even at moderate current densities. To overcome this, a substantial body of research has been carried out in compositing polymer electrolytes with inorganic solid electrolytes to improve these properties. However, whilst dispersed solid electrolyte particles improve the ionic conductivity compared to pure polymer electrolytes, conductivities remain lower than dense inorganic solid electrolytes. What is more, composites are “polymer-like” in the way in which they fail, i.e. addition of inorganic ceramic particles does not significantly improve the polymer electrolyte’s resistance to dendrite growth.[112]

1.3.1.5 Na-ion conducting electrolytes

Whilst much of this thesis focusses on Li metal anode solid-state batteries, in Chapter 3 the interface between a Na metal anode and a Na-ion conducting electrolyte is studied and so this introduction would be incomplete without a brief discussion of Na-ion conducting electrolytes. In general, Na-ion conducting solid phases have the same advantages and disadvantages as their Li analogues. Oxides have good stability against anode and cathode materials, but face challenges to integrate with the cathode and in manufacturing thin films, whereas sulphides don't require high temperature sintering and so are more facile to integrate in the composite cathode, but face problems of stability at both the anode and cathode interfaces.[113,114]

Whereas their general properties are similar, the electrolyte materials themselves are not directly structurally analogous. The most common Na-ion conducting oxides used in solid-state batteries are Na-β''-Alumina, which will be discussed in depth in section 1.3.2.2, and NASICON-type electrolytes such as $Na_{1+x}Zr_2Si_xP_{3-x}O_{12}$. The most common sulphide electrolytes are the thiophosphate phase Na_3PS_4 and phases that are related to it by doping or element substitution.

1.3.2 Solid electrolytes in this thesis

Having discussed in generality the properties of different types of solid electrolytes, the solid electrolytes used in this thesis will be discussed in greater detail, including their crystal structures, the mechanisms of their ionic conductivity and other research finding pertinent to their use in this thesis.

1.3.2.1 Li_6PS_5Cl

Li_6PS_5Cl is the solid electrolyte used in Chapters 4 and 5 of this thesis. It is a member of a family of Li-ion conductors with the argyrodite crystal structure, which also includes

related compositions such as Li_6PS_5Br, Li_6PS_5I and Li_7PS_6. Structurally, Li_6PS_5Cl can be considered in the $F\bar{4}3m$ space group, as shown in Figure 1.5a, in which S atoms occupy the 16*e* Wyckoff sites and P atoms occupy the 4*b* sites, forming a face-centred cubic array of PS_4 tetrahedra.[115] The 4*a* and 4*c* sites are occupied by an equal number of S and Cl anions, disordered across these sites. The S and Cl anions define a tetrahedrally coordinated

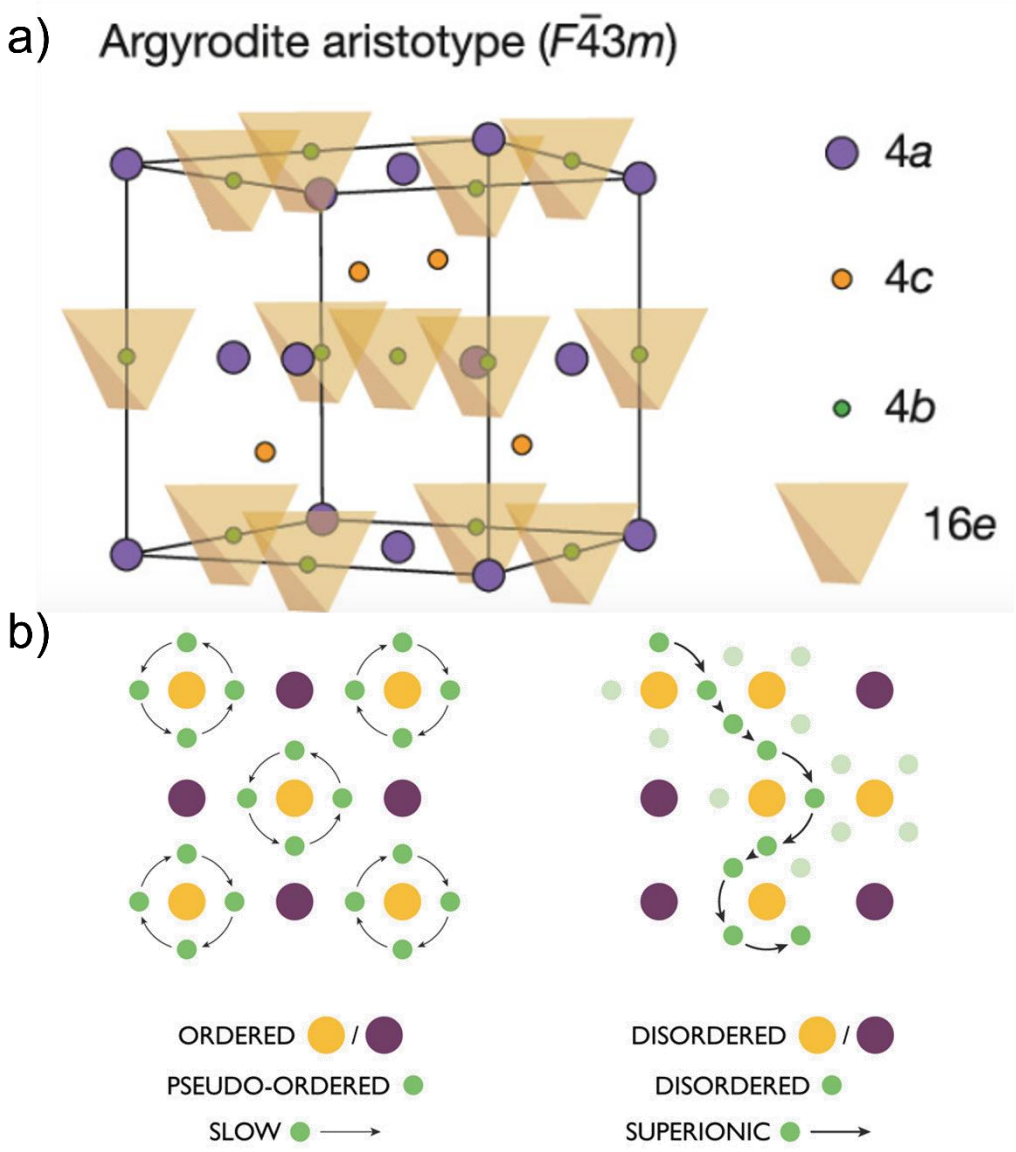


Figure 1.5: Figure showing a) the Argyrodite structure in which the 4*b* and 16*e* sites are PS_4 tetrahedra, 4*a* and 4*c* sites are occupied by an equal ratio of S and X (where X = Cl, Br, I) and the remaining tetrahedral sites are partially occupied by mobile Li-ions; and b) a schematic representation of how disorder of S^{2-}/X^- (yellow/purple) (where X = Cl or Br) leads to superionic conduction of Li-ions (green), but order of S^{2-}/I^- sites leads to slow ionic conduction of Li-ions. Reprinted with permission from Morgan, B. J. *Chem. Mater.* 2021, *33* (6), 2004–2018.[115] Copyright 2021 *American Chemical Society*.

lattice, in which the tetrahedral sites are partially occupied by Li cations. It is by Li-ion jumps between these tetrahedral sites that Li_6PS_5Cl can superionically conduct Li-ions.

It should be noted that whilst Li_6PS_5Cl, Li_6PS_5Br and Li_6PS_5I have the same structure, the conductivity of Li_6PS_5I is approximately three orders of magnitude lower than those of Li_6PS_5Cl and Li_6PS_5Br at room-temperature. The difference in conductivity is due to differences in the extent of S^{2-}/X^- (X = Cl, Br, I) site disorder. Whereas for X = Cl, Br there is disorder between the 4*a* and 4*c* Wyckoff sites, this is not the case when X = I. Li cations preferentially coordinate with S^{2-} rather than X^-, Figure 1.5b. It has been proposed that disorder between S^{2-}/X^- improves conductivity as it can lead to directly adjacent LiS_6 octahedra which would be expected to result in an unfavourably short Li – Li distance. To avoid this energetically unfavourable repulsive force, Li is instead "shared" between adjacent SLi_x polyhedra, facilitating fast Li-ion conduction.[115]

Li_6PS_5Cl powder is often synthesised by mechanical milling (as the material used in this thesis is), or by liquid-phase synthetic routes.[116] Ionic conductivities of cold-pressed Li_6PS_5Cl disks are often in the region of 2-5 mS/cm, increasing still further in more highly densified samples.[74] As described in the previous section, like many sulphide electrolytes Li_6PS_5Cl is unstable at both high and low voltages. In contrast to the earliest reports,[117] the oxidative stability of Li_6PS_5Cl is poor, decomposing at approximately 2.2-3.0 V vs Li^+/Li to form elemental sulphur, polysulphides, phosphates, Li_2S and LiCl.[118,119] In addition, Li_6PS_5Cl degrades below approximately 2 V vs Li^+/Li, forming Li_2S, Li_3P and LiCl.[79,119–121] More detail on degradation at the interface with Li metal, including experimental results, is given in Chapter 4.

1.3.2.2 Na-β''-Alumina

Na-β''-Alumina is a Na-ion conducting electrolyte which has historically been used at high temperatures (typically > 300 °C) in conjunction with molten-phase sodium anodes in batteries such as Na-S and ZEBRA batteries. As such, Na-β''-Alumina ceramics have been rigorously characterised in the literature.[113,114] Na-β''-Alumina is a metastable phase, and although stability can be improved by doping with MgO or Li_2O, it is rarely found to be phase pure. A commonly observed secondary phase is the related phase Na-β-Alumina, which is also a Na-ion conductor, but has a lower conductivity. The two structures are

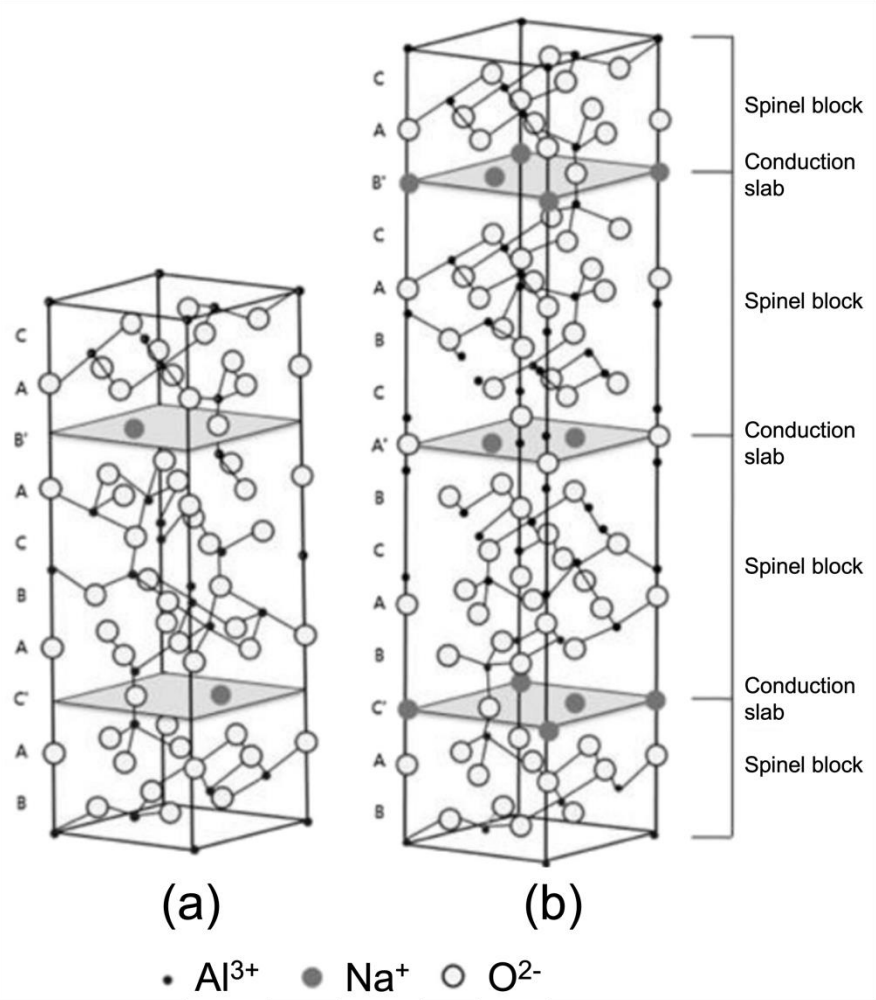


Figure 1.6: Figure showing the unit cells of a) Na-β-Alumina and b) Na-β''-Alumina. Both structures consist of alternating Al_2O_3 spinel blocks and Na_2O conduction planes but differ in stacking arrangement. Reprinted with permission from Lee, D. H.; Lee, S. T.; Kim, J. S.; Lim, S. K. *Mater. Res. Bull.* 2017, *96*, 143–148.[122] Copyright 2017 *Elsevier*.

closely related, as shown in Figure 1.6.[122] Both consist of alternating layers of Al – O spinel blocks and Na – O conduction planes. Conduction occurs exclusively in the conduction planes, with negligible ionic conductivity measured between conduction planes. As such, both Na-β-Alumina and Na-β''-Alumina are 2D conductors. The higher conductivity of the Na-β''-Alumina (approximately 2 mS/cm) is a result of higher Na-ion concentration in the conduction plane.[123–125]

Na-β''-Alumina offers many advantages for studying stripping/plating dynamics at the metal anode/solid electrolyte interface. A significant factor is that unlike an alternative such as Na_3PS_4, Na-β''-Alumina is completely unreactive when in contact with a Na metal anode, as was demonstrated by Janek and co-workers using PEIS (Figure 1.7a) and X-ray photoelectron spectroscopy (Figure 1.7b).[126] What is more, the failure modes of Na-β''-Alumina are extremely well characterised, indeed many of the earliest models for growth of dendrites through ceramic solid electrolytes were based on studies using Na-β''-Alumina (see Section 1.5.3.1).[127–129]

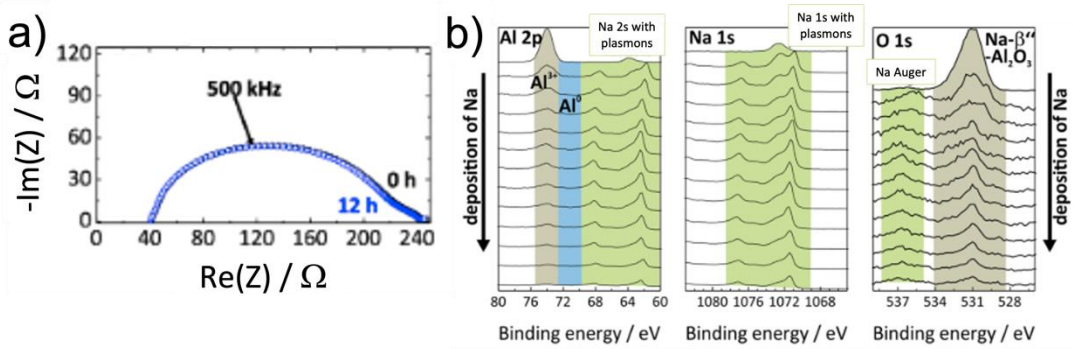


Figure 1.7: Figure showing the stability of Na-β''-Alumina against a Na metal anode. a) is potentiostatic electrochemical impedance spectroscopy (PEIS) showing no change in the Nyquist plot of a Na/Na-β''-Alumina cell with time; and b) shows X-ray photoelectron spectroscopy as Na is deposited onto the surface of Na-β''-Alumina, showing no change in the chemical states of Al or O. Reprinted (adapted) with permission from Wenzel, S.; Leichtweiss, T.; Weber, D. A.; Sann, J.; Zeier, W. G.; Janek, J. *ACS Appl. Mater. Interfaces* 2016, *8* (41), 28216–28224.[126] Copyright 2016 *American Chemical Society*.

1.4 Metal Anodes

1.4.1 Lithium anodes

Lithium metal has a low melting point of 180.5 °C and is a crystalline solid with a body-centred cubic lattice at room-temperature.[130] It has both a very low density and the lowest redox potential of any element (-3.04 V vs SHE), making it the optimum anode material for achieving the highest volumetric and gravimetric energy densities. However, although the very low redox potential makes it an attractive anode material, it also means that Li metal has a highly reducing nature.[33] It is not stable in air, forming a passivation layer of nitrides, carbonates, oxides and hydroxides, and is not stable against many solid electrolyte materials as discussed in Section 1.3 of this chapter.[131–133]

It is important to note that at room-temperature Li metal has a low electrical resistivity of approximately 10 nΩ·m.[134] As a result, the kinetics of processes at the interface are not determined by availability of electrons, but rather by Li atom transport within the Li metal.[33] As such, the transport properties of Li metal demand further discussion before interfacial processes can be discussed in Section 1.5.

1.4.1.1 Diffusivity

Self-diffusion within Li metal can be considered to be a process of monovacancy transport in which vacancies are created and then migrate.[135] The self-diffusion coefficient for Li, D_{SD}, can be written as:

$$D_{\mathrm{SD}} = D_{0,\mathrm{SD}}{}^{-E_{\mathrm{A}}/RT} \tag{1.1}$$

where $D_{0,\mathrm{SD}}$ is the pre-exponential factor for self-diffusion, T is the absolute temperature and the activation energy, $E_{\mathrm{A}} = H_{\mathrm{V}}^{\mathrm{F}} + H_{\mathrm{V}}^{\mathrm{M}}$ where $H_{\mathrm{V}}^{\mathrm{F}}$ is the enthalpy of formation of a vacancy and $H_{\mathrm{V}}^{\mathrm{M}}$ is the enthalpy of migration of a vacancy.[33]

Self-diffusion coefficients for Li have been measured experimentally using NMR techniques, with two studies by different methods giving room-temperature values of 7.8 $\times 10^{-11}$ cm^2/s and 9 $\times 10^{-11}$ cm^2/s with activation energies of 0.52 and 0.57 eV.[135,136]

1.4.1.2 Mechanical properties

At ambient temperatures, Li metal is readily plastically deformable under pressure and this deformation is an important process by which Li atoms are transported to the Li metal/solid electrolyte interface during battery operation (see Section 1.5).[137,138]

Plastic deformation is the change in size or shape of a material under an applied force which is not reversible when the applied force is removed.[139] For example, consider the curves relating the stress (ε) and strain (σ) of Li metal by Dasgupta and co-workers (Figure 1.8).[140] When low stresses are applied, the strain varies linearly, indicating that in this region deformation is elastic. The Young's modulus (E) is the gradient of the curve in this region

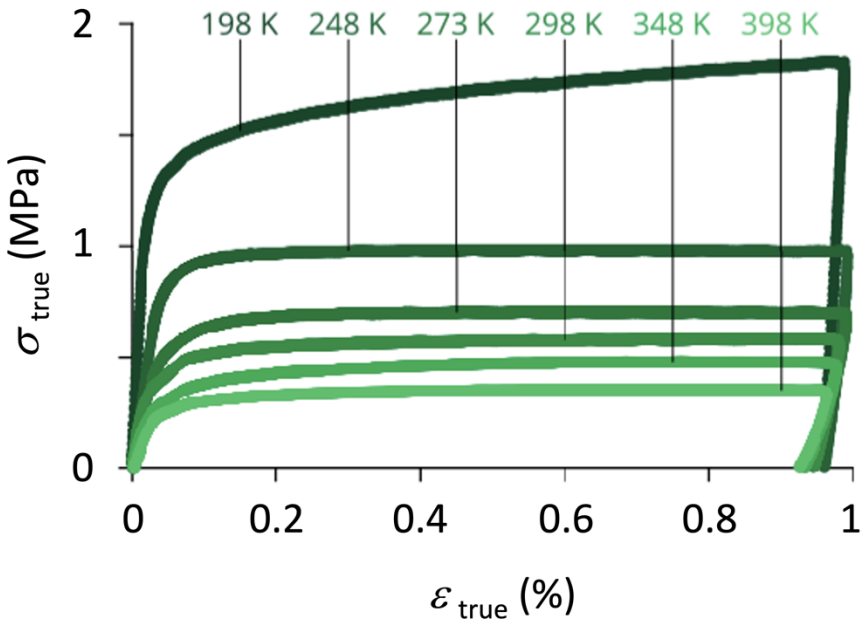


Figure 1.8: Figure showing the temperature-dependent response of a Li metal foil under a strain rate of 3×10^{-5} s^{-1}. Strain-hardening was observed at the lowest temperature of 198 K, but at higher temperatures creep was observed. Reprinted (adapted) with permission from LePage, W. S.; Chen, Y.; Kazyak, E.; Chen, K.-H.; Sanchez, A. J.; Poli, A.; Arruda, E. M.; Thouless, M. D.; Dasgupta, N. P. *J. Electrochem. Soc.* 2019, *166* (2), A89–A97.[140] Copyright 2019 *Institute of Physics*.

and gives an indication of the "stiffness" of a material as it deforms elastically. At higher strain rates, the stress-strain curves deviate from linearity, indicating that the material is deforming plastically by dislocation glide. The point of deviation is defined as the yield strength (σ_y). After a material such as Li has deformed plastically, upon release of the applied force the material will remain deformed and will be left with a residual strain, known as the plastic strain (ε_p).[137,138,140]

It should be noted that deformation can also occur below the yield strength of a material and this process is known as creep. Creep is dependent on the temperature and is expected to occur readily in a material at temperatures approaching the melting point. As Li has a low melting point, it undergoes creep at room-temperature. There are two types of creep; diffusional creep and power-law creep. Under the normal operating conditions of a battery,

Table 1.1: Summary of literature values of elastic moduli (top) and yield strength (bottom) of polycrystalline lithium metal.

Elastic Modulus		
Method	***E* (GPa)**	**Reference**
Wire bending	5.0	Bridgman *et al.* (1922)[142]
Tension	7.8	Tariq *et al.* (2003)[143]
Compression	1.9	Schulz *et al.* (2002)[144]
Acoustic	8.0	Robertson *et al.* (1960)[145]
Acoustic	7.8	Masias *et al.* (2019)[137]
Nanoindentation	9.4	Fincher *et al.* (2020)[146]

Yield Strength			
Method	**Strain Rate ($\times 10^{-3}$ s^{-1})**	**σ_y (MPa)**	**Reference**
Tension	0.11	0.60	Hull *et al.* (1959)[147]
Tension	2.0	0.76	Tariq *et al.* (2003)[143]
Tension	1.21	0.73-0.81	Masias *et al.* (2019)[137]
Tension	1.67	0.64	Schulz *et al.* (2002)[144]
Tension	0.5	0.57	Fincher *et al.* (2020)[146]
Compression	500	1.26	Fincher *et al.* (2020)[146]

where cycling occurs at near-room-temperature and cells are under a moderate stack-pressure, power-law creep is an important mechanism of Li atom transport within the anode.[140]

The mechanical properties of Li metal that have been reported in the literature vary widely, almost certainly due to the dependence of elastic modulus, yield strength and creep properties on 1) the method of measurement (measured in tension, compression or by acoustic techniques),[137] 2) whether experiments are carried out on the micro- or macro-scale (e.g. determination of mechanical properties based on nanoindentation might be affected by crystal orientation), 3) the length-scale of the measured sample, as nanoscale and bulk samples have been observed to show deviation in mechanical properties,[138,141] 4) strain-rate dependence of the mechanical properties, 5) temperature dependence of the mechanical properties[140], and 6) the dependence of mechanical properties on the processing history and impurity concentration.[33] Table 1.1 summarises key reports of the mechanical properties of Li metal from the literature.[137,142–147]

1.4.2 Comparison with sodium

Metallic bonding is weaker in descent of the Group 1 elements, and so the melting point of Na is lower than that of Li; only 97.8 ºC. In accordance with this, the self-diffusivity of Na metal is higher than for Li metal,[148] the yield strength is lower ($\sigma_{y,Na}$ = 0.19 – 0.28 MPa),[149,150] and Na creeps more readily at all length-scales as demonstrated by Pharr and co-workers, Figure 1.9.[150] Key findings on the mechanical properties of Na metal are summarised in Table 1.2.[149,150]

In general, mobility of Na atoms within a bulk Na anode is greater than the mobility of Li atoms within Li, both by self-diffusion and by deformation under applied pressure. This has consequences with regards to interfacial kinetics between the metal anode and solid

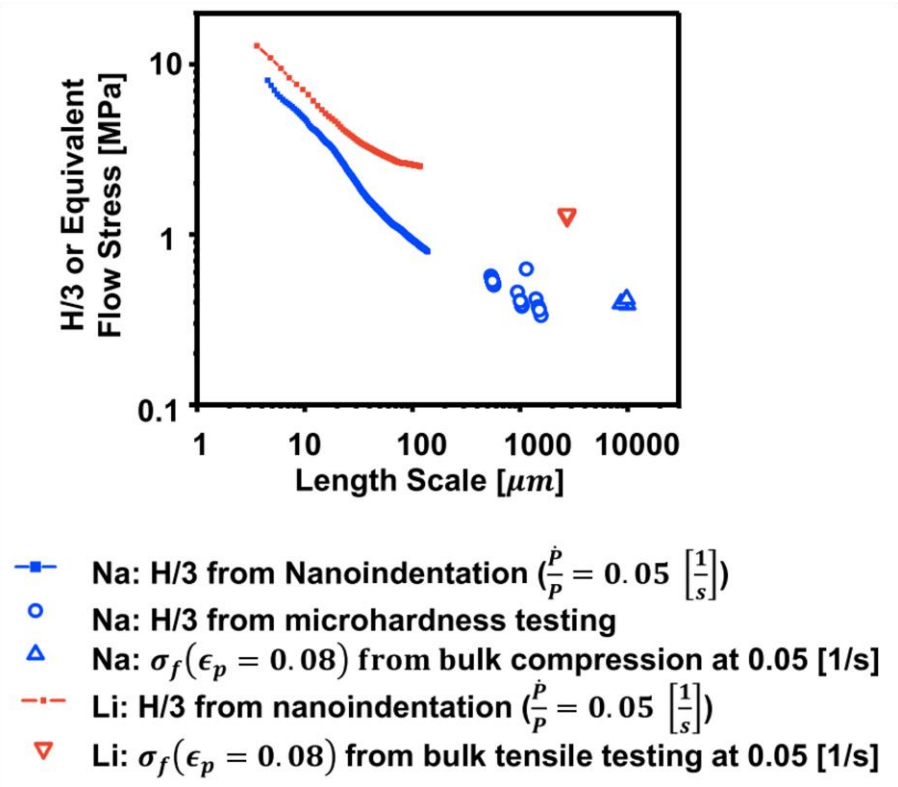


Figure 1.9: Figure showing the plastic properties of Na (blue) compared with Li (red). Flow stress or H/3 ($\sim\sigma_f$) is plotted as a function of length scale. H is hardness and σ_f is the flow stress. Reprinted with permission from Fincher, C. D.; Zhang, Y.; Pharr, G. M.; Pharr, M. *ACS Appl. Energy Mater.* 2020, *3* (2), 1759–1767.[150] Copyright 2020 *American Chemical Society*.

electrolyte, with Na anode SSBs showing less severe cycling rate limitations than their Li anode analogues,[151–153] a subject that will be expanded upon in Section 1.5.

Table 1.2: Summary of literature values of elastic moduli (top) and yield strength (bottom) of polycrystalline sodium metal.

Elastic Modulus		
Method	***E* (GPa)**	**Reference**
Acoustic	4.6	Wang *et al.* (2020)[149]
Nanoindentation	3.9	Fincher *et al.* (2020)[150]

Yield Strength			
Method	**Strain Rate ($\times 10^{-3}$ s^{-1})**	**σ_y (MPa)**	**Reference**
Tension	1.22	0.19-0.28	Wang *et al.* (2020)[149]
Compression	1.22	0.16-0.24	Wang *et al.* (2020)[149]
Compression	0.1-10	0.10-0.25	Fincher *et al.* (2020)[150]

1.4.3 Comparison with lithium alloys

Some lithium alloys have the advantage of higher Li self-diffusion coefficients than pure Li metal due to greater crystalline disorder.[154,155] Indeed, high Li diffusivities have been reported for alloys such as Li-Mg,[156] Li-Ag,[157] Li-Zn,[158] Li-In[159] and Li-Bi.[160]

However, whilst the self-diffusion properties of Li alloys are advantageous to battery applications, Li alloys have less propensity to deform under stack-pressure than Li metal. This is because it is more challenging for dislocations to move through the alloy crystal structure than through the pure Li metal structure.[139]

1.5 Lithium Anode/Solid Electrolyte Interfaces

Having discussed significant literature on common solid electrolytes (Section 1.3) and on metal anodes (Section 1.4), it is now possible to consider the interface between the two. The main causes of failure at the metal anode/solid electrolyte interface are 1) chemical/electrochemical degradation, potentially leading to Li loss, formation of a highly resistive interphase and capacity fade,[30] and 2) morphological changes at the interface as a result of the kinetic limitations of Li atom transport.[10,33,37] Different morphological changes occur during the processes of stripping and plating the Li metal anode, and so these are discussed separately in Sections 1.5.2 and 1.5.3, respectively.

1.5.1 Chemical and electrochemical stability

Whilst this thesis is primarily focussed on understanding morphological changes taking place during stripping and plating of the metal anode, it is important to do so with an understanding of the changes in chemistry, if any, that occur at the interface, so that these do not inhibit our ability to draw definitive conclusions.

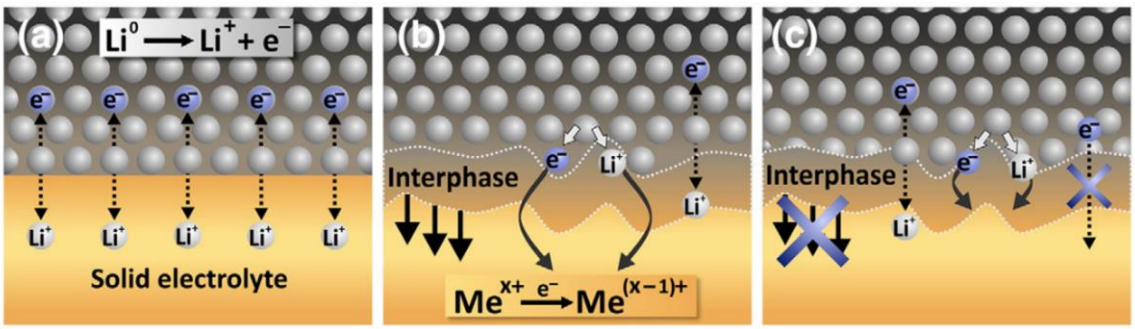


Figure 1.10: Schematic showing the three types of interface between metal anodes and solid electrolytes; a) a thermodynamically stable, non-reactive interface, b) a reactive interface forming a mixed conducting interphase (MCI), and c) a reactive interface forming a self-passivating solid electrolyte interphase (SEI). Reprinted with permission from Wenzel, S.; Leichtweiss, T.; Krüger, D.; Sann, J.; Janek, J. *Solid State Ionics* 2015, *278*, 98–105.[49] Copyright 2015 *Elsevier*.

When a solid electrolyte is brought into a contact with a metal anode, there are three types of interface that can form between the two phases.[49] These are summarised below, as well as schematically in Figure 1.10:

- Type 1: A thermodynamically stable interface, in which no interphase forms between the metal anode and solid electrolyte (Figure 1.10a). Among solid-electrolytes commonly considered for solid-state battery application, Na-β''-Alumina is uncommon as it appears to form a thermodynamically stable interface with Na metal.[126]
- Type 2: An unstable, non-passivating interface (Figure 1.10b). In this case, reaction between the metal anode and solid electrolyte leads to the formation of a mixed-conducting interphase (MCI) (both electronically and ionically conducting). Due to the electronic conductivity of the interphase, reduction of the solid electrolyte can continue to occur at the reaction front and the interphase does not self-passivate but instead continues to grow. Common examples of this behaviour have already been mentioned in Section 1.3, e.g. LAGP, LLTO and LGPS.
- Type 3: A thermodynamically unstable but self-passivating interface (Figure 1.10c). In this case, the solid electrolyte and metal anode react to form a solid-

electrolyte interphase which has negligible electronic conductivity and so does not continue to grow, but self-passivates. In many cases the ionic conductivity of the SEI, whilst not high, is not inhibitory due to the thinness of the interphase, and so these metal anode/solid electrolyte combinations can be considered for battery applications. Common examples of this behaviour are the interfaces between Li/Li_6PS_5Cl, Li/Li_3PS_4 and Na/Na_3PS_4.[79,126]

Methods to determine the stability of solid electrolytes against metal anodes have been developed, including powerful theoretical and computational tools, as well as practical methods.[30] Practically, Janek and co-workers have led the way on determining the stability of solid electrolytes, utilising potentiostatic electrochemical impedance spectroscopy (PEIS) collected sequentially over a number of days to probe for changes in interfacial resistance, coupled with XPS to observe changes in interfacial chemistry, e.g. Figure 1.7.[49,59,69,79,103,126,161] Similar techniques are used in Chapter 4 of this thesis.

1.5.2 Voiding when stripping the Li anode

At the beginning of this DPhil work, relatively little was known about the formation of voids in Li and Na metal anodes during the process of stripping. This section aims to lay out the state of knowledge at the start of the work and then goes on to describe significant works that have contributed to the growth of the field in recent years.

During the process of Li anode stripping, a Li atom at the Li/SE interface is oxidised to form a Li-ion whilst crossing the interface into the solid electrolyte, and an electron which travels around an external circuit. This leaves a vacancy at the interface which must be eliminated by diffusion of Li atoms if the contact area between the Li anode and solid electrolyte is to be maintained.[33]

1.5.2.1 Towards an understanding of voiding

Some of the earliest work on morphological instability between Li anodes and solid electrolytes was carried out in the 1980s. Due to the buried nature of the interface, no direct observations of interfacial contact loss were made, but 3-electrode cycling experiments revealed that contact was being lost at the interface during the process of stripping, for both Li/LiI and Li/Li_3N interfaces. This finding was recently corroborated by Koshikawa et al. for the more practically relevant Li/LLZO interface.[162–165] A number of these works posited that the loss of contact was likely due to the build-up of vacancies at the interface due to the slow diffusion kinetics of Li metal.

Recently, a number of studies have been conducted that have sought to pair similar electrochemical observations with other characterisation techniques to better understand the degradation happening at this interface during stripping. Janek and co-workers carried out pioneering work which paired 2-electrode cycling with EIS, showing that as the anode is stripped, interfacial vacancies accumulate into larger voids.[166] Voids were imaged for the

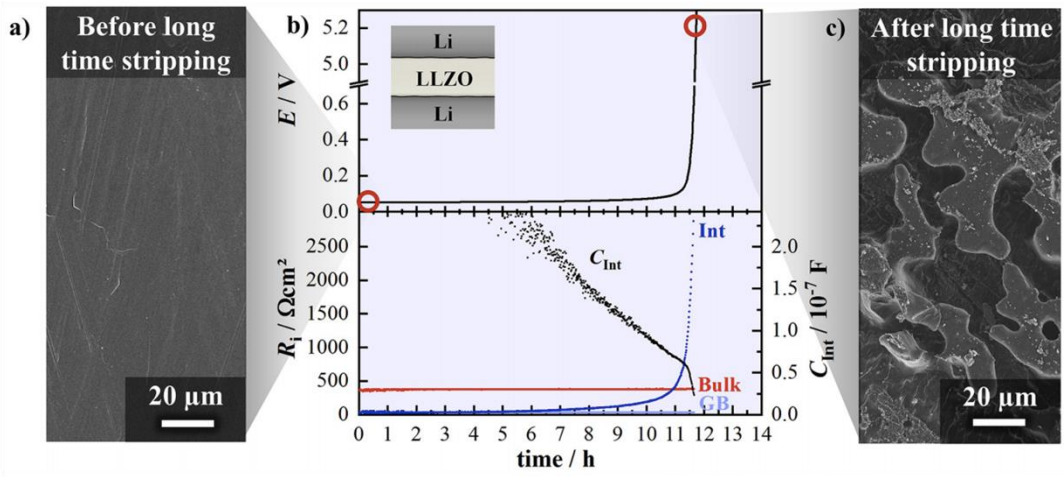


Figure 1.11: Figure showing the formation of interfacial voids during the process of stripping. a) shows an SEM of the pristine Li anode prior to cell cycling, b) shows the voltage profile during the process of stripping (top) and the evolution of bulk, grain boundary and interfacial resistances as well as interfacial capacitance throughout the stripping, and c) shows an SEM of the Li anode following stripping, in which void are present. Reprinted with permission from Krauskopf, T.; Hartmann, H.; Zeier, W. G.; Janek, J. *Appl. Interfaces Mater.* 2019, 11, 14463–14477.[166] Copyright 2019 *American Chemical Society*.

first time by scanning electron microscopy (SEM), in a simple comparison between the pristine (Figure 1.11a) and the stripped interface (Figure 1.11c). The dependence of void formation on the current density of stripping was also investigated for cells under no stack-pressure, finding that below a critical current (set by the self-diffusion in the Li anode) voids were not observed to form, but that above this current density interfacial contact loss occurred. Importantly, the critical current below which stripping was stable was predicted to be only 0.01 – 0.1 mA/cm^2, far too low for practical applications, a result which has motivated alternative strategies to increase the critical current for voiding, targeting the range of several mA/cm^2. Some of these strategies are described in Section 1.5.2.2.

Our concurrent work focussed on better understanding the process of voiding by coupling electrochemistry with imaging techniques not just over a single stripping, but over a longer duration of cycling.[120] It was found that following void formation on stripping, subsequent plating was able to reform the Li/SE interface, but left occluded voids set back from the interface within the Li metal. On subsequent stripping these voids would be uncovered and continue to grow in size. By this mechanism voiding would continue to worsen with each cycle. We introduced the concept of a critical current for void formation on stripping. Below this current the mass transport of Li to the interface exceeds the Li-ion flux away from the interface, and morphological stability is maintained during stripping, however above the critical current for voiding the transport of Li is insufficient, voids will form at the interface and worsen with cycle number until failure of the cell, Figure 1.12. No more detail will be given on this here, as this is the subject of Chapter 3 of this thesis.

Subsequently, other works have used X-ray computed micro-tomography to track void formation throughout cycling. A study by McDowell and co-workers investigated the dynamics of interfacial voiding during cycling in a system where continuous reactivity (Type 2, see Section 1.5.1) was occurring between the lithium anode and solid electrolyte,

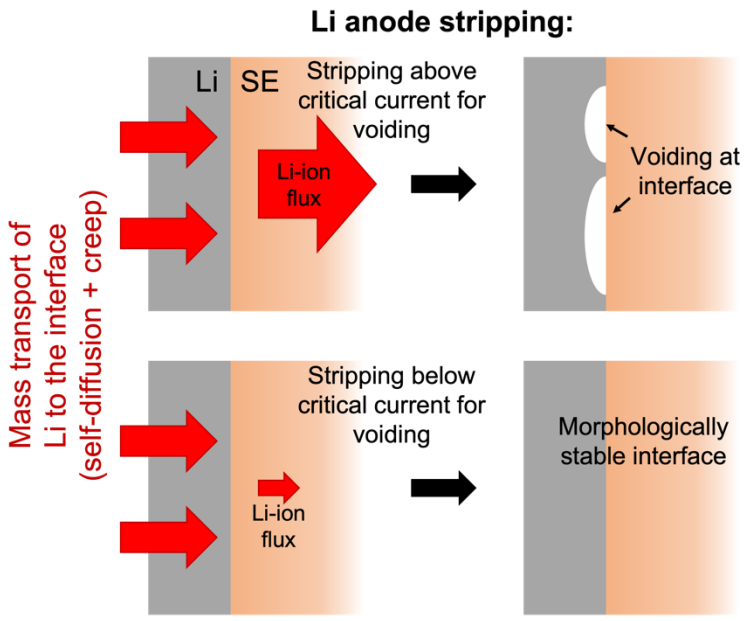


Figure 1.12: Schematic illustrating the concept of the critical current for voiding when stripping the metal anode of a solid-state battery. When stripping at a rate exceeding the rate of mass transport of Li to the interface, voiding occurs (top), whereas when stripping below the rate of mass transport of Li to the interface (bottom), the interface remains morphologically stable.

forming a continuously thickening resistive interphase.[167] Finally, a study by Hatzell and co-workers used machine learning to carry out segmentation of the XCT to overcome the challenge of differentiating between Li metal and void space (this challenge is discussed in Chapter 2, Section 2.2.5), and by-so-doing quantitatively record the extent of voiding in the anode.[168]

Finally, excellent theoretical work on how voids initiate and grow has been carried out in recent years. A number of factors have been posited to be related to propensity for void initiation and growth. Seymor *et al.* used a bond-breaking approach to suggest that interfacial adhesion between the metal anode and solid electrolyte plays a crucial role,[169] Deshpande and co-workers emphasise the importance of Li metal creep and propose that non-conducting impurities at the interface may participate in void initiation,[170] and Mo and co-workers modelled interfacial stripping to identify specific interfaces and cell operating conditions to prevent cell failure.[171]

1.5.2.2 Strategies to prevent voiding

It is clear that the formation and persistence of interfacial vacancies at the Li anode/solid electrolyte interface is responsible for formation of interfacial voids. This occurs when the rate of vacancy formation due to the current load exceeds the rate at which interfacial vacancies are eliminated by Li atom transport to the interface. Therefore, approaches that increase the rate of Li transport to the interface will increase the maximum current at which the interface will be stable.

Drawing on the earlier discussion of the transport properties of Li metal in Section 1.4 of this chapter, there are a number of methods by which the transport of Li atoms to the interface could be increased, and a number of these have already been explored in the literature:

- Stack-pressure. A number of studies, both experimental and theoretical have shown that stack-pressure can have a major impact on increasing critical current densities.[120,166,172–174] Self-diffusion alone gives Li atom transport rates that only enable very low rates of morphologically stable stripping. However, deformation of Li metal under an applied stack-pressure gives a second mechanism by which Li can be transported to the interface, increasing the critical current. For the Li/LLZO interface, Krauskopf et al. showed that application of a 35 MPa pressure could enable stable stripping at 0.1 mA/cm^2, a current density at which rapid failure due to voiding has been observed when no stack-pressure is applied.[166] Kasemchainan et al. showed for the Li/Li_6PS_5Cl interface that increasing the stack-pressure applied to the cell from 3 MPa to 7 MPa increases the critical current markedly from greater than 0.2 mA/cm^2 to greater than 1.0 mA/cm^2.[120] These studies are consistent with a study by Wang et al. which found that for a Li/LLZO interface, a pressure of 2 MPa was required to maintain stable stripping at 0.2 mA/cm^2.[172] In summary, quite high

stack-pressures, on the order of 10 MPa are required to increase the rate of transport of Li to the interface such that current densities of > 1 mA/cm^2 are accessible. The practical difficulties of applying such high stack-pressures are significant and would require additional components, adding expense and lowering energy density. For EV applications, these pressures are likely too high[37] and so other solutions must be examined.

- Operating temperature.[175] Not only will an increased operating temperature increase the rate of self-diffusion in the Li anode, but Dasgupta and co-workers have shown that a moderately increased temperature will also increase the rate of creep.[140] The effect of a moderately elevated operating temperature on the current for voiding is the subject of Chapter 4 of this thesis.
- Li alloy anodes. As discussed in Section 1.4.3, Li metal alloys often have higher self-diffusivity of Li than in pure Li metal. Krauskopf *et al.* studied Li-Mg alloy anodes, revealing that under no external pressure the Li-Mg showed a higher critical current for voiding than a pure Li metal anode.[156] This being said, whilst an improvement was observed, it was not so significant that stable stripping at practically high current densities were enabled. Under stack-pressures in the MPa range, the Li metal anode out-performed the Li-Mg alloy anode, presumably due to the superior creep properties of the Li compared to the Li-Mg.
- Na metal anodes. Na metal has both higher diffusivity and greater propensity to plastic deformation and creep than Li metal anodes and so should enable higher rates of stripping without the formation of interfacial voids. Determining critical currents for voiding of Na anode cells, and the dependence on stack-pressure, is the subject of Chapter 3 of this thesis.[151]

- Liquid metal anodes. Recent work by Park *et al.* showed that addition of a thin layer of Na-K liquid between LLZO and a Li anode doubled the critical current relative to an LLZO/Li interface.[153] The innovative use of a liquid interphase prevents interfacial vacancy or void formation, however the practical applicability to commercial cells has yet to be determined.

The importance of preventing the formation of interfacial voids cannot be overstated. Kasemchainan *et al.* showed that not only will contact loss increase cell overpotential during cycling, but local current densities at remaining areas of contact will increase. As voiding worsens with cell cycling, the area of contact between the metal anode and solid electrolyte decreases with each cycle and local currents increase until Li metal dendrites penetrate into the ceramic, eventually leading to total cell failure.[120] Dendrite growth, and preventative measures against dendrite penetration, are discussed in the following section.

1.5.3 Dendrite growth when plating the Li anode

The challenge of understanding and preventing dendrite growth when the Li anode is plated has received intense research scrutiny over several decades. Understanding and preventing dendrite penetration into inorganic solid electrolytes is at the very heart of making a successful solid-state battery, as only by doing so can Li anodes be safely used, unlocking high energy densities.[29] In the context of this thesis, whilst no part focusses on the specifics of dendrite growth, Chapter 5 explores the use of various carbon-based interlayers to protect the solid electrolyte from Li metal dendrite penetration and prevent cells from failing. Therefore, a detailed exploration of the challenges of dendrite growth is required to understand the motivations behind this work.

The process of plating is the direct reverse of the process of stripping. Under a current load, a Li-ion from within the solid electrolyte transfers across the Li/SE interface, where it is

reduced to form a Li atom. At an ideal, conformal interface, Li atoms are deposited evenly, layer by layer, and so no mechanical degradations at the interface would occur. However, real solid-state battery interfaces are far from ideal.[33] Insulating contaminants at the interface, flaws in the solid electrolyte, pre-existing porosity in the metal anode, electrode edge-related current enhancement, grain boundary effects and porous solid electrolytes, amongst other factors, can lead to inhomogeneous plating of Li, potentially resulting in growth of Li filaments into the solid electrolyte. However, whilst there are a multitude of observations of dendrite growth into solid electrolytes, there remains a great deal of debate as to the exact mechanism or mechanisms by which a metal as 'soft' as Li is able to cause fracture of high fracture strength inorganic solid electrolytes such that Li can traverse through the solid electrolyte and cause a short-circuit.

1.5.3.1 Towards an understanding of dendrites in solid electrolytes

The mechanism by which dendrites grow through liquid electrolytes is relatively well established.[176] Observations have shown the formation of 'mossy' Li (whiskers of Li insulated by SEI) at the surface of the Li anode, followed by the advance of 'tree-like' dendritic growths across the electrolyte. These differences in morphology have been explained as a transition from reaction-limited growth to diffusion-limited growth by Bai *et al.*, who investigated the mechanism of dendritic growth by coupling electrochemistry with optical microscopy, Figure 1.13.[177] Mechanistically, the formation of the 'tree-like' dendritic growths which lead to the cell short-circuit is of particular interest. Due to the low transference number of the liquid electrolyte, a depletion of salt concentration near the Li anode occurs during plating, leading to unstable Li deposition and the formation of dendrites.[178]

Unlike in liquid and polymer electrolytes, the transference number of inorganic solid electrolytes is unity, and so diffusion limitation near the electrolyte/anode interface cannot

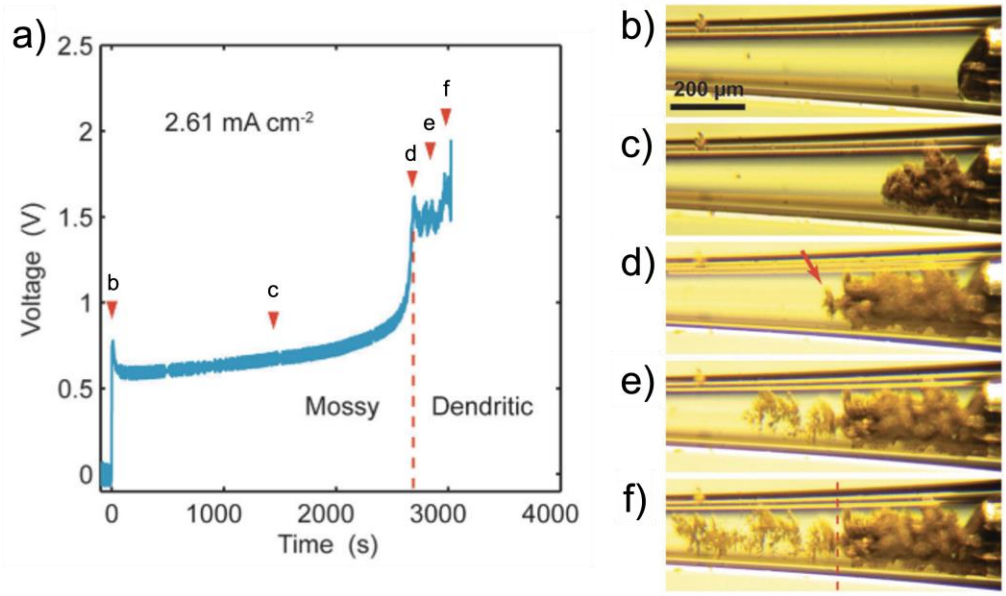


Figure 1.13: Figure showing the 'mossy' and then 'fractal' dendritic growth of Li through liquid electrolytes. a) shows the voltage response of the capillary cell when charged at 2.61 mA/cm^2. b)-f) show images of Li growth at different stages of plating, with the arrow in (d) indicating the beginning of 'fractal' dendritic growth and the red dashed line in (f) showing the morphological change from "mossy' to 'fractal' morphology. Reprinted (adapted) with permission from Bai, P.; Li, J.; Brushett, F. R.; Bazant, M. Z. *Energy Environ. Sci.* 2016, *9* (10), 3221–3229.[177] Copyright 2016 *The Royal Society of Chemistry*.

be responsible for dendrite growth.[33] As such, it is perhaps somewhat misleading to refer to Li that penetrates into a solid electrolyte as dendrites, however this is common practice in the literature and so the term 'dendrite' will be used to refer to a filament of Li metal that has penetrated into a solid electrolyte.

Importantly, dendrites are observed to penetrate into solid electrolytes only above a critical current density, termed the critical current density for dendrite growth on plating. These critical currents appear to be dependent on a number of factors such as the type of solid electrolyte, its porosity, its mechanical properties, its electronic conductivity and the properties of the metal electrode.[52,179–181] However, in general, critical currents for dendrite growth for common solid electrolyte materials are too low for practical applications, even with > 99 % density. It is therefore important to reach an understanding of how dendrites

initiate and grow in solid electrolytes, so that critical current densities can be increased by rational design of the solid electrolyte and its interface with Li metal.

Some clues as to the mechanism of Li dendrite growth into solid electrolytes are found in the many direct observations of dendrites in the literature. However, the many reports of dendrites penetrating into solid electrolytes are often conflicting, with widely different

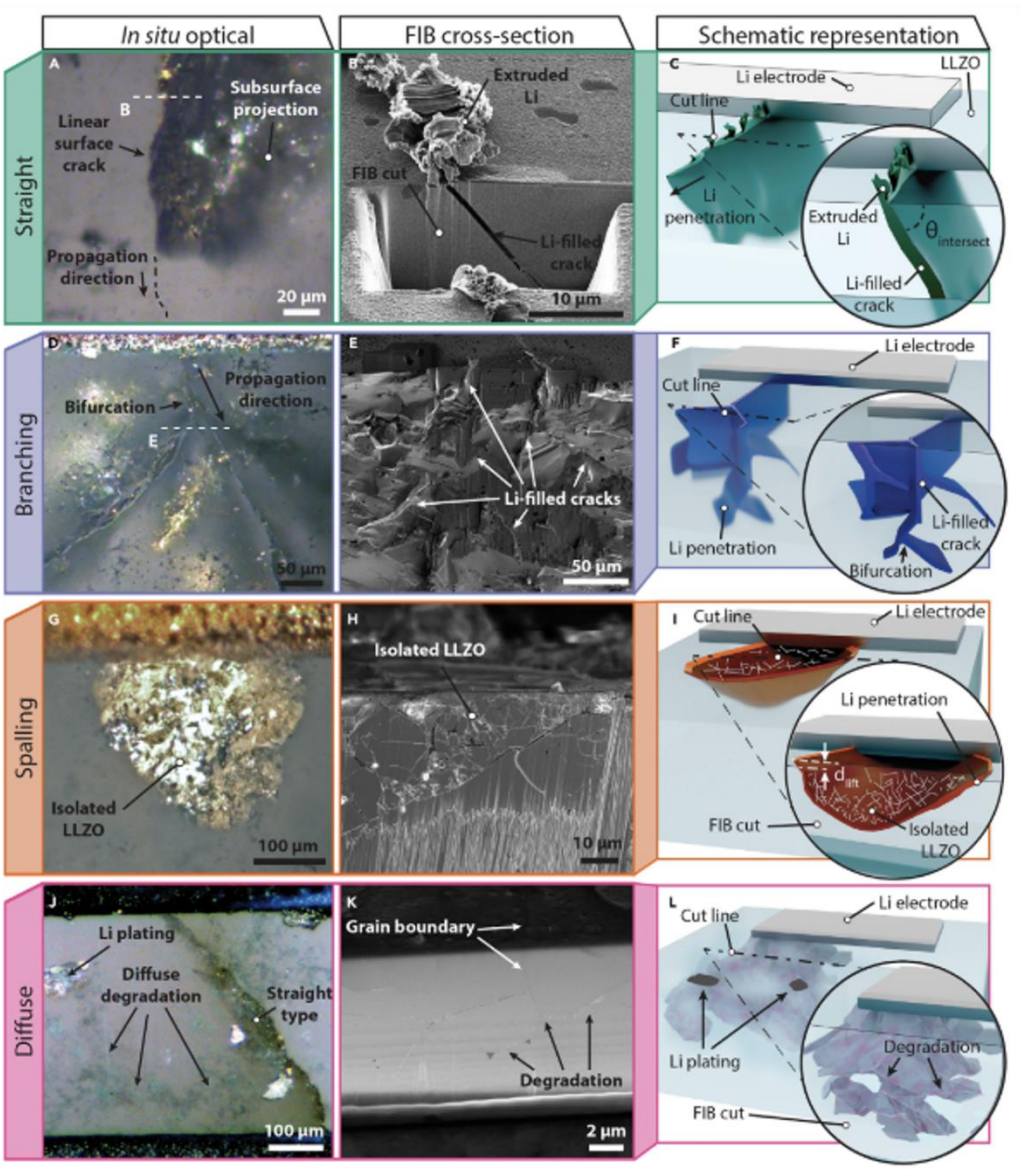


Figure 1.14: Figure showing different morphologies of Li penetration into LLZO. a)-c) show optical, SEM and schematic images of straight Li penetration (green). d)-f) show optical, SEM and schematic images of branching Li penetration (purple). g)-i) show optical, SEM and schematic images of spalling Li penetration (orange). j)-l) show optical, SEM and schematic images of diffuse Li penetration (pink). Reprinted with permission from Kazyak, E.; Garcia-Mendez, R.; LePage, W. S.; Sharafi, A.; Davis, A. L.; Sanchez, A. J.; Chen, K. H.; Haslam, C.; Sakamoto, J.; Dasgupta, N. P. *Matter* 2020, *2* (4), 1025–1048.[182] Copyright 2020 *Cell Press*.

dendrite morphologies and modes of failure observed in samples tested under different conditions. This is perhaps most clear in recent work by Dasgupta and co-workers, who used *operando* microscopy to identify four distinct morphologies of dendrites within a single system; straight, branching, spalling and diffuse (see Figure 1.14).[182]

The diversity in dendritic morphologies may go some way to explaining the wide range of models proposed for the mechanism of dendrite growth, and indeed different types of dendritic growth may be governed by different mechanisms. Whilst many different mechanisms have been proposed, there are two principal types of mechanism which encapsulate most of the modelling and theoretical work done in this field, and these will be briefly described here. These mechanisms are those based on Griffith flaws leading to stress-driven fracture, and on the non-negligible electronic conductivity of solid electrolytes.

Griffith flaws lead to stress-driven fracture

Models suggesting that flux imbalance at the metal anode/solid electrolyte interface can lead to cracking of the solid electrolyte and dendrite penetration into the ceramic were discussed in the literature for the interface between molten Na metal and Na-β''-Alumina in the 1970s. Whilst these models are for a molten rather than solid-state metal anode, the mechanisms proposed for dendrite growth are very closely related. The first model of this kind was proposed by Armstrong *et al.*.[127] They observed that Na dendrite propagation into the ceramic was dependent on the surface roughness of the Na-β''-Alumina, with rougher surfaces more likely to result in dendrite growth. They proposed that surface flaws or pores would act as Griffith-type flaws which could propagate into full dendritic cracks. In demonstration as to how this might be possible, they modelled a Griffith flaw in the solid electrolyte surface as a cylindrical pipe, filled with molten Na metal, as shown in Figure

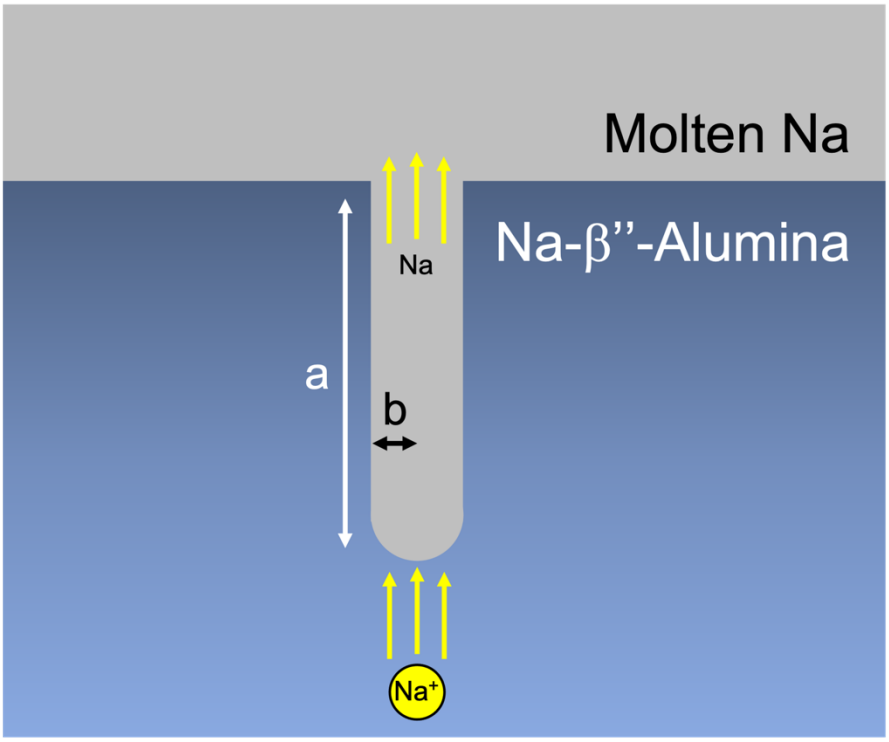


Figure 1.15: Figure showing a simplified model for dendrite growth on plating in which Na plates into a cylindrical surface flaw in the Na-β''-Alumina solid electrolyte. This plating can lead to a Poiseuille pressure, leading to crack propagation.

1.15. Flux of Na-ions into the cylindrical crack during plating results in a pressure difference, ΔP, across the length of the pipe known as the Poiseuille pressure:

$$\Delta P = \frac{8\eta i V_m a^2}{nFb^3} \qquad (1.2)$$

η is the viscosity of the molten Na, i is the current density normal to the crack tip, V_m is the molar volume of Na, a is the length of the pipe and b is the radius of the crack. Therefore, the higher the aspect ratio of the crack (longer cracks with smaller radii) and the greater the current density of plating, the greater the driving force for crack propagation. This is in line with the observation of a critical current density for dendrite growth. However, solid electrolytes, in particular sintered oxides like Na-β''-Alumina and LLZO, have high fracture strengths, and so the aspect ratio of a Griffith flaw needed to initiate a dendrite would have to be inconceivably large. Subsequent improvements to this simple model by

later studies to improve the assumed geometry of the crack and the flux of ions into the crack improved predictions somewhat, however given the sizes of surface flaws commonly observed for ceramics such as Na-β''-Alumina, the predicted critical current for dendrite growth is much higher than the experimentally determined critical current.[128,129,183]

Porz *et al.* proposed that an analogous mechanism can explain dendrite growth of solid Li metal into solid electrolytes, and a number of other mechanisms propose variations on this idea.[184,185] As discussed in Section 1.4.1, Li metal is highly deformable and will undergo viscous flow under moderate pressures.[137,140,146] As such, solid Li metal can be thought of as flowing out of a surface flaw during plating, creating a difference in pressure along the crack somewhat analogously to the flow of molten sodium in the studies on Na-β''-Alumina. This being said, it remains unclear how low yield strength Li can generate enough pressure within a realistically sized surface flaw under current densities on the order of 1 mA/cm^2 to result in fracture of a dense ceramic.[186] Instead, Li metal is expected to yield and flow out of the crack somewhat like toothpaste from a tube, without propagating the surface flaw into a dendrite. However recent findings suggesting that nano-scale lithium is harder and shows less propensity to creep might offer a possible explanation as to how crack propagation could occur by this mechanism.[141,146] Another proposition is that Li could be plated into grain-boundaries, which act as very high aspect ratio surface flaws and could therefore generate high stresses.[187] Experimental observations of Li metal plating along grain-boundaries and that critical current densities are higher in single crystals than polycrystalline materials support this theory,[188,189] however it cannot be considered a complete explanation as dendrites are still observed to propagate through grain-boundary-free electrolytes such as single crystals and glasses.[190]

A final drawback of this model is that it requires the entire crack to be filled with Li metal to generate the force to propagate the dendritic crack further into the solid electrolyte. If the crack were not entirely filled, the Li metal might be expected to yield to fill the crack prior to further propagation. Recent work by Ning *et al.* uses *in-situ* X-ray computed micro-tomography to show that straight, dry cracks propagate through the Li_6PS_5Cl electrolyte ahead of Li metal.[191] This therefore casts some doubt as to whether a Poiseuille-like pressure is propagating the dendritic crack.

Returning briefly to discussion of dendrite growth at the molten Na/Na-β''-Alumina interface, it is worth noting that as well as pressure-driven cracking, direct deposition of Na within Na-β''-Alumina was also observed, offering evidence that multiple failure mechanisms can occur within the same cell. De Jonghe *et al.* proposed that Na could nucleate within the solid electrolyte due to its non-negligible electronic conductivity following reduction by the molten Na electrode.[192]

Electronic conductivity of the solid electrolyte

Multiple reports of Li metal nucleation within seemingly isolated pores in solid electrolytes suggest that plating into these subsurface pores and resultant pressure build-up plays an important role in dendrite growth.[33,193] A number of works have proposed that the non-negligible electronic conductivity of solid electrolytes could lead to availability of electrons in the near-interface region of the solid electrolyte and that therefore Li metal can nucleate in free space within the electrolyte.[179,194] Whilst electronic conductivities in solid electrolytes are very low, often three orders of magnitude or more lower than ionic conductivities, even low electronic conductivities might have the potential to lead to Li nucleation within the solid electrolyte. An influential work by Han and co-workers observed isolated Li deposition within the solid electrolyte and correlated the electronic

conductivities of common electrolytes to their propensity to form dendrites.[179] In a recent work by Chi and co-workers, the electronic structure of the grain boundaries in LLZO was probed, finding a reduced bandgap in some cases, which might result in leakage of current into the grain-boundaries resulting in intragranular dendrite growth.[195] It is important to note that the electronic conductivities of grain boundaries might be affected by the sintering procedure of the solid electrolyte and factors such as doping, leading to different critical currents for dendrite growth.

1.5.3.2 Strategies to prevent dendrites

In order to enable faster rates of charge, the critical current for dendrite growth must be increased. A wide variety of strategies have been used to try and suppress dendrite growth, but the principal strategies can be divided into; 1) improving the mechanical properties of the solid electrolyte, 2) ensuring lower, more homogeneous local currents and 3) addition of an interlayer between the metal anode and the solid electrolyte to protect the electrolyte from dendrite penetration.

Mechanical properties of the solid electrolyte

It has been observed that as dendrites grow through solid electrolytes, they propagate cracks in the ceramic that offer routes for continued growth. Therefore, preventing crack propagation by toughening the solid electrolyte may offer a route to higher critical current densities. A well-known method to toughen materials is by addition of a secondary phase, and this method has been applied to solid electrolyte materials. For example, a zirconia secondary phase, which causes transformation toughening, is commonly added to β-Alumina-type solid electrolytes.[196–198] Other studies have added a number of different secondary phases to solid electrolytes, including non-conducting polymers such as PVdF, PTFE and PAA, and fibres of materials such as glass and Kevlar.[199–203] However, no previous studies have sought to directly link improved mechanical properties of the solid

electrolyte to changes in the critical current density, so this is an area demanding further study.

Lower, more homogeneous local currents

Although the exact mechanism of dendrite growth is not yet clear, most proposed models suggest that dendrite initiation and growth is caused or exacerbated by uneven current flux across the interface. Therefore, lowering local currents and improving the homogeneity of current flux to the interface may help to enable higher overall rates of charge. Sakamoto and co-workers have undertaken a number of works to improve the homogeneity of the interface between Li and LLZO, finding that surface treatment of the LLZO to remove common contaminants such as carbonates and hydroxides can lower the interfacial resistance and increase the critical current.[60,61] In a similar vein, Janek and co-workers used impedance spectroscopy to demonstrate the importance of an intimate interfacial contact between Li and LLZO, showing that higher interface formation pressures led to lower resistances at the interface associated with current constriction.[166] They go on to link this concept to the formation of voids on stripping, showing that it is important to prevent voids from forming to maintain a homogeneous interface and by-so-doing prevent dendrite growth.

Other approaches have sought to increase charging currents by increasing the surface area between the solid electrolyte and Li anode. In a number of studies, Hu and co-workers report a 3D garnet host structure that can be infiltrated with Li metal, creating a very high contact area. By this method, they report the ability to plate the interface at current densities as high as 10 mA/cm^2 (normalised for the planar contact area, rather than the larger, true area of contact). In these works, they also report coating the 3D structured interface with coatings including Al_2O_3, ZnO and carbon nanotubes which they report increase the homogeneity of Li plating/stripping by increasing the Li wettability.[204–209]

Interlayers

Interlayers between the metal anode and solid electrolyte have also been utilised to protect the electrolyte from penetration by Li metal. One type of interlayer that has been used are thinly deposited layers of alloying metals such as Mg, Al, Ge, In, Si, Sb, Au and Ag, which have been observed to increase critical current density.[164,210–221] In a paper utilising *operando* optical microscopy, Kim *et al.* uncover the reasons for the improved plating behaviour, observing that the alloy layer formed on charge can act as a buffer layer for Li redistribution and can act as a seed, directing Li precipitation to form more homogeneously plated Li as shown in schematic 1.16.[210]

Finally, a promising class of interlayers are carbon-based interlayers. Several recent, high-profile papers have utilised graphite anode-protective interlayers to achieve critical currents as high as 8.6 mA/cm^2 or even 10 mA/cm^2,[34,222] and researchers from Samsung have reported use of a carbon-silver nanoparticle composite interlayer which enabled them to achieve "anode-free" cycling at the high current density of 3.4 mA/cm^2, moving a capacity of 6.8 mA·h/cm^2 with a stable Coulombic efficiency of 99.8 % over 1000 cycles at 60 ºC.

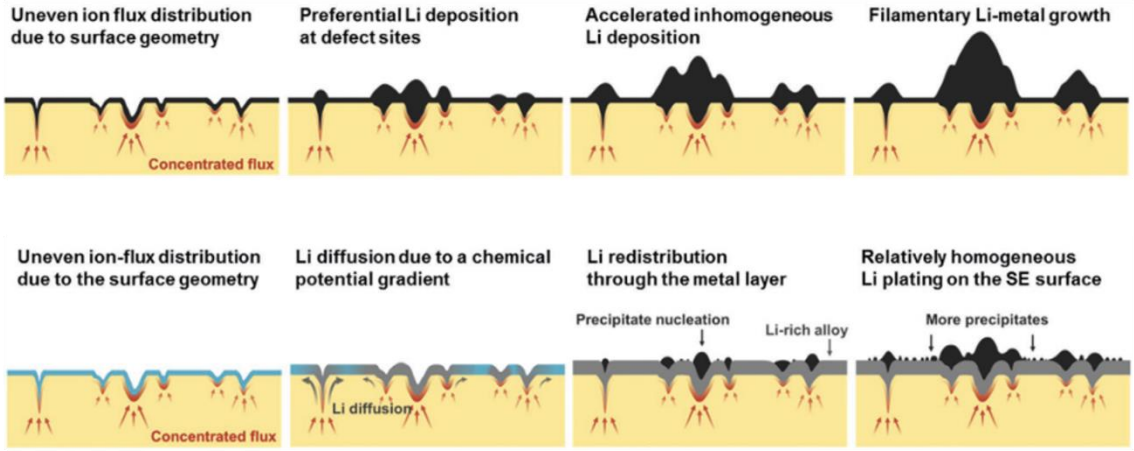


Figure 1.16: Plating Li without (top) and with (bottom) an alloying interlayer. Schematics show the advantages of the interlayer in nucleating more homogeneous Li and preventing dendrite growth. Reprinted (adapted) with permission from Kim, S.; Jung, C.; Kim, H.; Thomas-Alyea, K. E.; Yoon, G.; Kim, B.; Badding, M. E.; Song, Z.; Chang, J. M.; Kim, J.; Im, D.; Kang, K. *Adv. Energy Mater.* 2020, *10* (12), 1–11.[210] Copyright 2020 *Wiley*.

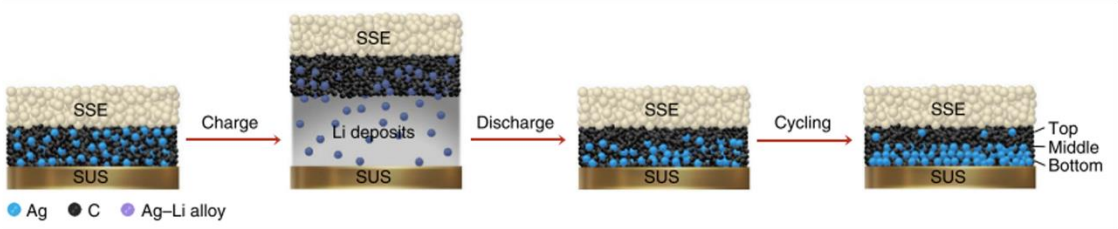


Figure 1.17: Schematic showing stable Li plating/stripping through the carbon-silver nanoparticle composite interlayer. Key to the success of the interlayer is that Li plates on the stainless-steel (SUS) current collector, rather than at the interface with the solid-state electrolyte (SSE). Reprinted with permission from Lee, Y. G.; Fujiki, S.; Jung, C.; Suzuki, N.; Yashiro, N.; Omoda, R.; Ko, D. S.; Shiratsuchi, T.; Sugimoto, T.; Ryu, S.; Ku, J. H.; Watanabe, T.; Park, Y.; Aihara, Y.; Im, D.; Han, I. T. *Nat. Energy* 2020, *5*, 299–308.[199] Copyright 2020 *Springer*.

Not only is the performance of this cell highly impressive, but so too is its high volumetric energy density of > 900 W·h/L.[199] Key to the successful operation of this cell is that, when charged, Li does not deposit directly at the interface with the solid electrolyte, but instead is observed by SEM and energy dispersive X-ray spectroscopy (EDX) to deposit behind the composite interlayer, nucleating on the stainless-steel current collector. As no Li nucleates at the solid electrolyte, there is no opportunity for the Li metal to penetrate into the electrolytes as dendrites, i.e. the silver-carbon composite layer acts as a protective barrier against dendrite growth, enabling high critical currents. This is shown schematically in Figure 1.17. Whilst these results are extremely promising, a clear mechanistic understanding of how these carbon-based interlayers work and why Li nucleates behind the interlayer rather than at the solid electrolyte interface has not yet been reached, and this is the subject of investigation in Chapter 5 of this thesis.

1.6 Thesis Aims

As outlined in this chapter, there are numerous challenges to achieving excellent cycling performance in solid-state batteries, in particular there are many associated with the interface between the metal anode and the solid electrolyte. The objective of this thesis is

to better understand the important failure mechanisms of voiding and dendrite growth, and to explore strategies to mitigate these failures.

After discussion of the experimental methods used in this thesis in Chapter 2, Chapters 3 and 4 both seek to deliver a more detailed understanding of void formation at metal anode/solid electrolyte interfaces during stripping. Chapter 3 explores use of a Na metal anode, which has the potential to enable higher rates of stable stripping than Li due to its higher self-diffusion coefficient and its greater propensity to creep. The chapter goes on to investigate the relationship between stack-pressure and stable rate of stripping. Subsequently, Chapter 4 returns to studying voiding at lithium/solid electrolyte interfaces and seeks to understand the role of moderately increased temperatures, e.g. 80 ºC, on the critical current for voiding and whether this is sufficient to enable practically relevant charging rates of several mA/cm^2.

Finally, Chapter 5 changes tack to investigate how graphite and graphite-silver composite interlayers can protect against dendrite growth. Understanding the mechanism of charge involves studying a number of different types of carbon-based interlayer, investigating how changing parameters such as the current density, the type of carbon, temperature, interlayer thickness and the presence of silver affect the ability of the interlayer to prevent dendrite growth and lead to homogeneously plated Li metal.

2 Experimental Techniques

2.1 Aim

This chapter aims to introduce the range of experimental techniques used throughout this thesis. The theory behind these techniques and some of the practical considerations for their use in studying solid-state battery materials are discussed.

2.2 Characterisation

2.2.1 X-ray Diffraction (XRD)

A crystalline solid is composed of an atom or group of atoms (the basis) located on a repeating, translationally related array of points in 3-dimensional space (the lattice). The distances between atoms in a crystalline solid are on the Angstrom length-scale meaning X-rays with similar length-scale wavelengths will interact strongly. X-rays are therefore a highly effective tool to probe the structures of crystalline materials. X-ray diffraction (XRD) is a powerful characterisation tool which is used to obtain a great deal of structural information including lattice parameters, atomic positions and symmetry.[223]

In an XRD experiment, X-rays interact with a sample and scatter without loss of energy from the electron density surrounding the atoms in the crystal. This is known as coherent

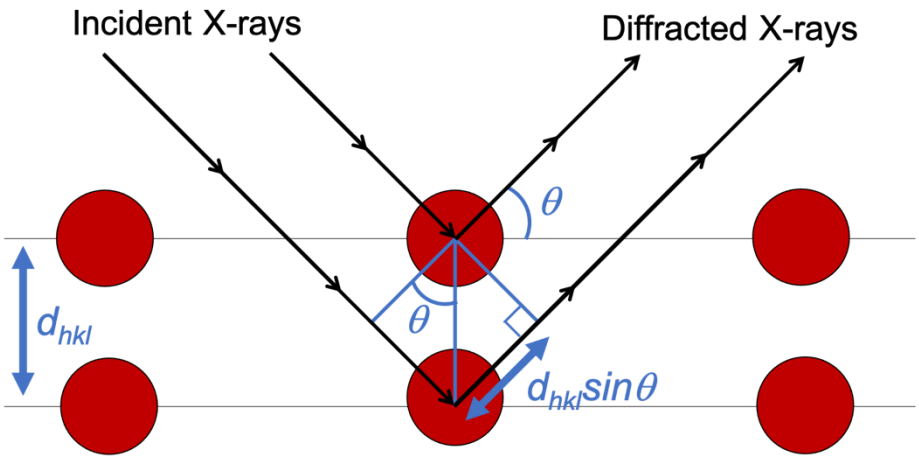


Figure 2.1: Schematic showing the origin of Bragg's Law of diffraction.

scattering. Most X-rays will scatter out of phase with one another, interacting destructively, effectively cancelling one another, and therefore will not be detected by the XRD detector. However, under specific conditions X-rays will be in phase, interacting constructively, and will therefore be detected. The conditions for constructive interference are described by Bragg's Law (Equation 2.1), which states that X-rays reflected from two planes will only interact constructively if the difference in path length ($2d_{hkl}\sin\theta$) is an integer number of wavelengths ($n\lambda$) (Figure 2.1), or:

$$n\lambda = 2d_{hkl}\sin\theta \qquad (2.1)$$

where d_{hkl} is the distance between the Miller planes and θ is the incident angle of the X-rays.

Therefore, as the angle is varied throughout an XRD experiment, a pattern is generated in which peaks will be observed at positions containing information about the distance between the Miller planes of the crystal. As well as the peak positions, peak intensities also contain structural information, since the peak intensity is directly proportional to $|F_{hkl}|^2$ where F_{hkl} is the structure factor:

$$F_{hkl} = \sum_{j=1}^{n} f_j\left[\cos 2\pi\left(hx_j + ky_j + lz_j\right) + i\sin 2\pi\left(hx_j + ky_j + lz_j\right)\right] \qquad (2.2)$$

f_j is the scattering factor of atom j (which is dependent on the atomic number) and x_j, y_j and z_j are the atomic coordinates.[224] Together, the positions and relative intensities of peaks in the diffraction pattern enable identification of crystallographic phases present in samples of interest.

Laboratory source X-rays are generated by firing high-energy electrons at a target, commonly Cu. The collision of an electron into the target causes an electron to be ejected

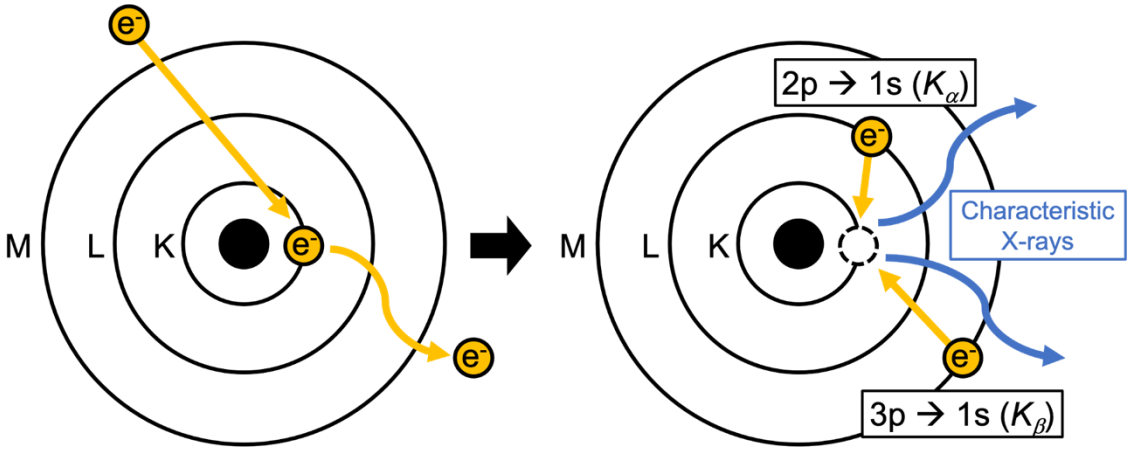


Figure 2.2: Schematic showing the the generation of X-rays by firing high energy electrons at a Cu target. M, L and K are the electron shells of the Cu atom and K_α and K_β denote the characteristic X-rays in Siegbahn notation.

from the Cu 1s orbital. To return to its lowest energy state, an electron drops down to fill the 1s electron hole and this releases an X-ray with the energy of that electron transition. Due to selection rules, the allowed electron transitions are from 2p → 1s (which releases K_α radiation) or from 3p → 1s (which releases K_β radiation). A monochromatic X-ray is required to collect high-resolution XRD patterns, and so K_β wavelengths are removed using a Ni filter. This process is shown schematically in Figure 2.2.[224]

When taking *ex-situ* XRD patterns, it is primarily important to maximise the angular resolution of the measurement. However, when carrying out *operando* XRD as described in Chapter 5, it is also important to maximise the time resolution of XRD pattern collection. When X-rays diffract from the sample, they do so in a series of concentric cones, known as a Debye-Scherrer cones. In most laboratory X-ray diffraction experiments, the detector is moved in an arc, measuring diffraction along a single axis. However, in the *operando* experiments carried out in Chapter 5, a 2D detector is used instead, which measures X-ray diffraction in a 2D plane, before converting the data into a 1D collection pattern. The advantage of 2D detection is that more X-ray intensity is detected per unit time, enabling a reduction in the collection time of each complete pattern.[225]

2.2.2 X-ray Photoelectron Spectroscopy (XPS)

X-ray photoelectron spectroscopy (XPS) is a technique used to study the bonding environments of near surface elements, utilising the photoelectric effect.[226] When the surface of a sample is irradiated by X-rays of a known energy, $h\nu$ (where h is Planck's constant and ν is the frequency), the energy of the X-rays will transfer to the atoms at the surface of the sample. If this energy overcomes the binding energy of the core-shell electrons (E_b), these electrons will be emitted as photoelectrons with an associated kinetic energy (E_k). The XPS detector can measure the amount and kinetic energy of the ejected photoelectrons, enabling determination of the binding energies since according to the law of conservation of energy:

$$E_b = h\upsilon - E_k - \phi \qquad (2.3)$$

where ϕ is an instrument-specific work function. The XPS measurement will therefore produce a spectrum consisting of a set of peaks that indicate the number of electrons at a given binding energy, which can be interpreted to give information on the elemental composition, electronic structure and local bonding environments present at the surface of a sample.

The mean free path of a photoelectron within a solid sample is very short, of the order of 10 nm. As such, XPS is only sensitive to the surface chemistry and not to the bulk of the sample. This can be problematic as the surface of a sample is often contaminated and is a poor representation of the bulk. In some cases this can be an advantage. For example, in Chapter 3 of this thesis XPS is used specifically to investigate the surface contamination on a ceramic solid electrolyte. However, in many solid-state battery studies, including work in Chapter 4 of this thesis, XPS is used to investigate the chemistry of an interface that is buried. The most common method for investigation of a buried interface is to pair XPS

with ion-beam etching to carry out depth-profiled measurements, however this can lead to sputter damage and altered surface chemistry.[227] Alternative techniques include sectioning the sample (as is used in Chapter 4) or carrying out hard X-ray photoelectron spectroscopy (HAXPES) through a very thinly deposited layer.[228]

2.2.3 Scanning Electron Microscopy (SEM)

SEM is a microscopy technique used for imaging samples at high magnifications, achieving high resolutions. It is an attractive technique for imaging battery materials as it can be used to investigate morphological changes at micron and sub-micron length-scales and can produce visually impactful images which give insights into specimen topology or composition.[224]

A simplified, schematic representation of the instrument is shown in Figure 2.3. Initially, primary electrons are produced from an electron gun within a column under ultra-high vacuum ($\backsim 10^{-10}$ mbar) (1). Typically, the electrons are generated by a thermionic process, by heating a tungsten or lanthanum hexaboride filament. The ultra-high vacuum within the column prevents scattering of the electrons by molecules of air. The electrons are accelerated through the gun column towards the sample chamber by a negatively charged anode (2) and are focussed from a broad, diverging beam into a small area electron spot by a number of electromagnetic focussing lenses (3). The focussed primary electron beam is directed by electromagnetic scanning coils (4), which raster the electron spot over the sample.

As electrons hit the sample, they either collide elastically or inelastically. Electrons that collide elastically often retain > 50 eV energy upon collision with the sample and are referred to as backscattered electrons (BSE). They are scattered back towards the electron gun column, where they are detected by the backscattered electron detector (5). The amount of BSE emitted from the sample correlates with the atomic number of the atoms with which

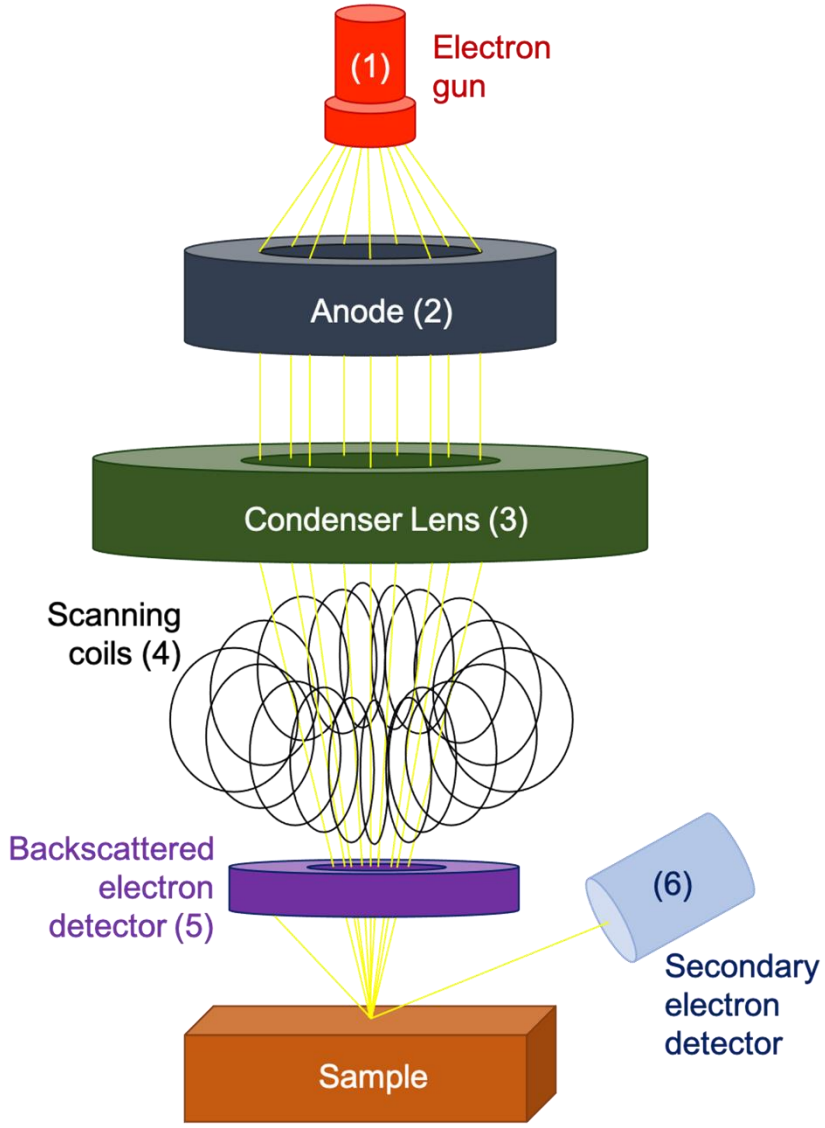


Figure 2.3: Schematic representation of a scanning electron microscope (SEM). The schematic shows: 1) the electron gun; 2) the anode; 3) the condenser lens; 4) the scanning coils; 5 the backscattered electron detector and 6) the secondary electron detector.

the electrons collide. As such, the grayscale of a BSE SEM image correlates with the atomic number of the local atoms and thus gives insights into the sample's composition. Other electrons collide inelastically, producing lower energy secondary electrons (SE) and energy in the form of characteristic X-rays and photons. The SEs are diverted to the secondary electron detector (6) by a positively biased grid. Because they are low energy, only near-surface secondary electrons escape to reach the detector. As such, secondary electron micrographs impart topological information within the image.[229]

During imaging, when the electron beam hits the sample, fewer electrons escape the sample as SE or BSE than strike the sample. If the sample is poorly electronically conductive it can become locally charged leading to image distortion, uneven brightness and image drift. Solid electrolytes by design are electronic insulators and as such imaging SSBs can be challenging. Effective methods to prevent charging effects include 1) coating the sample with a thin film of a metal, commonly platinum; 2) imaging using a lower acceleration voltage and 3) using a low current.[230] Of these methods, low voltages and currents are commonly used in this thesis to prevent charging effects.

As this thesis focusses on the buried interface between anode and solid electrolyte, cross-sections of the cell to image this interface are made throughout. Since the anode (lithium or sodium) is a soft, low melting point, easily deformable, air-sensitive metal and the solid electrolyte is hard, brittle, air-sensitive ceramic, special care must be taken to maintain the integrity of the sample and retain information at the interface. A method commonly used in the literature is FIB (focussed ion beam). FIB is a technique in which Ga^+ ions are focussed to sputter away material from a sample. In this case, it can be used to create a trench, revealing the anode/solid electrolyte interface. However, FIB is a high energy technique and causes melting of the lithium or sodium metal anode during milling, resulting in loss of interfacial information. It is generally acknowledged in the field that it is necessary to FIB under cryogenic conditions to prevent melting of the metal anode.[231] Unfortunately, a cryo-FIB has not been available throughout the course of this work, so alternative methods were considered. Instead, an ultrasonic blade (Sonotec) was used to create fracture surfaces for imaging, a method which has a basis in previous literature.[120,151] Although this method is not as ideal as using cryo-FIB, it was judged to be significantly more effective than carrying out FIB in non-cryogenic conditions.

2.2.4 Energy-dispersive X-ray Spectroscopy (EDX)

Energy-dispersive X-ray spectroscopy, EDX (sometimes referred to as EDS), is an analytical technique commonly used in conjunction with SEM. When electrons from a focussed electron beam collide inelastically with a sample, they scatter away as lower energy secondary electrons as described in Section 2.2.3. The lost energy is gained by the electrons at the surface of the sample, which become excited. If we consider a simplified model in which the electrons of the atoms at the surface of the sample are arranged in shells, the energy that they gain promotes core-shell electrons to the vacant outer shells, leaving electron holes. As electrons relax back to the lowest energy states, refilling the electron holes, they emit X-rays that are detected by the energy-dispersive spectrometer. This is similar to the generation of X-rays from a laboratory X-ray source depicted in Figure 2.2. Each element has a unique atomic structure and so the X-ray emission spectrum can be used to identify the local elemental composition.

Since the SEM 'rasters' the electron beam over the surface of the sample, EDX can be used to map the elemental distribution across the surface of the sample and this map can even be superimposed over the secondary electron SEM image to combine visual information with data on elemental compositions. Escape of characteristic X-rays to the detector is only possible for near-surface atoms and so EDX has a depth resolution in the order of a few microns.[232]

In some cases, EDX can be used as a quantitative technique to determine the relative amounts of each element in the measured area. However, there are stringent requirements for the type of sample that can be investigated truly quantitatively. The sample must be stable under the electron beam, homogeneous on the scale of the interaction volume, as well as flat and void free (Figure 2.4). The battery materials investigated throughout this thesis fall short of these requirements, particularly regarding the need for flat and void free

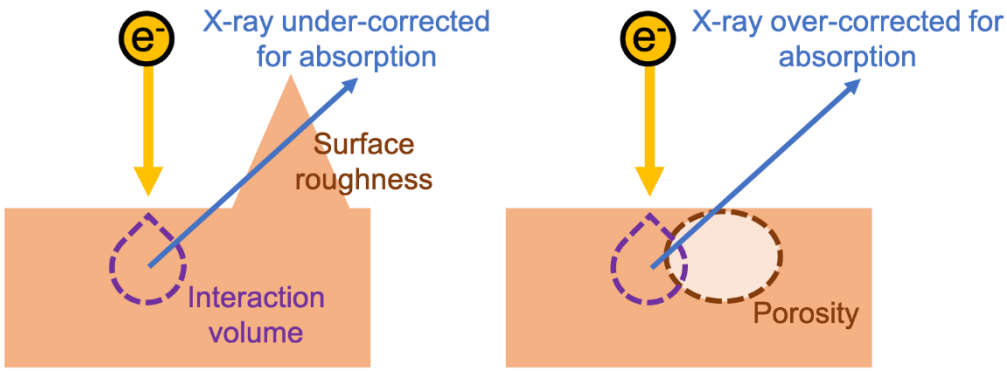


Figure 2.4: Schematic illustrating that sample surface roughness (left) or near-surface porosity (right) can lead to errors in the quantitative collection of X-ray signal when carrying out EDX.

surfaces, and so EDX was used solely as a qualitative tool to aid in interpretation of SEM images. Even as a qualitative tool EDX can occasionally fall short, as significant surface roughness can block the path of X-rays to the detector (Figure 2.5). It was important to minimise this through sample preparation and optimisation of the sample position relative to the detector.

Throughout this thesis EDX was carried out using a higher accelerating voltage than was used for the SEM imaging. The reason for this is that elements require a minimum voltage for detection. A voltage of 10 kV was commonly used as almost all elements are detectable and distinguishable with this acceleration voltage.

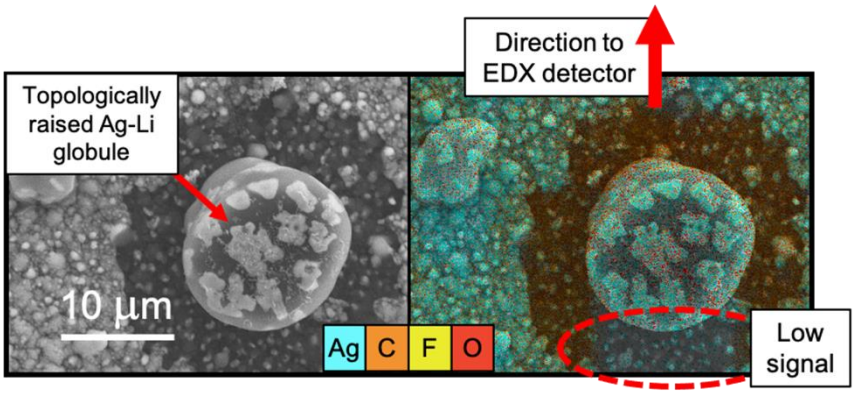


Figure 2.5: SEM image (left) and EDX maps overlayed on the SEM image (right) showing that a topologically raised Ag-Li alloy globule can act as a physical barrier, blocking X-ray signals from reaching the EDX detector. This can lead to inaccuracies in qualitatively interpreting data and makes quantitative analysis unfeasible.

2.2.5 X-ray Computed Tomography (XCT)

X-ray Computed Tomography (XCT) is a non-destructive 3D imaging technique which can be used to image the internal structure of samples by visualising the differences in X-ray attenuation of its component phases. Differences in experimental set-up can result in imaging over different length-scales, but in this thesis XCT refers to microtomography, which gives images with pixel sizes on the length-scale of a micron.

To carry out XCT, a sample is mounted on a rotating stage as shown in the set-up illustrated in Figure 2.6. At each individual angle X-rays are used to take a 2D projection image of the sample. As discussed previously in this chapter, X-rays interact with matter either by the photoelectron effect or by Compton scattering. At the high energies at which XCT is customarily carried out, Compton scattering from the electron density surrounding atomic nuclei tends to dominate. As the X-rays scatter from the electron density, they transmit through the sample to the detector and the measured intensity of the detected X-rays can be related to the attenuation of the sample by the Beer-Lambert Law:

$$I_\theta = I_0 e^{-\int \mu(x,y)ds} \tag{2.4}$$

where I_θ is the intensity of the X-rays transmitted through the sample at angle θ, I_0 is the intensity of the incident X-rays and $\mu\,(x,y)$ is the attenuation coefficient distribution through

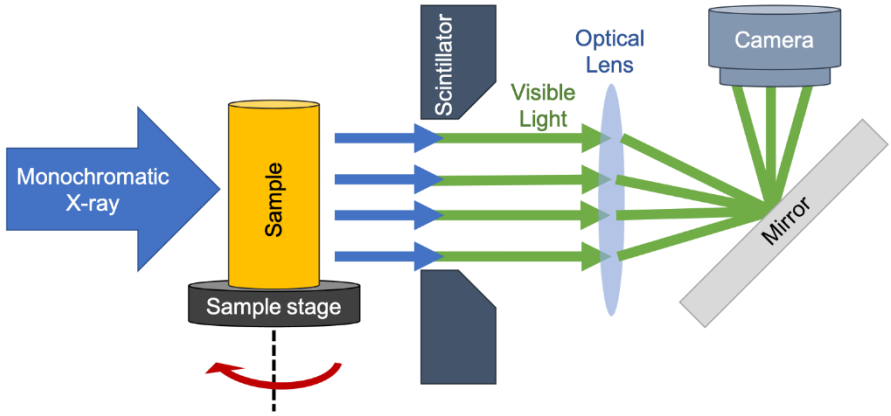


Figure 2.6: Diagram showing a schematic representation of the set-up for X-ray computed microtomography.

the sample at angle θ. The sample is commonly rotated through 180° or 360° collecting these 2D projection images. Following collection, the images are algorithmically reconstructed into a tomogram; a 3D image in which the grayscale of each voxel indicates the X-ray attenuation of that voxel's constituent phases. Darker shades indicate poorly attenuating phases and brighter shades indicate phases with higher X-ray attenuation. Since X-ray attenuation is a function of atomic number and sample density, XCT can give some qualitative information on sample composition, but should not be used for quantitative characterisation.[233]

Distinguishing between phases with similar attenuation can be extremely challenging by XCT. In the context of this thesis, one of the biggest such problems is the difficulty in distinguishing between poorly attenuating Li metal and the empty space of a void or an unfilled dendritic crack. One method that helps to overcome this is to carry out phase-contrast imaging.[168,191,234] During X-ray tomography, X-rays interact with a sample as described by its X-ray refractive index (n):

$$n = (1 - \delta) + i\beta \tag{2.5}$$

where $1 - \delta$ is the change the wavelength of an X-ray as it passes through the sample, and $i\beta$ is the change in amplitude. The change in amplitude of an X-ray ($i\beta$) is dependent on how attenuating the sample is, and is the basis for the differences in grayscale in an attenuation contrast XCT image. There will also be changes in wavelength ($1 - \delta$) as an X-ray passes from one phase to another within the sample. In attenuation-contrast XCT this gives an interference pattern superimposed on the attenuation-based image which often has the appearance of "bright fringes" at the boundary between two phases. However, in phase-contrast imaging an algorithm is used for reconstruction that uses the changes in X-ray wavelength in the reconstruction to give improved contrast at phase boundaries in

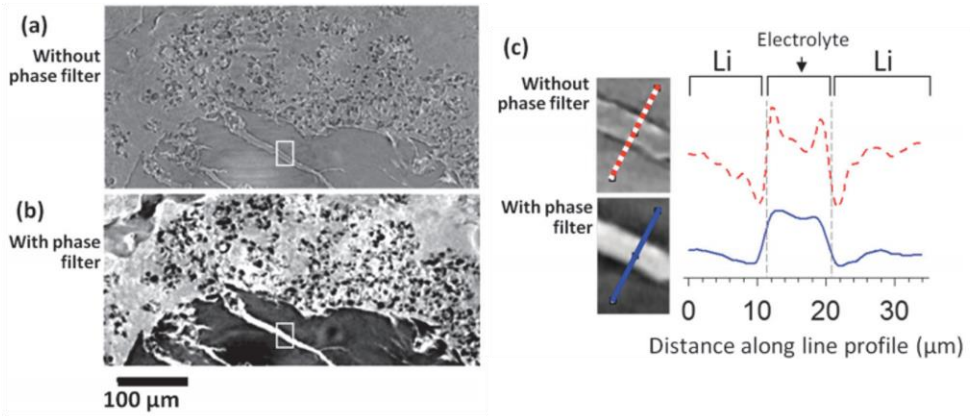


Figure 2.7: Figure demonstrating the benefits of phase contrast imaging for identifying lithium metal. a) An attenuation-contrast image of Li and electrolyte and b) the equivalent phase-contrast image showing clearer differentiation between the phases. c) Line profiles across the Li/electrolyte/Li interface show the phase-contrast enhancement. Reprinted with permission from Eastwood, D. S.; Bradley, R. S.; Tariq, F.; Cooper, S. J.; Taiwo, O. O.; Gelb, J.; Merkle, A.; Brett, D. J. L.; Brandon, N. P.; Withers, P. J.; Lee, P. D.; Shearing, P. R. *Nucl. Instruments Methods Phys. Res. Sect. B Beam Interact. with Mater. Atoms* 2014, *324*, 118–123.[234] Copyright 2014 *The Royal Society of Chemistry*.

reconstructed images. An example of the benefits of phase contrast imaging is shown in Figure 2.7, demonstrating the greater ease in distinguishing Li metal, both visually (Figure 2.7a,b) and by analysis of the grayscale (Figure 2.7c).[235]

2.3 Electrochemical Testing

2.3.1 Potentiostatic Electrochemical Impedance Spectroscopy (PEIS)

In the context of battery research, electrochemical impedance spectroscopy (EIS) is a method used to understand the transport processes occurring within a cell, across a wide range of length and time scales. To probe these processes, a perturbation is applied to the cell. In the case of potentiostatic EIS (PEIS) this is a voltage perturbation. The voltage perturbation applied to the electrochemical cell ($E(t)$) will result in a response in current ($I(t)$) which can be measured. In a linear or pseudo-linear system, this current response will share the same frequency, but may differ in phase and amplitude e.g. if a sinusoidal voltage perturbation is applied (Figure 2.8, blue curve), a phase-shifted sinusoidal current with a different amplitude might be measured (Figure 2.8, red curve). Analogously to Ohm's Law,

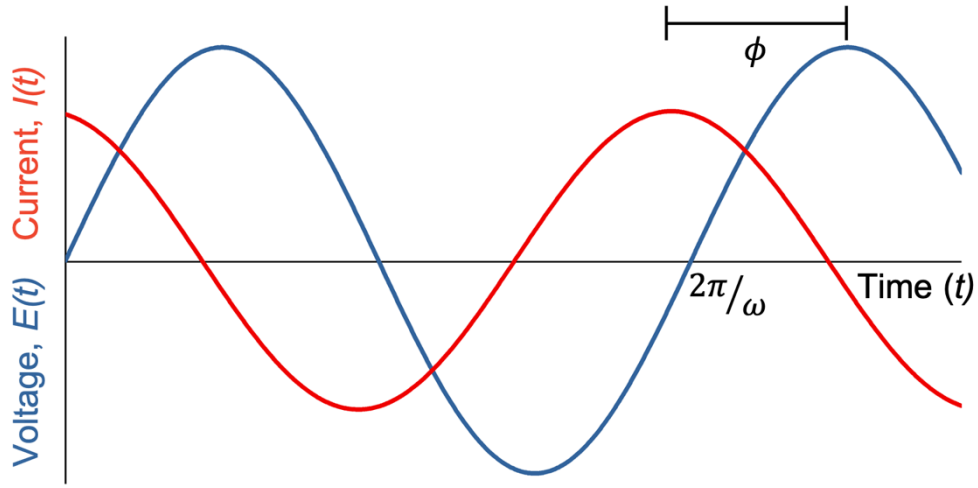


Figure 2.8: The relationship between applied voltage perturbation (blue curve) and measured current (red curve) in potentiostatic electrochemical impedance spectroscopy (PEIS). ω is the angular frequency and ϕ is the shift in phase.

it is the ratio of the applied voltage to the measured current which is the cell impedance (*Z(t)*):

$$Z(t) = {E(t)}/{I(t)} \tag{2.6}$$

In reality, electrochemical cells are not linear, however if a small enough AC voltage perturbation is applied, then the current response will be pseudo-linear at the excitation frequency. For this reason, very low voltage perturbations of 1-10 mV are commonly used.

For PEIS, *E(t)* and *I(t)* can be expressed as:

$$E(t) = |\Delta E| \sin(\omega t) = |\Delta E| e^{i\omega t} \tag{2.7}$$

$$I(t) = |\Delta I| \sin(\omega t + \phi) = |\Delta I| e^{i(\omega t + \phi)} \tag{2.8}$$

where $|\Delta E|$ and $|\Delta I|$ are the amplitudes of the voltage perturbation and current response, respectively, ω is the angular frequency, t is time and ϕ is the shift in phase. Therefore, *Z(t)* can be expressed as:

$$Z(t) = \frac{|\Delta E| e^{i\omega t}}{|\Delta I| e^{i(\omega t + \phi)}} = |\Delta Z| e^{-i\phi} = |\Delta Z|(\cos\phi + i \sin\phi) \tag{2.9}$$

i.e. the impedance is a complex number which can be expressed in terms of a magnitude, $|\Delta Z|$ and a phase shift, ϕ.[236–238]

There are two ways to represent impedance data graphically, the Bode plot and the Nyquist plot. Nyquist plots are used more extensively throughout solid-state battery literature and all data are in this thesis are presented in this way. A Nyquist plot represents impedance ($Z(t)$) as a vector on a complex plane, in which each point represents the real and imaginary components at a given frequency, and $|\Delta Z|$ and ϕ are the magnitude and phase angle of the vector. This is shown in Figure 2.9.

The impedances associated with ion conduction in an electrolyte, across a grain-boundary or at an interface with an ion-accepting electrode often appear as a semi-circles in a Nyquist plot. However, in real electrochemical cells there will be many different contributions and those with similar time constants will overlap, necessitating the use of modelling to

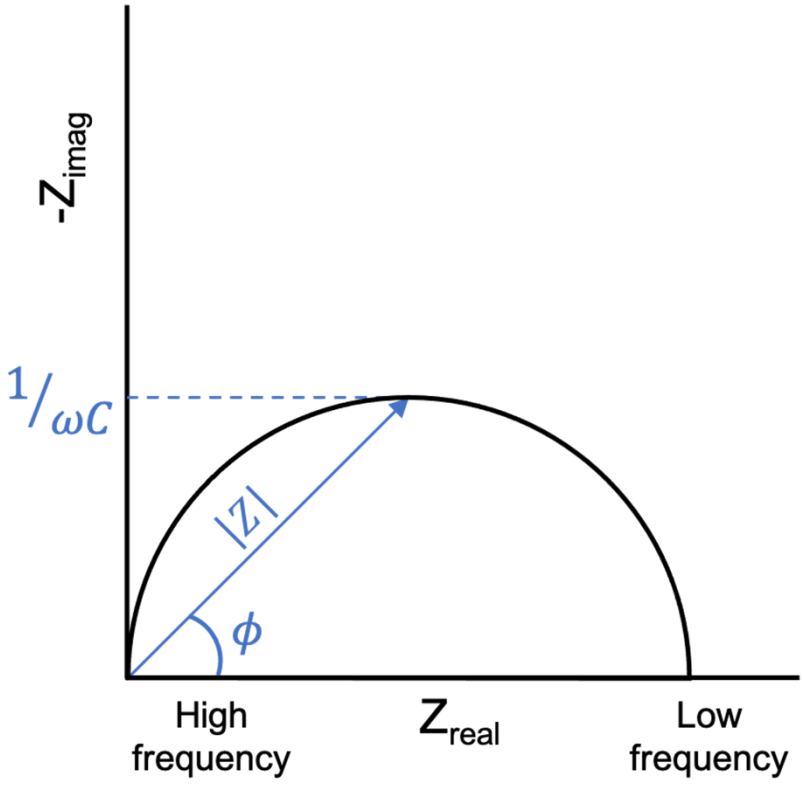


Figure 2.9: Nyquist plot showing the impedance, *Z*, on real and imaginary axes. $|Z|$ is the magnitude of the impedance, ϕ is the phase angle, ω is the frequency and *C* is the capacitance.

Table 2.1: Table by Vadhva *et al.* showing typical electrical elements used in modelling electrochemical impedance spectroscopy (EIS), and the physical phenomena within an electrochemical cell that they are used to model. Reprinted with permission from Vadhva, P.; Hu, J.; Johnson, M. J.; Stocker, R.; Braglia, M.; Brett, D. J. L.; Rettie, A. J. E. *ChemElectroChem* 2021, *8* (11), 1930–1947.[237] Copyright 2021 *Wiley*.

Element	Symbol	Physical Meaning
Resistor (*R*)		In ASBs this can represent bulk ionic and grain boundary resistance of the SE, and charge-transfer resistance between the SE and electrodes.
Capacitor (*C*)		This can be used to represent charge accumulation/depletion occurring across phase boundaries and at the SE/electrode interface.
Constant Phase Element (CPE, *Q*)		Used for non-ideal capacitances which may be caused by inhomogeneity and porosity of the electrochemical materials and interfaces. The value of α given to the CPE dictates its capacitative behaviour (where 0 is purely resistive, and 1 is an ideal capacitor). An α parameter close to 0.5 describes an infinite diffusion Warburg element.
Warburg (*W*)		Used for resistances that occur due to mass transfer (diffusion), which is most prominent at low frequencies.
Inductor (*L*)		Represents impedance contributions associated with wound wires/electrical connections at high frequencies and degradation processes at low frequencies.

interpret the data. Interpretation of impedance data is commonly done by a complex non-linear least-squares fitting of the data to an equivalent circuit model, in which electrical elements such as resistors and capacitors are used to model the impedances of physical electrochemical processes within the cell. Table 2.1 shows common electrical elements that are used in modelling and the physical processes which they are used to model.[236,237]

Modelling using an equivalent circuit model does not give a unique solution and implementing more complex models will often improve the goodness of fit to the data. However, for interpretation it is of the utmost importance that the equivalent circuit model is informed by the physical phenomena occurring within the cell, and for this reason the simplest equivalent circuit models are often the most effective.[236,237]

In this thesis PEIS is carried out on two different kinds of cells; 1) cells with blocking electrodes that are electronically conductive but are ion-blocking and 2) cells with reversible electrodes that facilitate both ionic and electronic transport.

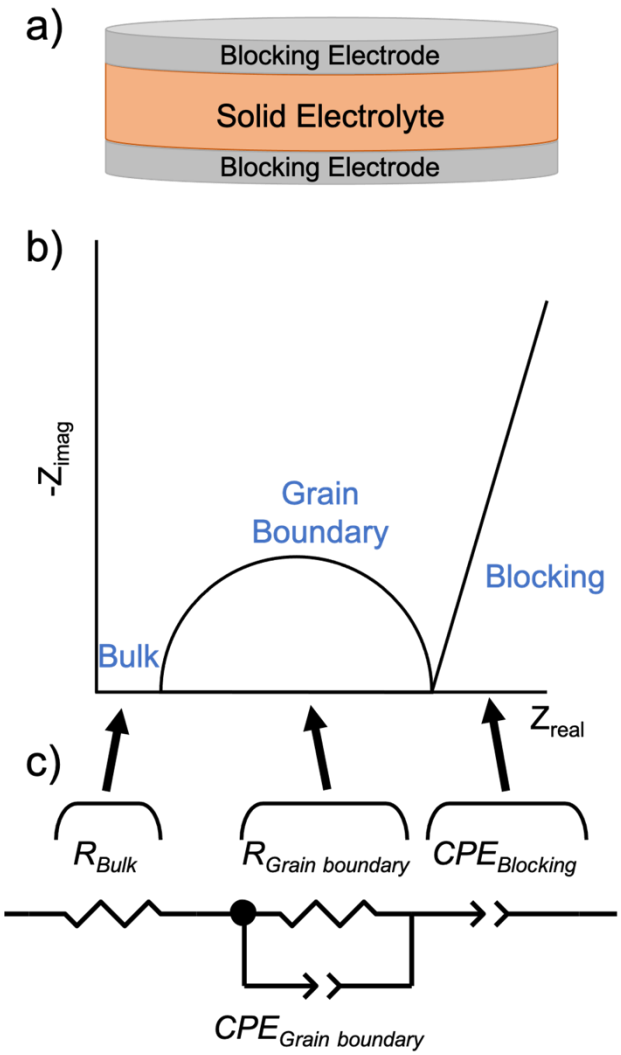


Figure 2.10: Figure showing a) a blocking electrode cell, b) an idealised Nyquist plot showing the potentiostatic electrochemical impedance spectroscopy (PEIS) of a polycrystalline solid electrolyte blocking electrode cell and c) an equivalent circuit model that could be used to fit the PEIS data of a blocking electrode cell.

Blocking electrode cells are utilised to investigate the impedance of the electrolyte (Figure 2.10a). The interface between an electrolyte and blocking electrodes is capacitive, so a high-gradient response will be observed in the low-frequency region of the Nyquist plot. This simplifies the Nyquist plot such that the only semi-circular contributions observed will be impedances from the electrolyte. For the polycrystalline solid electrolyte used throughout this thesis, impedance contributions are expected from conduction within the bulk of the material and from conduction across grain-boundaries (Figure 2.10b), which are often modelled as shown in Figure 2.10c. Blocking electrodes are most commonly

materials such as gold, platinum, or nickel. This being said, the area of contact between the electrodes and the electrolyte will affect the measured impedance and therefore a very intimate contact is vital. Best practice is to carry out physical vapour deposition of the electrode material onto the solid electrolyte surface, however since this equipment is not widely available an alternative is to use a platinum paste or a more malleable metal such as indium.

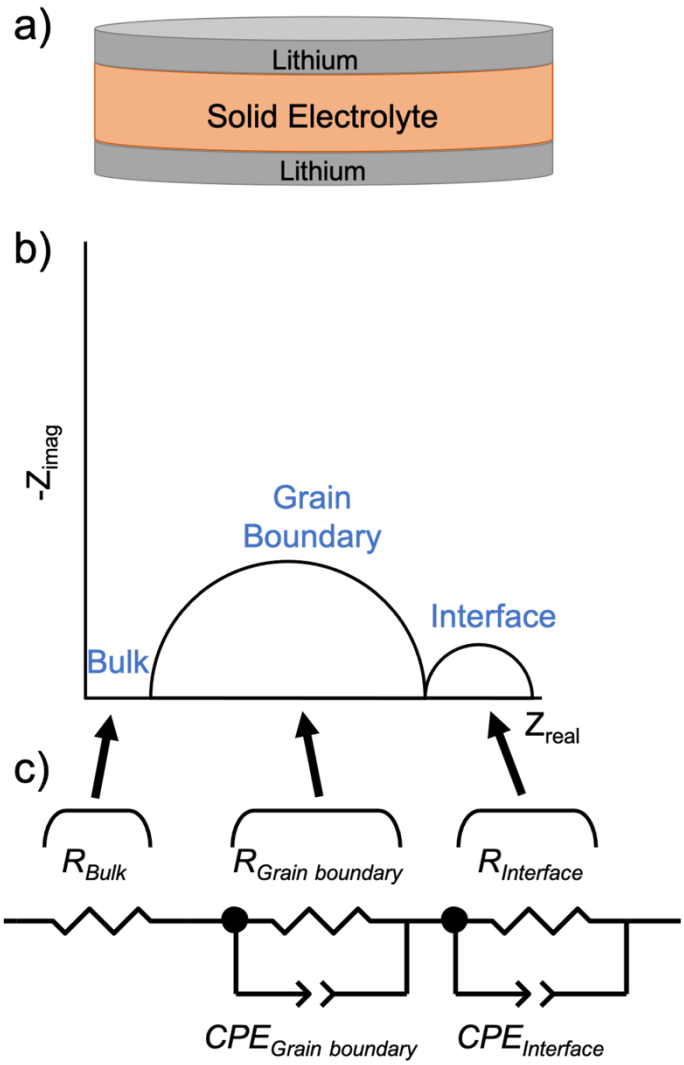


Figure 2.11: Figure showing a) a Li/solid electrolyte/Li cell, b) an idealised Nyquist plot showing the potentiostatic electrochemical impedance spectroscopy (PEIS) of a Li/polycrystalline solid electrolyte/Li cell and c) an equivalent circuit model that could be used to fit the PEIS data of a Li/solid electrolyte/Li cell.

The second type of cell uses reversible electrodes, in the case of this thesis either Li or Na metal. These cells are used to investigate the impedances of the interface between the electrolyte and the electrode. A schematic of such a cell is shown in Figure 2.11a, along with an idealised Nyquist plot (Figure 2.11b) and an example of how such a plot can be modelled (Figure 2.11c). These cells are often used to investigate how impedance of an interface changes and degrades as the cell is cycled. For example, multiple studies have investigated solid electrolyte interphase (SEI) growth and changes in interfacial resistance with cycle number.[79,126] However, it is important to remember that PEIS can only be carried out on a system which is in a steady-state, or approximately in a steady-state over the timescale of the measurement. When studying interfacial changes that are occurring over short timescales, it is important to minimise the collection time of the PEIS to ensure that the collected data are truly representative.[237]

2.3.2 Galvanostatic Cycling and Critical Current Determination

In galvanostatic cycling, a constant current (I) is applied between the working and counter electrodes and the voltage (E) is measured relative to a reference electrode. This technique is often used to test the electrochemical performance of cells, alternating the direction of the current periodically to cycle the cell.

According to Ohm's Law:

$$E = IR \tag{2.10}$$

so when cycling at a constant current, any change in voltage can be attributed to a change in resistance (R) as the cell cycles. Galvanostatic cycling is therefore an invaluable technique for determining to what extent degradations in cell performance are occurring. Coupling this with other powerful characterisation techniques described throughout this chapter can reveal the underlying reasons behind performance degradation and cell failure.

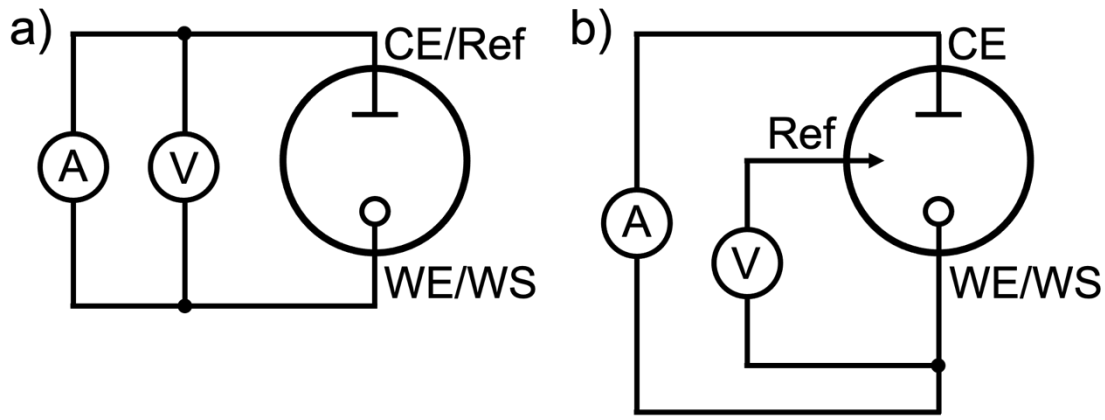


Figure 2.12: Diagrams showing a) 2-electrode set-up and b) 3-electrode set-up for galvanostatic cycling of electrochemical cells.

Galvanostatic cycling techniques can be powerful tools in their own right, particularly when moving beyond 2-electrode cycling techniques (Figure 2.12a) to 4- or 3-electrode set-ups (Figure 2.12b).[239] This thesis makes extensive use of 3-electrode cycling as it enables the effective isolation of voltage changes at a single electrolyte/electrode interface. In the context of the processes of stripping and plating of metal anodes described in Chapter 1 Sections 1.5.2 and 1.5.3, this is extremely important. For a 2-electrode Li/SE/Li symmetric cell, as one Li electrode is plated, the other is stripped and so the voltage changes at each are not clearly attributable to one process or the other. By contrast, in a 3-electrode cell the processes of stripping and plating can be separated and changes in the voltage profile can be attributed with confidence to physical changes at the interface such as contact loss or dendrite penetration.[120,151,164,175]

Determination of critical current densities by galvanostatic cycling is commonly carried out in the literature, however these techniques are far from standardised and differences in methodology can give widely different reported values.[180,240] Beginning by discussing methods for determining critical currents for dendrite growth, the most commonly used method is the ‘rate-test’ in which galvanostatic cycling is carried out and the current is increased in steps until a sudden drop in cell potential indicates failure due to dendrite

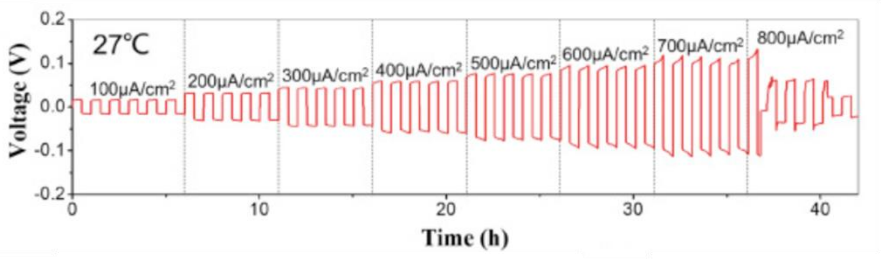


Figure 2.13: Galvanostatic 'rate-test' showing cycling in which the current density is increased in steps of 100 μA/cm^2 every five cycles. A sudden drop in cell voltage at the current density of 800 μA/cm^2 indicates that the critical current for dendrite growth has been exceeded. Reprinted with permission from Su, J.; Huang, X.; Song, Z.; Xiu, T.; Badding, M. E.; Jin, J.; Wen, Z. *Ceram. Int.* 2019, *45* (12), 14991–14996.[240] Copyright 2019 *Elsevier*.

growth.[180,222,241] Whilst this method is widely used, it is inaccurate and can give a range of different critical currents depending on factors from which the critical current is theoretically independent, e.g. the capacity passed, the number of cycles at each current density step and the size of the step increases in current density.[152,180] Alternative methods are explored in this thesis, for example in Chapter 3 single platings of the working electrode are carried out in a number of 3-electrode cells, each at a different current density, with a decrease in the plating potential indicating that the critical current for dendrite growth had been exceeded. Carrying out single platings has the advantage that any failures associated with voiding on stripping will not affect the determined critical current, however the method requires that each cell is closely similar and demands high standards of cell reproducibility.[120]

Determination of the critical current for voiding had not been done prior to the works described in this thesis, and so a number of different approaches were attempted. The two most successful approaches are used in this thesis. In Chapter 3, 3-electrode galvanostatic cycling at a single current density was used, with an increase in potential during stripping indicating failure due to voiding. The downside of this method is that separate cells must be used for each current density. In Chapter 4, an alternative method was utilised. Galvanostatic cycling of a 3-electrode cell was initiated at a low current density and the

current was increased every 5 cycles (similar to the ‘rate-test’). The critical current for voiding was deemed to have been exceeded at currents for which there was a sustained increase in cell voltage over the 5 cycles. This technique gave reproducible results and required fewer cells be tested for the determination of the critical current.

3 Voiding at the Na/Na-β''-Alumina Interface during Anode Stripping and the Effect of Stack-Pressure

3.1 Aim

The current density at which dendrites penetrate through the ceramic solid electrolyte is often considered to be the rate-limiting factor for solid-state battery cycling. However, recent work has revealed that voiding at the metal anode/solid electrolyte interface during discharge can also be contributory to battery failure. The aim of this chapter is to investigate the extent to which higher stack-pressures applied to solid-state batteries can prevent contact loss at this interface. Specifically, the relationship between the stack-pressure and the maximum current density of morphologically stable discharge (stripping the metal anode) is investigated. A symmetric Na/Na-β"-Alumina/Na cell was chosen as a model system for this investigation and the interface was probed by a combination of 3-electrode cycling, cross-sectional SEM and *in-situ* XCT to reveal the dynamics of plating and stripping Na metal during cycling.

3.2 Introduction

Prior to this project, there were relatively few investigations in the literature of failures associated with stripping alkali metal anodes in SSBs. However, studies had suggested that a failure due to contact loss was occurring when the metal anode was stripped. Jow and Liang and later Nakanishi and co-workers used 3-electrode cells to identify that some form of contact loss was occurring at the Li anode/solid electrolyte interface due to insufficient diffusion within the Li anode.[162–164]

Previous work contributed to by the author studied voiding at the Li/Li_6PS_5Cl interface by 3-electrode cycling and cross-sectional SEM.[120] These findings are important to discuss in

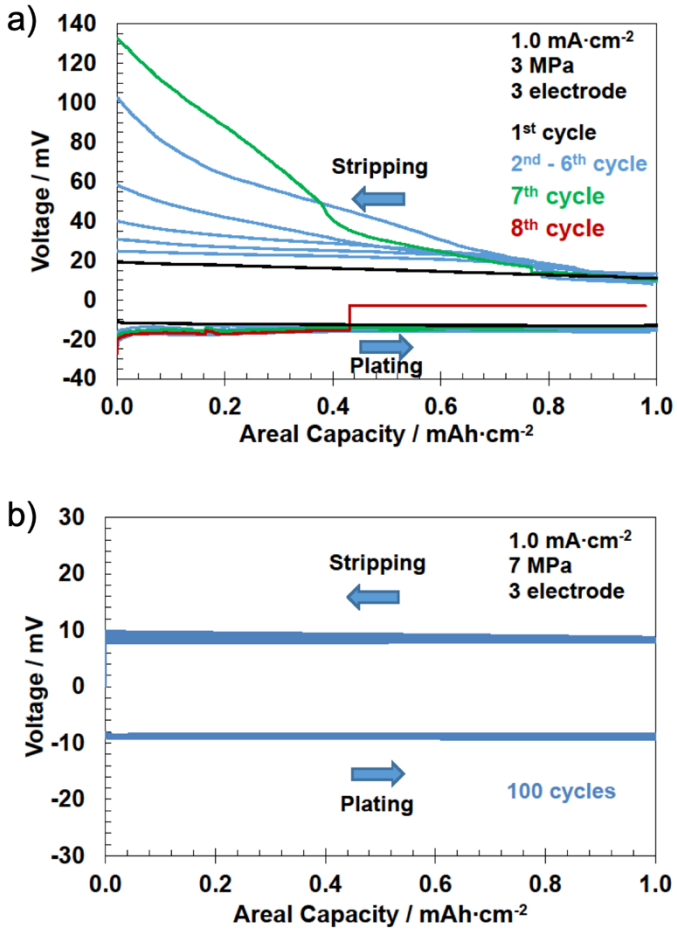


Figure 3.1: Voltage versus charge passed for 3-electrode cells on Li metal plating and stripping at the Li/Li_6PS_5Cl interface with a) at 3 MPa and 1.0 mA/cm^2 showing increasing polarisation on cycling due to voiding and b) at 7 MPa and 1.0 mA/cm^{2}showing no evidence of polarisation due to voiding. Data collected by Jitti Kasemchainan.

detail to contextualise the work in this chapter. Cycling of a 3-electrode cell at 1 mA/cm^2 under 3.5 MPa stack-pressure showed that cell polarisation was low and stable each time the working electrode was plated with Li, but each time the working electrode was stripped an increase in cell polarisation was observed, worsening each cycle (Figure 3.1a).

To better understand the asymmetry between stripping and plating, cells were cross-sectioned and imaged by SEM at different points in the cycling (Figure 3.2a). Whilst contact between the Li anode and Li_6PS_5Cl electrolyte is intimate in the pristine cell and following the 1st plating, after the 1st stripping some voiding is observed at the interface. By the end of the 6th stripping this voiding has worsened and interfacial detachment is

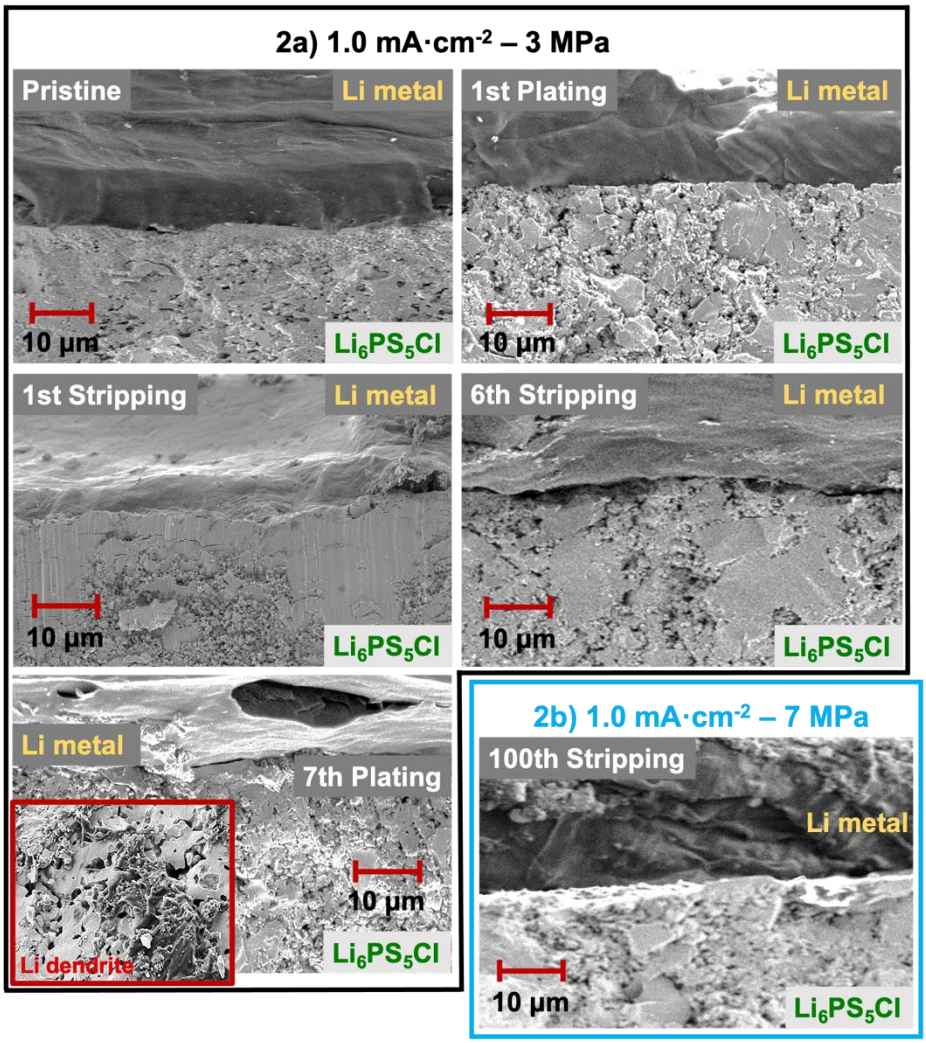


Figure 3.2: SEM cross-sections of the Li metal/Li_6PS_5Cl interface showing a) interfaces after cycling at 1.0 mA/cm^2 under 3 MPa when pristine, end of 1st plating, 1st stripping, 6th stripping and 7th plating and b) the interface after cycling at 1.0 mA/cm^2 under 3 MPa at the end of 100th stripping. SEM carried out by Stefanie Zekoll.

severe. As voiding worsens, the contact area between electrode and solid electrolyte decreases, leading to an increase in cell polarisation. These observations are in good agreement with the increasing polarisation seen in the 3-electrode cycling. Voids form when the rate of mass-transport of Li atoms to the interface is exceeded by the rate of Li-ion flux from the interface under current load during stripping, leaving Li vacancies at the interface that agglomerate into larger voids (see Chapter 1, Section 1.5.2 for further detail). As the Li-ion flux is dependent on the current density, there will exist a critical current for voiding above which voids will form and below which there will be no voiding. From these

data it is clear that the current density of 1 mA/cm^2 exceeds the critical current for voiding for this cell.

Given contact between the Li electrode and solid electrolyte degrades with cycling, how is it that the polarisation on plating remains unchanged with cycle number? The SEM image following the 7th plating gives an indication of how this is possible, as the large void is occluded and set back from the interface. It is proposed that early in the plating process Li deposition rapidly restores a high contact area interface by Li growth across the solid electrolyte from the triple point between Li anode (electron source), solid electrolyte (Li-ion source) and void (free space for Li deposition). However, whilst the plating temporarily

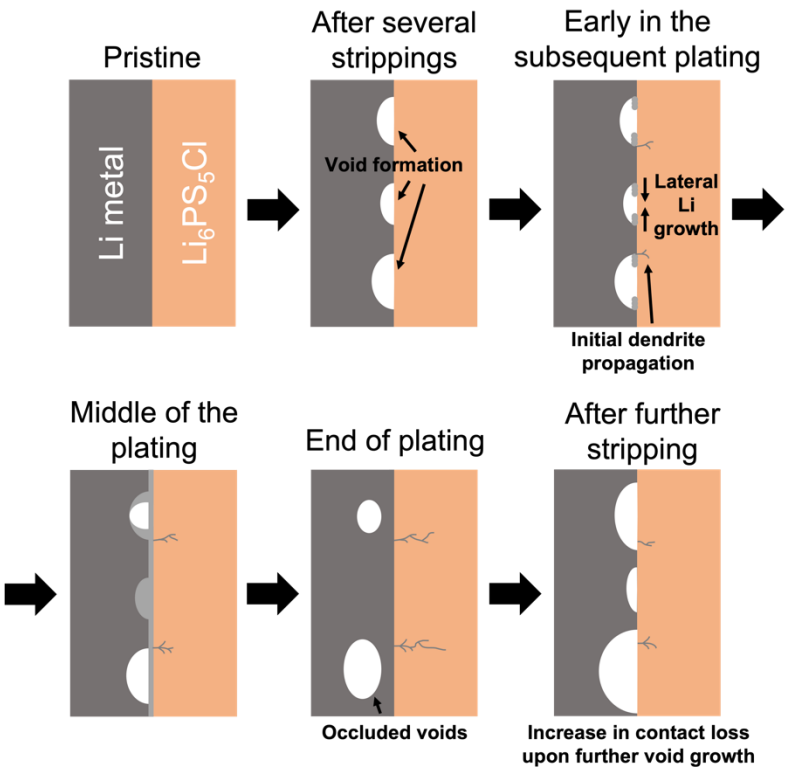


Figure 3.3: Schematic of Li metal/Li_6PS_5Cl interface cycled at an overall current density above the critical current for voiding. Sequence from pristine to after several strippings and platings of Li metal: voids form on stripping; lateral growth of a thin Li film across the electrolyte surface (nucleating where void edges meet the electrolyte) on subsequent plating results in low plating polarization and formation of occluded voids. Some voids are eliminated on plating, but the occluded voids re-open on subsequent stripping leading to accumulation of voiding and increasing loss of contact with cycling. This increases stripping polarization and results in dendrites on plating.

restores the interfacial contact between anode and solid electrolyte, the voids that were occluded on plating can readily be uncovered and grow further on the successive stripping, leading to void accumulation and growth throughout cycling. This is shown schematically in Figure 3.3. This progressive loss of interfacial contact is a significant contributory factor to cell death. As discussed in Introduction Section 1.5.3, dendrites have been observed to penetrate through ceramic solid electrolytes during plating above a critical current density. As contact is lost between the anode and solid electrolyte, current densities at the remaining areas of contact increase, until local current density at the interface exceeds the critical current for dendrite growth causing failure of the cell due to short-circuiting.

In a key observation, when a higher stack-pressure of 7 MPa rather than 3.5 MPa was applied to the cell, no polarisation was observed on stripping (Figure 3.1b) and very little contact loss was seen at the interface after 100 cycles (Figure 3.2b). This shows that the critical current for voiding is pressure dependent. At the higher applied pressures, higher rates of creep within the Li anode increase the rate of mass-transport of Li to the interface. As such, the cell can sustain a higher flux of Li-ions away from the interface without formation of voids. This pressure dependence of voiding on stripping was also noted in prominent works by Janek and co-workers and Sakamoto and co-workers.[166,172]

In this chapter a Na/Na-β”-Alumina/Na cell is used to progress understanding of voiding at alkali metal anode/solid electrolyte interfaces. Li metal anodes have garnered most attention for use in SSBs, due to their high theoretical capacity, however Na metal also promises significant improvements in anodic capacity over hard carbon anodes (1166 mA·h/g compared to approximately 300 mA·h/g).[242] What is more, it is particularly appealing to study interfacial dynamics of a Na metal anode as Na metal lends itself better to be studied by X-ray Computed Tomography (XCT) due to its higher attenuation of X-rays. Li is very poorly attenuating, making distinguishing between the Li anode and the

empty space of the void non-trivial, particularly when using a lab-based rather than synchrotron X-ray source.[168,191] On the other hand, more attenuating Na metal delivers good contrast against both the empty space of the voids and the Na-β”-Alumina electrolyte, enabling facile tracking of voids during cycling.

In this chapter, the similarities between the previously studied Li/Li_6PS_5Cl interface and the Na/Na-β”-Alumina interface are established by 3-electrode cycling and cross-sectional SEM, with voids observed to form above the critical current for voiding. *In-situ* XCT is then used to track voids through the first four complete cycles, with a combination of visual and quantitative analysis giving a more insightful view of how voids develop during cycling than has been possible for Li/solid-electrolyte interfaces. Finally, the pressure dependence of the critical current for voiding is explored in detail. Rather than simply examining a small number of stack-pressures as has been done previously, a range of pressures up to 12 MPa were used to determine the critical pressures at which voids form for current densities from 0.5-2.5 mA/cm^2. The results suggest that high stack-pressures may be required to enable stable discharge even at modest current densities, with > 9 MPa pressure predicted to be required for stable stripping at 2.5 mA/cm^2.

3.3 Experimental

3.3.1 Cell Preparation

3.3.1.1 Preparation of Na-β”-Alumina Disks

Na-β”-Alumina disks measuring 10 mm in diameter and 0.7 mm in thickness were purchased from Ionotec Ltd, a commercial manufacturer of β-alumina ceramics. The density of these pellets was determined to be > 97 % by comparing envelope density and the measured crystal density. The envelope density was determined using 7 cycles on a

Micromeritics GeoPyc 1360 envelope and T.A.P. density analyser and the crystal density was determined using 10 cycles on a Micromeritics AccuPyc II 1340 Gas Pycnometer.

Unless otherwise stated, Na-β”-Alumina disks described in this chapter were prepared as follows. Disks were polished using successively finer grits of SiC paper; 400, 600, 800, 1200 and finally 2500. The disks were transferred into an Ar filled glovebox (O_2 and H_2O concentrations < 1 ppm) where they were heat treated in a platinum crucible at 400 °C for 10 hours. This method was adapted from one described by Sakamoto and co-workers for the surface treatment of LLZO ceramics[61] and is similar to their later study describing surface treatment of Na-β”-Alumina, published after the project described in this chapter.[152]

3.3.1.2 2-Electrode and 3-Electrode Cells

Cells were used in both 2- and 3-electrode cell configurations. These cell configurations are shown diagrammatically in Figure 3.4. Whereas 2-electrode cells consist of only working and counter electrodes (WE and CE), 3-electrode cells also have a third reference electrode (RE). The reasons behind using these different cell configurations are discussed in greater detail in Section 2.3.2.

To prepare the Na/Na-β”-Alumina/Na cells, Na metal was cut from ingot within an Ar filled glovebox (O_2 and H_2O concentrations < 1 ppm) and surface film was removed using a scalpel. The Na metal was then pressed against aluminium spacers (which also act as WE and CE current collectors) to yield a thin Na film, approximately 100 μm thick and 5 mm in diameter. The Na-β”-Alumina pellet was masked using polypropylene tape such that only those areas of ceramic that would be in contact with Na were left exposed. The Na-covered aluminium spacers were then contacted against the exposed ceramic surfaces. In the case of a 3-electrode cell, an additional 1 mm diameter Na reference electrode was also

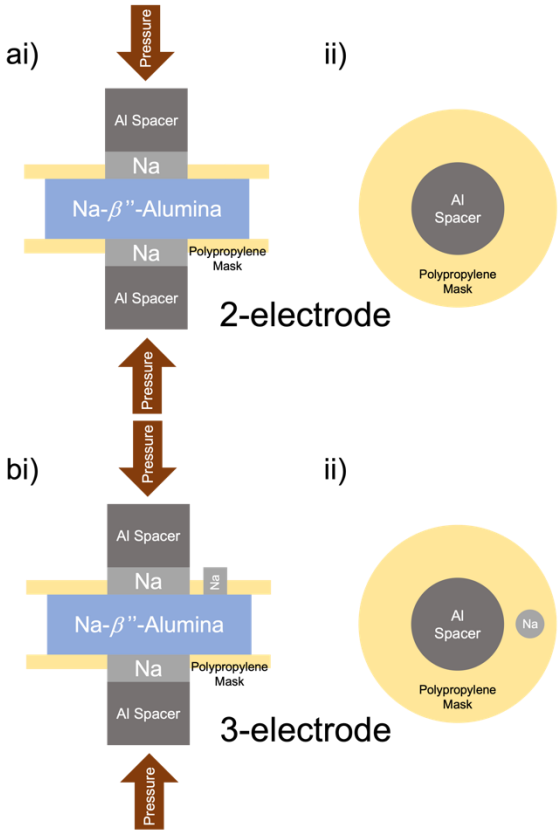


Figure 3.4: Schematics showing a) the 2-electrode and b) the 3-electrode cell configurations used in this chapter. i) and ii) show side and plan views respectively. Aluminium spacers are used such that stack-pressure is applied over a well-defined area.

contacted. The cell was then placed within a mylar-coated aluminium pouch cell body with aluminium current collectors and sealed under vacuum. Unless otherwise stated, cells were removed from the glovebox and pressed at 7 MPa overnight prior to testing, to create intimate Na/Na-β”-Alumina contact.

In most cases, stack-pressure on the cells was controlled using sprung clamps, with pressure set using a piezoelectric load cell (OMEGA). However, for determination of critical current for voiding and for *in-situ* cycling within the XCT, pressure was controlled using a Deben loading rig with a 5 kN stage.

3.3.2 Electrochemistry

PEIS was performed in the frequency range of 1 MHz to 1 Hz, taking 10 points per decade with a perturbation of 10 mV using a Gamry 1010E potentiostat. Unless otherwise stated,

cells were tested in the 2-electrode configuration. Analysis of the data was carried out using the ZView software package.

Galvanostatic cycling was done using a Biologic MPG-2 potentiostat. All cycling was conducted at room temperature, commencing with plating of the working electrode.

3.3.3 Characterisation

3.3.3.1 XRD

XRD was carried out in a glovebox with a nitrogen atmosphere (< 1 ppm O_2 and H_2O) to prevent exposure of the sample to air. The sample was loaded onto a low-background Si sample holder and the XRD pattern was collected with a Rigaku MiniFlex diffractometer using Cu Kα radiation.

3.3.3.2 XPS

XPS experiments were carried out by Dr. Phil Holdway from the Oxford Materials Characterisation Service using an ion-pumped ultrahigh-vacuum chamber fitted with a VG nine-channel CLAM4 electron energy analyser. Samples were transferred into the XPS chamber from a glovebox using a custom holder to prevent exposure to air. Collected spectra were corrected relative to the C 1s signal from adventitious carbon (248.8 eV).

XPS was used to assess surface impurities on the solid electrolyte disks and also to understand chemical reactivity at the electrode/solid electrolyte interface. The chemical reactivity at the Na/Na-β”-Alumina interface has already been well-defined in the literature[126] and hence the use of XPS was limited to determining the extent of success of the Na-β”-Alumina surface preparation procedure.

3.3.3.3 SEM

SEM was performed on cross-sectioned cells. Cross-sections were made in an Ar filled glovebox using an ultrasonic cutter (Sonotec) with a tungsten carbide blade. Copper tape was used to mount the cross-sectioned samples onto a custom-built stage. This stage was then loaded into an air-tight transfer holder (Gatan) and transferred into the Zeiss Merlin SEM through a purpose-built transfer chamber (Gatan).

Secondary electron imaging was carried out using an acceleration voltage of 5 kV and a probe current of 200 pA was used.

3.3.3.4 XCT and Image Reconstruction

Pouch cells were placed under pressure by a Deben CT5000 loading rig within the Zeiss Xradia Versa 510 XCT microscope for *in-situ* imaging. Cycling was paused after each charge and discharge to carry out XCT imaging. Images were taken using an acceleration voltage of 120 kV and a 30 s exposure time, rotating the sample through a full 360°. 1601 projections were taken for each *in-situ* image. This gave a voxel size of 2.2 μm/voxel.

Following the *in-situ* experiment, the cell was removed and the loading rig was replaced in the same position as for the experiment to take the reference image (average of 10 Flats). XRMDataExplorer was used to apply the reference image to each of the *in-situ* scans. These were subsequently reconstructed using the Zeiss XMReconstructor software package. The final reconstructed images were colourised, setting the grey levels consistent with Na metal as transparent such that the voids within could be clearly seen on the surface of the solid electrolyte. Imaging and reconstruction were carried out by Ziyang Ning.

3.4 Results and Discussion

3.4.1 Optimisation of Na-β”-Alumina and the Na/Na-β”-Alumina Interface

The Na/Na-β”-Alumina/Na cell was chosen as a model system for better understanding mechanical changes at the metal anode/solid electrolyte interface during cycling for a number of reasons:

- The Na/Na-β”-Alumina interface is well characterised in the literature, with robust evidence that there is no chemical reaction between electrode and electrolyte.[126,243,244] This lack of chemical reactivity means that changes in the voltage profile during cycling can be attributed to morphological rather than chemical changes in the cell. The failure modes of Na-β”-Alumina have also been extensively examined and give a basis for understanding the cell.[128,192,245]
- Na-β”-Alumina's high ionic conductivity of approximately 2 mS/cm makes it a realistic candidate for ASSBs and is used in commercially established Na-S and ZEBRA batteries.[246–250]
- Since it was planned to use XCT to track interfacial voids during cycling, it was decided to investigate a Na anode rather than a Li anode. Li is poorly attenuating to X-rays and therefore it is highly challenging to distinguish between Li metal and the empty space that is a result of voiding, often requiring a synchrotron X-ray source.[168,191] Na is more attenuating and therefore tracking interfacial voids is more facile.
- Na-β”-Alumina ceramics have high fracture strengths,[251] so can withstand relatively high stack-pressures without mechanical failure compared with sulphide ceramic electrolyte alternatives.[252]

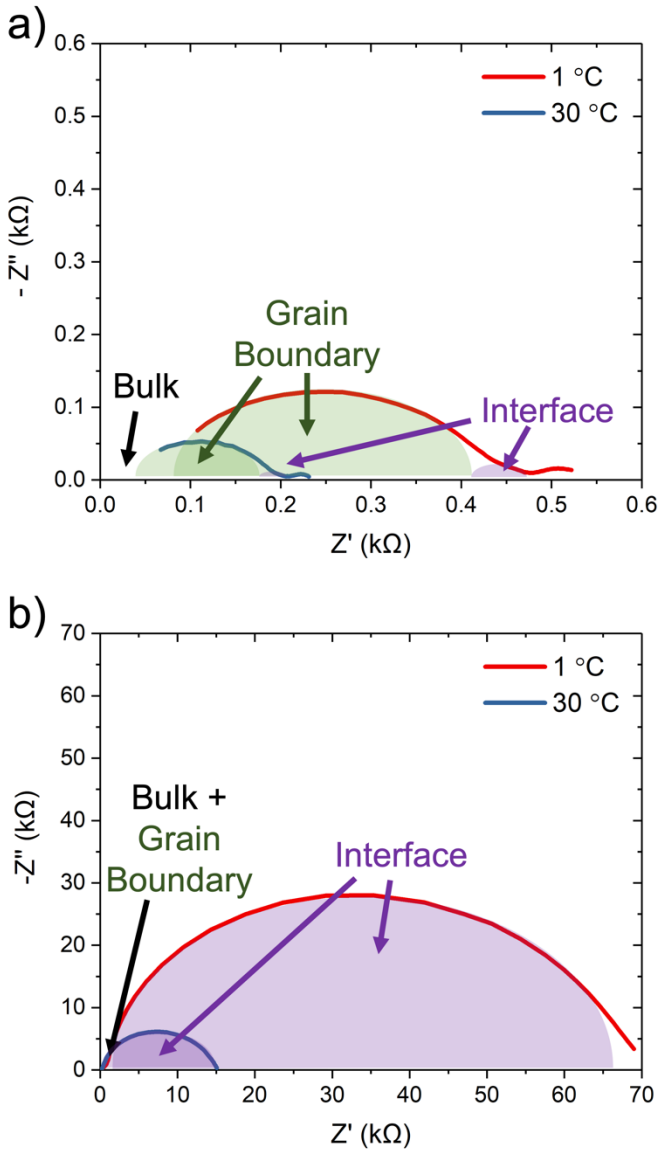


Figure 3.5: Nyquist plots of a) Na-β''-Alumina disks heat-treated at 400 ºC and b) untreated Na-β''-Alumina disks. PEIS was taken at 1 ºC (red) and 30 ºC (blue). Grain boundary and interfacial contributions and labelled and highlighted in green and purple, respectively. The bulk (intragrain) resistivity is given by the *x*-intercept.

However, at the time of this project no work had been published in the literature describing a solid Na anode interfacing with Na-β"-Alumina, although numerous studies on Na_{liquid}/Na-β"-Alumina interfaces at high temperatures had been carried out, dating as far back as the 1960s.[246] At the high temperatures required for use of a molten Na anode, the interfacial resistance is low and therefore careful surface treatment of the ceramic separator is not required. However, at room temperature, the interfacial resistance between Na and

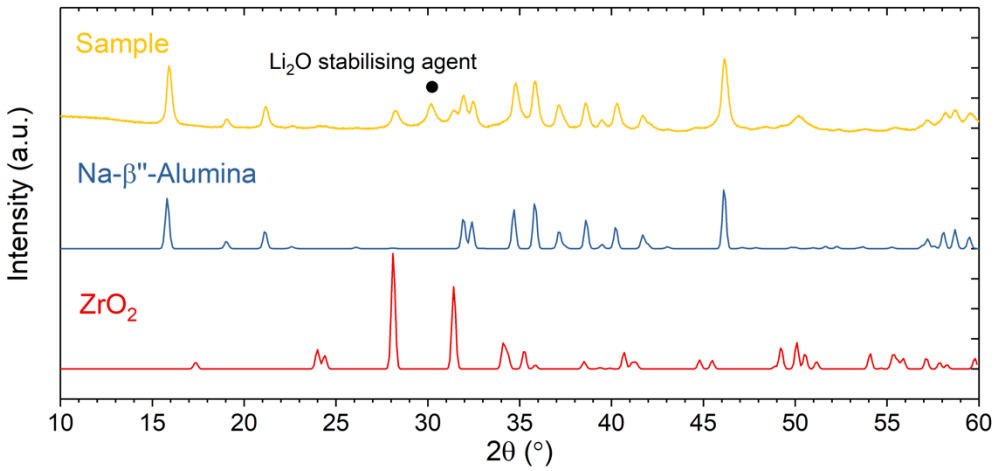


Figure 3.6: Collected XRD pattern of the Na-β''-Alumina used in this project (yellow). The data show that the primary phase is Na-β''-Alumina (blue), with secondary phases of ZrO_2 (red) which is added for transformation toughening, and Li_2O (black) which is added to stabilise the β'' phase over the β phase.

Na-β''-Alumina is found to be prohibitively high (Figure 3.5b). As a result, careful optimisation of the Na-β''-Alumina surface was necessary to give an interface with minimal resistance before studying the morphological changes at the interface would be possible.

Preparation of the Na/Na-β''-Alumina Interface

Before surface cleaning was carried out, the phase purity of the Na-β''-Alumina ceramic was established by XRD, as described in Section 3.3.3.1. The collected XRD pattern confirmed that the purchased ceramic contained only Na-β''-Alumina, zirconia which had been used as a sintering aid (see Section 1.5.3.2), and Li_2O which is added to stabilise the β'' phase (Figure 3.6).[196–198]

The optimal treatment of Na-β''-Alumina was determined by methods adapted from those used by Sakamoto and co-workers, who studied the Li-ion conducting oxide ceramic LLZO.[61] As described in Section 3.3.1.1, ceramic disks were ground with successively finer grades of SiC paper until a mirror-like shine was observed. The disks were then transferred into a glovebox and were either heat-treated at temperatures up to 400 °C or left untreated. At the time of this project, cooling limitations limited the maximum treatment

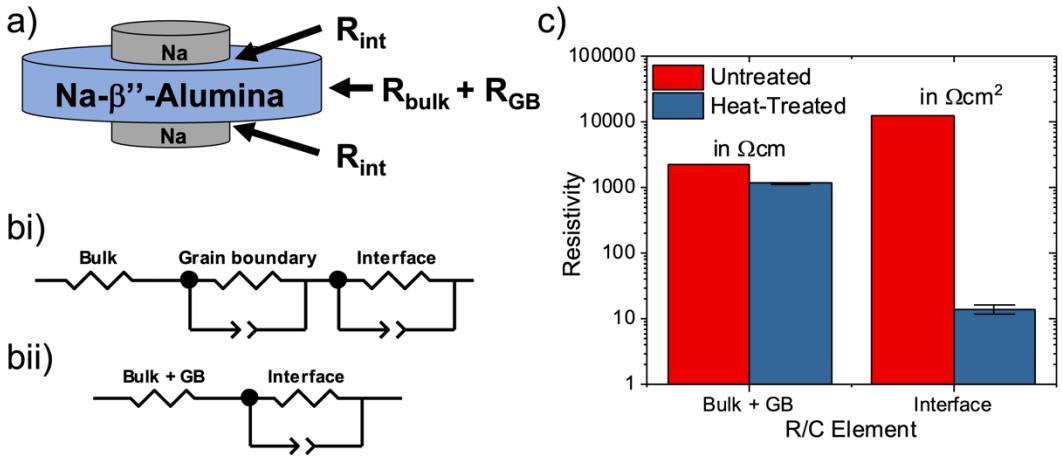


Figure 3.7: a) Schematic showing the origin of the bulk, grain boundary and interfacial resistances within a symmetric Na/Na-β''-Alumina/Na cell. b) Equivalent circuit diagrams which were used to model i) PEIS of the 400 ºC heat-treated Na-β''-Alumina cell and ii) PEIS of the untreated Na-β''-Alumina cell. c) Bar chart showing the differences in resistances between the untreated (red) and heat-treated (blue) cell resistances. This shows that the principal change in resistance is a significant decrease in interfacial resistance following heat-treatment.

temperature to 400 ºC within the Ar glovebox. Following heat treatment, the ceramics were used to make 2-electrode Na/Na-β''-Alumina/Na cells as described in Section 3.3.1.2 which were then tested by PEIS at temperatures of 30 ºC and 1 ºC. Nyquist plots are shown, comparing the untreated ceramic disk and a disk heat-treated at 400 ºC (Figure 3.5).

These Nyquist plots were interpreted using an equivalent circuit model in which each semi-circular contribution to the impedance is modelled as a resistor with a constant phase element in parallel (Figure 3.7b). Each contribution was then interpreted as a physical process within the cell from the characteristic capacitances of each process, as described by Irvine, Sinclair and West.[253] ZView was used to carry out this modelling and the fittings are summarised in Tables 3.1 and 3.2. Note that whilst impedances in the above Nyquist plots are shown in the unit kΩ, in the table interfacial contributions are in Ω·cm^2 (normalised for area) and bulk contributions are in Ω·cm (normalised for area and thickness).

The heat-treated Na-β”-Alumina showed lower impedances at both temperatures. Distinct contributions from the Na-β”-Alumina grain boundaries and from the Na/Na-β”-Alumina interface were observed, as was a clear *x*-intercept at high frequency giving the bulk (intra-granular) resistance of Na-β”-Alumina (Figure 3.5). As such it was modelled using the equivalent circuit shown in Figure 3.7bi. In contrast, the spectrum of the untreated disk shows a much greater impedance, strongly dominated by a single R/C element determined to be the Na/Na-β”-Alumina interface from the modelled areal capacitance value. As a result of the dominance of the interfacial contribution to the impedance, the higher frequency bulk and grain boundary contributions were found to not be well-resolved and were therefore modelled as a single resistive element in the equivalent circuit as shown in Figure 3.7bii. The extent of the effect of heat-treatment on the Na/Na-β”-Alumina/Na symmetric cell is shown most clearly in Figure 3.7c which demonstrates that whilst heat-treatment at 400 °C appears to have little effect on the resistance of the Na-β”-Alumina ceramic (i.e. bulk and grain boundary resistance), it has a significant impact on the resistance at the Na/Na-β”-Alumina interface, decreasing it by approximately three orders of magnitude.

It should be noted that the impedance spectrum for the Na/Na-β”-Alumina/Na cell utilising the heat-treated ceramic shows an additional impedance contribution at very low frequency which has not been included in the above discussion. When modelled using an additional R/C element in the equivalent circuit, this contribution is found to have an unusually high capacitance of approximately 0.05 F/cm^2, much higher than phenomena previously described in the literature, and so this contributing impedance has been left unassigned. A similar low-frequency semi-circle was observed by Janek and co-workers in their study of

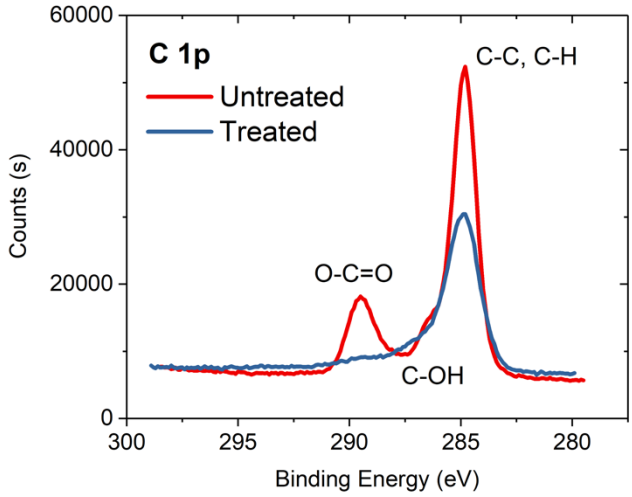


Figure 3.8: C 1p XPS of the untreated (red) and heat-treated (blue) Na-β''-Alumina disks. The spectra shows a marked decrease in the O-C=O peak in the 289.0-289.5 eV range after 400 ºC heat-treatment.

the Li/LLZO interface and although they too did not assign it to a specific physical process within the cell, they did speculate that it was likely a result of diffusion.[166]

To confirm that heat-treatment lowers Na/Na-β"-Alumina interfacial resistance by removing common oxide-ceramic surface contaminants such as carbonates and hydroxides,[60,61,254,255] XPS was performed on an untreated disk and a disk that had undergone heat treatment at 400 ºC (Figure 3.8). The C 1s spectra show a clear change in the surface species present upon heat treatment. Not only is there a decrease in the concentration of surface adventitious carbon species in the heat-treated sample, but the concentration of surface carbonates (peak at 289 eV) is observed to have greatly decreased.[61,152] These data show that heat treatment of the Na-β"-Alumina ceramic effectively removes poorly ionically conductive carbonate species from the ceramic surface and this accounts for the lower resistance observed in PEIS.

Further evidence for the success of the surface treatment can be seen by comparing 2-electrode rate-tests of untreated and 400 ºC treated disks. In each rate-test, the current density was increased in steps of 0.25 mA/cm^2 every 3 cycles, beginning from 0.25

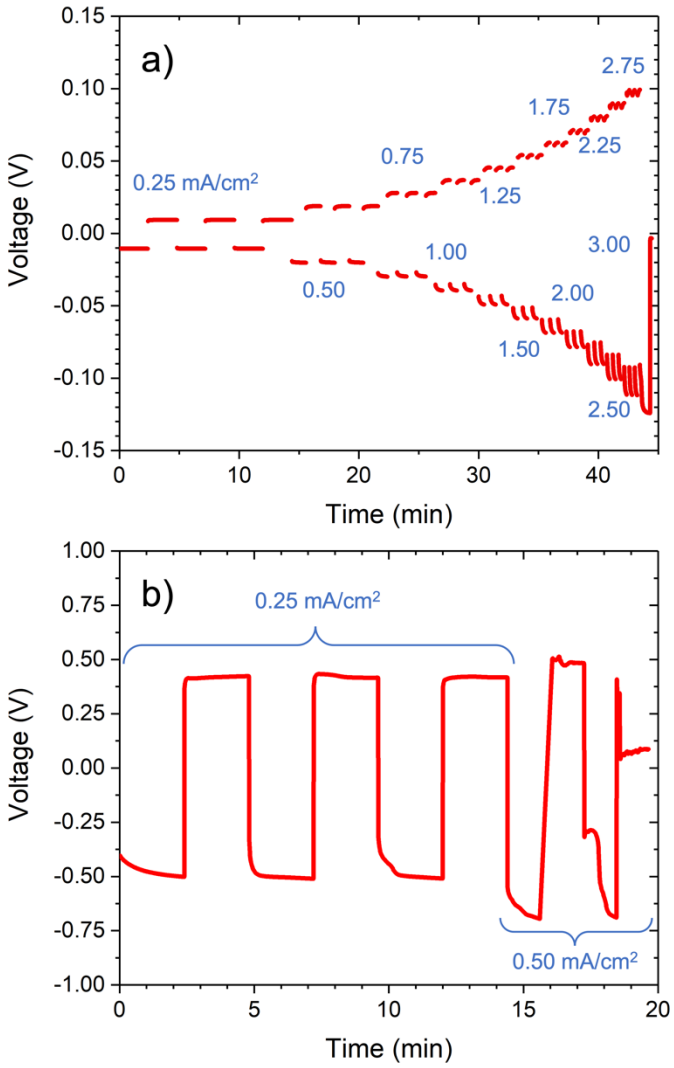


Figure 3.9: 2-Electrode cycling 'rate-tests' of a) 400 ºC heat-treated Na-β''-Alumina and b) untreated Na-β''-Alumina cells. Cycling was initiated at 0.25 mA/cm² and current density was increased in steps of 0.25 mA/cm² until cell failure. Failure was observed at 3 mA/cm² for heat-treated and 0.5 mA/cm² for untreated disks.

mA/cm². 0.5 mA·h/cm² capacity was moved in each half-cycle and cycling was carried out under 7 MPa stack-pressure. As shown in Figure 3.9, the treated disk was observed to have a significantly higher critical current for dendrite formation on plating than the untreated disk (approximately 3.0 mA/cm² compared to 0.5 mA/cm²). This suggests that the current density distribution across the heat-treated disk was more uniform than across the disk, likely due to the reduction in concentration of surface contaminants.

It was therefore established by a combination of PEIS, XPS and galvanostatic rate-tests that polishing and heat treatment was necessary to prepare a Na-β"-Alumina surface with

as few contaminating surface species as possible. Na-β”-Alumina disks were therefore polished and heat treated at 400 ºC prior to all further experiments in this chapter, as described in Experimental Section 3.3.1.1.

PEIS with Blocking Electrodes

Having established the phase purity of the purchased Na-β”-Alumina disks by XRD and optimised their surface treatment, the final task remaining before investigating the mechanics behind interfacial contact loss was to determine the conductivity of the ceramic disks in a symmetric cell with blocking electrodes. Commonly Pt, Au or Ni electrodes are sputtered onto the ceramic surface for use as blocking electrodes, however at the time of this investigation it was not possible to sputter metals within a glovebox atmosphere. Since it was not possible to carry out the sputtering in air due to the formation of Na-β”-Alumina surface contaminants observed earlier, indium (In) was chosen as the blocking electrode due to its reasonable blocking behaviour and the malleability of the metal meaning that good contact with the ceramic disc could be achieved by mechanical pressing, i.e. without the need for sputtering.

3 mm diameter In electrodes were pressed onto the ceramic to create a In/Na-β”-Alumina/In symmetric cell. The cell was sealed within a pouch cell body and PEIS was carried out at temperatures ranging from 1 ºC to 70 ºC. Figure 3.10 shows a) the Nyquist plots and b) the activation energy curve. Fitting of the Nyquist plot with ZView (as for Figure 3.6) gives an ionic conductivity of approximately 2 mS/cm at room temperature and the activation energy curve shows a linear relationship in this temperature range, giving an E_A of 0.21 eV. These values match closely with those previously reported in the literature.[192,248,256,257]

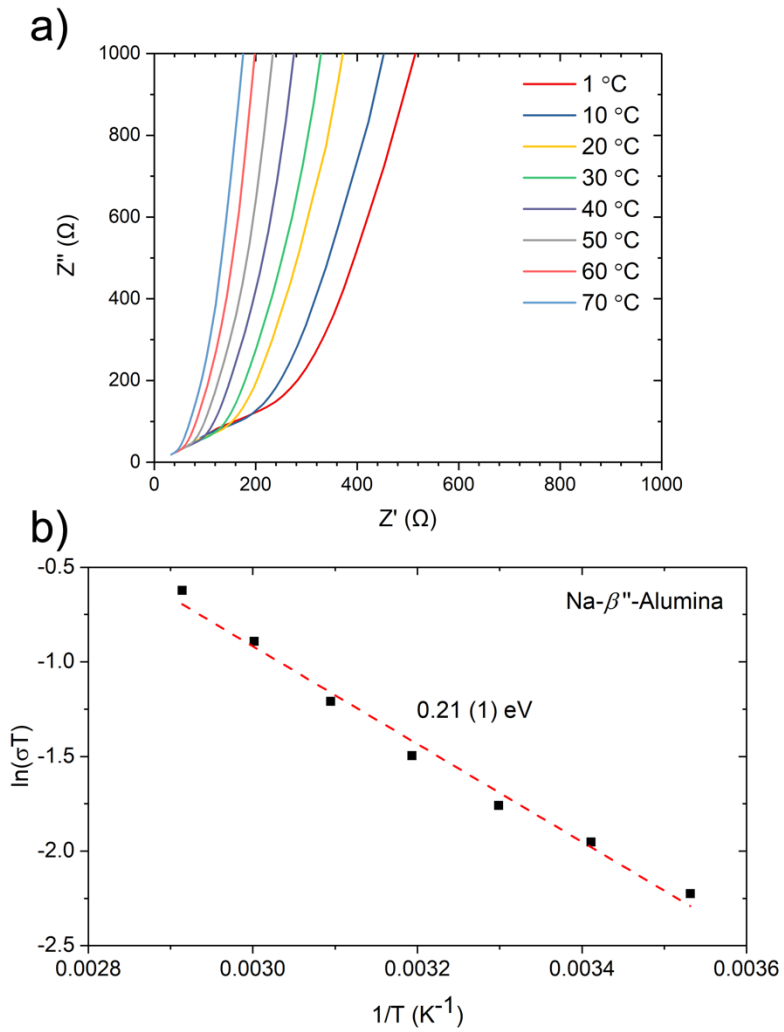


Figure 3.10: a) Nyquist plots showing PEIS of a In/Na-β''-Alumina/In blocking electrode cell in the temperature range of 1-70 ºC and b) the corresponding Arrhenius plot by which the Na-β''-Alumina activation energy of 0.21 (1) eV was determined. The reported error is the error in the linear fitting.

3.4.2 3- Electrode Cycling under 4 MPa of Pressure

3-Electrode cells were constructed as described in Section 3.3.1.2. The 3-electrode cell configuration was chosen as it enables the changes occurring at the working electrode/solid electrolyte interface to be studied in isolation from the counter electrode/solid electrolyte interface, effectively allowing for separate investigation of the processes of plating and stripping.

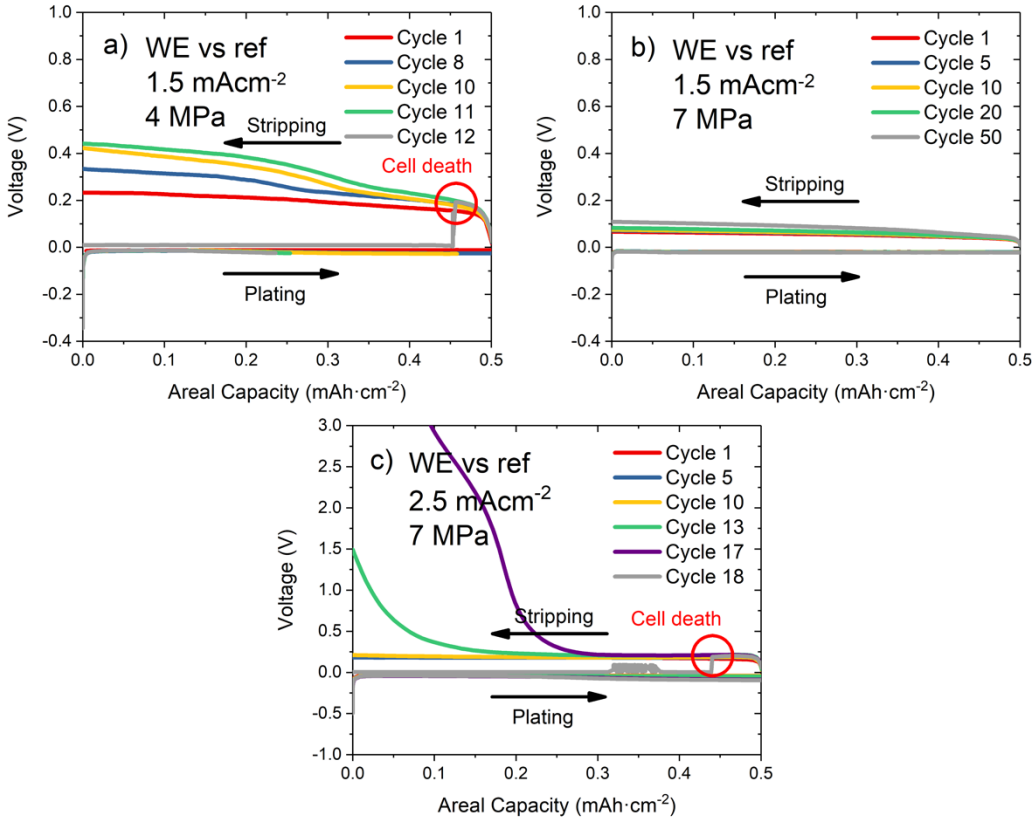


Figure 3.11: Voltage measured between working and reference electrodes when cycling at (a) 4 MPa and 1.5 mA/cm^2, (b) 7 MPa and 1.5 mA/cm^2, and (c) 7 MPa and 2.5 mA/cm^2. WE and ref are the working and reference electrodes, respectively.

The cells were cycled at 1.5 mA/cm^2, moving a capacity of 0.5 mA·h/cm^2 (equivalent to approximately 5 μm Na), beginning by plating the working electrode (and stripping the counter electrode), followed by stripping the working electrode (and plating the counter electrode). The cycling data (Figure 3.11) show severe asymmetry between the plating and stripping processes, as had been reported in previous literature (Section 3.2). The first plating of the working electrode occurs at a low and stable voltage of -12 mV. However, markedly different behaviour is observed for the first stripping of the working electrode. Whilst the voltage is also initially low, the cell polarisation increases significantly over the course of the 1st stripping to 0.23 V by the end of the first cycle (red). Interestingly, when the current is reversed and the working electrode is again plated, the potential falls rapidly, reaching approximately the same low voltage as on the first plating. This behaviour is

repeated on each plating of the working electrode, regardless of the polarisation on stripping. This is shown in Figure 3.11, with little change in cell potential observed from the 1st (red) to the 12th (grey) plating of the electrode.

The same cannot be said for stripping the working electrode. The cell polarisation on stripping worsens with each successive cycle, from 0.23 V at the end of the 1st stripping (red) to 0.42 V by the end of the 10th stripping (yellow). This is in close agreement with previous work, described in the introduction to this chapter, which showed for the Li/Li_6PS_5Cl interface that increasing cell polarisation with cycle number was a result of worsening interfacial contact due to void formation.

To confirm that worsening polarisation with cycle number is a result of interfacial voiding, cells were arrested at different points in cycling and were cross-sectioned as described in Experimental Section 2.2.3 for investigation by electron microscopy and these SE micrographs are shown in Figure 3.12. It should be noted that the surface of the Na metal has oxidised during the SEM transfer process which is thought to have led to the altered surface morphology.

Stripping

Figure 3.12c shows a cross-sectional image of the Na/Na-β”-Alumina interface following the first stripping. When comparing this to the pristine interface (Figure 3.12a) it is clear that the interface is less conformal, with a single void observed, approximately on a 10 μm length scale. Cross-sectional SEM of the interface following the 11th stripping shows multiple voids, each void larger than that observed following the 1st stripping. This demonstrates that there has been worsening interfacial voiding with cycle number and that the voids appear to have accumulated with each successive stripping.

As discussed in Section 3.2, the critical current for voiding on stripping is exceeded when the rate of Na-ion flux away from the Na/Na-β"-Alumina interface exceeds the mass transport of Na to the interface by self-diffusion and stress driven deformation:

Rate of Na diffusion + Rate of stress-driven deformation < Na-ion flux (3.1)

Since voiding is observed by SEM and 3-electrode measurements when the cell is cycled at 1.5 mA/cm^2 under 4 MPa stack-pressure, it can be concluded that under these conditions the Na-ion flux away from the interface under a 1.5 mA/cm^2 current load exceeds the mass-transport of Na to the interface, i.e. 1.5 mA/cm^2 > critical current for voiding.

Plating

Figure 3.12b shows an SEM image of the interface following the 1st plating of the working electrode. Little change is observed when compared with the pristine interface, Figure 3.12a. This is in agreement with the cycling data, which showed no change in polarisation during the 1st plating, emphasising that voiding is stripping phenomenon, and is not a result of plating.

Figure 3.12e shows the interface following the 12th plating and can reveal some insights when contrasted with the micrograph following the 11th stripping (Figure 3.12d). Following the 11th stripping, a number of large voids were observed at the interface, however following the 12th plating no voids were observed to be directly at the interface. Instead, the voids are set back a small distance from the interface behind a thin layer of Na metal that had been plated, occluding the voids. This offers an explanation for the earlier observation that the cell polarisation returns to a low and stable value on plating, regardless of the extent of void formation on stripping. Just as was observed for the Li/Li_6PS_5Cl interface (Section 3.2), early in the plating process the deposited Na metal is favoured to

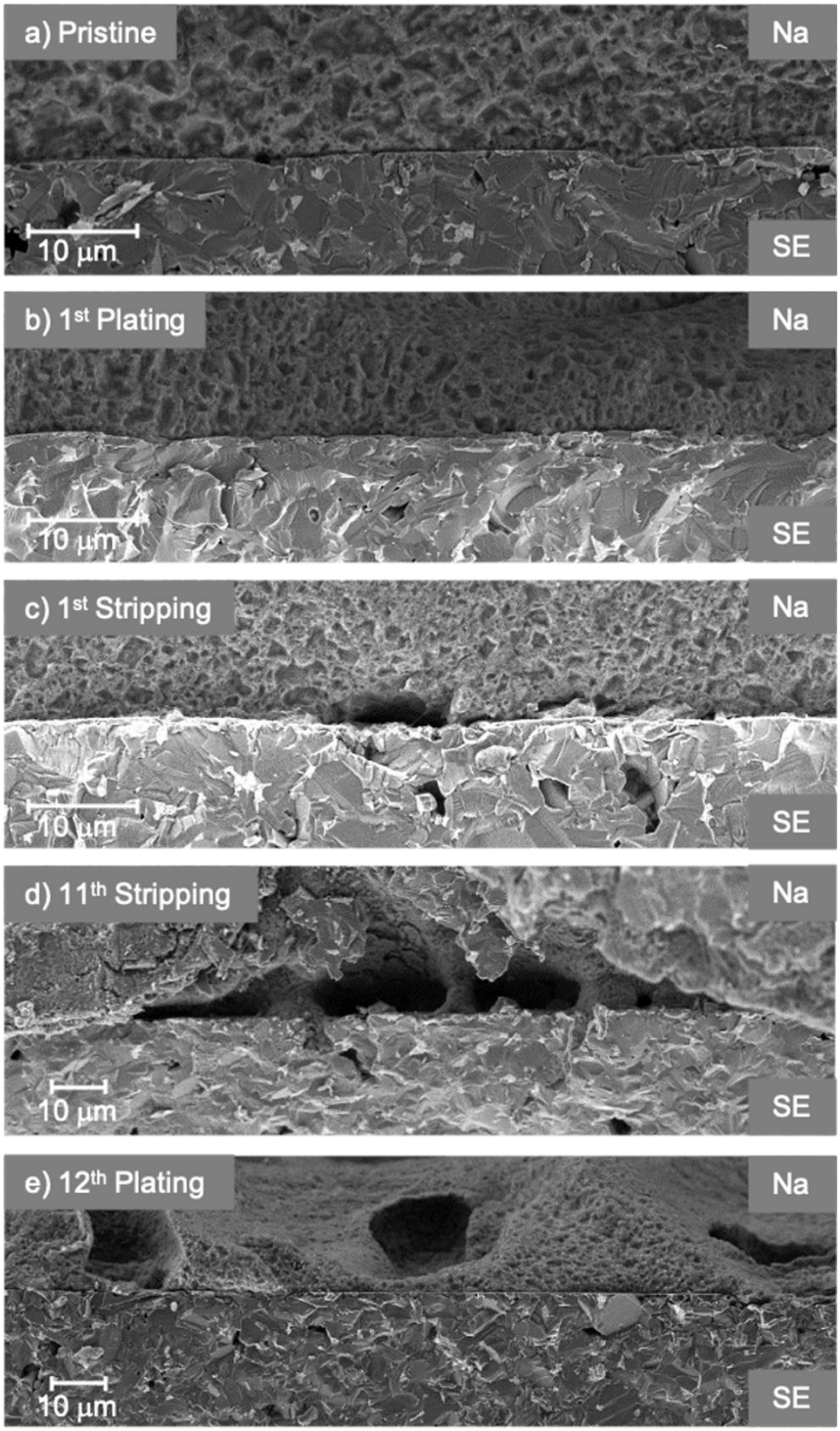


Figure 3.12: Cross-sectional SEM images of the Na/Na-β″-Alumina interface when (a) pristine and after (b) 1st plating, (c) 1st stripping, (d) 11th stripping, and (e) 12th plating after cycling under 4 MPa pressure at 1.5 mA/cm^2.

nucleate within the interfacial voids, at the triple point between the solid electrolyte (source of Na-ions), the Na metal (source of electrons) and empty space, shown schematically in Figure 3.13. Nucleation in empty space is favoured as no additional work is required to

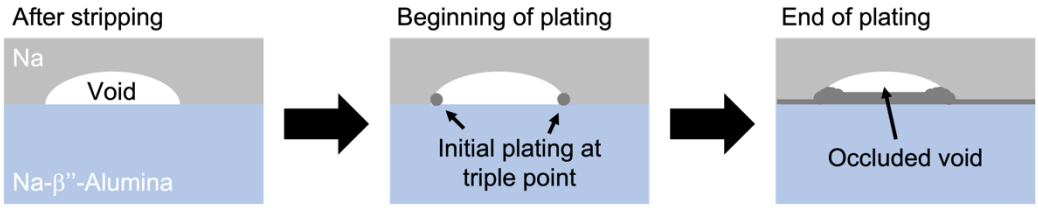


Figure 3.13: Schematic illustrating that when there are voids present at the metal anode/solid electrolyte interface, plating proceeds by nucleation of metal at the triple point between the metal anode, the solid electrolyte and the void.

create space for the Na deposition. In the very early stages of plating, a Na film will quickly grow to seal off the interfacial voids, which is in agreement with the rapid fall in cell potential in the very early stages of plating, returning to a low and stable potential. Once the voids are occluded, plating further capacity effectively pushes the occluded voids back from the interface.

Just as was found in analogous work on Li/solid electrolyte interfaces, after voids are occluded on plating, they can quickly be uncovered on the successive stripping before growing further in size. This is worsened by the fact that the local current density on stripping will also be higher at the triple point at the edge of the void, favouring void growth. In summary, whilst plating can temporarily 'heal' the Na/Na-β''-Alumina interface, returning it to approximately 100 % of the initial contact area, it does so by occluding voids which are quickly uncovered and grow on the successive plating.

Evolution of Voids on Cycling: In-situ XCT

In-situ XCT was carried out to further explore the morphological changes at the Na/Na-β''-Alumina interface during cycling. XCT was considered to be an attractive technique because:

1. It is non-destructive, so eliminates uncertainty associated with cross-sectioning the interface.

2. Imaging can be carried out *in-situ*, giving better insights into plating/stripping behaviours, as the same voids can be tracked over the course of cycling. This eliminates the conjecture that is necessary when interpreting a series of *ex-situ* SEM images.
3. The ability to image the whole interface, rather than just a cross-section, lends itself to carrying out a quantitative analysis of voiding, rather than a qualitative analysis.

XCT was carried out as described in Section 3.3.3.4 and reconstructed images of the Na/Na-β”-Alumina interface are shown in Figure 3.14. A colour-scale was applied to the images to clearly show the evolution of voids at the interface. Na-β”-Alumina solid electrolyte is

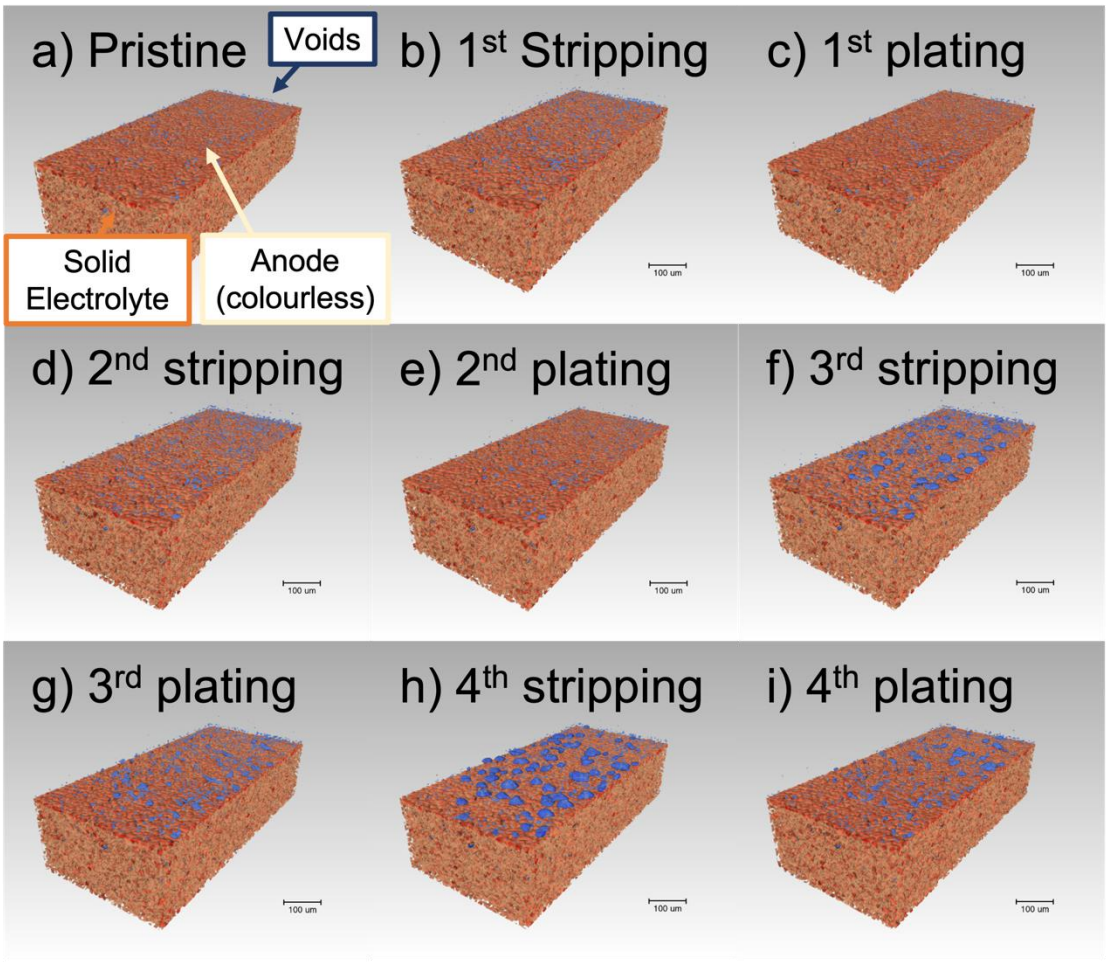


Figure 3.14: X-ray tomography images of the Na/Na-β″-Alumina interface when (a) pristine and after (b) 1st stripping, (c) 1st plating, (d) 2nd stripping, (e) 2nd plating, (f) 3rd stripping, (g) 3rd plating, (h) 4th stripping, and (i) 4th plating. Orange indicates the solid electrolyte, and blue indicates voids in the sodium anode (transparent). The cell was cycled at a pressure of 2 MPa and a current density of 1.5 mA/cm^2 with a capacity of 0.75 mA·h/cm^2.

shown as orange, the Na electrode is transparent, and empty space (voids) is shown in blue. The visual observations are closely supported by the quantitative analysis of the volume and number of voids at each stage of cycling (Figure 3.15). Both the total volume of voids at the interface (Figure 3.15a) and the number of voids in a certain volume range (Figure 3.15b) are determined for different stages of cycling. For the number of voids of a given size, the sizes are banded into categories of 1000-2500 μm^3 (small size, blue), 2500-10000 μm^3 (medium size, yellow) and > 10000 μm^3 (large, green). It should be noted that very small voids cannot be accurately resolved by XCT, so the total volume of voids will have been underestimated.

Visual and quantitative analysis of the cell reveals that the total volume of voids increases on each successive cycle (Figure 3.15a). Stripping increases the total volume of voids relative to the last cycle and plating decreases the volume of voids relative to the previous stripping. This is in accord with the conclusions of the 3-electrode cycling and SEM, that voiding is caused by Na metal stripping and that although Na plating can partially 'heal' a void, it often cannot do so completely.

A detailed cycle-by-cycle analysis of the interface reconstructions alongside the quantitative analysis gives further insights into the dynamics of Na stripping/plating:

- In the pristine cell, there are some small voids present at the interface (Figure 3.14a, Figure 3.15a) despite the efforts made to maximise the conformity of the interface prior to cycling (Section 3.3.1.2). This could be due to roughness in the solid-electrolyte surface or pre-existing porosity within the Na metal ingot. As mentioned

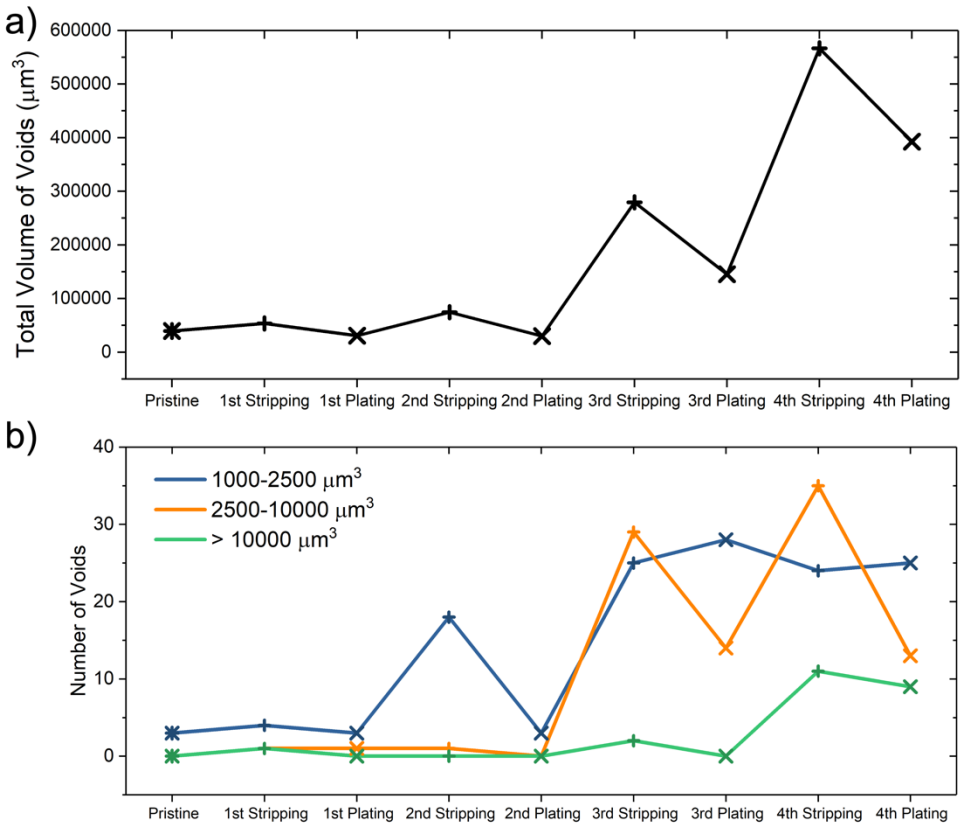


Figure 3.15: Quantitative analysis of X-ray Computed Tomography (XCT) data, showing (a) the total volume of voids in the Na anode and (b) the number of voids in the range 1000−2500 µm³ (blue), 2500−10 000 µm³ (orange), and >10 000 µm³ (green). The analysis was performed on a 6.58×10^{-2} mm³ volume of the cell interface.

previously, local currents can be higher at the edge of voids, so these pre-existing voids may act as initiation points for further contact loss.

- Following the 1st stripping (Figure 3.14b), there is an increase in the total volume of interfacial voids (Figure 3.15a). This is driven by an increase in the number of smaller voids observed across the interface increases, however no considerably larger voids are observed (Figure 3.15b). After the following plating (Figure 3.14c), fewer of these small voids are seen at the interface. This could either indicate the elimination of some voids during Na metal plating, or that some voids have fallen below the volume of the lower band limit (1000 µm³).

- Some evidence that the voids have fallen below the resolution of the lab-source XCT, rather than being totally eliminated on plating, is offered by the reconstruction of the interface following the 2nd stripping (Figure 3.14d). This shows not only more interfacial voids than were present after the 1st plating, but also more voids than following the 1st stripping. What is more, some voids reappear in locations where they had been observed following the 1st stripping but were not observed following the 1st plating. Following the 2nd plating, again the voids appear to decrease in both size and number as they are partially or completely filled by Na plating.
- A substantial change in the interfacial morphology is observed over the course of the 3rd stripping (Figure 3.14e). Not only are many new, small voids observed, now covering much of the interface, but for the first time a number of considerably larger voids (> 2500 μm^3) are seen. This shows that not only are new voids created with each successive stripping, but that voids also grow and agglomerate to form larger voids at the interface.
- Unlike in the first two cycles, following the 3rd plating (Figure 3.14g) the number of voids at the interface does not seem to decrease considerably, however the size of those voids that are present does appear to decease. This is clear in Figure 3.15b, as although there is a decrease in the number of voids in the 2500-10000 μm^3 and > 10000 μm^3 size bands, there is in fact an increase in the number of voids in the 1000-2500μm^3 size band, suggesting that larger voids are not being eliminated (or falling below the XCT resolution), but are just decreasing in size. In short, by the 3rd stripping, the interfacial voids have grown sufficiently large that even though the voids become occluded and partially filled by Na plating, they are still readily observable at the interface.

- This trend continues to the 4th cycle. After the 4th stripping considerable contact loss between the Na anode and Na-β”-Alumina is evident (Figure 3.14h). The number of > 10000 μm^3 interfacial voids has increased significantly and those large interfacial voids that were already present from the 3rd cycle have increased in volume. Whilst the total void volume decreases during the 4th plating (Figure 3.14i, Figure 3.15b), the contact loss remains substantial and indeed is greater than following the 3rd stripping. It is clear that it is not possible to 'heal' the Na/Na-β”-Alumina interface through plating, particularly once large voids are present at the interface, as it is not possible to refill these voids by plating and they simply become occluded close to the interface.

Relating these findings to local current densities emphasises why SSBs can fail rapidly if the critical current for voiding is exceeded and voids form. The local current density (I_{local}) can be expressed as:

$$I_{local} = {I_0}\Big/{\left(\frac{A}{A_0}\right)} \tag{3.2}$$

were I_o is the applied current density (under the assumption there is 100 % interfacial contact), A is the true area of interfacial contact and A_0 is the area assuming 100 % interfacial contact. Therefore, I_{local} is inversely proportional to the true local contact area, A, between Na and Na-β”-Alumina. The XCT data have shown that when the critical current for voiding is exceeded, interfacial voids increase in size and number during stripping, with contact loss progressively worsening with cycle number. As such, local current densities will also increase. Not only do high local current densities lead to inhomogeneous stripping of the Na anode, but they also cause dendrite penetration into the ceramic electrolyte on charge, as discussed in Section 1.5.3. Therefore, when the critical

current for voiding is exceeded, interfacial contact loss will worsen until local currents exceed the critical current for dendrite growth, at which point the cell will eventually short-circuit. For the cell in Figure 3.11a, this short-circuit was observed during the 12th stripping of the working electrode (grey), as is indicated by the sharp fall in cell potential to approximately 0 V.

3.4.3 Cycling 3-Electrode Cells under 7 MPa of Pressure

To begin to investigate the effect of pressure on the critical current for voiding, a further cell was cycled at the same current density (1.5 mA/cm^2), but under a higher stack-pressure of 7 MPa (Figure 3.11b). Under the higher stack-pressure, the increase in cell polarisation is low over 50 cycles, suggesting that there is no significant interfacial voiding over the course of the cycling. This is confirmed by cross-sectional SEM, which shows that intimate contact is retained between the Na anode and Na-β"-Alumina solid electrolyte after the 1st stripping (Figure 3.16ai), 25th stripping (Figure 3.16aii) and 50th stripping (Figure 3.16aiii).

However, when a cell was cycled under the same 7 MPa stack-pressure, but at a higher current density of 2.5 mA/cm^2, cell failure due to voiding was once again observed, with cell polarisation increasing to reach 3 V in cycle 17, immediately preceding cell failure due to dendrite growth on the 18th plating of the working electrode (Figure 3.11c). Cross-sectional SEM of a cell cycled under these conditions after the 17th (final) stripping of the working electrode confirmed that there was severe interfacial contact loss (Figure 3.16b).

It can therefore be concluded that at higher stack-pressure, the critical current for voiding has increased from less than 1.5 mA/cm^2 at 4 MPa, to greater than 1.5 mA/cm^2 but less than or equal to 2.5 mA/cm^2 at 7 MPa. Returning to Equation 3.1, it is clear that the increased stack-pressure increases the mass transport of Na metal to the interface by

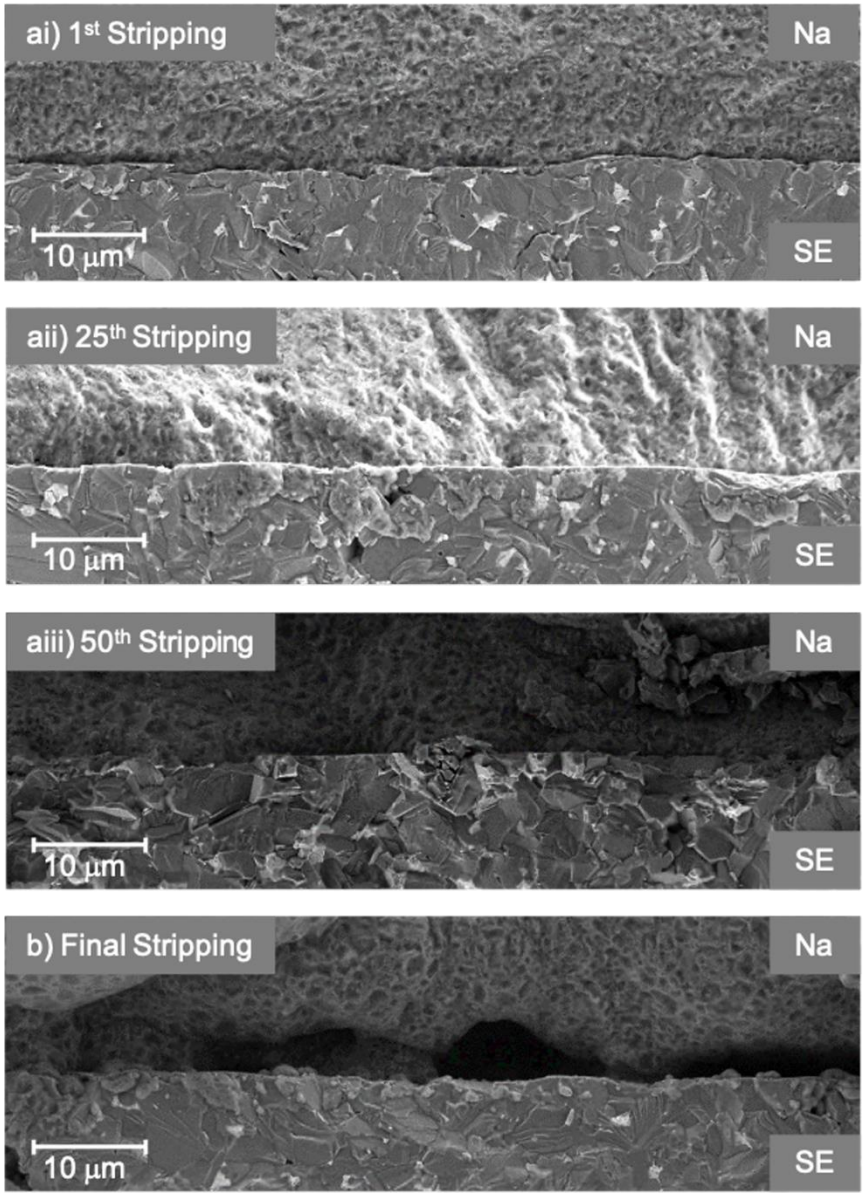


Figure 3.16: SEM images showing the Na/SE interface after ai) the 1st stripping, aii) the 25th stripping and aiii) the 50th stripping when cycling under 7 MPa pressure at 1.5 mA/cm^2 and b) the final stripping when cycling under 7 MPa pressure at 2.5 mA/cm^2.

increasing the rate of creep in the Na metal. The yield strength of Na is low, reported to be 0.19-0.24 MPa at a strain rate of ~ 10^{-3} s^{-1}, and therefore Na is expected to have a propensity to creep under the high stack-pressures used.[149] Higher stack-pressure is expected to increase the rate of Na creep to the interface, thereby increasing the rate of Na-ion flux away from the interface that can be sustained without leaving interfacial vacancies (the critical current for voiding).

3.4.4 Counter Electrode *versus* Reference Electrode

Three separate sets of 3-electrode cycling data have been presented in this chapter, each showing the working electrode *vs.* reference electrode data. These cells were cycled at 1.5 mA/cm^2 under 4 MPa, 1.5 mA/cm^2 under 7 MPa and 2.5 mA/cm^2 under 7 MPa (Figures 3.11a-c). Simultaneous to collection of the voltage of the working electrode *vs.* the reference electrode, the counter electrode *vs.* the reference electrode voltage was also collected and these data are shown in Figure 3.17a-c.

Previously it had been concluded from Figure 3.11b that 1.5 mA/cm^2 is below the critical current for voiding under 7 MPa and as expected, the corresponding counter electrode *vs.* the reference electrode data show no significant increase in polarisation over 50 cycles (Figure 3.17b). It had also been concluded that 1.5 mA/cm^2 is above the critical current for voiding under 4 MPa and that 2.5 mA/cm^2 is above the critical current for voiding under 7 MPa, since increasing working electrode *vs.* the reference electrode polarisation was observed. As anticipated, the polarisation was also observed to increase with cycle number in the corresponding counter electrode *vs.* the reference electrode cycling profiles (Figures 3.17a,c).

New insights are gained by examining the relative rates of polarisation on stripping at the working and counter electrodes. In the cell cycled at 1.5 mA/cm^2 under 4 MPa, the working electrode *vs.* reference electrode data showed the polarisation reaching a maximum of 0.44 V after 11 cycles, whereas polarisation at the counter electrode was much more severe, reaching the voltage limit of 3 V on the 10th stripping and on the cycles thereafter. The opposite was observed for the cell cycling at 2.5 mA/cm^2 under 7 MPa, with the working electrode reaching a polarisation of 3 V on the 17th stripping, but polarisation at the counter electrode reaching a maximum of only 0.74 V on the 18th stripping. It can therefore be concluded that contact loss occurs at different rates at the different electrodes. It had been

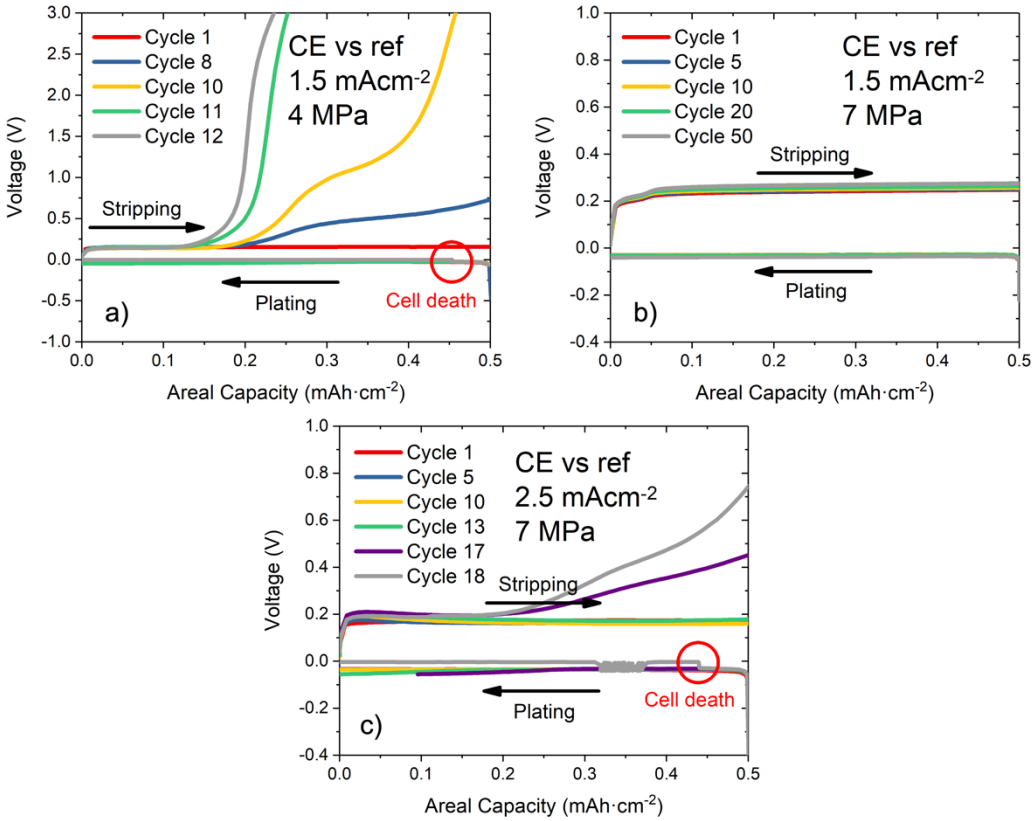


Figure 3.17: Voltage measured between counter and reference electrodes when cycling at (a) 4 MPa and 1.5 mA/cm^2, (b) 7 MPa and 1.5 mA/cm^2, and (c) 7 MPa and 2.5 mA/cm^2. Cycling data corresponds to the working electrode *vs.* reference electrode data shown in Figure 3.11. CE and ref are the counter and reference electrodes, respectively.

anticipated that the electrode that was stripped first (the counter electrode in each case) would undergo more severe contact loss throughout cycling, however this was not observed to be the case, with different electrode interfaces degrading more rapidly in each cell. It is likely that other factors may contribute to the relative rates of interfacial contact loss, such as the concentration of pre-existing voids at each interface and possible inhomogeneity of insulating surface contaminant species, such as residual hydroxides and carbonates.

3.4.5 Critical Pressure with Current Density

The functionality of the critical current for voiding with stack-pressure was explored to assess the pressures required to achieve practically relevant high rates of discharge for electric vehicles. Five 3-electrode cells were constructed for testing. Each was placed

within a Deben rig for dynamic control of stack-pressure. These stack-pressure dependent measurements were carried out with help from Dr. Ed Darnborough. Cells were pressed under a high stack-pressure of 15 MPa prior to any cycling to minimise the effects of any pre-existing interfacial voiding.

Cycling began by stripping the working electrode at a given current density for a capacity of 0.1 mA·h/cm^2 at a controlled stack-pressure and the change in cell polarisation was recorded. Following the stripping, the cell was re-pressed to 15 MPa to restore the interface by eliminating any interfacial voiding that had occurred during stripping. The working electrode was then stripped again, at the same current density but at a lower, controlled stack-pressure and the change in polarisation was recorded. This was repeated at progressively lower stack-pressures until the cell polarisation exceeded the voltage limit of 3 V over the course of a single stripping. The possibility of interfacial voiding from the previous measurements affecting the following measurement was minimised by carrying out the experiments from high to low pressure and by pressing the cells to reform the interface between measurements.

Each of the five cells was tested at a different current density; 0.5 mA/cm^2 (red), 1.0 mA/cm^2 (blue), 1.5 mA/cm^2 (yellow), 2.0 mA/cm^2 (green) and 2.5 mA/cm^2 (grey). These are shown in Figure 3.18. The data show that the functionality between the increase in voltage during stripping (which can be taken as a measurement of the extent of voiding), and the stack-pressure is the same regardless of the current density. At lower stack-pressures the polarisation is high, indicating that severe voiding is occurring, whereas at higher stack-pressures no sizable increase in polarisation is evident. However, as the stripping current densities increase, the curve shifts to the right, indicating that higher stack-pressures are required to prevent voiding from occurring. This is in line with the observations made earlier in this chapter. That the stack-pressure has this great an effect on

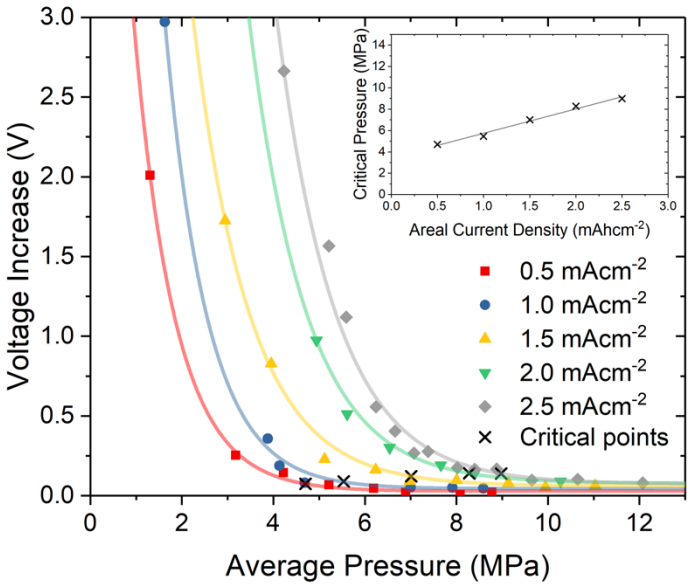


Figure 3.18: Figure showing the functionality between average pressure and voltage increase at 0.5 mA/cm^2 (red), 1.0 mA/cm^2 (blue), 1.5 mA/cm^2 (yellow), 2.0 mA/cm^2 (green), and 2.5 mA/cm^2 (grey) areal current densities. The inset shows how the critical pressure varies with areal current density.

current density at which Na can be stably stripped suggests that creep of Na metal is the dominant mechanism of the mass-transport of Na to the interface, over self-diffusion of Na, in this pressure range.

To draw more conclusions from the data, an attempt was made to estimate the critical pressures at which the critical current for voiding had been exceeded for each current density. A question that arises from this is, what, practically speaking, is the critical current for voiding? Previously in this chapter, as well as in the literature,[120] the critical current for voiding has been treated somewhat like a step function, with the suggestion that below a critical current density there is no interfacial voiding whatsoever and above the critical current density voiding will occur. However, the exponential decay of voltage increase with stack-pressure reveals some of the complexities of measuring the critical current for voiding. Even at very high stack-pressures, polarisation was always observed to increase by some millivolts on stripping, with these small increases being of a higher magnitude at

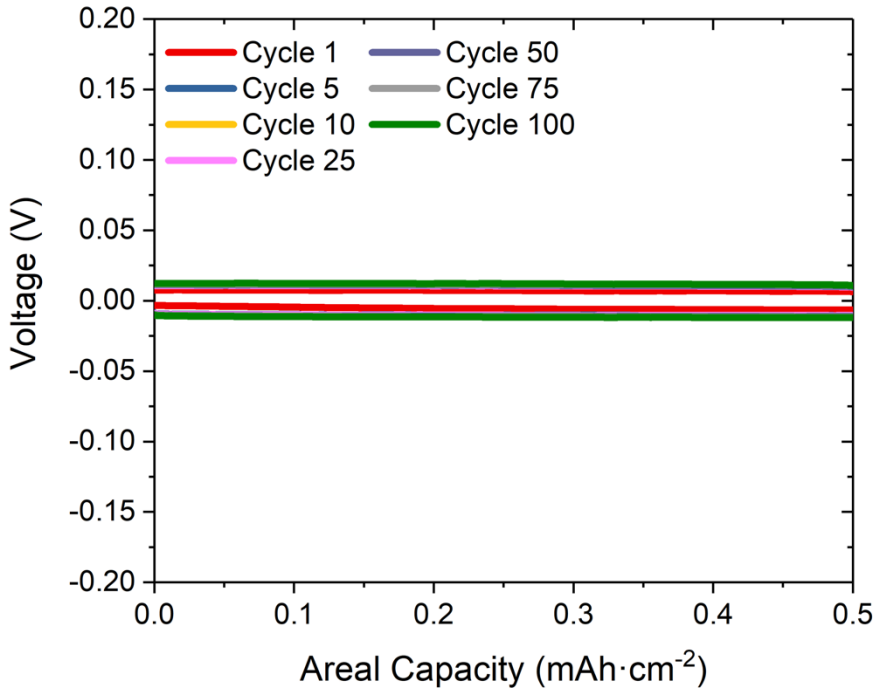


Figure 3.19: 2-Electrode cycling under 4 MPa at 0.1 mA/cm^2 over 100 cycles showing highly reversible stripping and plating of Na metal and no polarisation due to voiding.

higher current densities. If the critical current for voiding is taken as the current density at which a cell can be cycled with highly reversible stripping, this does not exclude the possibility of some voiding at the interface, but rather requires that that voiding be reversible on plating. Therefore, the critical pressures at which the critical current for voiding was exceeded were taken to be the points at which the fitted curves deviated from the horizontal of the high-pressure region. A deviation of dV/dP = -0.05 was chosen as the critical pressure, a value which was arbitrary, but informed by confidence that the change in voltage had increased with decreasing pressure.

These critical points are plotted as the inset to Figure 3.18 and show a linear increase in critical pressure with current density over this stack-pressure range. The plot successfully predicts the behaviours of the cells previously cycled in this chapter, predicting that 7 MPa is sufficient to sustain a stripping current density of 1.5 mA/cm^2, but is insufficient to sustain a current density of 2.5 mA/cm^2, and that a 4 MPa stack-pressure is insufficient to sustain a 1.5 mA/cm^2 stripping current. To test this further, a 2-electrode cell was cycled at

0.1 mA/cm^2 under a 4 MPa stack-pressure, conditions under which this cell is predicted to cycle stably. Encouragingly, stable cycling was observed over 100 cycles (Figure 3.19), with no polarisation increase due to voiding observed.

It is important to stress that this linear trend between critical pressure and stripping current density is only expected to hold over this region of stack-pressures. If the linear fitting were to be extrapolated, it would meet the *y*-axis, leading to a prediction that high pressures of > 3 MPa would be required to stably strip the Na anode even under negligibly low current densities. This is not the case, as it is known for Li anodes that self-diffusion alone is sufficient to sustain very low stripping current densities and that creep (and therefore stack-pressure) is not required.[166] The self-diffusion coefficient of Na metal is greater than that of Li, giving the ability to sustain higher currents in the absence of stack-pressure, i.e. the complete plot of current density *vs.* critical pressure is expected to have a *x*-intercept, rather than a *y*-intercept. It is likely that as the stack-pressure falls towards the yield strength of Na, and creep is no longer dominant over self-diffusion of Na metal to the interface, the relationship diverges from the linear relationship observed in the 0.5-2.5 mAcm^{-2} current density range.

Having discussed the inability to extrapolate this linear relationship to the low current density region, extrapolation to higher current densities is discussed. Can ever higher stack-pressures enable stable cycling at ever higher current densities? Figure 3.20a-b presents data showing single platings of 3-electrode cells at different current densities under stack-pressures of 4 MPa and 12 MPa. The cells show stable plating at current densities of 1.0 mA/cm^2 (blue) and 1.5 mA/cm^2 (yellow), with the cells under higher pressure observed to give a lower cell overpotential. When plating the working electrodes at 3 mA/cm^2, cells at both pressures show a sudden decrease in potential, consistent with dendrite penetration through the solid electrolyte. This is in agreement with there being two critical current

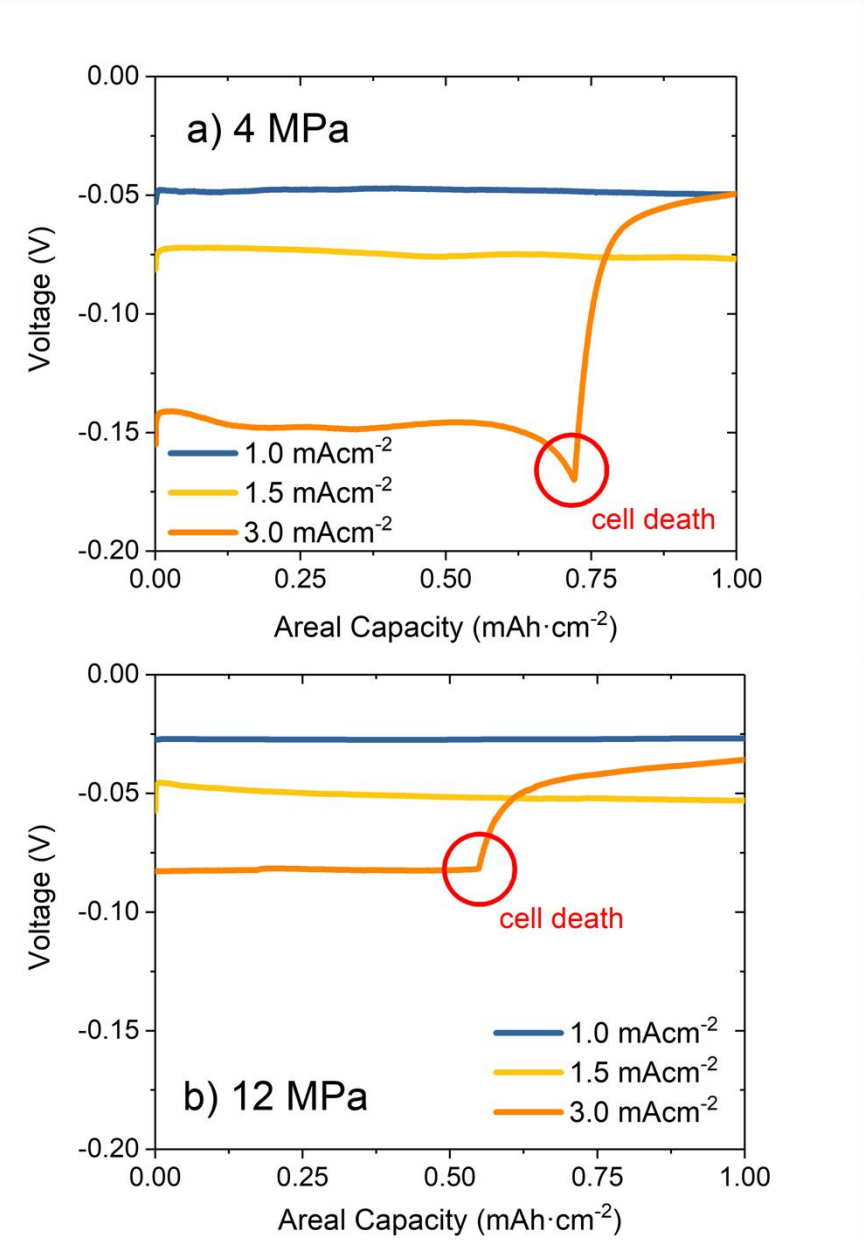


Figure 3.20: Potential between the working and reference electrodes for a single plating at 1.0 mA/cm^2 (blue), 1.5 mA/cm^2 (yellow), and 3.0 mA/cm^2 (orange) when (a) at 4.0 MPa and (b) at 12.0 MPa. Cells short-circuit due to dendrite penetration at 3.0 mA/cm^2 regardless of stack-pressure.

densities as discussed in Section 1.5, the critical current for voiding and the critical current for dendrite formation. Cycling current densities can only be increased by increasing stack-pressure up to the limit of the critical current for dendrite growth, which is dependent not on stack-pressure, but on the properties of the solid electrolyte, as discussed in Section 1.5.3. For the Na/Na-β”-Alumina cell, the critical current for dendrite growth is greater

than 2.5 mA/cm^2, but less than or equal to 3.0 mA/cm^2, as Figure 3.20 shows that dendrite growth occurs on plating at 3.0 mA/cm^2, regardless of stack-pressure. Prevention of voiding alone is not an answer to achieving ever higher cycling current densities, and prevention of dendrite initiation and propagation at high current densities remains important.

3.5 Conclusions

This chapter has explored void formation at the Na/Na-β”-Alumina, using 3-electrode cycling, cross-sectional SEM and *in-situ* XCT to better understand the dynamics of Na plating/stripping at the interface. These techniques have shown that voiding is a phenomenon that occurs only on stripping, when the flux of Na-ions away from the interface exceeds the rate of mass-transport of Na to the interface. XCT was used to quantify the interfacial contact losses occurring, showing that it is the inability to eliminate voids on plating that leads to progressively worsening contact as voids continuously grow in size and number. These observations have implications for better understanding not only Na/Na-β”-Alumina, but other alkali metal/solid electrolyte interfaces.

It is then demonstrated that Na/Na-β”-Alumina interfacial voiding is pressure dependent and that the critical current for voiding is approximately a linear function of stack-pressure. This is consistent with creep being the dominant mode of mass-transport of Na to the interface in this pressure range. It is shown that pressures in the order of several megapascals are required to sustain morphologically stable stripping at high discharge rates, with > 9 MPa stack-pressure predicted to be required to enable a discharge rate of 2.5 mA/cm^2. Given the requirement of high stack-pressures, it is important to explore alternative methods to increase the rate of creep of the metal anode to the anode/solid electrolyte interface. One possible solution is to operate SSBs at a raised temperature, as

this will increase the propensity of the metal anode to creep at a given pressure, potentially enabling higher current densities. This is the subject of Chapter 4 of this thesis.

4 Temperature Dependence of Lithium Anode Voiding in Argyrodite Solid-State Batteries

4.1 Aim

This chapter builds on the work of Chapter 3 and other works which have shown that the maximum rate at which an alkali metal anode can be stripped during discharge of a solid-state battery (SSB) is set by the rate of mass-transport of alkali metal atoms to the interface. This mass-transport is a combination of self-diffusion and creep of the metal anode. Operating a solid-state battery at an elevated temperature increases both the rates of self-diffusion and creep in the metal anode and so should enable stable discharge at higher current densities. This hypothesis is tested for the Li/Li_6PS_5Cl interface in the temperature range of 25-80 °C at the relatively low stack-pressure of 1 MPa. Later, a higher stack-pressure of 5 MPa is used in order to demonstrate high, stable discharge rates. In addition, the temperature and pressure dependence of the Li/Li_6PS_5Cl cell resistances are explored, with the aim of better understanding the challenges of forming and maintaining low-resistance Li anode/solid electrolyte interfaces.

4.2 Introduction

As discussed in Chapter 3, the maximum current density at which a solid-state battery can be discharged while maintaining a morphologically stable metal anode/solid electrolyte interface is determined by the rate of mass-transport of Li atoms to the interface.[120,151,166] In the absence of any stack-pressure to induce creep in the metal anode, the only mechanism by which vacancies created at the interface can be eliminated is by the self-diffusion of Li atoms.[33,166] As described in the Chapter 1 Section 1.4.1.1:

$$D_{\mathrm{SD}} = D_{0,\mathrm{SD}}{}^{-E_{\mathrm{A}}/RT} \tag{4.1}$$

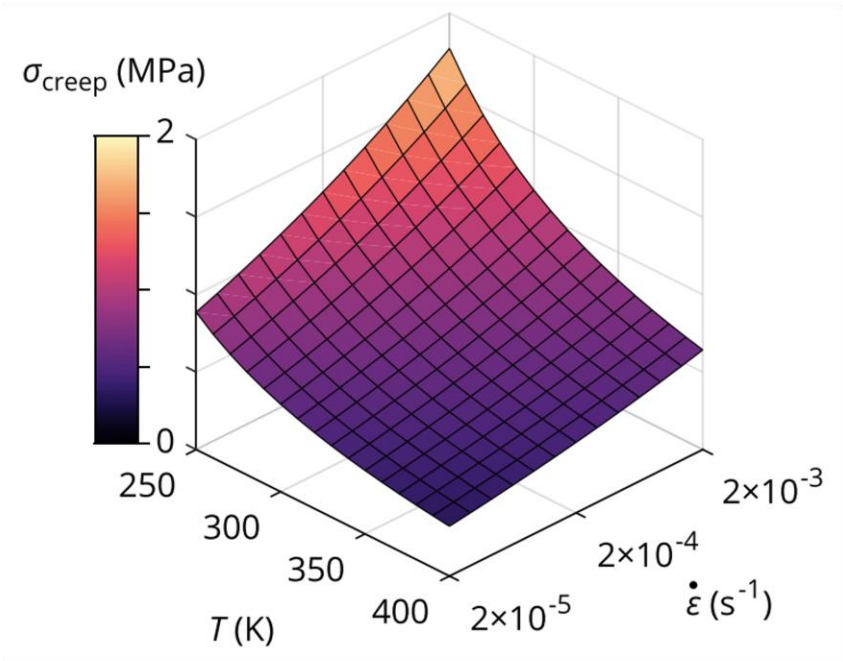


Figure 4.1: Figure showing the dependence of σ_{creep} of Li metal on temperature and strain rate. Reprinted with permission from LePage, W. S.; Chen, Y.; Kazyak, E.; Chen, K.-H.; Sanchez, A. J.; Poli, A.; Arruda, E. M.; Thouless, M. D.; Dasgupta, N. P. *J. Electrochem. Soc.* 2019, *166* (2), A89–A97.[140] Copyright 2019 *Institute of Physics*.

where D_{SD} is the self-diffusion coefficient of the Li anode, $D_{0,SD}$ is the pre-exponential factor for self-diffusion, E_A is the activation energy for monovacancy transport and T is the absolute temperature. Therefore, as the temperature of the system increases, so too does the diffusivity in the Li anode. As this self-diffusion in the anode is a key transport mechanism of Li to the interface, stripping the Li anode at a higher temperature would be expected to enable a higher stable current density.

Most solid-state batteries operate under a stack-pressure, as this leads to mass transport of Li to the interface by a second mechanism, creep.[37] The work of Dasgupta and co-workers has shown that creep of Li metal depends strongly on temperature, and that even moderately elevated temperatures can significantly increase Li's propensity to creep (Figure 4.1).[140] Therefore, discharging a solid-state battery at elevated temperatures should increase the critical current for voiding by increasing both the self-diffusion and creep under stack-pressure in the Li anode (Figure 4.2).[175]

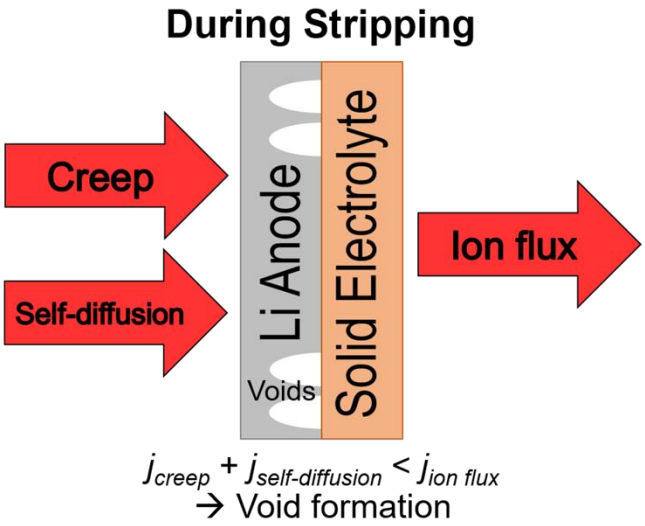


Figure 4.2: Schematic representation of the factors determining whether voids form at the Li anode/solid electrolyte interface during stripping. A Li-ion flux creates vacancies at the interface as current is passed. If the rates of creep and self-diffusion of Li atoms are insufficient to fill the vacancies, voids will form at the interface.

This chapter investigates the temperature dependence of the critical current for voiding, finding that under a 1 MPa stack-pressure increasing the operating temperature from 25 ºC to 80 ºC can increase the critical current for voiding from < 0.25 mA/cm^2 to > 0.5 mA/cm^2, and that under a 5 MPa stack-pressure an even greater effect is observed, increasing from < 1.0 mA/cm^2 to > 2.5 mA/cm^2.

4.3 Experimental

4.3.1 Preparation of Cells

In order to avoid exposure of air-sensitive battery materials to air, all cell preparation and testing was carried out in an Ar-filled glovebox (O_2 and H_2O < 1 ppm).

4.3.1.1 Preparation of Li_6PS_5Cl Disks

Li_6PS_5Cl powder with an approximate particle size of 1-10 μm was purchased from AMPCERA, a commercial supplier of solid electrolyte materials. 30 mg of powder was loaded into a die-set and was pressed under a 400 MPa uniaxial pressure to form Li_6PS_5Cl disks that were 5 mm in diameter and approximately 1 mm in thickness. Disks were

transferred to a furnace and were sintered in an Ar atmosphere at 300 °C for 30 minutes in a gold crucible. Reasoning behind this sintering procedure is discussed in Section 4.4.1.1.

4.3.1.2 $Li/Li_6PS_5Cl/Li$ Cell Assembly and Testing Conditions

Two types of cell design were used in this chapter; pouch cells and cylindrical cells made from polyether ether ketone (PEEK). Schematics of these cells are shown in Figure 4.3. Pouch cells were used for 2- and 3-electrode cycling experiments. 2-Electrode pouch cells were constructed by pressing 3 mm diameter Li foils with an approximate thickness of 50 µm onto both sides of the solid electrolyte disk. Li foils were produced by calendaring Li metal ingot. 3-Electrode cells were made by affixing an additional Li metal foil reference electrode with an approximate diameter of 1 mm (Figure 4.3a). Cells were sealed under vacuum within mylar-coated aluminium pouch cells, with each electrode contacting a copper foil current collector. Cells were left under pressure at 80 °C overnight for intimate Li/Li_6PS_5Cl interfaces to form.

PEEK cells were used in a 2-electrode configuration for variable pressure potentiostatic electrochemical impedance spectroscopy (PEIS) measurements (Section 4.4.2) and for

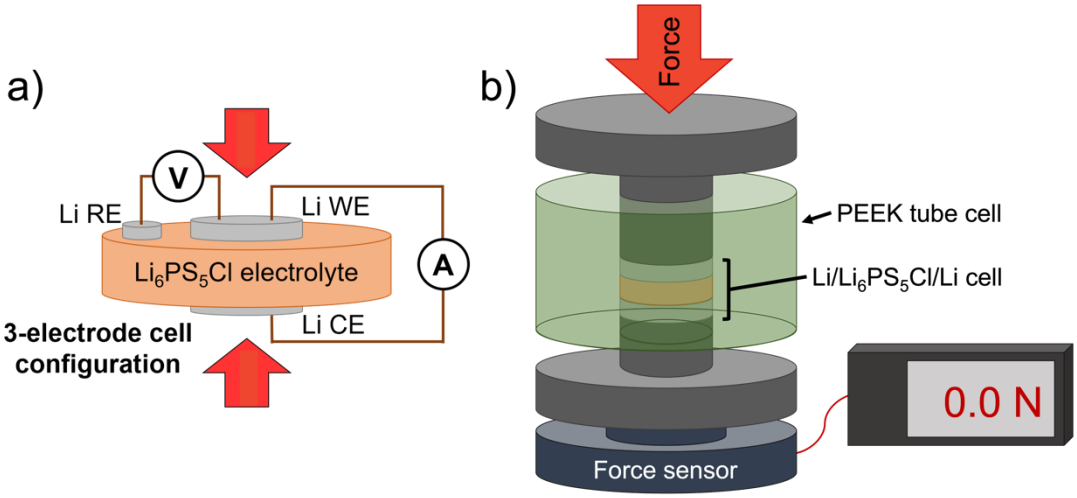


Figure 4.3: Schematic representations of cells used in this chapter. a) shows a 3-electrode cell. These were sealed within pouch cells and placed under a constant stack-pressure for the duration of the experiment. b) shows a PEEK tube cell which was used for experiments where the pressure was varied.

assessing the necessity of continuous stack-pressure (Section 4.4.5). A schematic is shown in Figure 4.3b. For the variable pressure PEIS measurements, 5 mm diameter Li foils were pressed onto each face of a sintered Li_6PS_5Cl disk and this cell was loaded into a PEEK tube with an internal diameter of 5 mm. Stainless-steel rods were then inserted into each side of the PEEK cell for application of pressure. The cell for assessing the necessity of continuous stack-pressure differed as the Li_6PS_5Cl powder was pressed under 400 MPa to form the solid electrolyte disk within the PEEK tube. The Li_6PS_5Cl ceramic was left unsintered and the 5 mm diameter Li foils and copper current collectors were loaded into each side of the die-set and were pressed onto the ceramic disk under a 100 MPa pressure using a uniaxial press (Specac).

Careful control of temperature and pressure was important throughout this chapter. Temperature was controlled to an error of ±0.02 °C using Huber temperature control chambers that were located within an Ar-filled glovebox (MBRAUN). Pressure was controlled using a pressure cell with an OMEGA piezoelectric sensor, as described in Chapter 3.

4.3.2 Electrochemistry

Both cycling and PEIS were carried out using a Gamry 1010E potentiostat. When cycling, the capacity passed each half-cycle was set to 1.0 $mA \cdot h/cm^2$, equivalent to moving approximately 5 μm of Li metal. As in Chapter 3, cycling always began by plating the working electrode (and stripping the counter electrode).

PEIS was taken using a 5 mV perturbation, collecting 10 points per decade. A frequency range of 1 MHz – 1 Hz was most commonly used, however on occasion data were collected to lower frequencies and in such cases the frequency range is stated in the figure caption.

PEIS data were analysed and fitted to equivalent circuit models using the ZView software package.

4.3.3 Characterisation

4.3.3.1 X-ray Diffraction (XRD)

A PXRD pattern of the Li_6PS_5Cl solid electrolyte was collected on the Rigaku MiniFlex which was located in a glovebox with a nitrogen atmosphere, as described in Chapter 3. The sample was loaded on a low-background, single crystal silicon sample holder.

Temperature dependent XRD was carried out on a 9 kW Rigaku Smartlab diffractometer, using Cu Kα radiation. The experiment was carried out using a Rigaku-designed temperature stage for XRD. An inert environment was maintained by passing Ar gas over the sample throughout the experiment. XRD patterns were collected as the sample temperature was increased from room-temperature to 800 °C using a ramp rate of 1 °C/min. Patterns were acquired every 10 min throughout ramping. This experiment was carried out with the help of Dr. Robert House.

4.3.3.2 X-Ray Photoelectron Spectroscopy (XPS)

XPS of Li_6PS_5Cl disks before and after contact with Li metal were collected by Dr. Phil Holdway, from the Oxford Materials Characterisation Service. To explore the result of contact with Li metal, a Li foil was pressed against the Li_6PS_5Cl ceramic and left for 250 h. The Li foil was subsequently removed with a clean scalpel and the Li_6PS_5Cl disk, together with a pristine Li_6PS_5Cl, disk were transferred into the XPS using a custom-built air-tight transfer holder. The XPS used an ion-pumped ultrahigh-vacuum chamber fitted with a VG nine-channel CLAM4 electron energy analyser. The data were analysed using CasaXPS software and peak positions were normalised relative to adventitious elemental

carbon, which is expected to have a binding energy of 284.8 mV.[258–260] This work was conducted with Dr. Jitti Kasemchainan.

4.3.3.3 X-ray Computed Tomography (XCT)

Following cycling, cells were disassembled including removal of the copper current collectors. The Li/Li_6PS_5Cl/Li stacks were then resealed into plastic pouches and transferred to the XCT to be scanned.

XCT was carried out using the Zeiss Xradia Versa 510 X-ray computed tomography microscope, with an acceleration voltage of 80 kV and a current of 87.5 μA. 2401 projections were taken over 360° for each tomographic image, giving a voxel size of 1.99 μm/voxel. Reconstruction of the images was carried out using Zeiss Scout and Scan System Reconstructor to produce 16-bit tiff images of the imaged volume. These tiff images were then resliced to show virtual cross-sections of the Li/Li_6PS_5Cl interface, showing interfacial voids.

As discussed in Chapter 3, due to the low X-ray attenuation of Li metal, it can be challenging to clearly differentiate between Li and empty space (voids).[168,191] To help in distinguishing between Li and void, the virtual cross-sectional images were segmented and colourised in Avizo Fire. The grayscale images were filtered using a non-local means filter, which is a common method for removing Poisson noise from the image.[261] The cross-sectional image was then colourised into a diverging colour map. To give a clear colour contrast between Li metal and voids, the Li metal, Li_6PS_5Cl electrolyte and voids were segmented out by grayscale thresholding. The grayscale of the segmented Li metal colourised separately (as green), whilst the grayscale of the Li_6PS_5Cl and voids were colourised on a scale from low attenuation (blue) to high attenuation (yellow). XCT, reconstruction and segmentation was carried out by Ziyang Ning.

4.4 Results and Discussion

4.4.1 Characterisation of Li_6PS_5Cl and the Li/Li_6PS_5Cl Interface

Before the temperature dependence of the Li/Li_6PS_5Cl interface can be studied, it is important that both the Li_6PS_5Cl ceramic disks and their interface with Li metal are rigorously characterised.

4.4.1.1 Preparation of Li_6PS_5Cl Disks

Phase purity of Li_6PS_5Cl was established by PXRD as described in Section 4.3.3.1. The collected pattern is given in Figure 4.4 and shows an acceptably high phase purity of Li_6PS_5Cl,[262] with a minor secondary phase of Li_2S which is commonly found in argyrodites.[263–265]

XRD was also carried out to determine the temperature stability of the Li_6PS_5Cl ceramic across a temperature range from room-temperature to 800 °C. These variable temperature

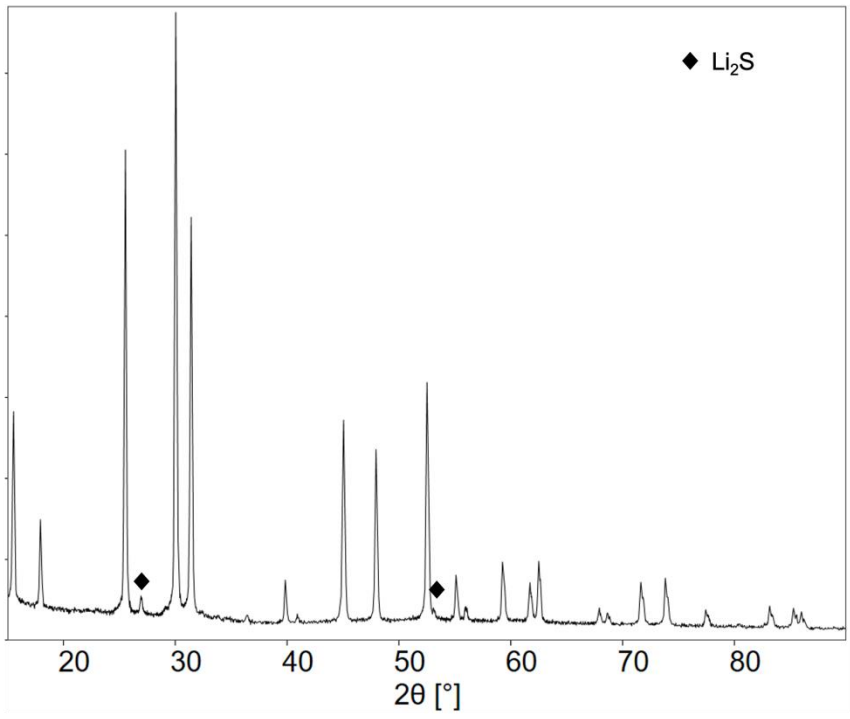


Figure 4.4: Powder X-ray Diffraction (PXRD) of Li_6PS_5Cl. All Peaks are assigned to cubic Li_6PS_5Cl except for those marked by ♦, which are assigned to a secondary phase of Li_2S.

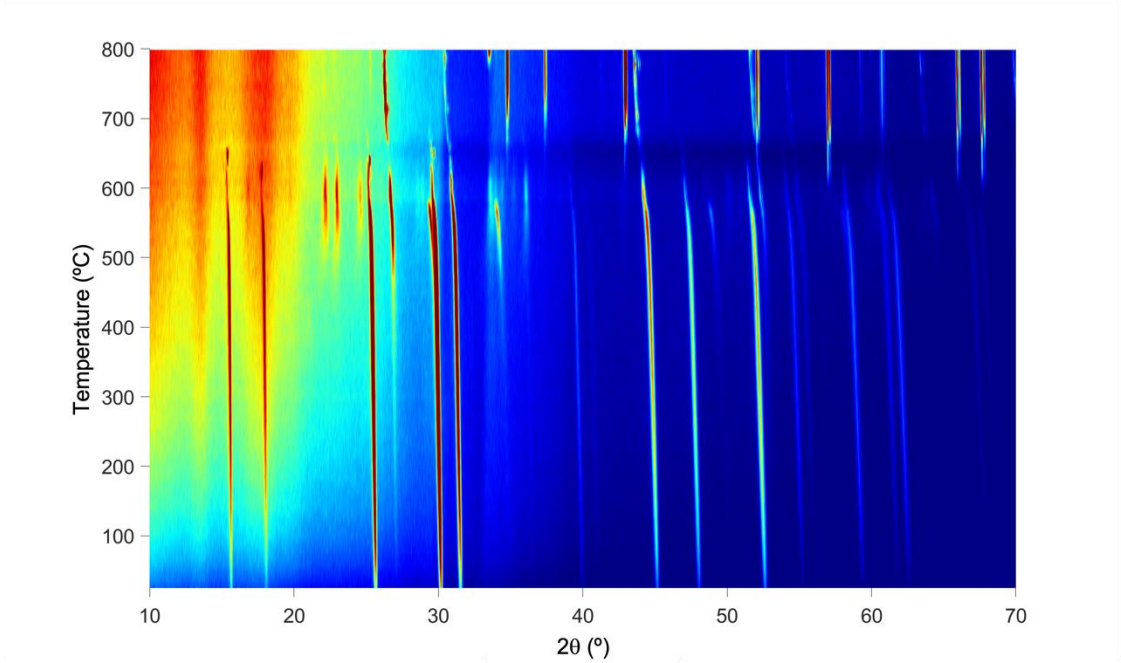


Figure 4.5: X-ray Diffraction (XRD) map showing the intensity of the diffraction peaks as a function of 2θ for Li_6PS_5Cl in the temperature range of 25-800 ºC. Warmer colours indicate higher measured intensity.

XRD data are shown in Figure 4.5, in which the colour indicates the absolute intensity of the diffraction peaks as a function of 2θ and the temperature at which the pattern was collected. The Li_6PS_5Cl electrolyte is stable in the cell operating range of temperatures below 80 °C and also offers insight into why previous works have chosen to densify Li_6PS_5Cl solid-electrolytes at 300 °C.[120] As the temperature is increased, there is an increase in background intensity at lower angles, perhaps indicating some slight melting or amorphization of the Li_6PS_5Cl phase.[266] No other changes are observed until a temperature above 400 °C, where new peaks corresponding to impurities including Li_3PO_4 are observed at low intensity, increasing in intensity until a temperature of approximately 600 °C where total degradation of the Li_6PS_5Cl phase occurs.[266]

Due to the relatively low degradation temperature of Li_6PS_5Cl demonstrated in Figure 4.5, many works in the literature use Li_6PS_5Cl and other argyrodite-type solid electrolytes without sintering at an elevated temperature. However, even though high temperature

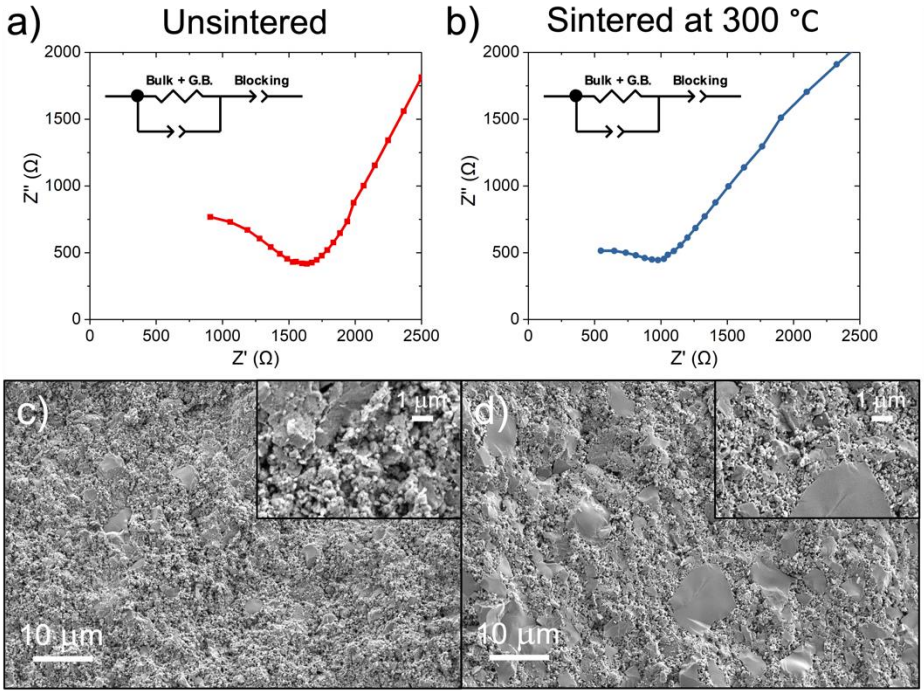


Figure 4.6: PEIS of Li_6PS_5Cl disks with 1.5 mm diameter blocking electrodes of a) an unsintered disk and b) a disk sintered at 300 ºC. SE micrographs showing fracture surfaces of c) the unsintered ceramic and d) the disk sintered at 300 ºC. Insets show higher magnifications of the ceramic microstructure.

sintering conditions are not available for this material, sintering at low temperatures is still observed to increase the conductivity of the solid electrolyte (Figure 4.6a-b), with some slight improvements also observed in the microstructure of the ceramic (Figure 4.6c-d). The PEIS spectra of the 300 °C sintered and unsintered solid electrolytes were fitted to an equivalent circuit model and these fittings are shown in Table 4.1. Normalising for the dimensions of the Li_6PS_5Cl disk, it is clear that a sizable decrease in impedance has

Table 4.1: Potentiostatic electrochemical impedance spectroscopy fittings of Blocking/Li_6PS_5Cl/Blocking cells for unsintered Li_6PS_5Cl electrolyte and Li_6PS_5Cl sintered at 300 ºC, showing lower resistance in the sintered ceramic. Bracketed resistivity and capacitance values correspond to the error in the least-squares fitting.

	Bulk + Grain Boundary	
	Resistivity (Ω·cm)	**Capacitance (F/cm)**
Unsintered	272 (2)	5.0×10^{-10} (1.2×10^{-10})
Sintered at 300 °C	142 (2)	9.7×10^{-10} (1.4×10^{-10})

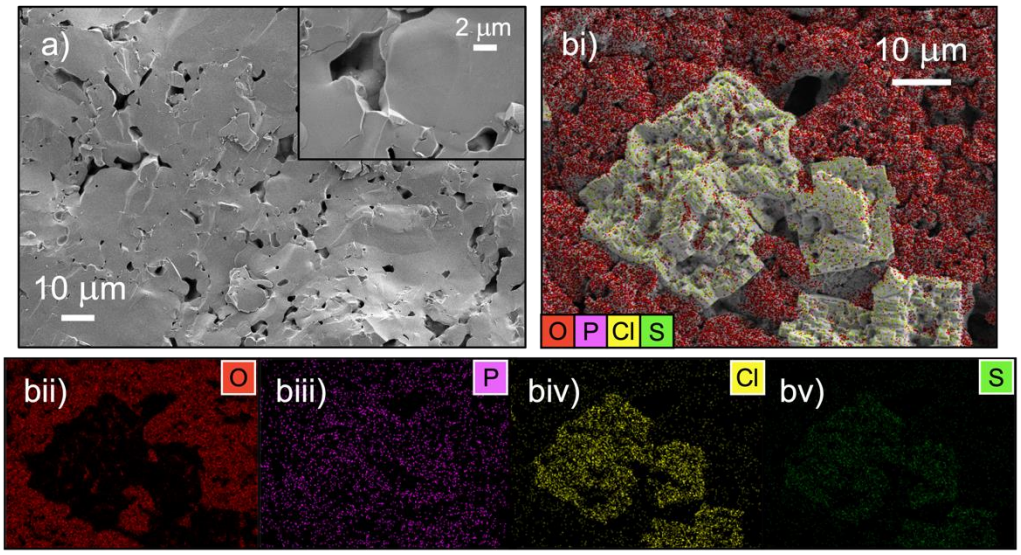


Figure 4.7: Sintering Li_6PS_5Cl ceramic at 550 ºC. a) SEM showing the Li_6PS_5Cl microstructure in cross-section. bi) EDX maps overlayed on an SEM showing the surface of the Li_6PS_5Cl ceramic at 550 ºC, with individual EDX maps shown for O (red), P (pink), Cl (yellow) and S (green) in bii-v, respectively.

occurred upon sintering, from 272 Ω·cm (unsintered, red) compared to 142 Ω·cm (300 °C sintered, blue). Further details on the fitting procedure are provided later in this chapter.

Sintering at a higher temperature of 550 ºC can result in significant improvements in the Li_6PS_5Cl microstructure (Figure 4.7a), however cell resistance was observed to be adversely affected due to the formation of a thick phosphate layer on the surface of the ceramic disk (Figure 4.7b). This is in good agreement with the earlier observations of the temperature-dependent XRD (Figure 4.5). For this reason, Li_6PS_5Cl solid electrolyte disks sintered at 300 °C were used for the remainder of this chapter.

4.4.1.2 Characterising Reactivity at the Li/Li_6PS_5Cl Interface

Previous studies have determined that chemical degradation occurs at the Li/Li_6PS_5Cl interface.[78,79,119,120,267] It is important to rigorously understand this chemical degradation and the associated changes in cell resistances before studying voiding at the Li/Li_6PS_5Cl interface, as it is vital to be able to attribute changes in cell voltage during stripping to the formation of voids rather than to chemical degradation with a high level of confidence.

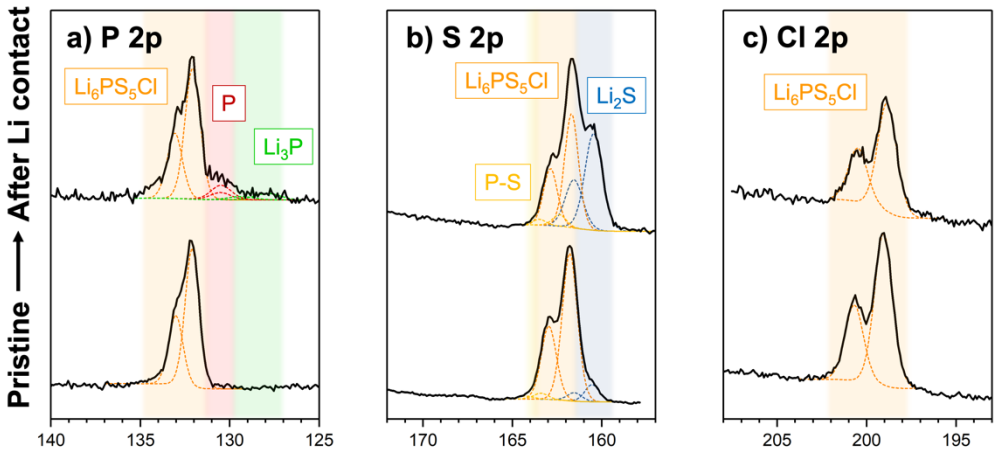


Figure 4.8: XPS of the surfaces of Li_6PS_5Cl disks before (bottom) and after (top) contact with a Li metal foil for 250 h. a) P 2p region of the spectrum showing degradation of Li_6PS_5Cl (orange) into Li_3P (green) and reduced phosphorous species (red); b) S 2p region of the spectrum showing degradation of Li_6PS_5Cl (orange and yellow) into Li_2S (blue) and c) Cl 2p region of the spectrum showing no clear change.

Chemical composition of the Li/Li_6PS_5Cl interface:

To understand the chemical reaction between Li and Li_6PS_5Cl, XPS was carried out on the surface of a pristine Li_6PS_5Cl ceramic and Li_6PS_5Cl that had been contacted with Li metal for 250 h as described in Section 4.3.3.2. The P 2p, S 2p and Cl 2p spectral regions are shown in Figure 4.8. The P 2p region of the spectrum (Figure 4.8a) reveals that there is some chemical degradation of the PS_4^- tetrahedra in Li_6PS_5Cl (orange doublet), into reduced phosphorous species (red) and Li_3P (green). The S 2p region of the spectrum (Figure 4.8b) shows that the doublet attributed to Li_2S (blue) increases significantly in relative intensity from a minor phase of the pristine electrolyte to a major constituent of the interphase between Li and Li_6PS_5Cl. Finally, little change is observed in the Cl 2p spectrum (Figure 4.8c), however it is likely that the reaction between Li and Li_6PS_5Cl forms LiCl, but that this is not clearly observed due to the similarity in binding energy between LiCl and Li_6PS_5Cl as has been suggested in previous studies of the interface.[79,267]

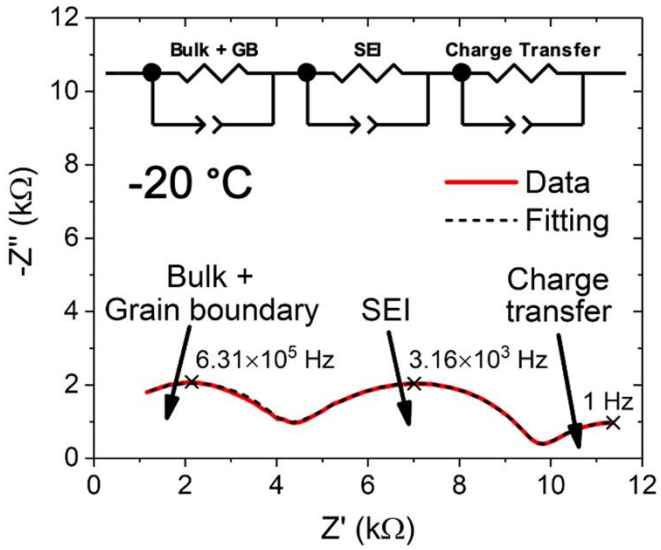


Figure 4.9: Nyquist plot of a Li/Li_6PS_5Cl/Li cell at −20 °C and 1 MPa stack-pressure, showing the experimental data (red) and the fitting from the equivalent circuit model (black). The bulk and grain boundary, SEI, and charge transfer contributions to the impedance are identified. The equivalent circuit model by which the spectrum used for the fitting is shown as an inset.

In conclusion, these data are in close agreement with previous studies of the Li/Li_6PS_5Cl interface, revealing that chemical degradation occurs, forming an interphase composed primarily of Li_2S but also consisting of Li_3P, LiCl and phosphorous species.

Understanding the Li/Li_6PS_5Cl interface through PEIS:

To gain a better understanding of the Li/Li_6PS_5Cl interface, a PEIS spectrum was collected at -20 °C and was fitted to an equivalent circuit model. The low temperature was used as it aids in clearly distinguishing between different contributions to the impedance. The Nyquist plot and equivalent circuit model are shown in Figure 4.9.

The spectrum was modelled as three parallel R/C elements in series which were assigned according to their respective capacitances, shown in Table 4.2.[253] The highest frequency semi-circle was assigned as the bulk + grain boundary impedance. In some cases, bulk and grain boundary impedances can be modelled separately (as in Chapter 3) and are expected to have characteristic capacitances of ~10^{-12} and ~10^{-9} F/cm, respectively. However, in

Table 4.2: Normalized resistivities and capacitances from the equivalent circuit model fitting of a 2-electrode $Li/Li_6PS_5Cl/Li$ cell at −20 °C. Errors in the least-squares fitting are shown in brackets.

R/C Element	Resistivity	Capacitance
Bulk + Grain boundary	2901 (18) Ωcm	8.7×10^{-11} (1.0×10^{-11}) Fcm^{-1}
SEI	402 (4) Ωcm^2	1.2×10^{-7} (1.8×10^{-8}) Fcm^{-2}
Charge Transfer	229 (31) Ωcm^2	7.0×10^{-4} (1.8×10^{-4}) Fcm^{-2}

other cases, including previous modelling of the PEIS of argyrodites,[262,268] it is not possible to deconvolute the bulk and grain boundary contributions and they are instead modelled together, with an expected characteristic impedance of ~10^{-10} F/cm.

The next highest frequency semi-circle is assigned as the impedance of the solid electrolyte interphase (SEI) between Li and Li_6PS_5Cl which was shown earlier to consist primarily of Li_2S. This semi-circle is assigned not only by its characteristic capacitance of ~10^{-7} F/cm^2, but also because this impedance increases the most with time after contacting Li_6PS_5Cl with a Li foil as the SEI forms and thickens. This time-dependent change in the SEI resistance is discussed in greater detail later in the chapter.

Finally, the lowest frequency semi-circle is assigned to the charge transfer (CT) impedance by its characteristic frequency of ~10^{-5} F/cm^2. As it has been shown that a SEI exists at the Li/Li_6PS_5Cl interface, this charge transfer impedance is actually the impedance between the Li_2S-rich SEI and the Li foil electrode. The dependence of charge transfer impedance on temperature and pressure is studied later in this chapter (Section 4.4.2) to determine conditions that will minimise interfacial resistance.

As this chapter explores changes at the Li/Li_6PS_5Cl interface as a function of temperature, it is interesting to examine how these impedance contributions change with temperature. PEIS spectra were taken from -20 °C to 80 °C in steps of 10 °C and are plotted in Figure 4.10a. It is observed that at low temperatures of -20 °C (red) to 10 °C (green) all three R/C

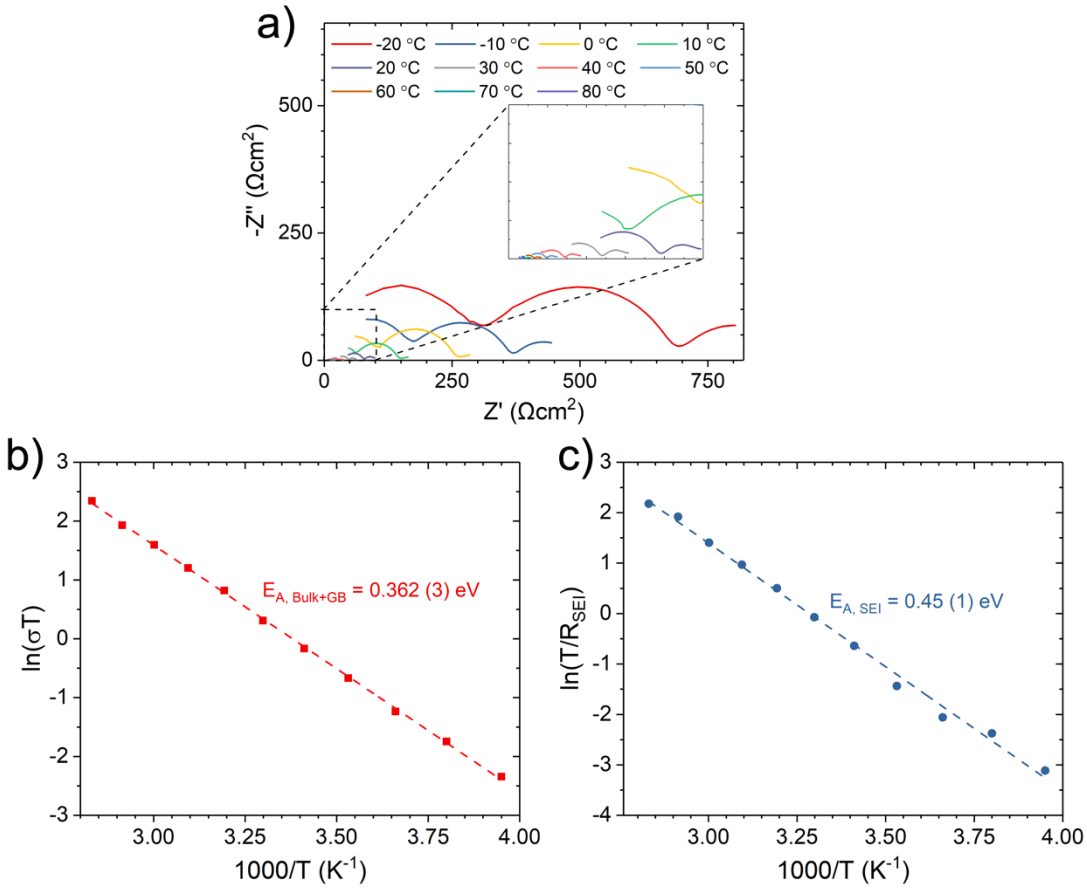


Figure 4.10: a) Nyquist plot showing PEIS at temperatures from -20 °C to 80 °C at 1 MPa stack-pressure; b) Arrhenius plot showing the calculated activation energy of Li_6PS_5Cl bulk + grain boundary conductivity; c) Arrhenius plot showing the calculated activation energy of Li/Li_6PS_5Cl SEI resistance. Errors in the activation energy from the linear fitting are shown in brackets.

elements (bulk + grain boundary, SEI and charge transfer) are well resolved, however at higher temperatures the bulk + grain boundary impedance is not clearly distinct. This necessitates modelling the PEIS spectrum differently at higher temperatures, as a resistor in series with two R/C elements.

The equivalent circuit models were used to determine bulk + grain boundary and SEI resistances across this temperature range, enabling the determination of the of their respective activation energies as 0.36 eV (red) and 0.45 eV (blue) from Arrhenius plots. These values were found to be consistent with previous literature.[117,269–271] These Arrhenius plots differ slightly in that for the bulk + grain boundary resistance it is possible to plot

ln(σT) as the *y*-axis because the pellet has a well-defined thickness (Figure 4.10b). On the other hand, the SEI does not have a well-defined thickness, so $\ln(T/R_{SEI})$ is plotted as the *y*-axis (Figure 4.10c). An Arrhenius plot is not made to determine the activation energy of the charge transfer process, as it is not possible to fit the charge transfer contribution to the PEIS over the full temperature range. At temperatures above 50 °C, the charge transfer resistance was found to be much lower in magnitude than the other contributions and so it was not possible to rigorously determine how this resistance was changing at the higher temperatures.

Finally, it is important to understand how the cell impedance changes with time as the SEI layer forms. After contacting Li_6PS_5Cl with the Li metal electrodes, the cell was assembled, heated to 80 °C and a PEIS spectrum was taken after 2 h (once the cell temperature had equilibrated). PEIS was subsequently taken 12 h after cell construction and at 12 h intervals for 5 days. Individual spectra were fitted to the equivalent circuit model and the resultant values of interfacial resistance (R_{int}) are plotted as a function of time in Figure 4.11. These data show that there is a marked increase in SEI resistance from the 2nd hour to the 12th, in line with the formation and thickening of the SEI, which is composed of less ionically

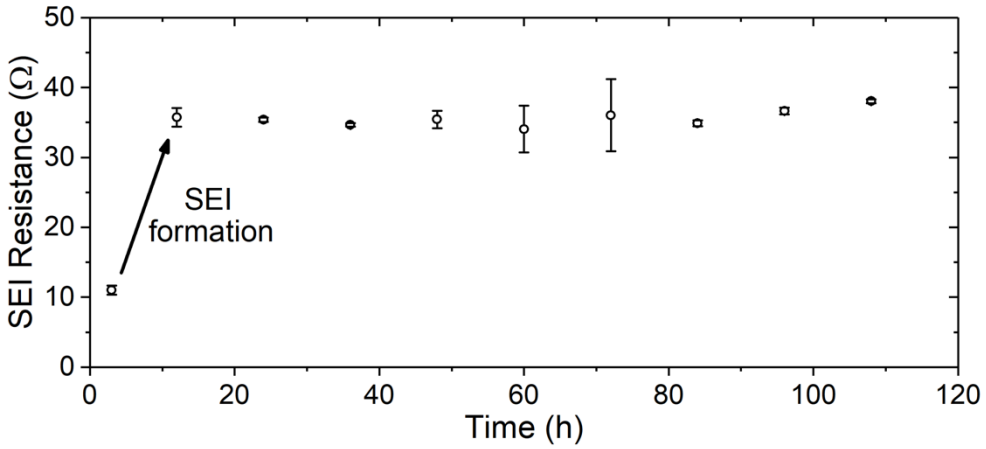


Figure 4.11: Plot showing the change in solid electrolyte interphase (SEI) resistance as a function of time at 80 ºC. A marked increase in resistance is observed over the first 12 h of contact between Li and Li_6PS_5Cl. Error bars show the error in least-squares EIS fitting.

conductive Li_2S. However, after the 12th hour very little increase in the SEI resistance is observed, in line with the SEI having formed and self-passivated, rather than continuing to thicken with time.

The self-passivation of the SEI layer could be consistent with previous findings by Janek and co-workers, who observed that the SEI resistance at the Li/Li_6PS_5Cl interface increases linearly with $t^{0.5}$ (where t is the time after contacting Li with Li_6PS_5Cl) as is expected for diffusion-controlled solid-state reactions.[79] This differs substantially from the interfacial reactivity between Li metal and other sulphide solid electrolytes such as LGPS, which see continual growth of the SEI layer, eventually consuming the solid electrolyte in its entirety and leading to cell death.[69] The difference between these cases is that reduction of Li_6PS_5Cl at the interface with Li produces only electronically insulating products that are less ionically conductive than the Li_6PS_5Cl electrolyte. As a result, as Li_6PS_5Cl reacts to form the SEI, continued reduction of the Li_6PS_5Cl electrolyte is not possible, as the SEI layer creates a barrier preventing access to electrons. On the other hand, when LGPS is contacted with Li metal and reduction occurs, reduced germanium species are an electronically conductive product, giving the SEI layer both electronic and ionic conductivity. As such, the solid electrolyte can continue to be reduced through the interphase, as electrons are readily accessible at the LGPS/interphase interface.[30]

The self-passivation of the SEI formed between Li and Li_6PS_5Cl is a key reason why Li_6PS_5Cl is considered to be a realistic candidate for Li anode SSBs and is a reason why it has been chosen for this study. As shown in Figure 4.11 and in previous literature, the SEI layer forms rapidly, and at 80 °C the interphase has been formed 12 h after contact with Li metal. For this reason, all cells were left under pressure for at least 12 h at 80 °C prior to any cycling, as described in Section 4.3.1.2. In this way, changes in voltage during cell

cycling could be attributed to morphological changes at the Li/Li_6PS_5Cl interface (such as voids and dendrites), rather than due to SEI formation.

4.4.2 Influence of Temperature and Pressure on Charge Transfer Resistance

In Chapter 3, it was demonstrated that the properties of the alkali metal anode, and in particular its deformability by creep under pressure, are important in determining whether voids form at the interface when the metal anode is stripped during cell discharge. However, the deformability of Li is also of importance to a cell at rest. Janek and co-workers used PEIS to demonstrate that increasing stack-pressure reduced the resistance at the Li/LLZO interface, decreasing to very low values as the Li metal deformed to form an interface with close to 100 % contact between the LLZO electrolyte and the Li metal electrode.[166]

To explore the effect of stack-pressure and temperature on the resistances of the Li/Li_6PS_5Cl/Li symmetric cell, PEIS was taken as a function of stack-pressure at 25 °C and -20 °C (Appendix Figure A4.1). The PEIS spectra were fitted to an equivalent circuit model as described in Section 4.4.1.2 to give insights into the changes in cell resistances as a function of pressure at temperatures of 25 °C and -20 °C.

Of particular interest is how the interfacial charge transfer resistance changes with increasing stack-pressure, as this gives insight into the degree of contact between the Li electrode and solid electrolyte (Figure 4.12). At 25 °C, it is observed that the charge transfer resistance falls rapidly under low stack-pressures, reaching a minimum value which remains relatively constant up to high stack-pressures (Figure 4.12a). This suggests that at room temperature Li behaves plastically, deforming to give a more intimate interfacial contact. The greater contact between the Li anode and solid electrolyte lowers the constriction resistance at the interface, lowering the measured charge transfer resistance.

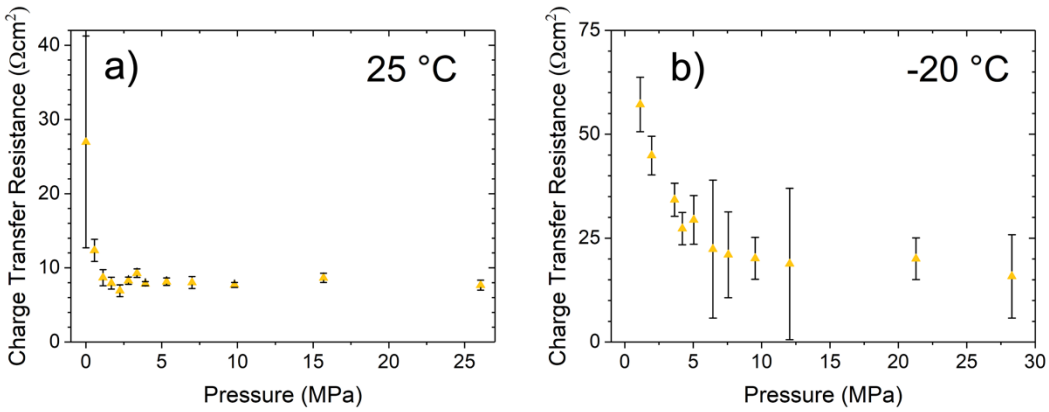


Figure 4.12: Pressure dependence of charge-transfer resistance at the interface at (a) 25 °C and (b) −20 °C. Note that the error bars give the error in the least-squares fitting of the charge-transfer resistance contribution only.

That this occurs in the low-pressure range is in good agreement with the reported yield strength of Li metal (σ_{Li} = 0.73-0.81 MPa). At the lower temperature of -20 °C, again a decrease in interfacial resistance is observed with increasing stack-pressure, however at this lower temperature the decrease occurs over a wider pressure range and a minimum is not reached until a stack-pressure of approximately 12 MPa has been applied (Figure 4.12b). At lower temperatures, the Li metal shows less propensity to deform at low stack-pressures, giving evidence of the change in the material's mechanical properties with temperature.

The importance of minimising the interfacial charge transfer resistance is not that this resistance has a relatively high magnitude. In fact, examining the -20 °C Nyquist plot in Figure 4.9 and the corresponding fitting in Table 4.2 it is evident that the interfacial resistance has a relatively low magnitude. The importance of the interfacial charge transfer resistance is that it is this resistance that sees very significant growth when voiding occurs. As discussed in Chapter 3, it is highly likely that imperfect interfacial contacts at the interface act as initiation points for voiding and therefore it is of vital importance to minimise the interfacial charge transfer resistance of the cell at rest. It can be concluded

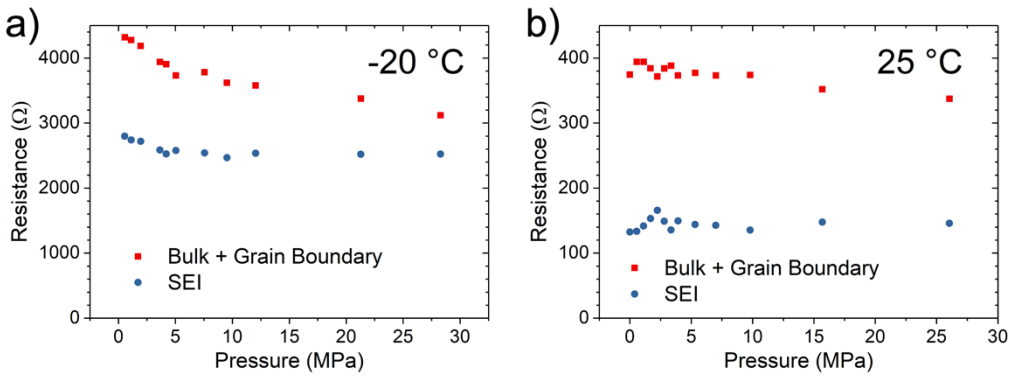


Figure 4.13: The pressure dependence of bulk, grain boundary and SEI resistance of a Li/Li_6PS_5Cl/Li cell at a) -20 °C and b) 25 °C.

from Figure 4.12 that higher stack-pressures are required at low temperatures, and that at a temperature of -20 °C the stack-pressure required to minimise the interfacial charge transfer resistance might be prohibitively high.

For completeness, the variation of bulk + grain boundary and SEI resistances with stack-pressure are shown for -20 °C (Figure 4.13a) and 25 °C (Figure 4 13b). In both cases the SEI resistance remains relatively constant over the pressure range (blue), whereas the bulk + grain boundary resistances were observed to decrease with increasing stack-pressure (red). It is considered likely that for a highly porous ceramic such as Li_6PS_5Cl, even low stack-pressures can materially improve grain-grain interfacial contacts within the electrolyte, lowering the grain boundary resistance as observed.

4.4.3 Effect of Temperature on the Critical Current for Voiding

Having characterised the Li_6PS_5Cl electrolyte, the chemical reactivity at the interface with Li metal, and the conditions required to minimise interfacial resistance of the cell, the temperature dependence of void formation at the interface was explored by 3-electrode cycling, supported by XCT imaging of interfacial voids.

4.4.3.1 Temperature Dependence of 3-Electrode Cells under 1 MPa

3-Electrode cells were constructed and cycled at temperatures of 25 °C, 60 °C and 80 °C under 1 MPa stack-pressure. In each case, cycling initiated at 0.25 mA/cm^2. After 5 cycles the current density was increased to 0.5 mA/cm^2 and was subsequently increased in steps of 0.25 mA/cm^2 every 5 cycles until cell failure was observed. These cycling profiles are shown in Figure 4.14. Just as in Chapter 3, the 3-electrode cell configuration was used to identify the current density at which voiding occurs, with an increase in cell polarisation only during the process of stripping but not on plating previously having been attributed to the loss of contact that occurs as voids form at the interface between the anode and the solid electrolyte.

3-Electrode Cycling at 25 °C

A cell was cycled at 25 °C under a 1 MPa stack-pressure, beginning by cycling at 0.25 mA/cm^2 (Figure 4.14a, red curve). Even at this very low current density, increases in cell voltage during stripping were observed, indicating that voids were forming at the interface. The cell potential increased by approximately 26 mV on the 1st stripping of the working electrode and continued to increase with each successive stripping, reaching approximately 200 mV polarisation on the 4th stripping immediately prior to cell failure due to dendrite penetration during the 5th plating. These observations are in accord with the behaviour described in Chapter 3. Even at the low current density of 0.25 mA/cm^2, under the cycling conditions of 25 °C and 1 MPa stack-pressure the critical current for voiding has been exceeded. As a result, voids form at the interface during stripping, growing and accumulating with cycle number until the interfacial contact loss is so severe that dendrites form at the remaining areas of contact on plating.

3-Electrode Cycling at 60 °C

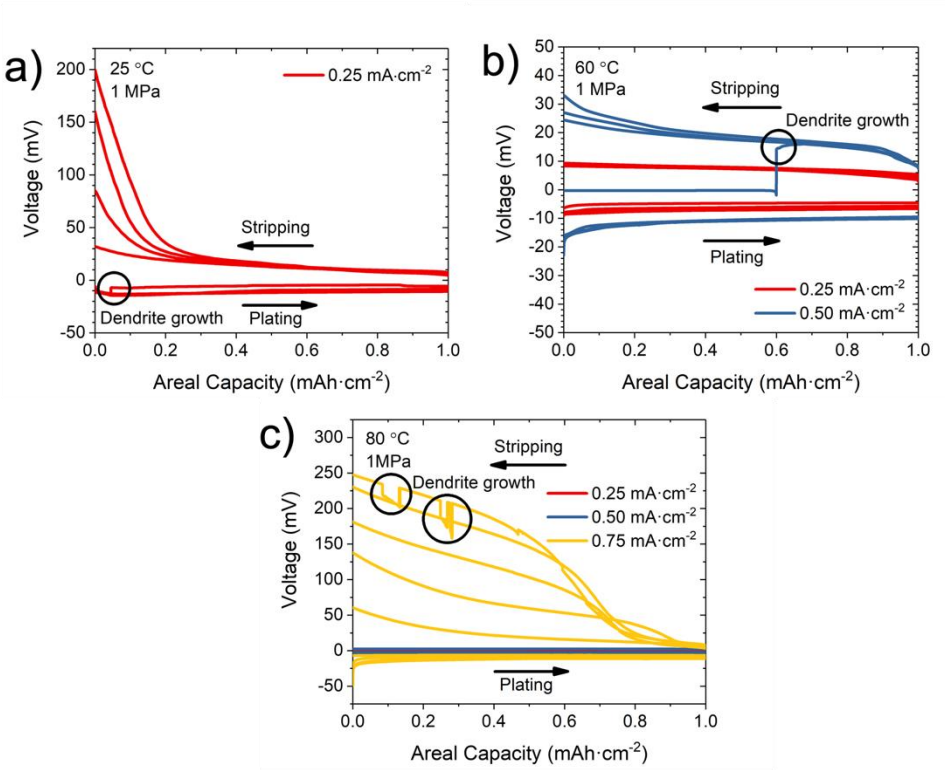


Figure 4.14: 3-Electrode cycling under 1 MPa pressure moving 1 mA·h/cm^2 capacity at (a) 25 °C, (b) 60 °C, and (c) 80 °C. The working electrode was plated first in each case.

In contrast, at the higher temperature of 60 °C the potential is observed to be low and stable at the 0.25 mA/cm^2 current density (Figure 4.14b, red curve), indicating that increasing the temperature from 25 °C to 60 °C has increased the critical current for voiding from < 0.25 mA/cm^2 to > 0.25 mA/cm^2. After 5 cycles the current density was increased to 0.5 mA/cm^2 and behaviour associated with interfacial voiding was once again observed (blue curve). The voltage between the working and reference electrodes increased from 8 mV to 24 mV during the 1st stripping, reaching 27 mV at the end of the 2nd stripping and 33 mV at the end of the 3rd. As previously, following this increase in polarisation, cell failure due to dendrite growth was observed on the 4th stripping, with the cell potential falling to 0 V.

3-Electrode Cycling at 80 °C

Finally, a 3-electrode cell was cycled in the same manner at 80 °C (Figure 4.14c). The measured voltage remained low and cycling was highly reversible both at 0.25 mA/cm^2

(red curve) and at 0.5 mA/cm^2 (blue curve). However, at the higher temperature of 0.75 mA/cm^2 (yellow curve) there were indications of severe voiding on stripping, with the voltage observed to increase from 6 mV to 61 mV during the 1st stripping, reaching 248 mV by the end of the 5th stripping. Whilst final cell death was not observed for this cell, clear indications of dendrite penetration into the ceramic electrolyte were evident, with stochastic variations in the cell potential during the 5th stripping clear signals that cell failure had begun.

4.4.3.2 Imaging Voids: XCT of the Li/Li_6PS_5Cl Interface

To be assured that increases in cell polarisation were a result of interfacial voiding, 2-electrode cells were constructed as described in Section 4.3.1.2 and were cycled at 80 °C; one at a current density of 0.75 mA/cm^2 (above the critical current for voiding predicted by Figure 4.14c) and the other at 0.5 mA/cm^2 (below the predicted critical current for voiding). These cycling data are shown in Figure 4.15. These data are in close agreement with the 3-electrode cycling data. The cell cycled at 0.5 mA/cm^2, below the predicted critical current for voiding, showed highly reversible cycling over 25 cycles with no increase in cell

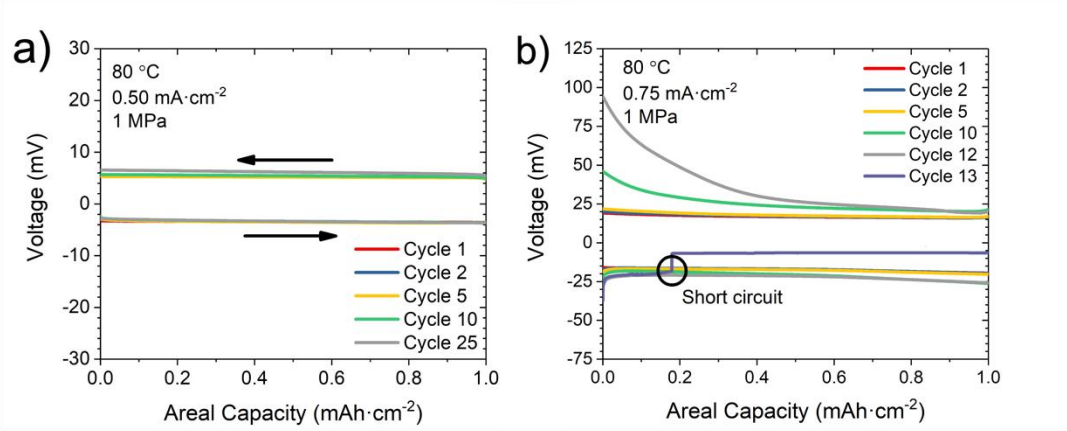


Figure 4.15: 2-Electrode cycling of a Li/Li_6PS_5Cl/Li cell at 80 °C under 1 MPa at (a) 0.5 mA/cm^2 and (b) 0.75 mA/cm^2. Cycling below the critical current for voiding leads to reversible, stable cycling (a), whereas cycling above the critical current leads to voiding and eventual cell failure (b). Cycling data correspond to X-ray computed micro-tomography images shown in Figure 4.16.

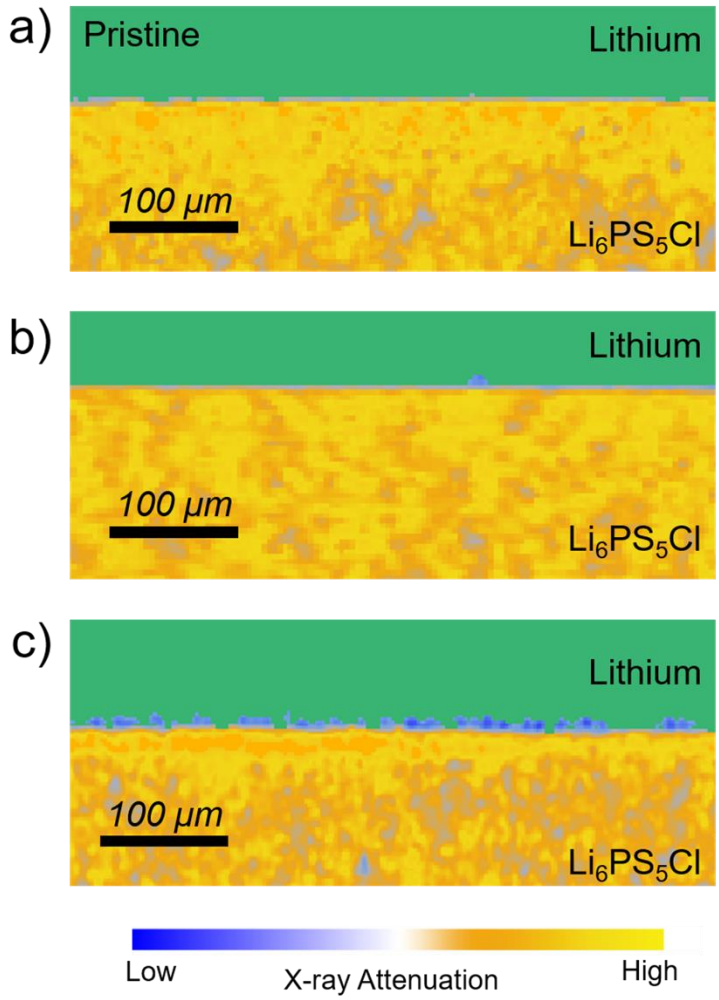


Figure 4.16: X-ray tomography cross-sectional images of the Li/Li_6PS_5Cl interface for (a) the pristine cell and (b) after cycling at 0.5 mA/cm^2 corresponding to (Figure 4.15a) and (c) 0.75 mA/cm^2 corresponding to (Figure 4.15b). Green, blue, and orange/yellow indicate lithium, voids, and Li_6PS_5Cl, respectively. The values and associated colour scale correspond physically to the X-ray attenuation and therefore the scattering by the constituent atoms. Green (lithium) does not appear on the colour scale as lithium was segmented out by grayscale thresholding and colourised separately to increase contrast between lithium and voids. Unsegmented XCT images are shown in Appendix Figure A4.2.

polarisation (Figure 4.15a). After 25 cycles the cell was prepared for tomography and XCT was carried out as described in Section 4.3.3.3. A reconstructed cross-section of the interface is shown in Figure 4.16b and shows very little voiding (blue) at the interface between Li_6PS_5Cl (orange/yellow) and Li metal (green). Indeed, the interface is comparably conformal to the interface of a pristine cell, shown for reference as Figure

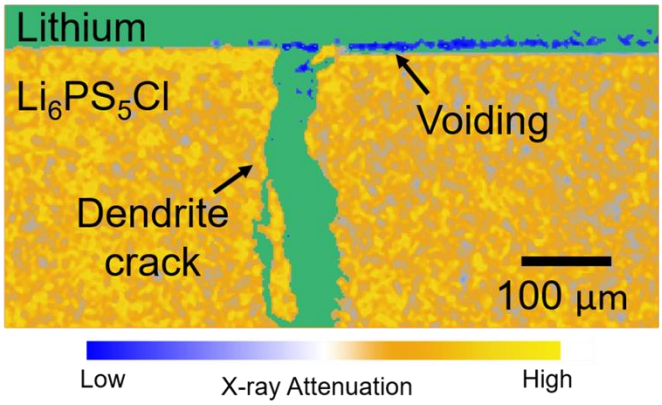


Figure 4.17: XCT cross-section showing dendrite crack through Li_6PS_5Cl electrolyte associated with the edge of an area of severe voiding in the Li anode. The cell failed after cycling at 0.75 mA/cm^2 at 80 °C under 1 MPa. Green, blue and orange/yellow indicate lithium, empty space (void) and Li_6PS_5Cl electrolyte, respectively. Green (lithium) does not appear on the colour scale as lithium was segmented out by grayscale thresholding and colourised separately to increase contrast between lithium and voids.

4.16a. The one small area of voiding at the interface, indicated by blue, represents a contact loss of only ~3% at the interface.

By contrast, when a 2-electrode cell is cycled at 0.75 mA/cm^2, above the predicted critical current for voiding, worsening cell polarisation was observed over 12 cycles, followed by critical failure of the cell due to dendrite growth on the 13th cycle (indigo) (Figure 4.15b). A reconstructed cross-section of the interface shows severe voiding and significant contact loss between the Li electrode and Li_6PS_5Cl electrolyte (Figure 4.16c). What is more, XCT reveals several sizable cracks traversing the solid electrolyte that appear to be filled, or partially filled, with Li metal (Figure 4.17). In addition to the segmented and colourised XCT reconstructions, original grayscale reconstructions are also given in Appendix Figures A4.2 and A4.3.

It can be concluded that the critical current at which voiding occurs increases with increasing cell operating temperature, from < 0.25 mA/cm^2 at 25 °C, to > 0.25 mA/cm^2 at 60 °C and > 0.5 mA/cm^2 at 80 °C. This is in line with the hypothesis put forward in the introduction to this chapter, that since the critical current for voiding is limited by the mass-

transport of Li metal, increasing the rate of that mass-transport by increasing the temperature (which increases both the rates of self-diffusion and, most importantly, creep of Li metal) will improve the rate at which a SSB can be discharged.

4.4.4 High Critical Current for Voiding with Moderate Temperature and Pressure

These experiments have established the temperature dependence of the critical current for voiding. However, it is also clear that moderate temperatures alone are insufficient to increase the critical current to practically relevant rates,[37,272] with a relatively modest current density of only 0.5 mA/cm^2 enabled at 80 °C under 1 MPa stack-pressure. Previous research has also established that application of moderate stack-pressure alone is insufficient. At room temperature, stable stripping at the Li/Li_6PS_5Cl interface was only possible at 0.2 mA/cm^2 under 3.5 MPa and at 1.0 mA/cm^2 under 7 MPa stack-pressure.[120]

To increase the critical current further, it is necessary to induce higher rates of mass-transport of Li to the Li_6PS_5Cl interface. Since very high temperatures or stack-pressures are unlikely to be viable in practice, a realistic way in which to achieve this is by applying a moderate stack-pressure as well as operating the cell at a modestly elevated temperature in order to increase the rate of Li metal creep to the interface. In order to test the effectiveness of this strategy, two further 3-electrode cells were constructed and were cycled under the higher pressure of 5 MPa to determine the critical current for voiding, one at 25 °C (Figure 4.18a) and the second at 80 °C (Figure 4.18b). As before, cycling was initiated at 0.25 mA/cm^2 and was increased in steps 0.25 mA/cm^2 every 5 cycles. Above a current density of 1.0 mA/cm^2, the current density was increased in larger steps of 0.5 mA/cm^2 until cell failure. For clarity, only the key current densities are shown in Figure 4.16, with full cycling profiles shown in Appendix Figure A4.4.

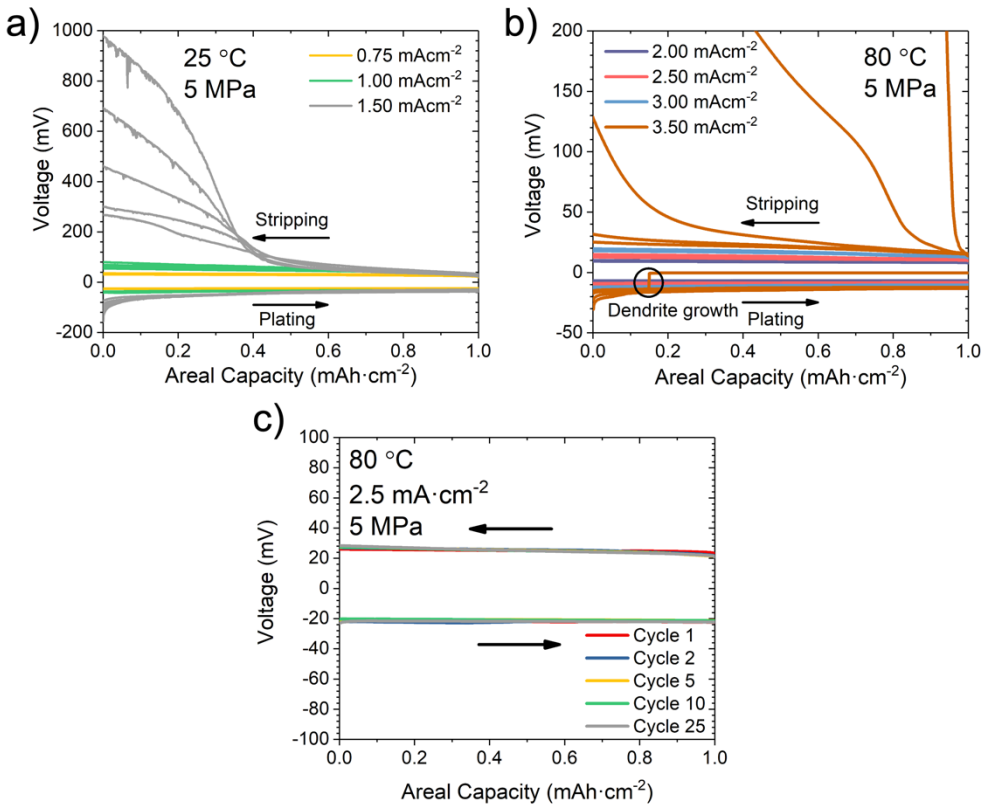


Figure 4.18: 3-Electrode cycling under 5 MPa pressure moving 1 mA·h/cm^2 capacity at (a) 25 °C and (b) 80 °C. Complete voltage profiles for these cells are shown in Appendix Figure A4.4, including additional current densities. Cell cycling began by plating the working electrode in each case. (c) Cycling of a 2-electrode Li/Li_6PS_5Cl/Li symmetric cell at 2.5 mA/cm^2 at 80 °C under 5 MPa stack-pressure, showing highly reversible plating and stripping over 25 cycles.

When cycling under 5 MPa but at only 25 °C (Figure 4.18a), the cell maintains a stable and reversible voltage on stripping up to and including the current density of 0.75 mA/cm^2 (yellow curve). However, as the current density is increased still further to 1.0 mA/cm^2 (green curve) a slight increase in voltage between working and reference electrodes indicates some minor voiding at the interface over 5 cycles. At 1.5 mA/cm^2, it is immediately clear that voiding is severe at this current density, reaching almost 1 V over 5 cycles (grey curve). As described previously, stochastic variation in the voltage indicates that dendrites have penetrated into the solid electrolyte and that if cycling is continued at this current the cell would surely fail. From these data, it is clear that when cycling at 25 °C under 5 MPa the critical current for voiding has been exceeded at 1.0 mA/cm^2. Whilst

this demonstrates an improvement in critical current when compared to cycling at 25 °C under 1 MPa, where the critical current was exceeded at 0.25 mA/cm^2 (Figure 4.14a), this critical current for voiding is still prohibitively low.

Significant improvement is seen when cycling under 5 MPa at 80 °C (Figure 4.18b). No increase in polarisation on stripping is observed up to and including the high current density of 2.5 mA/cm^2 (pink curve). Only at 3.0 mA/cm^2 (light blue curve) is a slight increase in voltage on stripping observed indicating some mild void formation over 5 cycles, and only at 3.5 mA/cm^2 is severe voiding observed (brown curve), with the potential reaching approximately 1.5 V by the end of the 5th stripping. It is therefore very clear that the application of both a moderate stack-pressure of 5 MPa and a moderately high operating temperature of 80 °C enables a significant improvement in the rate of void-free stripping by increasing the rate of mass-transport of Li metal to the Li_6PS_5Cl interface. Indeed, the critical current is improved by an order of magnitude from < 0.25 mA/cm^2 when cycling at 25 °C under 1 MPa, to > 2.5 mA/cm^2 when cycling at 80 °C under 5 MPa. To confirm cycling stability at the high current density of 2.5 mA/cm^2, a 2-electrode Li/Li_6PS_5Cl/Li cell was cycled at 80 °C under 5 MPa for 25 cycles. The voltage profile from cycling is shown as Figure 4.18c. The cycling is both stable and reversible as predicted, with no polarisation increase observed from the 1st cycle (red curve) to the 25th (grey curve).

However, whilst this experiment successfully demonstrates a stable metal anode/solid electrolyte interface at current densities approaching those that would be relevant for commercial electric vehicles, it must be acknowledged that realising even these modestly high pressures and temperatures at pack-level, rather than laboratory cell scale, poses enormous challenges. For example, applying a 5 MPa to an A5 sized pouch cell would require 0.155 MN of force. The cell apparatus to apply such forces, as well as heating systems to control the cell temperature, would require non-active components that would

take up both weight and volume in the full battery system, possibly negating the benefits afforded by the all-solid-state battery. In addition, the engineering challenges to apply such high forces evenly across the cell area and to prevent lateral flow are considerable.[37,137]

4.4.5 Importance of Continuous Stack-Pressure

Both this chapter and the last have emphasised the importance of creep in the alkali metal anode to achieving high rates of stable discharge. Therefore, continuous stack-pressures are surely necessary for stable cycling at high rates, rather than simply forming the interface under a high stack-pressure and operating the cell under a low stack-pressure. To demonstrate this, a 2-electrode Li/Li_6PS_5Cl/Li symmetric cell was prepared in which the Li anodes were uniaxially pressed onto an unsintered Li_6PS_5Cl disk at the high pressure of 100 MPa, forming a highly conformal interface with excellent initial contact between electrodes and electrolyte. The pressure was then released and the cell was cycled under no stack-pressure at 80 °C. Cycling was initiated at 0.25 mA/cm^2 and the current density was increased after 5 cycles. These data are shown in Figure 4.19.

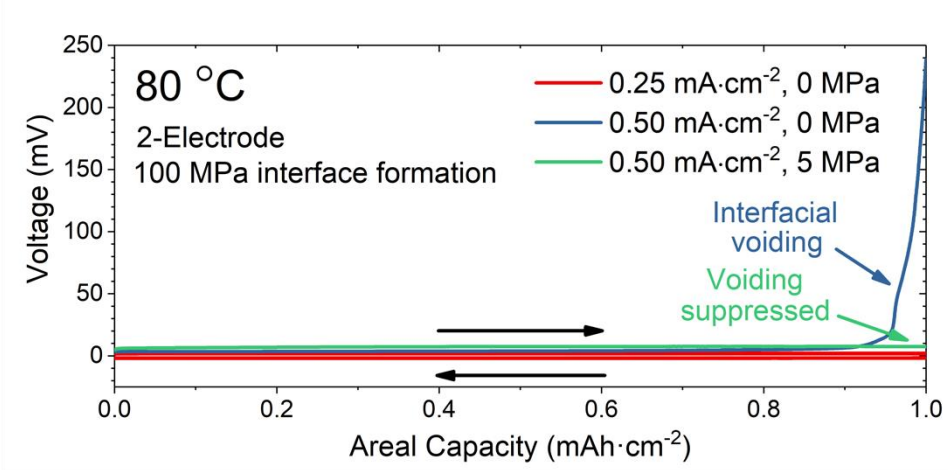


Figure 4.19: Cycling of a 2-electrode Li/Li_6PS_5Cl/Li symmetric cell made under a 100 MPa formation pressure. Cycling was initially carried out under no stack-pressure. Voltage was stable for five cycles at 0.25 mA/cm^2 (red curve) but severe polarization was observed at 0.5 mA/cm^2 (blue curve). The interface was subsequently recovered by re-pressing at 100 MPa. The cell was then cycled under 5 MPa stack-pressure, achieving stable potential (green curve).

Under a current density of 0.25 mA/cm^2 cycling is observed to be highly reversible for 5 cycles (red curve), suggesting that the critical current for voiding has not yet been exceeded, even under no external pressure. Whilst creep (and therefore stack-pressure) is necessary to achieve high rates of stable stripping, self-diffusion alone can be sufficient to enable stable cycling at lower rates, as has previously been demonstrated by Janek and co-workers.[166] It is of interest that stable cycling at a current density as high as 0.25 mA/cm^2 can be enabled under no stack-pressure at the elevated temperature of 80 °C. It is considered likely that this is possible due to a very low concentration of pre-existing voids at the interface; a result of the very high cell formation pressure.

After 5 cycles, the current density was increased to 0.5 mA/cm^2 (blue curve) and a marked increase in cell potential to almost 0.25 V indicated that the critical current for voiding had been exceeded and contact loss was occurring at the stripped Li/Li_6PS_5Cl interface. To demonstrate that this failure can be prevented by continuous application of stack-pressure, the cell was repressed under 100 MPa pressure to restore the intimate Li/Li_6PS_5Cl interface. After pressing, the cell was placed under a 5 MPa pressure and the cell was again cycled at 0.5 mA/cm^2 (green curve). This time, under the continuous stack-pressure, the cell did not fail due to voiding, demonstrating the importance of creep of the Li metal to achieving current densities as high as the 2.5 mA/cm^2 shown in Section 4.4.4.

4.5 Conclusions

A moderately elevated operating temperature results in more favourable dynamics at the Li/Li_6PS_5Cl interface. As described in Chapter 3, the maximum rate at which the Li metal anode can be stably and reversibly stripped is determined by the mass transport of Li to the interface, which is dependent on the self-diffusion and, when the cell is under a stack-pressure, creep of Li atoms to the interface. Raising the cell temperature increases both the

rates of self-diffusion and creep and therefore increases the rate at which a SSB can be discharged without failure. When under a low stack-pressure of 1 MPa an increase in the critical current for voiding from < 0.25 mA/cm^2 at 25 °C to > 0.5 mA/cm^2 at 80 °C was observed, but when coupled with a higher stack-pressure of 5 MPa, stable cycling at 2.5 mA/cm^2 was observed. What is more, the charge transfer resistance at the interface was determined to be strongly dependent on the temperature of cell operation, with significantly higher stack-pressures required to minimise interfacial resistance at -20 °C than at 25 °C, even for a cell at rest. Together, these results show that forming and maintaining an intimate Li/Li_6PS_5Cl interface is strongly dependent on the propensity of the Li metal anode to creep, which is favoured at higher temperatures and pressures. Whilst this study was conducted with the Li_6PS_5Cl electrolyte, it is anticipated that these findings will translate to other Li-ion conducting solid electrolytes and indeed other metal anode solid-state batteries.

5 Graphite and Graphite-Silver Anode Protective Interlayers for Lithium Solid-State Batteries

5.1 Aim

This thesis has explored common anode-side failures of solid-state batteries, with dendrite growth during charge and voiding during discharge explored in most depth. Prominent works in the literature have shown that use of a graphite interlayer or an interlayer composed of carbon and silver nanoparticles can prevent these failures at high current densities, offering a route to solid-state batteries that can operate at commercially relevant charging rates. A fundamental understanding of how these interlayers work has not been achieved. In this chapter, various carbon, silver, and carbon-silver composite interlayer solid-state batteries are studied by SEM/EDX and *operando* XRD to reveal the underlying mechanisms behind the charging process. The critical current density for dendrite growth in these cells is determined and approaches to increase this critical current are explored.

5.2 Introduction

As discussed in Section 1.5.3.2, a composite anode protective interlayer consisting of carbon and silver nanoparticles was described by researchers at Samsung in 2020.[199] This work attracted great attention in the solid-state battery research community, as the interlayer enabled the authors to achieve exceptional cell performance, far superior to the performance of solid-state batteries previously described in the literature.[272–274] What is more, the outstanding performance of this cell demonstrated for the first time solid-state battery performance that was competitive with commercial Li-ion cells, with a volumetric energy density of 942 Wh/L, compared to 676 Wh/L (Panasonic NCR18650B).[275,276]

To achieve such a high volumetric energy density, a Li-free anode was used (otherwise known as an “anodeless” cell). Rather than using a thin foil of Li metal as the battery anode

in the pristine state of the cell, the Li anode is formed *in-situ* during the first charge of the battery, i.e. all the Li within the cell is in the form of intercalated Li-ions within the cathode active material or within the solid electrolyte. This idea is very attractive as it eliminates the cell mass and volume wasted by the use of the excess Li in the foil, as well as reducing the battery cost, as production and utilisation of thin foils of highly reactive Li metal is extremely challenging.[277–280] A comparison between SSBs with Li foil and Li-free anode designs is shown schematically in Figure 5.1. Li-free anode cells face serious challenges, in particular due to the inhomogeneity of Li plating on the current collector during charge.

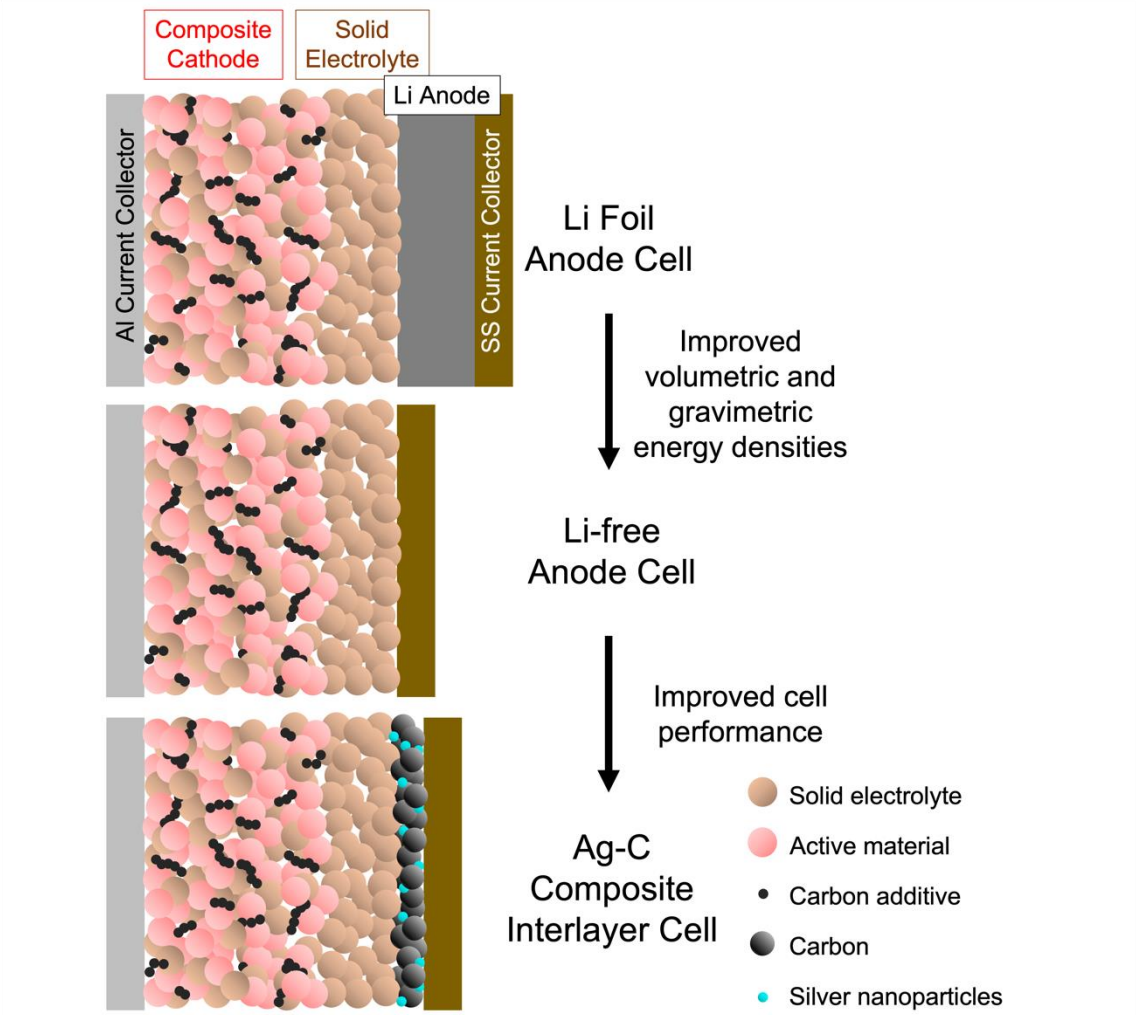


Figure 5.1: Schematic showing the differences between a conventional Li foil anode solid-state battery (top), a Li-free anode cell (middle), and a Li-free Ag-C composite interlayer cell (bottom). The schematic highlights that Li-free anode cells have higher volumetric (and often gravimetric) energy densities than Li foil anode solid-state batteries.

As the Samsung researchers and others have shown, Li has a propensity to nucleate inhomogeneously and grow in a columnar manner, rather than forming a dense layer by epitaxial growth.[199] This can lead to locally high current densities and lead to failures such as dendrites and voiding.

A key advantage of the interlayer employed by the researchers at Samsung is that Li forms a highly dense Li_9Ag_4 alloy layer upon charge as they demonstrate by SEM and XRD. It is of the utmost interest that this Li_9Ag_4 alloy layer forms at the interface between the carbon interlayer and the current collector, with the silver migrating out of the composite carbon-silver layer during the first charge, as is demonstrated by EDX. The result is that the carbon interlayer, now devoid of silver nanoparticles, remains as a physical barrier between the Li_9Ag_4 layer and the Li_6PS_5Cl solid electrolyte. It seems that this interlayer is highly effective at preventing the ingress of Li dendrites into the solid electrolyte, enabling the cell to charge at a high current density of 3.4 mA/cm^2 at 60 °C without any dendrite growth, i.e. the use of the silver-carbon interlayer substantially increases the plating critical current density of the solid-state cell. This result is not unique, with subsequent reports that graphite interlayers can also considerably increase critical current densities.[281] Recent works by Ye at al. have shown cells capable of achieving current densities of 8.6 mA/cm^2 over 10,000 cycles without Li dendrite growth.[34,222]

The use of these carbon and silver-carbon interlayers is clearly a topic of great importance, as they appear to enable solid-state cells capable of achieving commercially relevant fast-charging rates, as well as showing great promise at enabling Li-free anode cells. However, there is still no clear, fundamental understanding of how these interlayers work. Why does Li nucleate at the interlayer/current collector interface rather than the interlayer/solid electrolyte interface? What roles do the carbon and silver play within the interlayer? What

factors are important to maximise cell performance? This chapter seeks to answer these questions, principally by studying cells with six different types of interlayer:

- Carbon black
- Graphite
- Silver
- Graphite-silver nanoparticle composite
- Graphite/silver bilayer (graphite contacting the solid electrolyte and silver contacting the current collector)
- Silver/graphite bilayer (silver contacting the solid electrolyte and graphite contacting the current collector)

A comparison of these six systems using electrochemistry, SEM, EDX and *operando* XRD gives a clearer understanding of the charging process of these interlayers, and by-so-doing should facilitate improved future interlayer design and solid-state cell performance.

5.3 Experimental Methods

5.3.1 Cell Fabrication

Six types of anode-protective interlayer are tested in this chapter, consisting of carbon interlayers, silver interlayers and carbon-silver composites. This section on cell fabrication will firstly describe the methods of fabrication of the interlayers and then go on to detail how each of the six cells was produced.

5.3.1.1 Preparation Carbon Containing Interlayer Cells

Carbon-containing interlayer cells were prepared by spray printing a carbon layer onto a stainless-steel current collector and then uniaxially pressing the current collector against Li_6PS_5Cl to form a disk of the ceramic electrolyte with the carbon-containing interlayer and stainless-steel current collector laminated on top. Three different types of interlayer cells

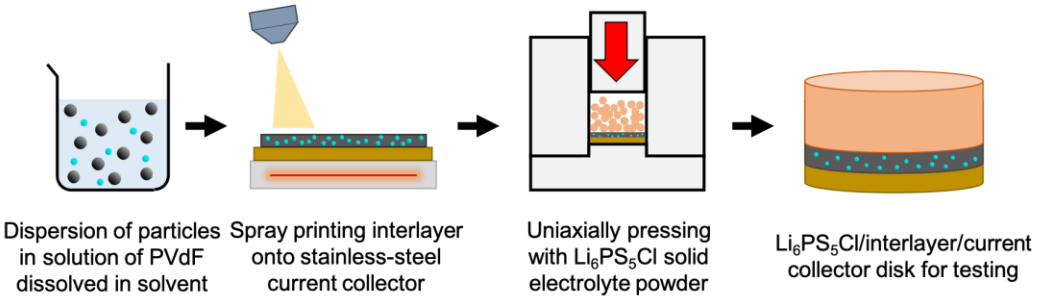


Figure 5.2: Schematic showing the processing sequence for preparation of carbon-containing interlayer cells (carbon black, graphite and graphite-silver nanoparticle composite interlayers). The sequence includes 1) creating a suspension of particles for spraying; 2) spray printing the interlayer onto a stainless-steel current collector mounted on a heated vacuum chuck; 3) Cutting the interlayer to size and loading it, together with Li_6PS_5Cl powder into a die-press for uniaxial pressing at 400 MPa. This yields a Li_6PS_5Cl/interlayer/current collector disk for testing.

were prepared in this way; those with the carbon black interlayer, the graphite interlayer and the graphite-silver nanoparticle composite interlayer. The cell preparation process is shown schematically in Figure 5.2.

Spray-printing the carbon-containing layers onto the stainless-steel current collector was carried out by a collaborator, Chris Doerrer, using an in-house developed suspension atomisation and spray deposition system within an Ar-filled glovebox.[282,283] A suspension, consisting of PVdF dissolved in organic solvents (see Table 5.1) and the suspended material (carbon black, graphite or a mixture of graphite and silver nanoparticles) was created by stirring for 10 min with a magnetic stirrer, followed by 5 min sonication. For the graphite-silver nanoparticle composite, an Ag:C weight ratio of 1:3 was used, as this had been optimised in previous research.[199] The suspension was fed into a spray-nozzle, where it was atomised by compressed argon gas and sprayed onto the stainless-steel substrate. The stainless-steel substrate was mounted onto a vacuum chuck that was heated to 110 °C, such that the carrier solvent evaporated approximately instantaneously, yielding a mixture of precipitated PVdF and the previously suspended material adhered to the stainless-steel substrate. 10 × 10 cm^2 layers were built up to the desired thickness by programmed

Table 5.1: Experimental details of the sprayed layers and their respective suspension composition.

Sprayed layer	Spray material	PVdF Binder	Solvent (fugitive)
Graphite	250 mg Graphite (90 wt%)	10 wt%	97 mL IPA, 3 ml NMP
Carbon black	250 mg Carbon black (90 wt%)	10 wt%	97 mL IPA, 3 ml NMP
Graphite-silver nanoparticle	187.5 mg Graphite (67.5 wt%), 62.5 mg Ag (22.5 wt%)	10 wt%	97 mL IPA, 3 ml NMP

movements of the spraying nozzle in the *x* and *y* planes. Details of the individual interlayers are shown in Table 5.1.

The carbon-containing interlayers were cut from the resultant sheet using a hollow punch tool to control the area. These were then dried at 70 °C under vacuum for at least 2 hours before being transferred into an argon-filled glovebox. They were then loaded into the bottom of a stainless-steel die-set (5 mm internal diameter) carbon side up. 30 mg of Li_6PS_5Cl powder (AMPCERA), with an approximate particle size of 1-10 μm was weighed, loaded into the die-set and pressed under 400 MPa pressure in a uniaxial press, yielding an Li_6PS_5Cl disk adhered to the carbon-containing interlayer and stainless-steel current collector.

5.3.1.2 Preparation of Silver Interlayer Cells

The silver interlayer cell fabrication method is described schematically in Figure 5.3. Cells with silver interlayers were prepared by physical vapour deposition. Li_6PS_5Cl disks were pressed and were masked to the desired area using Kapton tape, mounted onto glass slides and then loaded into the PVD chamber from within an argon-filled glovebox. The chamber was evacuated to a pressure of $< 5\times10^{-6}$ mbar before proceeding with the deposition. A silver target was sputtered using an argon flow rate of 10 sccm at a chamber pressure of 5×10^{-3} mbar with a power of 40 W. The thickness of the deposited layer was controlled

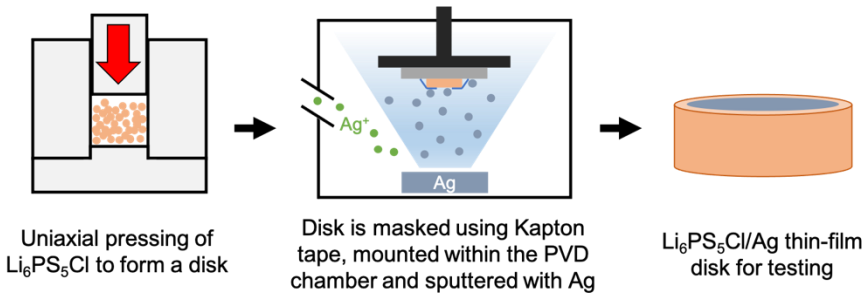


Figure 5.3: Schematic showing the processing sequence for preparation of silver thin-film interlayer cells. The sequence includes 1) uniaxially pressing Li_6PS_5Cl powder into a ceramic disk and 2) masking the ceramic disk to the desired area, mounting it within the PVD chamber and sputtering silver onto the surface. This yields a Li_6PS_5Cl/Ag thin-film disk for testing.

using a crystal sensor and confirmed by subsequent cross-sectional SEM. Following the deposition, the chamber was refilled with argon gas and the samples were removed to the argon-filled glovebox.

5.3.1.3 Preparation of Bilayer Interlayer Cells

The preparation methods of the bilayer interlayer cells are shown schematically in Figure 5.4. To create the graphite/silver bilayer, a graphite interlayer cell was produced just as

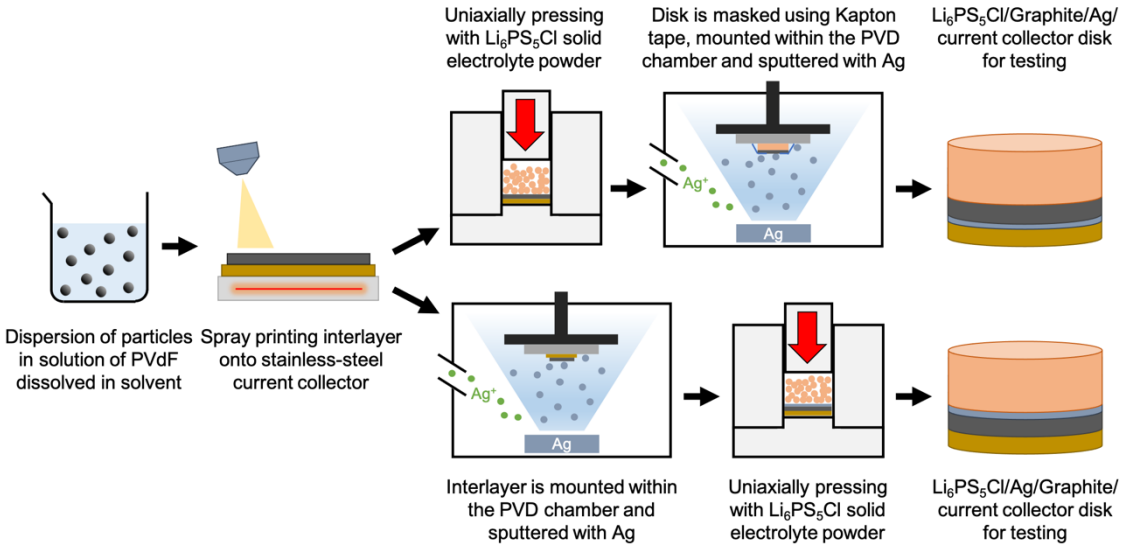


Figure 5.4: Schematic showing the processing sequence for preparation of graphite-silver bilayer cells. The sequence includes 1) creating a suspension of particles for spraying and 2) spray printing the interlayer onto a stainless-steel current collector mounted on a heated vacuum chuck. The method then deviates with one method (top) proceeding by uniaxial pressing followed by Ag sputtering to form a Li_6PS_5Cl/graphite/Ag/current collector disk, and the second method (bottom) proceeding by Ag sputtering followed by uniaxial pressing to form a Li_6PS_5Cl/Ag/graphite/current collector disk for testing.

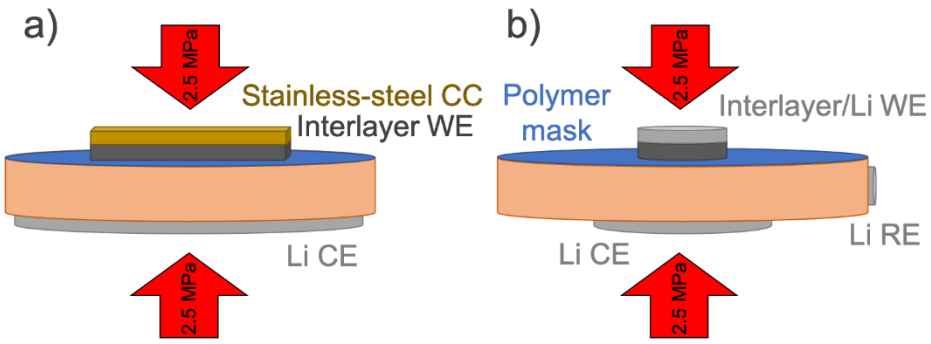


Figure 5.5: Schematic showing a) 2- and b) 3-electrode cell designs. CC, W, CE and RE stand for current collector, working electrode, counter electrode and reference electrode respectively.

described in Section 5.3.1.1 and the stainless-steel current collector was carefully removed to reveal the graphite interlayer. The cell was then masked using Kapton tape and loaded into the PVD chamber for a silver thin-film to be deposited directly onto the graphite layer. A new stainless-steel current collector was then cut for use in the finished cell.

To prepare the silver/graphite bilayer, the graphite spray-coated stainless-steel sheet was mounted directly within the PVD chamber and silver was sputtered to cover the graphite layer. This stainless steel/graphite/silver sheet was then cut to size, loaded into a die-set and uniaxially pressed with Li_6PS_5Cl powder as described previously.

5.3.1.4 Final Cell Construction

Both 2- and 3-electrode cells were utilised in this chapter. Two electrode cells were made by affixing a 4 mm diameter Li foil counter electrode to the opposite side of the ceramic disk to the interlayer. The Li foil used was approximately 50 μm in thickness and was produced by calendaring. 3-Electrode cells were fabricated by pressing a 3 mm diameter counter electrode of Li foil onto the opposite side of the ceramic disk, as well as a 1 mm diameter Li reference electrode. In the 3-electrode cell, an additional Li foil was pressed behind the interlayer on the working electrode, such that the effects of Li loss were not

observable in the cycling data. Schematic representation of these cells are shown in Figures 5.5.

The cells were then sealed under vacuum into pouch cells with stainless steel current collectors and removed from the glovebox for testing.

5.3.2 Electrochemical Testing

Potentiostatic Electrochemical Impedance Spectroscopy (PEIS) was conducted using a Gamry 1010E potentiostat. 10 points were collected per decade in a frequency range of 1 MHz – 1 Hz, using a 5 mV perturbation.

Galvanostatic cycling was performed on a Biologic VMP-3 potentiostat. A stack-pressure of 2.5 MPa was applied to pouch cells using sprung clips and the cells were submerged within an oil bath and left for 2 hours for the temperature to equilibrate. All cells were tested at 60 °C unless otherwise specified.

5.3.3 Characterisation

5.3.3.1 SEM/EDX

SEM/EDX was carried out on the top surface and cross-section of pristine and cycled cells. Cells were disassembled in a glovebox and cross-sectioning was carried out as described in Section 2.2.3. Samples were mounted on a plate using carbon adhesive tape and the plate was sealed within an air-tight transfer holder which was used to move the samples to a Merlin SEM (Zeiss) without exposure to air. SEM was initially carried out using an acceleration voltage of 3 kV and a probe current of 200 μA. For SEM/EDX, data were collected at a higher voltage of 10 kV. The EDX was carried out within the Zeiss Merlin instrument using a X-Max 150 Silicon Drift detector (Oxford Instruments). Collection and analysis were carried out using the Aztec software package.

5.3.3.2 *Operando* and *Ex-Situ* XRD

Operando XRD data were collected on a 9 kW Rigaku Smartlab diffractometer, equipped with a 2D detector, using Cu Kα radiation. An air-tight battery cell (Rigaku), designed for *operando* XRD, was used for cycling. XRD was conducted through a beryllium window, which was protected from reactivity with Li metal during charge by a 1 μm copper foil, which was thin enough to be sufficiently X-ray transparent. Stack-pressure was maintained within the cell using a conical spring.

Ex-situ XRD patterns were collected on a Rigaku MiniFlex diffractometer using Cu Kα radiation. The diffractometer was located within a nitrogen-filled glovebox and cell disassembly was carried out in an inert atmosphere. Samples were mounted on low-background silicon sample holders.

5.4 Results and Discussion

5.4.1 Cell Fabrication

5.4.1.1 Preparation of Li_6PS_5Cl Disks

Whilst the Li_6PS_5Cl solid electrolyte used in this chapter is the same as that used in Chapter 4, here the ceramic is left unsintered rather than sintering at 300 °C. Sintering was not considered to be an option for this work as the sintering temperature could lead to decomposition of the polymer binder in the carbon-based interlayers and might result in unanticipated interfacial reactivity between cell components. The Li_6PS_5Cl electrolyte was also unsintered in the previous work by Samsung.[199] Therefore, the Li_6PS_5Cl ceramic electrolyte used throughout this chapter is more porous and has a higher impedance associated with grain boundary resistance (see Chapter 4 Section 4.4.1.1) and is considered to be more susceptible to dendrite penetration.

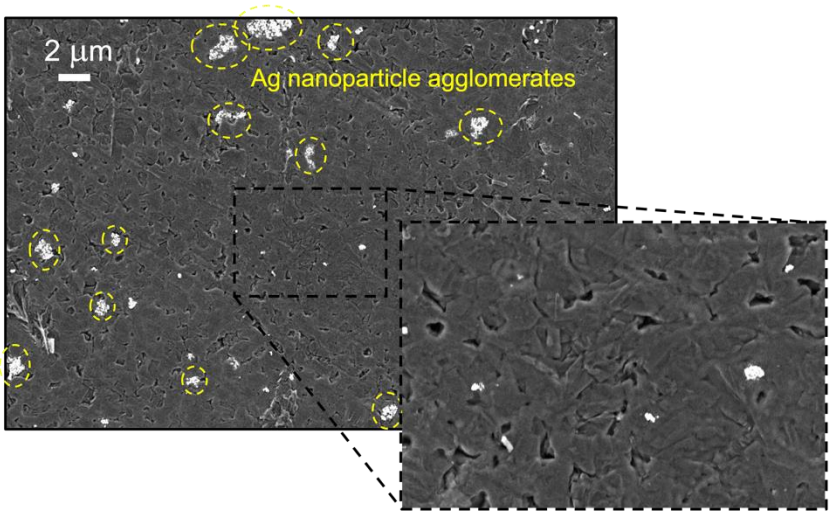


Figure 5.6: SE micrograph showing the Ag nanoparticle distribution in the graphite-silver nanoparticle composite interlayer. The inset shows a magnified area of good Ag nanoparticle distribution. Areas of Ag nanoparticle agglomeration are highlighted (yellow).

5.4.1.2 Preparation Carbon Containing Interlayers

The sprayed carbon-containing interlayers were examined using SEM and were judged to be of reasonably uniform thickness and pinhole free when 20 layers or more were sprayed. Prior to uniaxial pressing, the sprayed layers on the current collector were observed to be undesirably porous, however once they were pressed with the Li_6PS_5Cl solid electrolyte powder under 400 MPa they displayed greatly reduced thickness and a lower porosity.

As described in Section 5.3.1.1, silver nanoparticles were added to the graphite interlayer to produce a composite. Whilst most silver particles remained well-dispersed throughout the spraying procedure yielding an even distribution of silver within the graphite layer, it is also clear there was some agglomeration of nanoparticles, leading to some highly silver-rich regions of the carbon-silver composite interlayer (Figure 5.6).

5.4.1.3 Preparation of Silver Interlayers

The layer thickness was controlled by a crystal sensor during the sputtering deposition process and the thickness and uniformity of silver interlayers was also checked by SEM/EDX. It was particularly important to establish that the layer thickness was properly

controlled whether the deposition substrate was the Li_6PS_5Cl disk (in the case of cells with a single interlayer composed only of silver) or if the substrate was graphite (in the case of cells using dual interlayers of graphite and silver). The layer thicknesses were determined to be approximately 200 μm, regardless of the substrate upon which the silver was deposited.

5.4.2 First Charge Voltage Profiles

The six cells were charged at a low current density of 0.1 mA/cm^2, moving a capacity of 2.0 mA·h/cm^2 under a stack-pressure of 2.5 MPa at a temperature of 60 °C. Cells were left at temperature for 2 h prior to cycling and were determined to have the anticipated initial

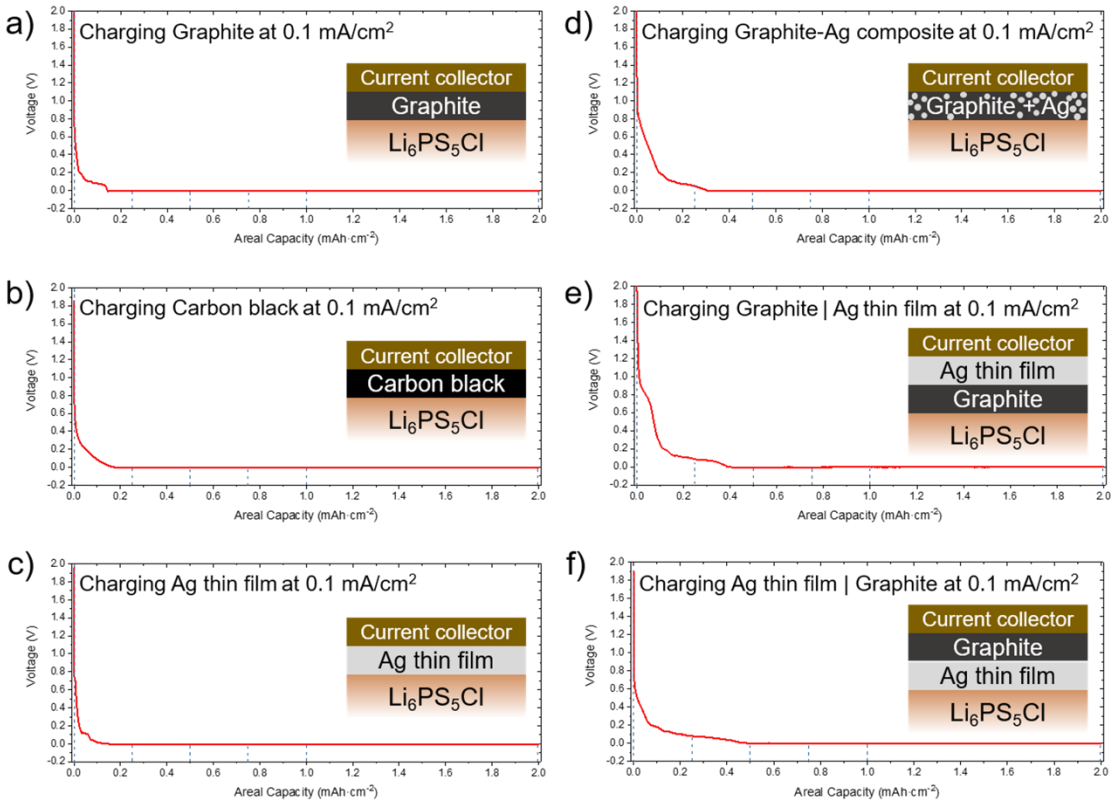


Figure 5.7: First charge voltage profiles of cells with interlayers composed of a) Graphite; b) Carbon black; c) Silver thin film; d) Graphite-Silver nanoparticle composite; e) Graphite/silver bilayer and f) Silver/graphite bilayer. Insets show schematic representations of the anode-side of these cells. All cells were charged at 0.1 mA/cm^2 at 60 ºC under 2.5 MPa.

OCV of approximately 2 V vs Li^+/Li before initiation of the charge. Voltage profiles accompanied by schematics of each of the six cells are shown in Figure 5.7.

5.4.3 Charging Graphite and Carbon Black Interlayers

Charging Graphite Interlayers:

The voltage profile for the first charge of a graphite interlayer is shown in Figure 5.7a. The shape of the charge curve is consistent with previous literature on graphite anode charging.[284–286] The initial cell voltage is approximately 2.4 V vs Li^+/Li, dropping rapidly upon passing current. Features in the voltage profile are observed at approximately 200 mV, 105 mV and 80 mV vs. Li^+/Li. After moving approximately 0.15 $mA{\cdot}h/cm^2$ capacity, the cell voltage reaches a minimum of -7.3 mV, before finally plateauing at approximately -3 mV until the end of charge. To further understand the structural changes within the graphite interlayer during the charging process, *operando* XRD was carried out in a cell as described in Section 5.3.3.2. As it was not possible to carry out charge at elevated temperature, and to enable high time resolution of the collected XRD data, the charge was carried out at a slower rate of 20 $\mu A/cm^2$ at room temperature.

The charge profile and heat-map showing the change in XRD peak positions in the 2θ region of 23-27° are shown in Figure 5.8. Graphite lithiation and delithiation are extremely well-characterised in the literature.[285,287–294] During lithiation, graphite is understood to transition through a number of phases, conventionally described as stages of lithiation (1L, 4L, 3L, 2L, 2 and 1), with changes in the potential gradient indicating the two-phase regimes between stages. In the early stages of intercalation 1L, 4L, 3L and 2L (Li_xC_6, $x < 0.25$) Li is intercalated between AA stacked graphene layers with no in-plane order. At higher degrees of lithiation (stages 2 and 1), layers have an AB stacking. Stages of lithiation are clearly identifiable in the voltage profile and XRD data. The data reveal that:

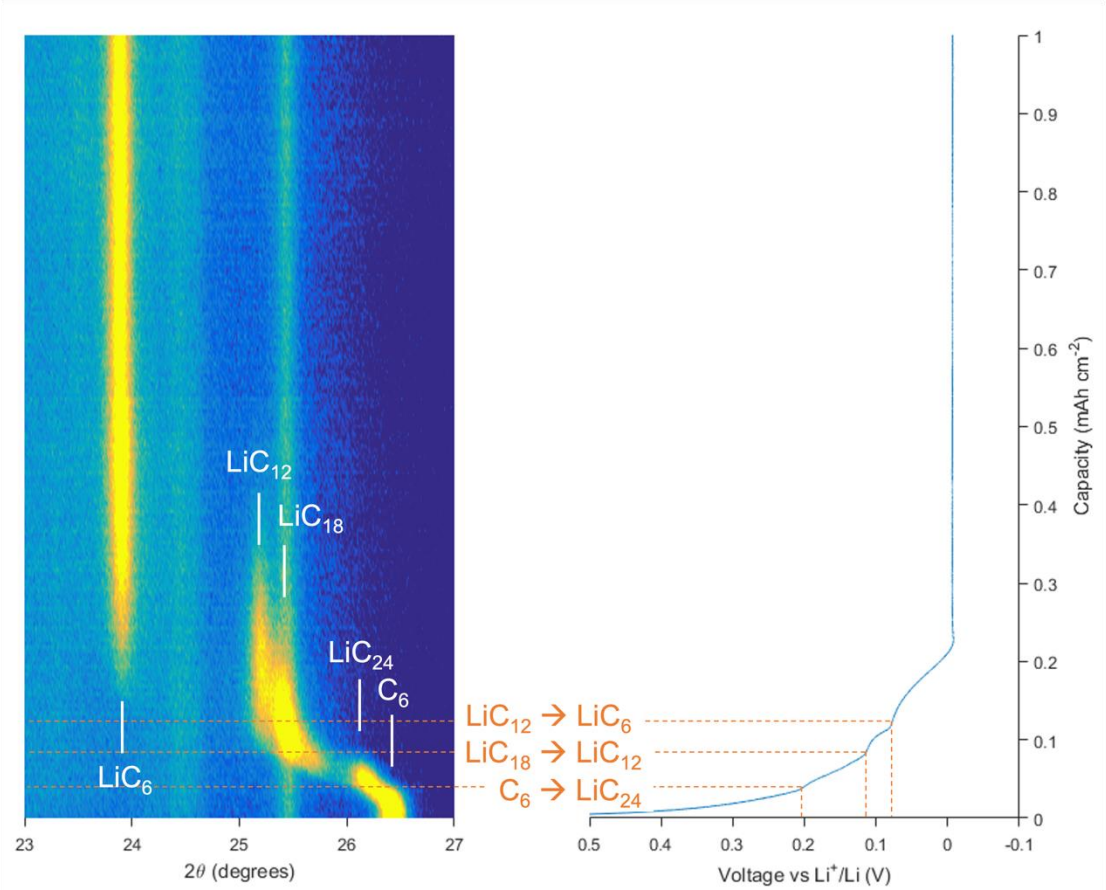


Figure 5.8: *Operando* XRD and corresponding electrochemistry of a graphite interlayer cell. The left-hand panel shows a heat-map, indicating changes in reflection intensity as the graphite interlayer lithiates in the 2θ region of 23° - 27°. The right-hand panel shows the corresponding voltage profile. The cell was charged at room temperature at a rate of 20 μA/cm^2.

1. Initially, before the passage of charge, the intense peak is the [0,0,2] of graphite, C_6, at 26.4°.
2. As the first charge is passed and the graphite begins the first stages of lithiation, the [0,0,2] peak position remains relatively unchanged as the cell voltage drops. At this point the dilutely lithiated graphite is in a solid solution phase.
3. As the cell reaches the change in gradient in the voltage profile at approximately 200 mV vs Li^+/Li, a peak shift to lower angle is observed in the XRD, indicating a structural transition. This transition is the 1L → 4L transition from the sold solution phase to LiC_{24} (4L).

4. Following the voltage feature at 200 mV, the cell voltage continues to fall. In this region, a clear discontinuity is observed in the XRD, with the peak at approximately 26.1° decreasing in intensity and a new peak appearing at approximately 25.4°. This transition is the 4L → 3L transition (LiC_{24} → LiC_{18}). It should be noted that a further structural transition from 3L → 2L has sometimes been observed to immediately follow this in the literature, however it is not clearly observed either in the voltage profile or in the XRD in these data, as has been the case in other studies.[290,291]
5. Upon moving more capacity, the subsequent voltage feature at approximately 105 mV corresponds to a further structural transition and at this capacity a decrease in intensity of the peak at 25.5° and an increase in intensity of the peak at 25.25° indicates that this structural transition is from LiC_{18} to LiC_{12} (3L → 2) and the observed peak is the [0,0,2] peak of LiC_{12}.
6. After passing more charge, the final voltage feature at 80 mV is reached. This is the final two-phase transition of the graphite layer (2 → 1) in which LiC_6 is formed as is indicated by the intense [0,0,1] peak at 23.9°.
7. After moving more capacity, the cell voltage falls to a negative value, accompanied by the increase in intensity of a peak at 36°, corresponding to the plating of Li metal after the graphite layer has been fully lithiated (Appendix Figure A5.1).[295]

In summary, the charge of a graphite interlayer proceeds as has previously been observed for bulk graphite anodes, with the complete lithiation of the graphite layer through the anticipated LiC_x phases. Upon complete lithiation of the graphite layer to LiC_6, lithium metal plates at the anode-side.

Charging Carbon Black Interlayers:

In contrast, charging of carbon black interlayers does not proceed by intercalation, but rather by the direct deposition of lithium, as is indicated by the smooth decrease in voltage

during charge with no features in the voltage profile (Figure 2.7b). The plating potential goes through a minimum at -11 mV vs Li^+/Li, plateauing at a potential of -3 mV.

Imaging Lithium Plating:

To better understand the plating of lithium metal, cross-sectional SEM/EDX was carried out on pristine cells and cells charged with 2.0 mA·h/cm^2 capacity. Micrographs and EDX maps showing the Li_6PS_5Cl/carbon interface are presented in Figure 5.9.

In the graphite interlayer cell, the pristine micrograph (Figure 5.9a) shows a coherent interface between the solid electrolyte, indicated by the presence of sulphur (blue, aiii), and an approximately 4.5 μm layer of graphite on the surface, indicated by the presence of carbon (orange, aii). After charging the cell, good contact seems to have been retained

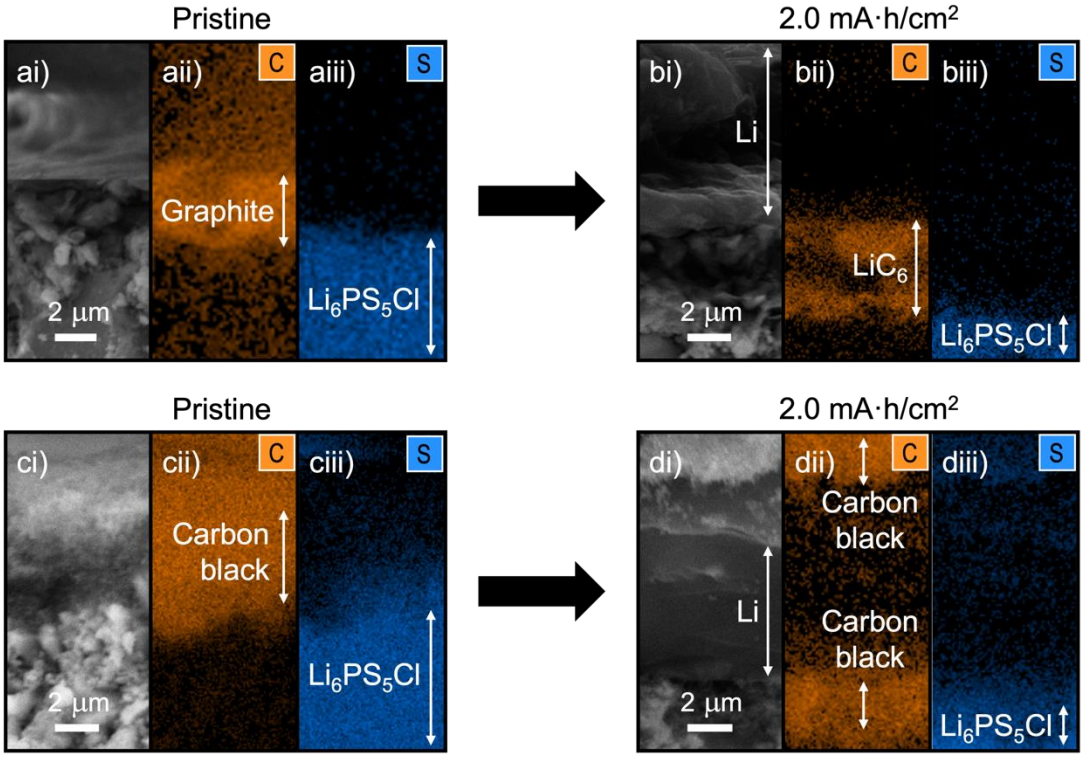


Figure 5.9: Cross-sectional SEM/EDX of Li_6PS_5Cl/interlayer interfaces when pristine and after charge. The figures show a) the pristine Li_6PS_5Cl/graphite interface; b) the Li_6PS_5Cl/graphite interface after charging, showing a layer of Li metal at the graphite/current collector interface; c) the pristine Li_6PS_5Cl/carbon black interface and d) the Li_6PS_5Cl/carbon black interface after charging, showing Li metal bifurcating the carbon black layer. i), ii) and iii) show the SE micrograph, the C EDX map (orange) and the S EDX map (blue) respectively.

between the solid electrolyte and the now lithiated LiC_6 interlayer (Figure 5.9b). In the charged state, a thick layer of > 5 μm of lithium can be observed plated at the graphite/current collector interface. This is a key result as it demonstrates the same advantageous Li plating behaviour that was achieved by researchers from Samsung; that interlayers can prevent nucleation of Li metal at the solid electrolyte/interlayer interface, and that, instead, nucleation at the interlayer/current collector interface can be preferred. In the case of the Samsung research, this exact behaviour appeared to enable cells to reach high charging current densities without failure.[199]

On the other hand, after charging the carbon black interlayer, Li is observed to plate both within the carbon black layer, as shown in Figure 5.9c-d, and at the interlayer/solid electrolyte interface (Appendix Figure A5.2). The conformal interface between Li_6PS_5Cl observed in the pristine cell (Figure 5.9c), is not retained as Li metal nucleates within the carbon black layer and at the carbon black/solid electrolyte interface. The nucleating material is identified as Li metal as it does not display a clear EDX signal (Figure 5.9d). Li filaments are observed to penetrate the ceramic electrolyte material (Appendix Figure A5.2), confirming that if Li is deposited at the interlayer/solid electrolyte interface rather than the interlayer/current collector interface, the interlayer cannot act as a physical barrier against dendrite penetration into the solid electrolyte and critical cell failure will occur.

Further cells with graphite and carbon black interlayers were charged and arrested at different stages of charge; 0.25 $mA{\cdot}h/cm^2$, 0.5 $mA{\cdot}h/cm^2$, 0.75 $mA{\cdot}h/cm^2$, 1.0 $mA{\cdot}h/cm^2$ and 2.0 $mA{\cdot}h/cm^2$. Following charge, the cells were disassembled, and the stainless-steel current collectors were carefully removed. The cells were then imaged by SEM from the top down. In agreement with the findings of the cross-sectional SEM/EDX, cells utilising a graphite interlayer showed Li deposition above the interlayer at what would have been

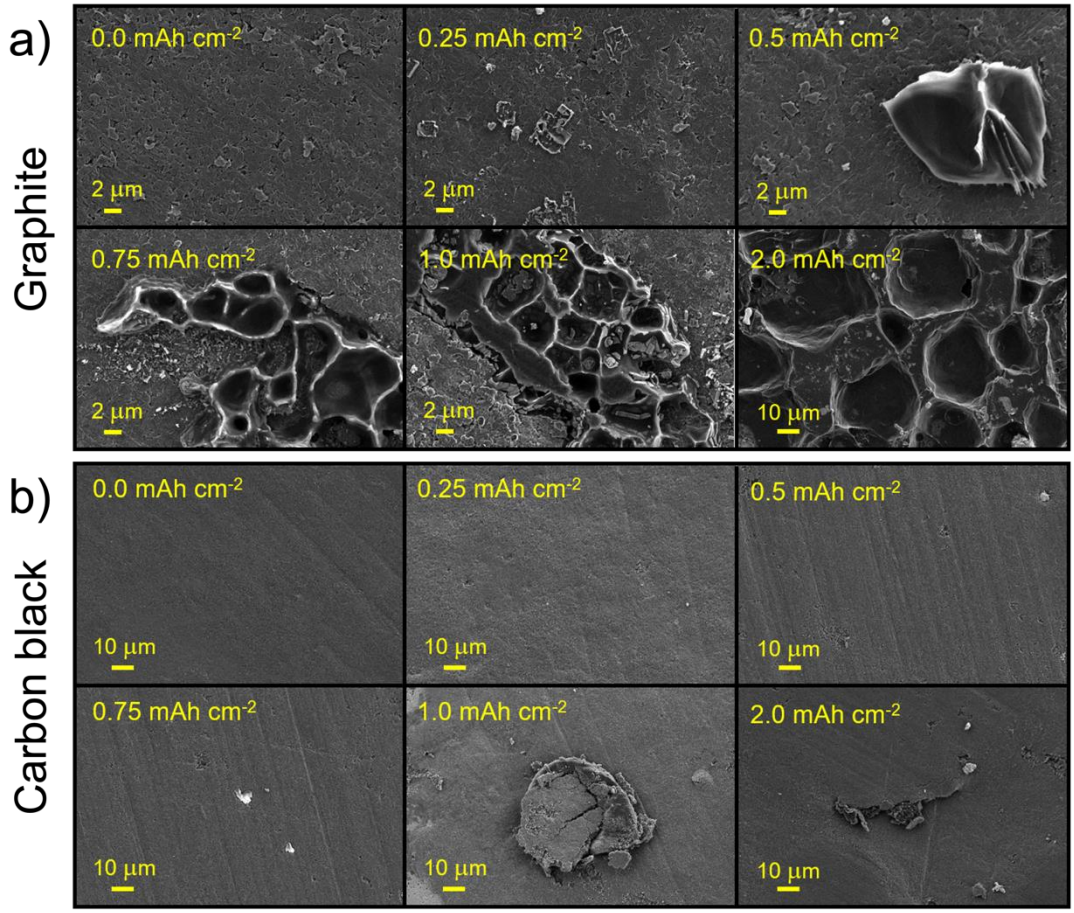


Figure 5.10: Top-view SEMs of a) the graphite interlayer and b) the carbon black interlayer following removal of the current collector. Each panel shows a separate cell arrested at a different point in charge; after 0.0 mA·h/cm^2, 0.25 mA·h/cm^2, 0.5 mA·h/cm^2, 0.75 mA·h/cm^2, 1.0 mA·h/cm^2 and 2.0 mA·h/cm^2.

the interlayer/current collector interface (Figure 5.10a). As more charge is passed, more Li is observed on the surface of the graphite, with small, geometric nucleates of Li observed after only 0.25 mA·h/cm^2, growing to a more complete layer after passing 2.0 mA·h/cm^2 capacity. Top-down imaging gives some information about the morphology of the plated Li, although it must be acknowledged that cell disassembly and removal of the current collector is expected to cause some disturbance. Whilst this method is imperfect, it was also considered to be unavoidable, since other methods such as use of a mesh or a conductive carbon paper were determined to be less successful than peeling away the stainless-steel current collector and checking that the current collector remained visually

clean, indicating that neither deposited Li metal, nor the interlayer had been wholly or partially removed with it. This method also has a basis in previous literature.[277]

By contrast, upon charging a carbon black interlayer, no Li was observed to be deposited at the current collector interface (Figure 5.10b). At low capacities of 0.25 – 0.75 mA·h/cm^2, only carbon black is observed from the top view, with the Li instead nucleating at the interlayer/solid electrolyte interface or indeed as filaments within the Li_6PS_5Cl electrolyte as observed previously in cross-sectional SEM/EDX. At high capacities of 1.0 – 2.0 mA·h/cm^2, Li is observed to rupture through the carbon black interlayer, mechanically breaking it. In addition, areas can be seen in which the interlayer is warped from Li deposition beneath, but not broken.

Critical Current Density Dependence on Interlayer Thickness:

To investigate the effect of interlayer thickness on critical current density, 3-electrode cycling experiments were performed. Graphite interlayers of two different thicknesses were prepared by the spraying method described in the Experimental Methods, Section 5.3.1.1. Upon pressing onto Li_6PS_5Cl ceramic, these layers were determined to have thicknesses of approximately 4.5 μm and 11 μm. Cross-sectional SEM/EDX is shown in Figures 5.12b and c, in which the graphite interlayer is characterised by the presence of carbon signal (orange), indicative of the graphite, and fluorine signal (yellow), indicative of the PVdF binder.

3-Electrode cells were constructed as described in Section 5.3.1.4 and cycling was carried out beginning with charge of the graphite interlayer, followed by a slow discharge. It should be noted that for these experiments, a thin 50 μm Li foil was placed behind the graphite interlayer in the pristine cell to provide an excess of Li. The discharge rate is 0.1 mA/cm^2 relative to the 1.5 mm diameter graphite working electrode, or 0.025 mA/cm^2 relative to

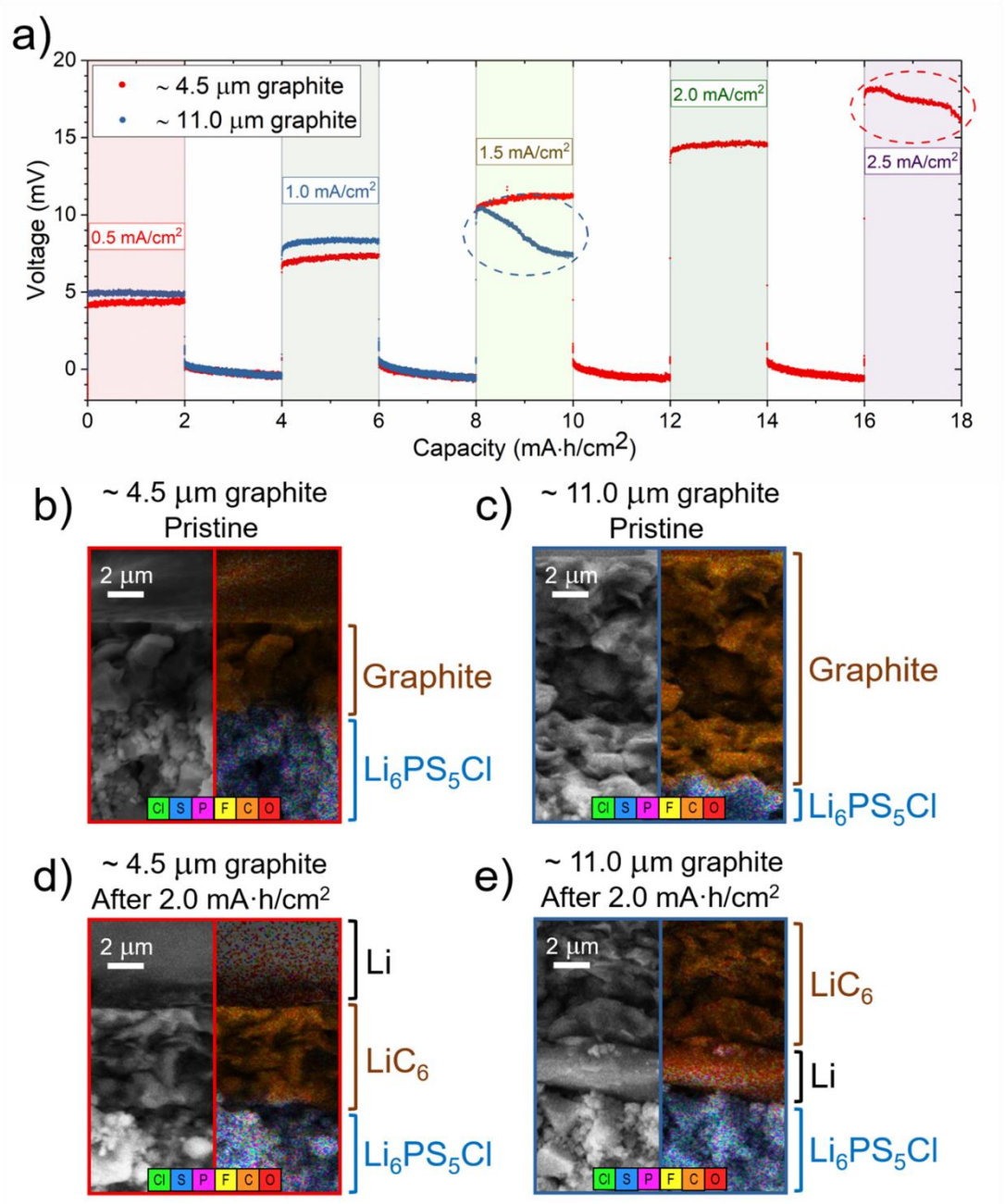


Figure 5.11: a) Cycling performance of 3-electrode cells with a ~ 4.5 µm graphite interlayer (blue) and a ~ 11.0 µm graphite interlayer (red). Current densities of 0.5, 1.0, 1.5, 2.0 and 2.5 mA/cm² are highlighted by red, blue, yellow, green, and purple backgrounds respectively. SE micrographs and elemental EDX mapping of cells showing b) interface with ~ 4.5 µm graphite interlayer when pristine; c) interface with ~ 11.0 µm graphite interlayer when pristine; d) interface with ~ 4.5 µm graphite interlayer after charging at 2.0 mA/cm² and e) interface with ~ 11.0 µm graphite interlayer after charging at 2.0 mA/cm².

the 3 mm diameter lithium counter electrode. The extremely low discharge rate was used to prevent the formation of dendrites at the counter electrode interface, which was not protected by an interlayer. Each cycle, the rate of charge was increased in steps of 0.5

mA/cm^2 until a voltage drop on charge indicated failure of the cell. The current density of discharge remained constant for each cycle. The cycling profiles are displayed in Figure 5.11a.

Just as described in previous chapters, use of the 3-electrode cell allows for the voltage changes at the working electrode/solid electrolyte interface to be studied in isolation. For the cell with the approximately 4.5 μm interlayer (red curve), the initial charge at 0.5 mA/cm^2 showed a low and stable voltage of 4-5 mV (red background), indicating a stable Li deposition without penetration of dendrites into the solid electrolyte. The following discharge showed a very low and stable voltage, showing that stripping lithium from the working electrode at the low rate of 0.1 mA/cm^2 is highly stable. When the cell is charged at the higher current densities of 1.0, 1.5 and 2.0 mA/cm^2 (blue, yellow and green backgrounds, respectively), the voltage on charge remains relatively stable for each, at approximately 7.5 mV, 11 mV and 14.5 mV. However, at the higher current density of 2.5 mA/cm^2, the cell voltage begins to fall during the charge, from approximately 18 mV to 16.5 mV. Whilst the cell continued to cycle at even higher current densities, from this point the cell voltage continued to gradually fall. It is clear that this decrease in cell voltage is indicative of Li metal deposition at the graphite/solid electrolyte interface and within the solid electrolyte, as has been established for other battery systems.[120,190]

A cell with a thicker graphite interlayer, approximately 11 μm, was also cycled in the same way (blue curve). As anticipated, the cell displayed higher overpotential due to the increased thickness of the graphite layer. Stable charging was observed at 0.5 mA/cm^2 and 1.0 mA/cm^2 at potentials of 5 mV and 8.5 mV respectively (red and blue backgrounds). However, unlike the thinner interlayer, at a current density of 1.5 mA/cm^2 (yellow background) the cell polarisation began to fall during charge, from approximately 10.5 mV

to 7.5 mV, indicating plating of Li metal at or within the solid electrolyte. It therefore appears that the current density of cell failure decreases as the graphite interlayer thickness increases.

To probe this further, two more cells, one of each interlayer thickness, were constructed and both were charged at 2.0 mA/cm^2 for 2.0 mA·h/cm^2 under the same conditions. After charge, the cells were cross-sectioned to determine the position of the plated Li. For the thinner graphite layer which displayed stable cycling at this current density, the Li was observed to have formed a layer between the graphite and the current collector, Figure 5.11d. However, for the thicker graphite interlayer at this current density, at which the cell was observed to fail, Li metal was observed to nucleate and grow in a layer at the solid electrolyte/graphite interface, Figure 5.11e. It can be concluded that graphite interlayer cells have a thickness-dependent critical current density for charge below which Li metal will nucleate at the current collector interface and above which Li metal will nucleate at the solid electrolyte interface and that this critical current sets the practical limit for the rate of fast-charging.

Critical Current Density Dependence on Interlayer Temperature:

A further 3-electrode cell was constructed with an approximate interlayer thickness of 4.5 μm and was cycled at a lower temperature of 30 ºC, Figure 5.12a. Just as described above, the working electrode of Li metal, protected by a graphite interlayer, was charged at a rate of 0.5 mA/cm^2 before being stripped at a lower rate of 0.1 mA/cm^2. On following cycles, the charging rate was increased in steps of 0.5 mA/cm^2 until signs of cell failure.

When the graphite-interlayer-protected Li anode was charged at a rate of 0.5 mA/cm^2 (red background), there were immediately signs of different cell behaviour to the equivalent cell at 60 ºC (Figure 5.11a, red curve). Whereas at 60 ºC cycling initiated at a low potential, at

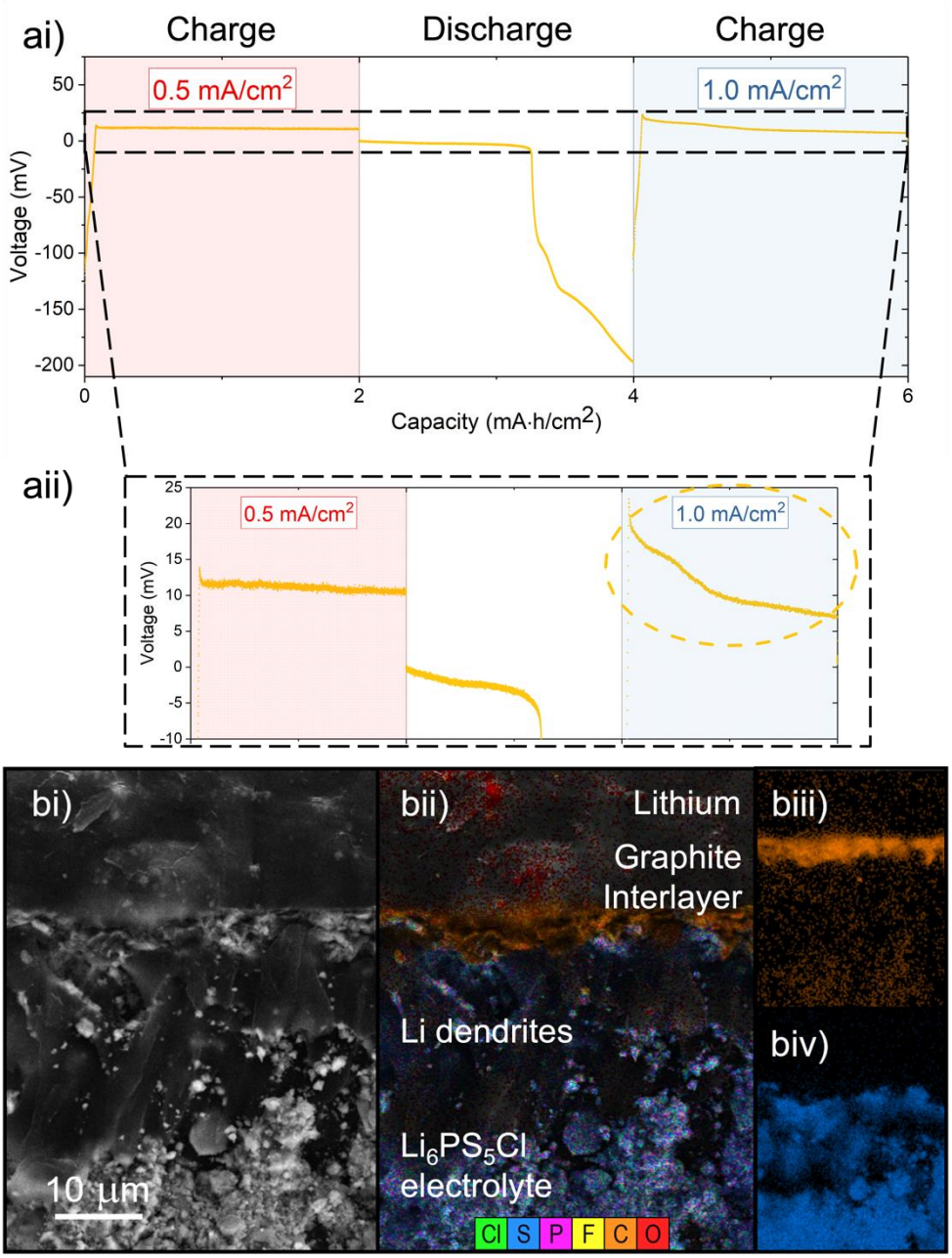


Figure 5.12: a) Cycling performance of 3-electrode cells with a graphite interlayer charged at 30 ºC (yellow). Current densities of 0.5 and 1.0 mA/cm^2 are highlighted by red and blue backgrounds respectively. i) Shows the complete cycling data and ii) shows a magnification of the key region. b) SE micrographs and elemental EDX mapping of cells showing the interface at the end of the cycling in (a), where the cell has been charged at 1.0 mA/cm^2 at 30 ºC. i) Shows the SE micrograph; ii) shows the micrograph with the full EDX colour map superimposed; iii) shows the C EDX map and iv) shows the S EDX map. It is clear there has been substantial Li metal plating below the graphite interlayer, within the Li_6PS_5Cl electrolyte.

30 ºC the initial cell potential is approximately 125 mV vs Li^+/Li, indicating that the graphite interlayer is not fully lithiated from having been pressed against the Li foil in the cell's pristine state i.e. the kinetics of Li transport from bulk Li into the graphite interlayer

are somewhat limiting at the lower temperature. Upon charging, the cell potential passes through the expected features in the voltage profile and reaches a stable potential of approximately 11 mV. On the first discharge the cell begins at a low and stable voltage as observed at 60 ºC, but after discharging 1 mA·h/cm^2 capacity, the cell potential rapidly changes, passing through the voltage features indicative of graphite deintercalation. Whilst this chapter does not focus on discharge of interlayer-protected Li anodes, it is interesting that these data suggest that at a discharge rate of 0.1 mA/cm^2, the rate of diffusion of Li from Li metal into the graphite interlayer is insufficient to maintain full lithiation of the graphite throughout discharge at 30 ºC, but that the rate of diffusion is sufficient at 60 ºC.

The graphite-protected Li anode was then charged at the higher current density of 1.0 mA/cm^2 (blue background). Intercalation to form LiC_6 occurred rapidly, and the cell reached a potential of approximately 20 mV. However, this was short lived as the cell potential began falling during the charging process, indicating cell failure as described previously. Over the course of the charge, the voltage fell to approximately 7 mV, below the cell potential of the lower current density charge. This is shown clearly in the magnification of the cycling data, Figure 5.12aii.

To determine the cause of failure, the cell was cross-sectioned following the charge at 1.0 mA/cm^2 and the interface was imaged by SEM and EDX (Figure 5.12b). There were clear indications that Li was plating at the Li_6PS_5Cl/graphite interface, rather than at the graphite/lithium interface at this current density at 30 ºC. A dark metallic material was observed beneath the graphite interlayer, within the Li_6PS_5Cl (Figure 5.12bi). EDX mapping clearly showed little or no elemental signal in this area (Figure 5.12bii-iv), indicating that the subsurface structure is likely to be Li metal dendrites. This shows that the critical current density is significantly lower at 30 ºC (0.5 mA/cm^2 < CCD < 1.0 mA/cm^2) than at 60 ºC (2.0 mA/cm^2 < CCD < 2.5 mA/cm^2).

Importance of Li-Ion Transport in Carbon Interlayers:

It has been observed that multiple factors can affect the location of Li plating in carbon-based interlayer solid state batteries; the type of carbon (graphite or carbon black), the thickness of the interlayer, the temperature of cell operation and the rate of charge. Taken together, it is clear that it is the rate of Li^+ transport across the interlayer that is rate limiting. Li metal preferentially nucleates at the current collector interface under conditions that favour high rates of Li^+ transport through the interlayer, i.e. when charging the cell at higher temperature, through a thinner interlayer and using an interlayer with a higher Li^+ diffusivity such as graphite. This reveals that Li nucleation at the current collector interface is thermodynamically favoured over nucleation at the solid electrolyte interface. Discussion of why this might be the case follows later. Conditions that give low rates of Li^+ transport across the interlayer (lower temperature, thicker graphite layer and use of non-intercalation carbon such as carbon black) result in Li nucleation at the interlayer/solid electrolyte interface. Therefore, under a particular set of cycling conditions, it is the rate of diffusion of Li^+ across the interlayer (D_{Li}) compared to the rate of flux of Li^+ ions to the interlayer/solid electrolyte interface (j_{Li+}) that determines the critical current for cell failure, Figure 5.13. If the $D_{Li} > j_{Li+}$ then Li metal can nucleate at the thermodynamically favoured position, however if $D_{Li} < j_{Li+}$ then nucleation at the current collector becomes kinetically inhibited and instead plating at the solid electrolyte interface takes place.

So why is Li nucleation at the current collector interface, rather than the solid electrolyte interface, thermodynamically favoured? That it is thermodynamically favoured means that Li nucleates at the current collector interface at lower potential and that therefore the work associated with nucleating Li between graphite and the stainless-steel current collector ($W_{Graph \cdot Li \cdot CC}$) is less than that associated with nucleating Li between the Li_6PS_5Cl solid electrolyte and the graphite interlayer ($W_{SE \cdot Li \cdot Graph}$). The work required to break the adhesion

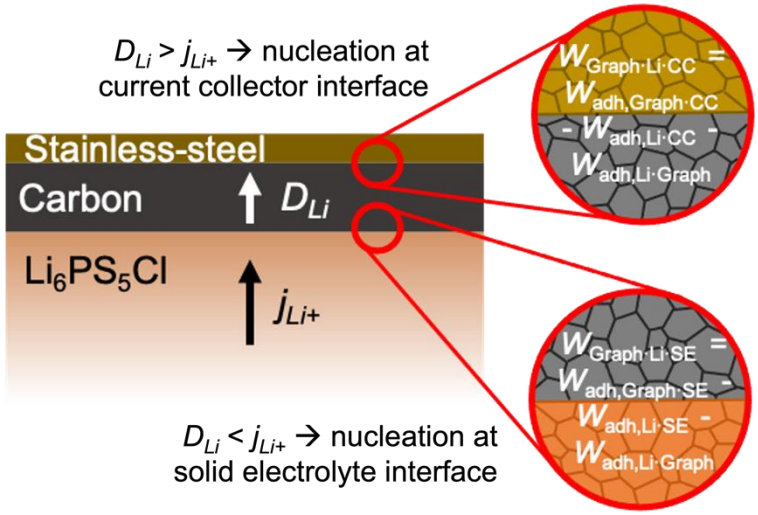


Figure 5.13: Schematic showing the importance of lithium diffusion through the carbon layer (D_{Li}) relative to the flux of Li-ions (j_{Li+}) to the location of Li nucleation. The red circles indicate the two interfaces at which Li can nucleate, with the insets giving the work associated with nucleation.

at the existing interface relative to the work of forming two new interfaces and can be expressed as follows:

$$W_{Graph·Li·CC} = W_{adh,Graph·CC} - W_{adh,Li·CC} - W_{adh,Li·Graph} \quad (5.1)$$

$$W_{Graph·Li·SE} = W_{adh,Graph·SE} - W_{adh,Li·SE} - W_{adh,Li·Graph} \quad (5.2)$$

where $W_{adh,x·y}$ is the work of adhesion between phases x and y.[277]

Experimental observation that Li nucleates preferentially at the current collector indicates $W_{Graph·Li·CC} < W_{Graph·Li·SE}$. Expressing this inequality as $W_{adh,Graph·CC} - W_{adh,Li·CC} < W_{adh,Graph·SE} - W_{adh,Li·SE}$ helps clarify some of the reasons that nucleation at the current collector might be thermodynamically favoured. Firstly, $W_{adh,Li·CC}$ is likely to be greater than $W_{adh,Li·SE}$, as wettability (and adhesion) of lithium on many ceramic substrates is extremely poor,[61,217,254,296] whereas wettability of molten Li metal against metallic substrates is better, suggesting that $W_{adh,Li·CC} > W_{adh,Li·SE}$.[296,297] An additional factor is that $W_{adh,Graph·CC}$ is likely less than $W_{adh,Graph·SE}$. When preparing the cells as detailed in Section 5.3.1.1, after pressing

the Li_6PS_5Cl/graphite/current collector stack, the stainless-steal current collector is very easily removed, often becoming detached when removing the disk from the die-set and shows no sign of adhesion between the carbon-PVdF composite to the stainless-steel. By contrast, there is no such ease in removal of the graphite interlayer from the Li_6PS_5Cl solid electrolyte, and SEM/EDX (Figure 5.11b) shows that these layers are very intimately adhered. Taken together, these two factors may account for the thermodynamic preference for the Li to nucleate at the current collector interface, rather than the solid electrolyte interface.

5.4.4 Charging Silver Interlayers

Before silver-carbon composite interlayers can be discussed, it is imperative to understand the charging process of silver interlayers. The voltage profile of the first charge, shown in Figure 5.7c, shows a series of voltage plateaus at low capacities, with the potential dropping below 0 V at approximately 0.15 $mA{\cdot}h/cm^2$. The majority of the charge (0.15-2.0 $mA{\cdot}h/cm^2$) occurs at a stable, negative potential.

Operando XRD was again used to investigate the structural changes occurring during charge. To achieve a high time resolution, a 2D detector was utilised to minimise the time taken to collect a full diffractogram and the cell was charged at a slow rate of 50 $\mu A/cm^2$. A thicker Ag interlayer (750 nm rather than 200 nm) was used to increase the intensity of reflections of Ag-containing phases. Figure 5.14 shows key 2θ regions of the XRD pattern alongside the associated voltage curve. Reference is also made to the Ag-Li phase diagram shown in Figure 5.15, as this aids in understanding the alloy phases observed during charge. The charging process can be understood as follows:

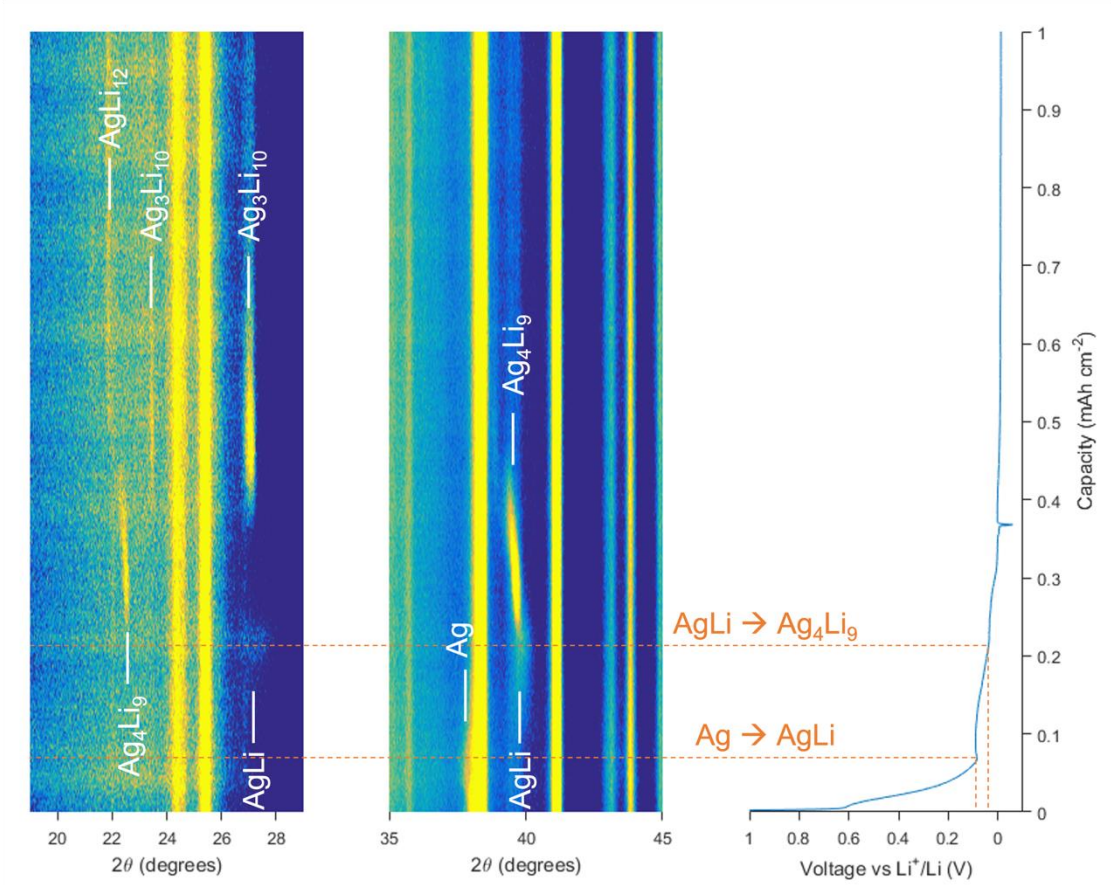


Figure 5.14: *Operando* XRD and corresponding electrochemistry of a silver interlayer cell. The left-hand and central panels show heat-maps in the 2θ regions of 21º - 29º and 35º - 45º, indicating changes in reflection intensity as the silver alloys with lithium. The right-hand panel shows the corresponding voltage profile. The cell was charged at room temperature at a rate of 50 μA/cm^2.

1. Initial cell voltage is approximately 2 V, indicative of the potential difference between lithium and pure silver. An intense diffraction peak corresponding to silver can be observed at a 2θ value of approximately 38°.[298]
2. As charge is passed, the cell potential drops very rapidly to approximately 600 mV and then more slowly to a plateau at approximately 90 mV. The XRD reveals that during this initial stage of charge, no structural change is occurring, although the peak at 38° appears to undergo a small shift to lower angle as charge is passed, revealing a change in lattice parameter as Li is doped into the silver crystal structure.

This observation is in agreement with the phase diagram (Figure 5.15) that shows no structural phase is expected to occur until > 34 atomic % Li doping.[299,300]

3. At approximately 90 mV there is a voltage plateau at which the XRD indicates that a phase with the Ag crystal structure is present, as well as a new phase. The peak intensities of the new phase (approximately 27.5°and 39.5°) increase with increasing capacity passed and the peak intensities of the Ag crystal structure phase decrease. The new phase is identified to have the AgLi crystal structure, corresponding to the β phase of the phase diagram.
4. After passing more capacity, only the AgLi phase remains until a further voltage plateau at approximately 40 mV is reached. At this plateau, the peaks indicative of the AgLi phase begin to decrease in intensity, and the diffraction pattern of a new phase, Ag_4Li_9, the γ_3 phase, begin to increase in intensity at 2θ angles of approximately 22.5° and 39°.[301]
5. As further charge is passed, the cell voltage falls below 0 V, which might usually indicate the nucleation of Li metal. However, no diffraction peaks indicative of Li metal are observed. Instead, the diffraction peaks of the Ag_4Li_9 alloy phase decrease in intensity and peaks characteristic of the γ_2 phase, Ag_3Li_{10}, are observed at a 2θ angles of approximately 23.5° and 27°.[299,302]
6. As more charge is passed, the voltage remains low and negative. The peaks associated with the Ag_3Li_{10} decrease in intensity and a new phase, identified as $AgLi_{12}$ (γ_1), is observed, with an intense reflection at 21.9°. This phase remains the only Ag-Li alloy phase observed over the remainder of the charge, and no peaks associated with Li (δ) are detected.[299,302]

In summary, during charge, the Li-ions reduce to alloy with the Ag layer. As more capacity of Li is moved, the Ag-Li alloys undergo structural changes as they become more Li-rich,

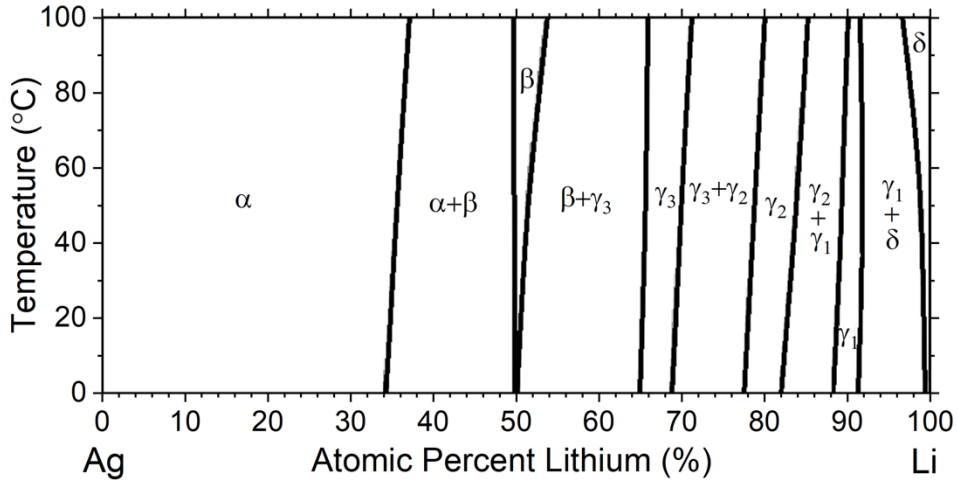


Figure 5.15: Ag-Li phase diagram showing the phases reported by Freeth and Raynor (1953).

following the phase diagram, Figure 5.15. After having moved 2.0 mA·h/cm^2 capacity, the most Li-rich phase, $AgLi_{12}$ (γ_1), has been formed. No nucleation of Li metal is observed at any point in the charging process.

Imaging Lithium Alloying:

Pristine and charged cells were prepared as described previously and cross-sectional and top-down SEM/EDX was carried out. The cross-section of the interface of the pristine cell (Figure 5.16a) shows a thin film of silver (turquoise), approximately 200 nm in thickness, on top of the Li_6PS_5Cl solid electrolyte, which is indicated in the EDX by the presence of sulphur (blue). After charging the cell (Figure 5.16b), the SEM micrograph shows a thick layer of Ag-Li alloy, identified by the diffuse silver signal (turquoise) in the EDX (Figure 5.16bii), formed on the surface of the solid electrolyte. This alloy layer appears to be highly dense and is assumed to have the $AgLi_{12}$ crystal structure, as determined by the *operando* XRD.

Whilst not directly relevant to the general narrative of this chapter, it is interesting to note that at the interface between the Ag-Li alloy and the Li_6PS_5Cl solid electrolyte, there is a

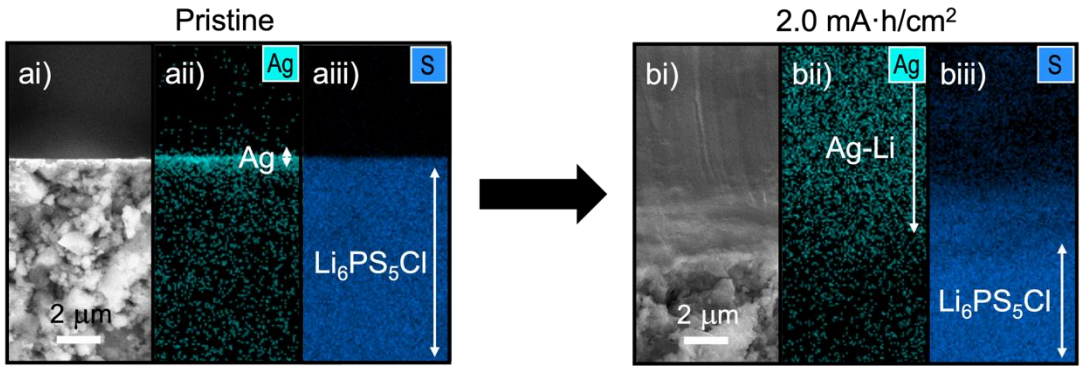


Figure 5.16: Cross-sectional SEM/EDX of a) the pristine Li_6PS_5Cl/silver thin-film interface and b) the Li_6PS_5Cl/silver thin-film interface after charging, showing a layer of Ag-Li alloy. i), ii) and iii) show the SE micrograph, the Ag EDX map (turquoise) and the S EDX map (blue) respectively.

layer, approximately 2-3 μm in thickness, that shows clear signal of both Ag (turquoise) and S (blue), with somewhat lower intensities than the signal observed in the Ag-Li and Li_6PS_5Cl phases themselves. It is possible that this is a thick interphase caused by reduction of the solid electrolyte at the interface between the sulphide solid electrolyte and the Ag-Li alloy at low potential. It is interesting to note that this interphase is thick enough to be observable by SEM/EDX. This is in contrast to the interphase formed between Li_6PS_5Cl and Li metal at low potential, composed primarily of Li_2S, which is generally considered to be so thin (tens or hundreds on nanometres) as to be unobservable by electron microscopy.[79,119,120] The thickness of the interphase at the Ag-Li/Li_6PS_5Cl interface suggests that it is considerably more electronically conductive than the interphase formed at the Li/Li_6PS_5Cl interface,[49] and may be a result of conductive Ag nanoparticles left in the interphase following reduction of the solid electrolyte. A separate, in-depth study, utilising techniques such as XPS and SIMS, is required to fully understand the reduction occurring at this unprotected Ag-Li/Li_6PS_5Cl interface.

Top-down SEM was carried out to determine the evolution of the Ag-Li alloy morphology throughout the charging process, Figure 5.17. In the pristine sample, it is clear that the

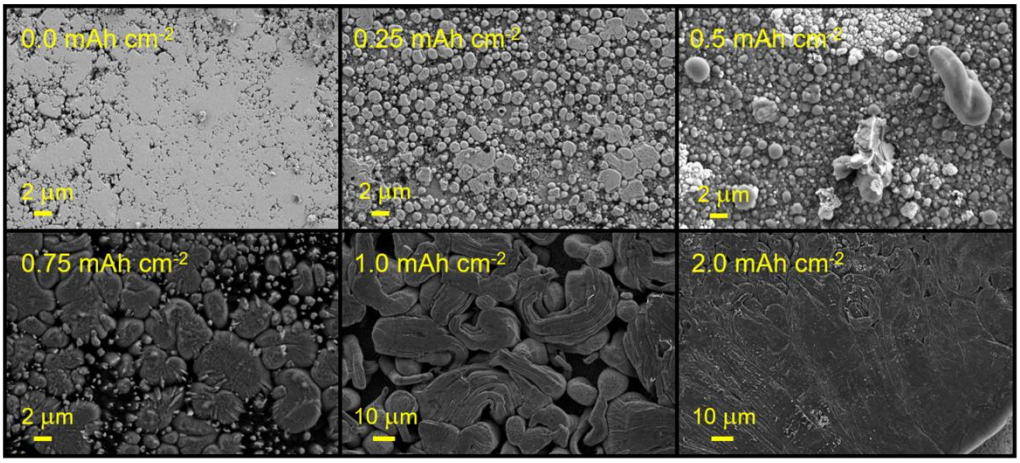


Figure 5.17: Top-view SEMs of the interlayer following removal of the current collector. Each panel shows a separate cell arrested at a different point in charge; after 0.0 mA·h/cm^2, 0.25 mA·h/cm^2, 0.5 mA·h/cm^2, 0.75 mA·h/cm^2, 1.0 mA·h/cm^2 and 2.0 mA·h/cm^2

silver nanolayer follows the highly porous surface morphology of the Li_6PS_5Cl electrolyte that was used as the substrate during the sputtering process. After having moved 0.25 mA·h/cm^2, the silver no longer has a film-like structure, but instead globules of Ag-Li alloy are observed covering the surface. As more charge is passed, these globules seem to increase in size and several much larger globules are observed. After having moved 0.75 mA·h/cm^2, the morphology appears different once again, with the layer becoming increasingly dense and darkening in colour, perhaps indicative of the increasing Li content in the Ag-Li alloy. At 1.0 mA·h/cm^2 the Ag-Li alloy covers most but not all of the solid electrolyte surface. Finally, after moving 2.0 mA·h/cm^2, a dense layer of Ag-Li is observed across the whole surface.

Comparing the morphology of this Ag-Li phase to the morphology of Li nucleated at the graphite/current collector interface (Figure 5.10a) demonstrates one clear advantage of the Ag thin-film interlayer. Whereas Li nucleated at a graphite/current collector interface is highly inhomogeneous growing in columns or webs, growth of the Ag-Li layer as it lithiates is considerably more homogeneous, eventually forming a highly dense layer. A homogeneous, dense anode layer is decidedly preferable over an inhomogeneous layer, as

inhomogeneity can lead to concentrated local currents during battery charge and discharge, potentially contributing to degradation and failure of the cell over multiple cycles.

So why are thin-film silver interlayers not considered to be solutions that enable high-performance Li-free anode solid-state batteries? Although silver interlayers do improve the homogeneity of the Li stored on charge, they do nothing to overcome the severe limitation of charging rate associated with Li metal anode cells. Whereas graphite interlayer cells are able to charge at a high rate of 2.0 mA/cm^2 because the graphite interlayer acts as a physical barrier to dendrite growth, silver interlayer cells do not have this physical barrier and are therefore expected to be susceptible to cell failure.

5.4.5 Charging Silver-Carbon Interlayers

Composite Interlayer of Graphite and Silver Nanoparticles:

In the first instance, work focussed on replicating the silver-carbon composite interlayer published by researchers at Samsung.[199] A silver-graphite composite layer, composed of graphite particles and silver nanoparticles was sprayed onto a stainless-steel current collector and a cell was constructed as described in Section 5.3.1.1. The cell was charged, with the voltage profile shown in Figure 5.7d. In many of its features, the charging profile is similar to that of graphite, shown in Figure 5.7a and Figure 5.8, with the principal voltage plateaus observed at approximately 200 mV, 105 mV and 80 mV. However, the voltage profile of the composite differs to that of that graphite interlayer in a number of ways:

1. At the beginning of charge, rather than the voltage dropping rapidly to the first feature at 200 mV, the voltage instead drops to approximately 850 mV before falling more slowly to the first feature of the voltage profile at 200 mV. Just as in the silver interphase cell, this is thought to be indicative of the initial doping of the Ag nanoparticles with lithium, but without a significant structural transformation to

form a new Ag-Li alloy phase. It is also possible that some of this capacity is a result of degradation at the Li_6PS_5Cl/graphite interface.[285]

2. The voltage plateau at approximately 80 mV and the subsequent drop in cell voltage down to 0 V is extended over a greater capacity (approximately 0.125 $mA{\cdot}h/cm^2$ compared with 0.06 $mA{\cdot}h/cm^2$ of the pure graphite interlayer), indicating that some extra capacity is provided by the alloying of the silver nanoparticles. This fits with the *operando* XRD of the silver interlayer (Figure 5.14), which found that alloying to form the β-phase Ag-Li alloy (AgLi) occurred in this voltage range.
3. The combination of these two effects is that the total capacity range between the onset of charging and the cell reaching a potential of 0 V is much greater in the composite interlayer than in the graphite interlayer (0.31 $mA{\cdot}h/cm^2$ compared to 0.14 $mA{\cdot}h/cm^2$). This indicates that although many of the features of the charge curve resemble those of the graphite interlayer, it is clear that during the early stages of charging, the silver nanoparticles within the composite interlayer are also lithiating and storing capacity.

A pristine cell and a cell that had been charged to 2.0 $mA{\cdot}h/cm^2$ capacity were cross-sectioned as described previously and were imaged by SEM/EDX. The micrographs and EDX spectra associated with these cells are shown in Figure 5.18. EDX of the pristine interface (Figure 5.18a) shows some of the larger agglomerates of silver nanoparticles (turquoise) within the graphite layer (orange), which is well adhered to the Li_6PS_5Cl solid electrolyte (blue).

After charging the cell, it can be observed that a thick Ag-Li layer has formed at the interlayer/current collector interface (Figure 5.18b), which is in line with the observations of the researchers at Samsung described at the beginning of this chapter.[199] Also in agreement with their observations, little silver remains within the interlayer following

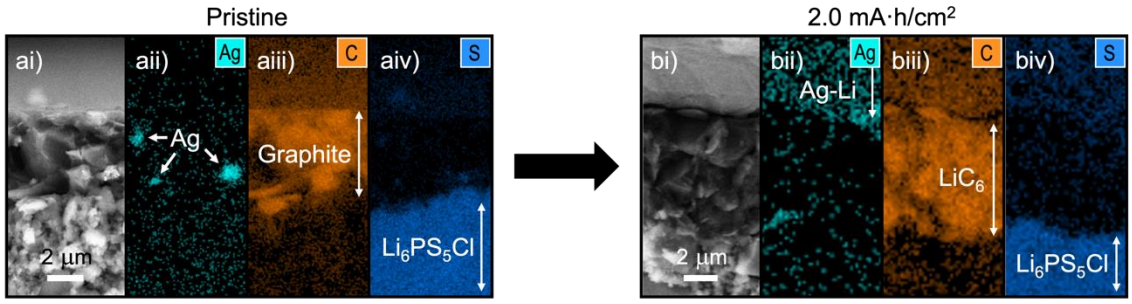


Figure 5.18: Cross-sectional SEM/EDX of a) the pristine Li_6PS_5Cl/graphite-silver nanoparticle interface and b) the Li_6PS_5Cl/ graphite-silver nanoparticle interface after charging, showing a layer of Ag-Li alloy behind the LiC_6 interphase. i), ii), iii) and iv) show the SE micrograph, the Ag EDX map (turquoise), the C EDX map (orange) and the S EDX map (blue) respectively.

charge, suggesting that the silver is mobile and can migrate from the interlayer to form the Ag-Li alloy layer at the interlayer/current collector interface. Some silver is observed at the solid electrolyte/graphite interface (Figure 5.18bii), possibly due to interphase formation between Li_6PS_5Cl and Ag-Li alloy, or because it does not have a pathway to migrate to the current collector interface. The exact mechanism of this migration is undetermined and is discussed later in this chapter.

It can be concluded that we are able to charge a silver-graphite composite interlayer which shares many similarities with the silver-carbon composite interlayer described by researchers from Samsung. However, can we uncover more about the underlying charging mechanism for these composite interlayers, and can these learnings lead to better rational design of interlayers for faster charging Li-free anode solid-state batteries? To aid in answering these questions, a different assembly of graphite-silver composite interlayer was used to simplify the cell and aid in gaining fundamental understanding of the system.

Layered Graphite/Silver Composite Interlayers:

Two different layered approaches were used as model systems to investigate the fundamental aspects of charging. The cells are best described as; 1) Current Collector/Li/Li_6PS_5Cl/Graphite/Silver/Current Collector, which will be referred to as the

graphite/silver interlayer cell (Figure 5.7e); and 2) Current Collector/Li/Li_6PS_5Cl/Silver/Graphite/Current Collector, which will be referred to as the silver/graphite interlayer cell (Figure 5.7f).

The graphite/silver composite interlayer is key to understanding the charging mechanism of these cells for a number of reasons. Firstly, the layered geometry provides high surface areas of both graphite and silver, which enables better XRD pattern collection, particularly of the silver component, than the graphite/silver nanoparticle composite interlayer alternative. Therefore, *operando* XRD can be used to understand the phase transitions of both the graphite and the silver as they lithiate and the order in which they do so. Secondly, the layered geometry allows us to answer the question as to whether the silver component of the composite interlayer lithiates electrochemically or chemically, a question that will be returned to later.

The conclusion from examining the voltage profile of the first charge of the graphite-silver nanoparticle composite interlayer was that in the early stages of charge the graphite and silver lithiate simultaneously. The charging profile of the graphite/silver bilayer interlayer (Figure 5.19) is approximately similar. The voltage curve features that were assigned to the lithiation of the silver were observed to be more pronounced, and the total capacity passed before the cell voltage reached 0 V was higher, reflecting that there is a greater amount of silver in the layered cell than in the nanoparticle composite. *Operando* XRD of the cell, using a 2D detector to achieve a high time resolution, reveals that the charging process can be understood as follows:

1. As the cell potential falls from an initial value of approximately 2 V to the first change in gradient in the voltage profile at approximately 200 mV, the XRD patterns reveal a slight shift in the C_6 graphite peak at 26.5° to a lower angle, indicating lithiation without a structural transition, just as was observed for the

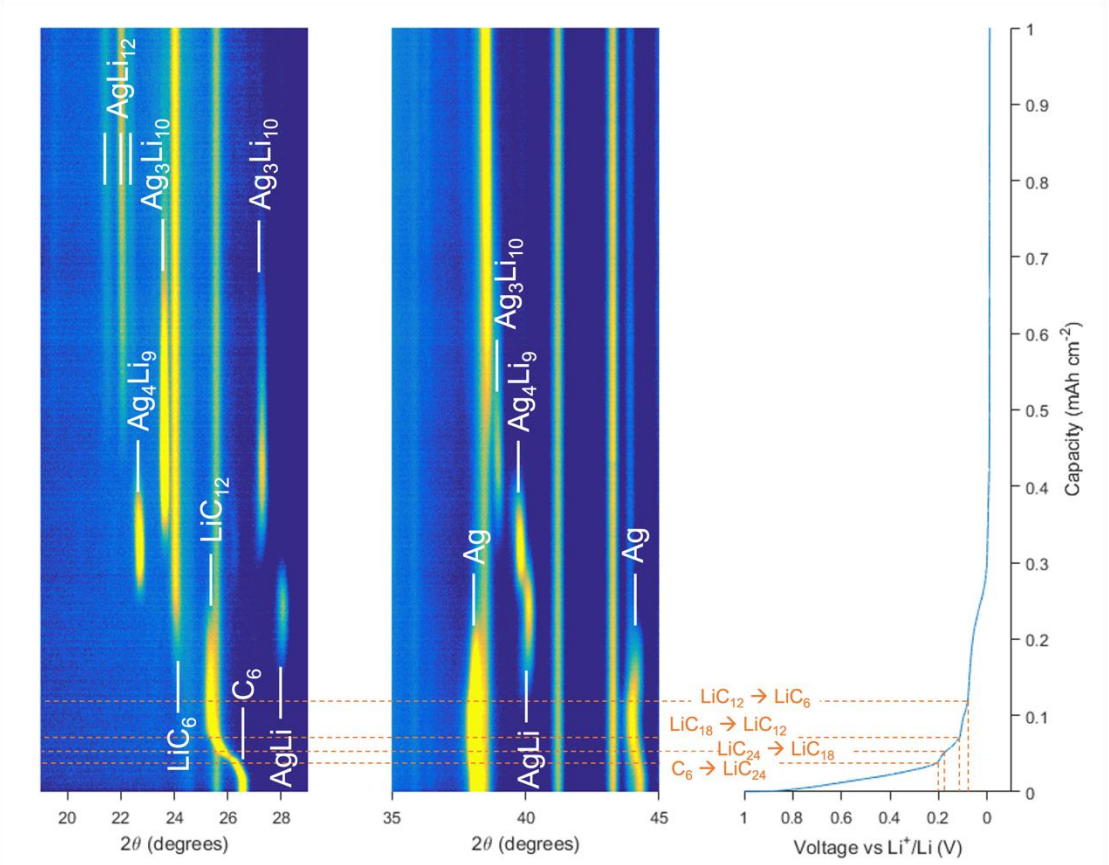


Figure 5.19: *Operando* XRD and corresponding electrochemistry of a graphite/silver interlayer cell. The left-hand and central panels show heat-maps in the 2θ regions of 21° - 29° and 35° - 45°, indicating changes in reflection intensity as the graphite intercalates and as the silver alloys with lithium. The right-hand panel shows the corresponding voltage profile. The cell was charged at room temperature at a rate of 50 μA/cm^2.

graphite interlayer in Section 5.4.3. In addition, there are slight shifts to lower angles of the two Ag peaks at 38° and 44.5°, just as was observed for the pure silver interlayer described in Section 5.4.4. One benefit of using the layered structure for this study is that it is known that there is no direct contact between the solid electrolyte and the silver layer. Therefore, it can be concluded that in this early stage of charge there is already enough Li mobility in the dilutely lithiated graphite phase for Li transport to occur across the graphite/silver interface to begin alloying with silver.

2. As more charge is passed, the cell potential reaches a feature in the voltage profile at 200 mV. Just as observed in the graphite interlayer cell, this is accompanied by

a discontinuity in the XRD pattern indicating a structural transition of the lithiated graphite (1L → 4L) to the more Li-rich LiC_{24} phase.

3. After passing more current, the cell potential continues to fall, passing through a discontinuity in gradient together with a new XRD peak at 25.5°, which is the LiC_{24} → LiC_{18} structural transition. As charge is passed, the potential falls to a gradient change in the voltage profile at approximately 105 mV potential vs Li^+/Li, accompanied by a discontinuity in the XRD pattern in which the lithiated graphite peak shifts to a lower angle of 25.25°, signalling a structural transition from LiC_{18} to LiC_{12} (3L → 2).
4. Moving more capacity results in a further drop in cell potential to a plateau in the voltage profile at approximately 80 mV. As predicted by the earlier data on charging of the graphite interlayer cell, this plateau is associated with a new XRD peak at approximately 24°, revealing a further change in the structure of the lithiated graphite phase from LiC_{12} to the phase of the fully lithiated structure, LiC_6 (2 → 1). In addition to this structural change in the lithiated graphite phase, a change is observed in the structure of the lithiated silver phase. Once the structural transition to LiC_6 takes place, new peaks indicative of the AgLi β-phase appear in parallel at 28° and 40°.
5. There is no change in the structure of the LiC_6 phase as charging continues. As more capacity is passed, only the Ag-Li phase changes in structure, firstly transitioning to Ag_4Li_9 as the cell potential falls below 0 V, and then transitioning to Ag_3Li_{10} and finally to $LiAg_{12}$ as more charge is passed, just as was observed when charging the pure silver metal interlayer, Section 5.4.4. Once again, these structural transitions are not associated with an observable change in cell voltage, with the cell potential remaining low and stable for the remainder of charge. It should be noted that in this

cell, the Ag-Li alloy phase reaches more lithiated phases than the silver-carbon composite interlayer cell described by Samsung. Their work used XRD to determine that the silver alloy has the Ag_4Li_9 phase when fully charged, in contrast to this cell which accesses the much more Li-rich $AgLi_{12}$ phase which has been reported in other silver-anode battery literature.[302] Operated in this way, composite silver-graphite interlayer cells can achieve extremely high anodic capacities without nucleating Li metal.

Due to restraints on the testing conditions of the *operando* XRD cell, these data were collected at room temperature rather than at 60 °C, which was the temperature used for the voltage profiles during charge of the cells shown in Figure 5.7. In addition, a lower charging rate of 50 $\mu A/cm^2$ was used to achieve a high time resolution.

Imaging Charge of the Graphite/Silver Composite Interlayer

As before, pristine and charged cells were cross-sectioned and analysed by SEM/EDX. The pristine cell (Figure 5.20a) shows that the components are discretely layered, with the silver thin-film (turquoise) clearly separated from the Li_6PS_5Cl electrolyte (blue) by an approximately 5 μm thick layer of graphite (orange) and all components intimately contacted together. Upon charge, the graphite layer and the Li_6PS_5Cl electrolyte remained intimately adhered and the silver thin-film has undergone a large volume expansion to form the thick $AgLi_{12}$ layer between the graphite layer and current collector (Figure 5.20b). It is evident that a graphite/silver bilayer shows the desired characteristics during the charging process, with Ag-Li formation occurring behind the protective graphite buffer layer and no evidence of Li nucleation at the Li_6PS_5Cl/graphite interface, indicating that this cell, under these conditions, will not suffer failure due to dendrite growth.

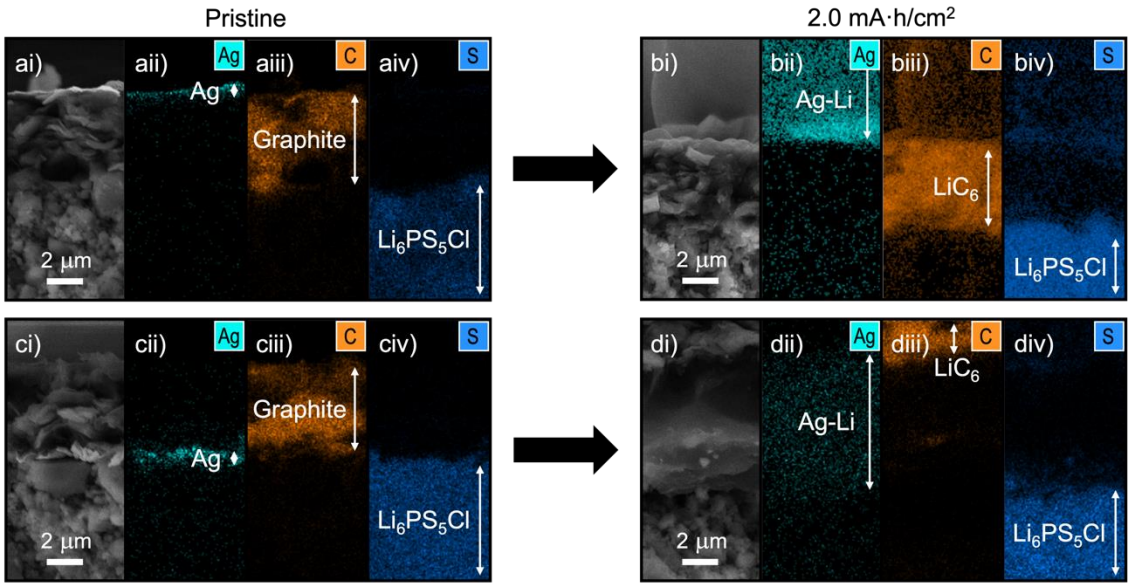


Figure 5.20: Cross-sectional SEM/EDX of a) the pristine Li_6PS_5Cl/graphite/silver interface; b) the Li_6PS_5Cl/graphite/silver interface after charging, showing a layer of Ag-Li alloy behind the LiC_6 interphase; c) the pristine Li_6PS_5Cl/silver/graphite interface and d) the Li_6PS_5Cl/silver/graphite interface after charging, showing a layer of Ag-Li alloy between the Li_6PS_5Cl electrolyte and graphite layer. i), ii), iii) and iv) show the SE micrograph, the Ag EDX map (turquoise), the C EDX map (orange) and the S EDX map (blue) respectively.

Top-view SEM/EDX reveals the benefits of silver within the interlayer. Figure 5.21 contrasts the graphite only interlayer with the silver/graphite bilayer. As discussed earlier, nucleation of Li metal at the graphite/current collector interface is highly inhomogeneous. A significant portion of the interface shows no Li metal deposition after moving 0.75 mA·h/cm^2 capacity, as indicated by the surface being dominated by the carbon signal from the graphite (Figure 5.21dii). Figure 5.21f reveals that even after having passed 2.0 mA·h/cm^2 capacity there is still not complete coverage of the graphite interlayer, with a high proportion uncovered (carbon signal visible – orange) and quite localised Li deposition (no EDX signal). When utilising the graphite/silver bilayer the morphology changes during charge are very different, with the silver layer undergoing similar morphological changes during alloying as were described for the silver interlayer in Section 5.4.4. In the early stages of charge, the silver layer breaks up, forming small globules of Ag-Li alloy that swell in size as more capacity is moved. After having moved 1.0 mA·h/cm^2

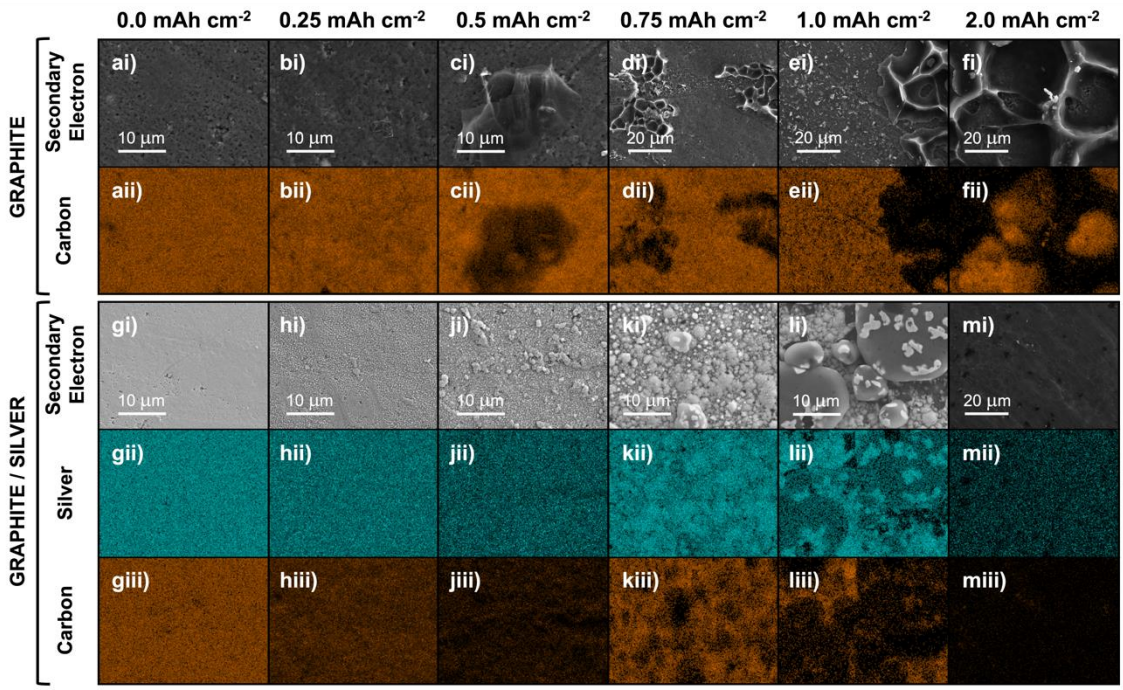


Figure 5.21: UPPER shows top-view SEM/EDX of the graphite interlayer after careful removal of the current collector after moving a capacity of a) 0.0 mA·h/cm^2; b) 0.25 mA·h/cm^2; c) 0.5 mA·h/cm^2; d) 0.75 mA·h/cm^2; e) 1.0 mA·h/cm^2 and f) 2.0 mA·h/cm^2. i) and ii) show SE micrographs and C EDX maps respectively.
LOWER shows top-view SEM/EDX of the graphite/silver interlayer after careful removal of the current collector after moving a capacity of g) 0.0 mA·h/cm^2; h) 0.25 mA·h/cm^2; j) 0.5 mA·h/cm^2; k) 0.75 mA·h/cm^2; l) 1.0 mA·h/cm^2 and m) 2.0 mA·h/cm^2. i), ii) and iii) show SE micrographs, Ag EDX maps and C EDX maps respectively.

capacity, large, dappled globules are observed to cover the graphite/current collector interface. SE micrographs show these globules to be composed of darker and lighter coloured regions. EDX reveals the globules to be two phases of Ag-Li alloy, with the larger darker regions being a Li-rich Ag-Li phase and the smaller lighter coloured regions being an Ag-rich Ag-Li phase (Figure 5.21l). After having passed 2.0 mA·h/cm^2 capacity, a dense layer of the darker coloured Li-rich Ag-Li alloy has formed across the graphite/current collector interface (Figure 5.21m). This is indicated by the extremely low carbon signal in the EDX, revealing that the graphite layer is fully covered, and the low but non-negligible silver signal, suggesting that the Ag-Li alloy formed is Li-rich, in agreement with the *operando* XRD which shows the phase to be the γ_3-phase, $AgLi_{12}$.

Mechanistic Understanding of the Graphite/Silver Composite Interlayer

The graphite/silver bilayer cell also offers a model system for better understanding the underlying electrochemistry and chemistry occurring within the carbon-silver composite anode during charge. Here, the model system is used to propose that lithiation of the silver within the carbon-silver composite occurs by a chemical reaction with lithiated graphite, rather than occurring electrochemically.

In a chemical reaction, electrons are transferred directly between reactants. However, in an electrochemical reaction, both electrons and ions must be transferred by separate electronically and ionically conducting circuits respectively. In this battery, the ionic circuit is the Li_6PS_5Cl electrolyte, and the electronic circuit is made up of the Li metal counter electrode, the cell current collectors and the external circuit and potentiostat. Both components of the interlayer (the silver and graphite layers) also belong to the electronic circuit, as both components have substantially higher electronic conductivities than they have Li^+ diffusivities.[303,304] In some literature, lithiated graphite is described as a mixed ion-electron conductor (MIEC).[305] However, it must be noted that although graphite's capacity to transport Li-ions is vital to its role within this cell, its electronic conductivity is orders of magnitude greater than its Li^+ diffusivity. During cell charge, the potentiostat drives a constant current in the electronic circuit, making electrons available for electrochemical reduction of Li-ions at the Li_6PS_5Cl/graphite interface and their intercalation into the graphite structure. Thus the electrochemical reaction front is at the Li_6PS_5Cl/graphite interface, not at the graphite/silver interface. As both materials are electronic conductors, there is no electric potential difference between the graphite and the silver, only a chemical potential difference. As such, the bilayer cell, in which there can be no contact between the silver and the Li_6PS_5Cl electrolyte, successfully demonstrates that

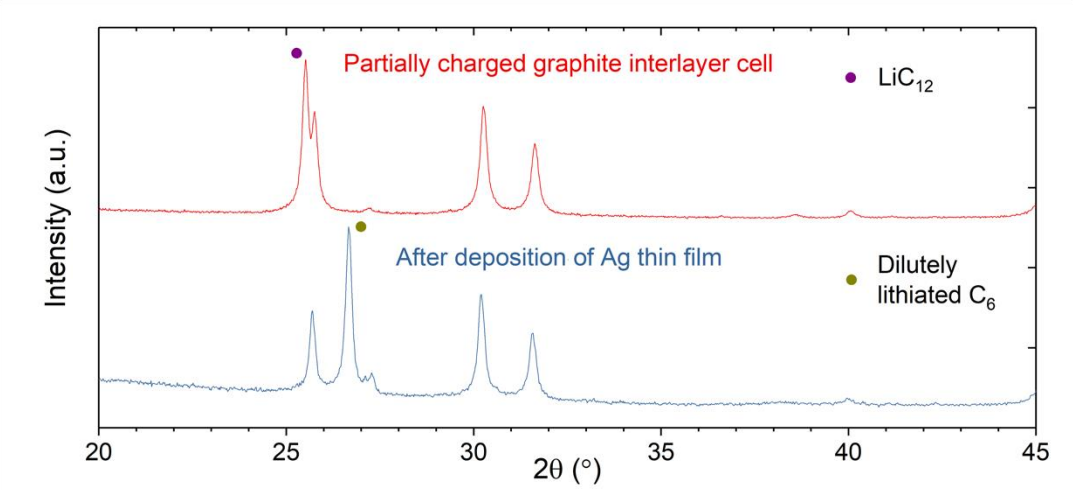


Figure 5.22: XRD patterns of a graphite interlayer after partial charge to form LiC_{12} (red), and after deposition of a 200 nm thin film of Ag on the LiC_{12} surface, resulting in partial delithiation of the graphite layer (blue). This demonstrates chemical reactivity between lithiated graphite phases and silver. Unlabelled reflections are from the Li_6PS_5Cl electrolyte.

the lithiation of the silver in the composite anode is due to chemical reactivity with the lithiated graphite phase, not by an electrochemically driven lithiation.

To further test this hypothesis, an experiment was conducted to determine whether lithiated graphite would react with silver to lithiate the silver phase in the absence of any electrochemistry. A partially lithiated graphite layer (LiC_{12}) was prepared by arresting a cell at the voltage determined in Figure 5.8. An XRD pattern of the layer was then collected to confirm the phase, Figure 5.22 (red). The layer was then mounted on a glass slide, placed within the PVD chamber and 200 nm layer of silver was sputtered over the surface. The sample was then removed, sealed under vacuum and heated to 60 °C (the temperature of cell charging throughout this chapter) for 2 h, followed by collection of an XRD pattern (blue). It is very clear that a chemical reaction has occurred. There is a significant change in the structure of the lithiated graphite, with LiC_{12} (peak at 25.5°) deintercalating to form a much more dilute phase of lithiated graphite (peak at 26.6°). Due to the low quantity of silver, no Ag reflection was observed at 38° in the XRD, however the delithiation of the

graphite phase would suggest that this is accompanied by a lithiation of silver by a chemical reaction.

The implication of this is significant. Whereas in an electrochemical reaction the rate of redox can be controlled by the current load, the rate of a chemical reaction cannot be driven in this way. This could lead to second order effects which could detrimentally affect the cell performance. For example, compare the composite interlayer to the graphite interlayer described earlier in this chapter. For the graphite interlayer, the rate of reduction of Li-ions at the Li_6PS_5Cl/graphite interface is determined by the flux of Li-ions to the interface driven by the current load. As discussed earlier, when the rate of Li^+ transport through the graphite layer exceeds the flux of Li-ions, Li^+ will be intercalated into the graphite structure and can eventually nucleate at the current collector interface. However, when the rate of Li-ion transport across the graphite layer is insufficient, Li-ions will instead reduce to nucleate as Li metal at the Li_6PS_5Cl/graphite interface. It is only the rate of Li^+ transport across the interlayer relative to the current load which determines the cell's critical current density i.e. there are no second order chemical effects. In the silver-graphite composite, the factors affecting cell failure are more complex. Just as with the graphite interlayer, in the composite interlayer it is again the rate of Li^+ transport across the graphite component of the composite relative to the ion flux which determines whether Li intercalates into the graphite interlayer or nucleates at the Li_6PS_5Cl/graphite interface, and this again sets the upper limit of current density for cell operation. However, what happens if the rate of Li^+ transport across the graphite layer exceeds the rate of Li^+ flux to the interface, but also exceeds the rate of chemical reaction between the lithiated graphite and silver? When the graphite interlayer is fully saturated with Li, if the rate of reaction between LiC_6 and Ag-Li is insufficient, Li-ions must still accept an electron to nucleate as Li metal because the rate of the

electrochemical reduction of Li-ions is fixed by the current load. This is shown schematically in Figure 5.23.

Previously in this chapter, no Li metal has been observed by SEM/EDX or by XRD when using the silver-graphite composite interlayer. It can therefore be concluded that under these conditions of cell cycling (0.1 mA/cm^2 at 60 °C under 2.5 MPa stack-pressure) the rate of chemical reactivity between lithiated graphite and Ag-Li is sufficient such that no Li metal nucleates at either interface. XRD and SEM/EDX give an indication of what happens when the cell is charged at higher rates such that the rate of silver alloying is insufficient. Figure 5.24a shows the XRD pattern of a cell that was charged at a higher rate of 1.5 mA/cm^2, arresting charge after passing 1.0 mA·h/cm^2 capacity (red). The *operando* XRD of the cell charged at 0.1 mA/cm^2 showed that the bilayer had formed the Li-rich phases LiC_6 and $AgLi_{12}$ after moving 1.0 mA·h/cm^2 (Figure 5.19), however these XRD

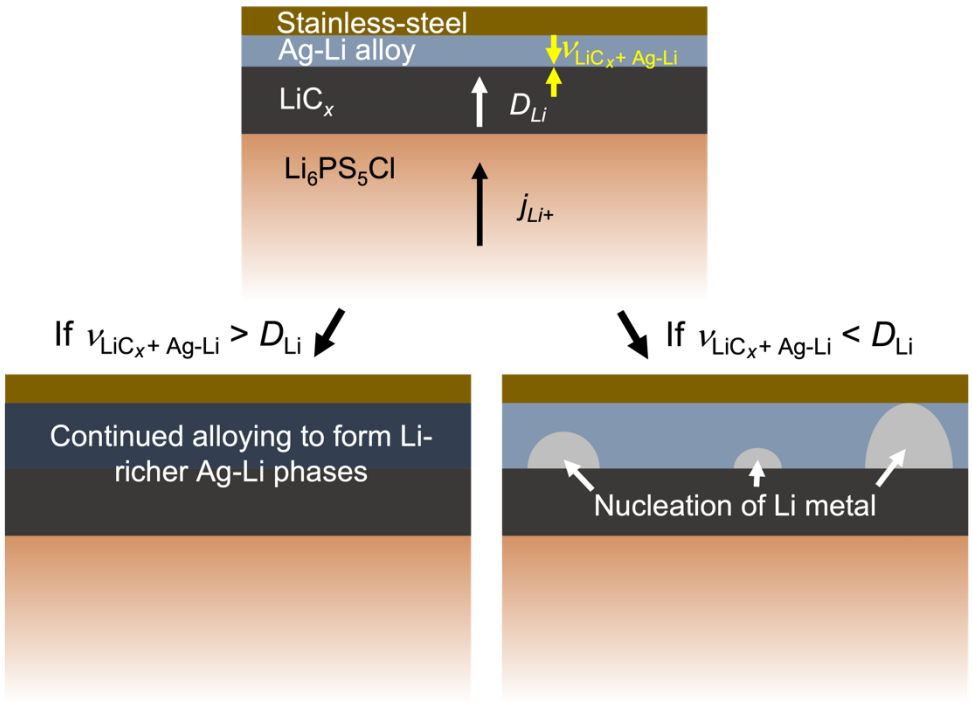


Figure 5.23: Schematic emphasising the importance of the rate of chemical reaction between lithiated graphite and Ag-Li, $v_{LiCx + Ag-Li}$. If this rate is insufficient, Li metal will nucleate at the lithiated graphite/Ag-Li interface (right).

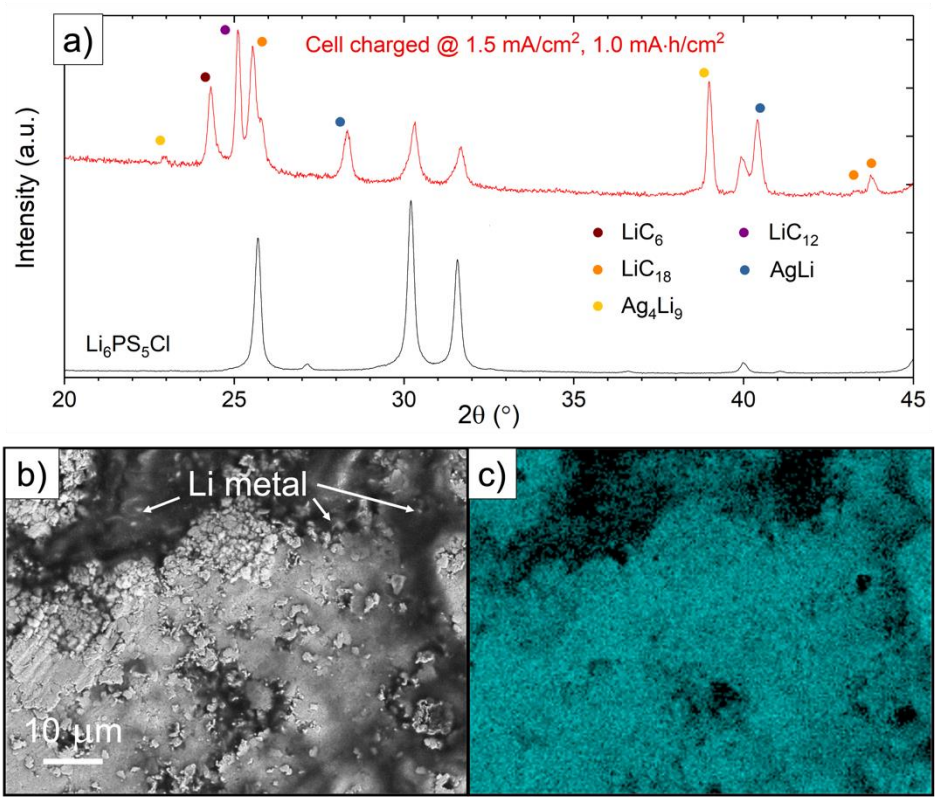


Figure 5.24: a) XRD patterns of Li_6PS_5Cl (black) and of the top surface of a cell charged at 1.5 mA/cm^2 for 1.0 mA·h/cm^2 at 60 ºC (red). The pattern shows the presence of LiC_6, LiC_{12}, LiC_{18}, AgLi and Ag_4Li_9 in the charged bilayer. b) SE micrograph showing a top-view of the charged graphite/silver bilayer after careful removal of the current collector and c) the corresponding Ag EDX map. The absence of Ag signal indicates the presence of Li metal.

data show a less homogeneous mix including Li-poorer phases LiC_{12}, LiC_{18}, AgLi and Ag_4Li_9. Since these phases are Li-poorer after moving the same capacity, there must be some unaccounted-for Li, the origin of which is identified by top-view SEM/EDX of the cell (Figure 5.24b-c). In addition to lighter-coloured Ag-Li alloy phases, darker precipitants with an absence of Ag in EDX are observed, particularly nearer the edges of the electrode. This suggests that at high rates of charge, as well as alloying, there is Li metal nucleation at the interlayer/current collector interface.

It can therefore be concluded that chemical reactivity between lithiated graphite and silver can be rate limiting. However, positively, when this occurs Li metal nucleates at the current collector interface rather than the Li_6PS_5Cl interface, meaning that the graphite layer can

still act as a physical barrier towards dendrite growth. The downside is that, as discussed earlier, Ag-Li shows a propensity to grow more homogeneously than Li metal, so at high rates this could have a detrimental impact on cycling performance. The limiting rate of chemical reactivity between lithiated graphite and Ag-Li may have determined Samsung's choice of a composite interlayer utilising silver nanoparticles distributed within the carbon layer as opposed to a bilayer. In this design, the surface area between the silver nanoparticles and the carbon is maximised, minimising the rate limitation of chemical reactivity at this interface, and therefore reducing the chance of nucleation of Li metal rather than Ag-Li alloy formation.

Charge of the Silver/Graphite Composite Interlayer

For completeness, a silver/graphite bilayer in which the silver is in direct contact with the Li_6PS_5Cl electrolyte, and the graphite is in direct contact with the current collector, was also investigated. The voltage profile of the first charge appears approximately similar to those of the graphite/silver bilayer and the graphite-silver nanoparticle composite, Figure 5.7f. Cross-sectional SEM/EDX of the cell before and after charge shows that in the pristine cell (Figure 5.21c-d) the Li_6PS_5Cl layer (blue) and the graphite layer (orange) are separated by an approximately 200 nm thin-film of silver (turquoise). On charge, the Ag layer alloys, forming a thick, dense layer of Ag-Li alloy separating the Li_6PS_5Cl electrolyte and graphite layer. Clearly, this is not the desired behaviour on charge as the Ag-Li alloy interfaces directly with the ceramic electrolyte and therefore the cell is at risk of failure due to dendrite growth at high rates of charge.

Interestingly, XRD of the cell following charge reveals not only that the silver has alloyed to form Ag-Li, but also that the graphite layer has lithiated. This is consistent with the visual change in the graphite layer's colour from black to a gold colour. This indicates that not only can lithiated graphite chemically react with silver to form an Ag-Li alloy, but the

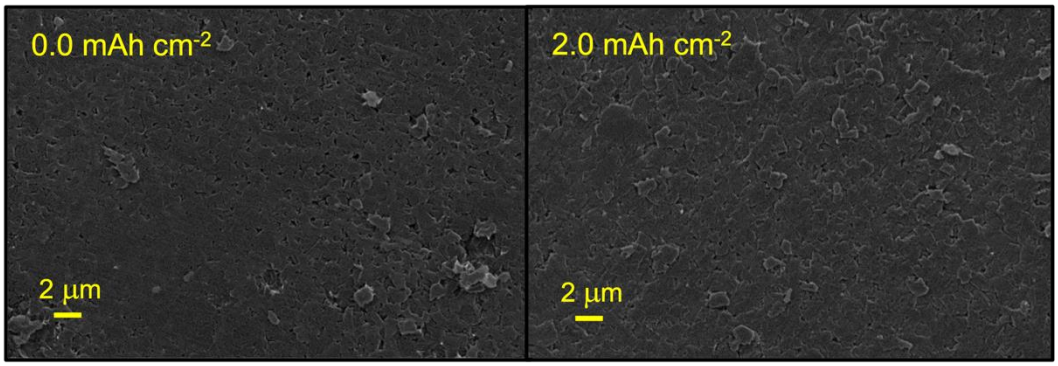


Figure 5.25: SE micrographs showing the top-view of silver/graphite bilayers after careful removal of the current collector. The micrographs show no evidence of Li nucleation at the graphite/current collector interface after charging the cell.

reverse is possible, with the electrochemically formed Ag-Li alloy reacting with the graphite layer to lithiate it. However, the cross-sectional SEM shows that after Li-Ag alloy formation and lithiation of the graphite layer, there does not appear to be any nucleation of Li metal at the graphite/current collector interface. This is supported by top-down SEM after arresting cells at various stages of the charging process, showing no indication of any Li metal deposition above the graphite layer at the interface with the current collector (Figure 5.25). Instead, it appears that as further capacity is moved, the Ag-Li continues to accommodate more Li, forming highly Li-rich Ag-Li phases.

5.5 Conclusions

In this chapter it has been demonstrated that carbon and carbon-silver composite interlayers can protect the solid electrolyte from Li dendrite growth, enabling higher rates of charge. An investigation of carbon-based interlayers revealed the crucial role of Li^+ transport across the interlayer, which depends on the Li^+ diffusivity, to its role in preventing Li metal nucleation at the solid electrolyte interface. Use of a carbon with higher Li^+ diffusivity, a thinner interlayer, and a higher operating temperature favoured higher rates of Li^+ transport across the carbon interlayer and thus enabled charging at higher current densities without cell failure.

Investigation of a silver interlayer and graphite-silver composite interlayers gave important insights into the role of silver in facilitating the formation of a homogeneous Ag-Li alloy layer rather than inhomogeneous islands of Li metal. O*perando* XRD and SEM revealed the structural and morphological changes that occur within the interlayer on charge and use of a model system demonstrated that lithiation of the silver in a graphite-silver composite proceeds by chemical reactivity between lithiated graphite and silver, rather than occurring as an electrochemically driven reaction. This work has helped to elucidate some of the fundamental mechanics of what is happening to graphite and silver-graphite composite interlayers during charge, and opens interesting avenues for future research that could further improve the performance of such interlayers.

5.6 Future Direction of Interlayer Research

Methods for Achieving Higher Critical Current Densities during Charge

Given that the critical current densities of carbon-containing interlayers are determined by the rate of Li^+ transport across the carbon layer relative to the flux of Li^+ to the solid-electrolyte/interlayer interface, increasing the rate of Li^+ diffusion in the carbon is vital to achieving higher charging rates. Some approaches to this have been investigated in this chapter, but a more in-depth study on these aspects could unlock the ability to charge SSBs at higher rates. Two methods that were touched on in this chapter are decreasing the thickness of the carbon layer and increasing the cell operating temperature. Further decreasing the thickness of the graphite layer will require research into manufacturing methods such that as the layer is thinned it remains pin-hole free, which is critical to its efficacy. Investigating the effect of increasing the cell operating temperature can be achieved utilising the manufacturing process and testing outlined in this chapter, however higher operating temperatures become impractical for use in EVs, making this a less attractive route to increasing the cell critical current density.

A further approach to increasing Li^+ transport across the carbon interlayer has also already been touched on in this chapter, and that is increasing the Li^+ diffusivity of the interlayer by tailoring the choice of carbon. As shown in Section 5.4.3, use of a carbon black with a very low Li^+ diffusivity resulted in cell failure even at a very low rate of 0.1 mA/cm^2, whereas use of a carbon graphite with a higher Li^+ diffusivity enables charging rates of 2 mA/cm^2. Not all carbons are created equal, with the many different types of carbon displaying different Li^+ diffusivities. To complicate matters further, intercalation carbons have different Li^+ diffusivities depending on the extent of lithiation.[303] The simple comparison between a lower Li^+ diffusivity carbon and a higher Li^+ diffusivity carbon in this chapter is far from an exhaustive exploration, and fundamental study into Li^+ diffusivity of various carbons across their composition ranges could be used to identify the most highly permeable interlayer, enabling the highest charging critical current density. In this area there is ample opportunity to transfer learnings from fast charging of carbon anodes in conventional liquid electrolyte batteries. For example, a recent study by Dasgupta and co-workers suggests that addition of hard carbon to a graphite anode can enable higher rates of charge by increasing the Li^+ diffusivity in the anode.[306]

Alternative Metal Alloys

This chapter has revealed that the key role of silver in the carbon-silver composite anodes is to facilitate the formation of a homogeneous layer of Ag-Li alloy during charge. However, using silver within a battery is not highly desirable due to its high raw material cost and its high relative molecular mass which can lead to low cell gravimetric energy density. A wide variety of alloying metals have been described in the literature, both for solid-state batteries and conventional Li-ion batteries, and many of these could give improvements over silver with regards to cost and/or relative molecular mass. Examples include Mg, Al, Si, Zn and Sn.[307,308] Exploration of deployment of these metals in carbon-

metal composite interlayers and comparison to the carbon-silver composite interlayer could prove a fruitful area of further study. However, other factors, such as the large volume changes of some of these materials, will also need to be considered.[154,309,310]

What is more, as discussed in this chapter there is still no consensus on the mechanism by which silver or other metal nanoparticles migrate out of the carbon interlayer to form a Li alloy at the current collector interface during charge. Understanding of this mechanism could lead to improved interlayer design and may inform which alternative metal alloys are suitable for use in carbon-metal nanoparticle interlayers.

Fundamentals of Discharge of Carbon-Metal Composite Interlayers

Chapters 3 and 4 highlighted that dendrite formation during charge is not the only important failure mechanism of SSBs, and that formation of voids during discharge also leads to cell failure and is perhaps even more limiting. Given that the carbon interlayer is the only component in direct contact with the solid electrolyte on the anode side, will this prevent cell failures during discharge? The study by researchers at Samsung might suggest that this is the case, as they successfully cycle a full cell utilising the carbon-silver composite anode at 3.4 mA/cm^2 for 1000 cycles, achieving 99.8 % capacity retention.[199] However, whilst the carbon layer may provide a physical barrier against void formation, the composite anode may not be a guarantee of failure-free discharge. For example, both graphite and Ag-Li will undergo volume contractions as they delithiate. The graphite volume contraction is not severe, contracting by 13.2 % on deintercalation.[288,289,311] However, over multiple cycles this has the potential to lead to SE/graphite interface delamination or cracking within the graphite layer, as has been observed in related studies.[285] The Ag-Li alloy undergoes a much more severe volume contraction upon delithiation, in the order of 100 %.[312] This too could lead to cell failure due to delamination between the Ag-Li layer and the graphite layer during discharge. Replacement of Ag with an alternative alloying material such as Si or Sn

could lead to more severe mechanical degradation of this kind, with these Li alloys undergoing much greater volume expansions/contractions of approximately 300 % each.[154,313] As such, a detailed understanding of the mechanism of delithiation of the carbon-metal composite interlayers is required, as is a thorough understanding of the mechanisms of failure during discharge.

6 Conclusions and Outlook

Higher rates of solid-state battery charge and discharge must be realised before deployment in applications such as electric vehicles. However, the rate of charge is limited by the penetration of dendrites through the inorganic solid electrolyte, and the rate of discharge is severely limited by void formation at the metal anode/solid electrolyte interface even at relatively low current densities.

Chapters 3 and 4 of this thesis have focussed on understanding voiding during stripping and have explored methods to increase the critical currents at which voids are observed to form. Work previous to this thesis has established that voids form at and above a critical current where the flux of ions away from the interface exceeds the mass-transport of metal atoms to the interface, and that the mechanisms by which metal atoms can be transported to the interface are by self-diffusion and plastic deformation (in particular by power-law creep) within the metal anode. Therefore, the critical current for voiding should be increased by approaches that increase the self-diffusion or creep within the metal anode.

Chapter 3 investigated voiding in at the Na/Na-β''-Alumina interface. Since the self-diffusion coefficient of Na is higher than that of Li and, more importantly, the propensity of Na to creep under pressure is much greater, Na anodes might be expected to enable higher critical currents for voiding than Li anodes, and higher stack-pressures should enable higher critical currents for voiding by increasing creep. These hypotheses are borne out in the results, which find that the critical current for voiding is strongly pressure dependent, and that a high, stable discharge rate of 2.5 mA/cm^2 is enabled under stack-pressures of > 9 MPa at room temperature. The Na/Na-β''-Alumina interface also proves to be a useful model system for understanding the fundamentals of how voids evolve and grow through successive strippings and platings of the Na anode. The higher X-ray attenuation of Na

(relative to Li) enables clear resolution of voids by X-ray computed micro-tomography and *in-situ* experiments tracking voids during cycling reveal mechanistic insights into this type of failure.

Chapter 4 continues to investigate voiding, this time the temperature dependence of voiding at the Li/Li_6PS_5Cl interface is investigated. Just as for the pressure dependence in Chapter 3, elevated temperatures are anticipated to increase the critical current for voiding as it increases both self-diffusion and creep of Li. This hypothesis is borne out in the results. Under a stack-pressure of 1 MPa, increasing the cell temperature from 25 °C to 80 °C was observed to increase the critical current for voiding from < 0.25 mA/cm^2 to > 0.5 mA/cm^2, but perhaps more significantly under a stack-pressure of 5 MPa the same increase in temperature was observed to increase the critical current for voiding from < 1.0 mA/cm^2 to > 2.5 mA/cm^2, i.e. application of a moderately elevated stack-pressure of 5 MPa and a moderately elevated temperature of 80 °C was observed to increase the rate at which a cell can be stably, reversibly discharged by an order of magnitude relative to cycling at room-temperature under 1 MPa stack-pressure.

Critical currents for voiding on stripping can be prohibitively low. Indeed, they are often even more limiting than the more-heralded critical current for dendrite growth on plating. Taken together, the results of Chapters 3 and 4 are of significance. Not only are the mechanics of void formation better understood, but three methods for mitigating void formation are explored. These are switching from a Li anode to a Na anode, increasing the stack-pressure on the cell and increasing the operating temperature of the cell. Whilst these methods, particularly in combination, have proved successful at enabling current densities approaching practical requirements of several mA/cm^2, the practical applicability of these methods is in question. The theoretical capacity of Na anodes is considerably lower than

for Li anodes, and application of high stack-pressures or elevated operating temperatures will require additional non-active pack components, adding additional expense and sacrificing gains in gravimetric and volumetric energy density. Therefore, further research is required in this area to find approaches to enable stable discharge at high rates without necessitating prohibitively challenging operating conditions.

Previous research and the results presented in this thesis suggest that a carbon-based interlayer can protect the solid electrolyte against Li dendrite penetration, increasing the critical current for dendrite growth. In Chapter 5, new insights into the charging mechanism of these interlayers were revealed. Whether the interlayer could successfully protect against dendrite growth was determined to be dependent on whether Li metal nucleates at the current collector interface (protecting against dendrites) or at the solid electrolyte interface (offering no protection), which is dependent on the rate of transport of Li^+ across the interlayer. Factors such as using a carbon with a higher Li^+ diffusivity, a thinner interlayer and higher operating temperature were all determined to enable higher rates of dendrite-free charge.

Previous research by researchers from Samsung had added silver nanoparticles to a carbon interlayer, achieving excellent performance. Chapter 5 also explored the role of silver in such interlayers, determining that formation of a Li-rich Ag-Li alloy at the current collector interface led to an extremely favourable, homogeneous layer, whereas when no silver was present inhomogeneous Li nucleation was observed, potentially decreasing the cyclability of the cell. *Operando* XRD and model systems were used to gain insights into the mechanism of charging graphite-silver composite interlayers, revealing that charge proceeded by electrochemical lithiation of the graphite followed by chemical reaction between the lithiated graphite and the silver to form an Ag-Li alloy.

Important questions remain to be answered to fully assess the full potential of carbon and carbon-silver composite interlayers. Firstly, a detailed study on the mechanism and rate capability of discharge must be carried out, in particular to determine whether these interlayers have the potential to mitigate the formation of voids at high rates of discharge as well the penetration of dendrites on charge. Going forward it will also be important to study alternative alloying metals to silver, as cheaper, lower density alternatives may prove to be more readily deployable in real devices.

7 References

(1) Masson-Delmotte, V.; Zhai, P.; Pirani, A.; Connors, S. L.; Péan, C.; Berger, S.; Caud, N.; Chen, Y.; Goldfarb, L.; Gomis, M. I.; et al. *IPCC, 2021: Summary for Policymakers*; 2021. https://doi.org/10.1260/095830507781076194.

(2) UK Government. Government takes historic step towards net-zero with end of sale of new petrol and diesel cars by 2030.

(3) The White House. Statements on the Biden Administration's Steps to Strengthen American Leadership on Clean Cars and Trucks. 2021.

(4) Trahey, L.; Brushett, F. R.; Balsara, N. P.; Ceder, G.; Cheng, L.; Chiang, Y. M.; Hahn, N. T.; Ingram, B. J.; Minteer, S. D.; Moore, J. S.; et al. Energy Storage Emerging: A Perspective from the Joint Center for Energy Storage Research. *Proc. Natl. Acad. Sci. U. S. A.* **2020**, *117* (23), 12550–12557. https://doi.org/10.1073/pnas.1821672117.

(5) Kuhn, H.; Seitz, A.; Lorenz, L.; Isikveren, A. T.; Sizmann, A. Progress and Perspectives of Electric Air Transport. *28th Congr. Int. Counc. Aeronaut. Sci. 2012, ICAS 2012* **2012**, *6* (September), 4886–4899.

(6) Browne, N.; Bikal, P. South Australia's Power Sector: Renewables, Batteries and the Future Role of Gas. *APPEA J.* **2018**, *58*, 505–507.

(7) Armand, M.; Tarascon, J. M. Building Better Batteries. *Nature* **2008**, *451* (7179), 652–657. https://doi.org/10.1038/451652a.

(8) Crabtree, G. The Coming Electric Vehicle Transformation. *Science (80-.).* **2019**, *366* (6464), 422–424. https://doi.org/10.1126/science.aax0704.

(9) Tian, Y.; Zeng, G.; Rutt, A.; Shi, T.; Kim, H.; Wang, J.; Koettgen, J.; Sun, Y.; Ouyang, B.; Chen, T.; et al. Promises and Challenges of Next-Generation "beyond Li-Ion" Batteries for Electric Vehicles and Grid Decarbonization. *Chem. Rev.* **2021**, *121* (3), 1623–1669. https://doi.org/10.1021/acs.chemrev.0c00767.

(10) Albertus, P.; Anandan, V.; Ban, C.; Balsara, N.; Belharouak, I.; Buettner-Garrett, J.; Chen, Z.; Daniel, C.; Doeff, M.; Dudney, N. J.; et al. Challenges for and Pathways toward Li-Metal-Based All-Solid-State Batteries. *ACS Energy Lett.* **2021**, *6* (4), 1399–1404. https://doi.org/10.1021/acsenergylett.1c00445.

(11) The Royal Swedish Academy of Sciences. Press release: The Nobel Prize in Chemistry 2019 https://www.nobelprize.org/prizes/chemistry/2019/press-release/ (accessed Aug 23, 2021).

(12) Goodenough, J. B. How We Made the Li-Ion Rechargeable Battery: Progress in Portable and Ubiquitous Electronics Would Not Be Possible without Rechargeable Batteries. John B. Goodenough Recounts the History of the Lithium-Ion Rechargeable Battery. *Nat. Electron.* **2018**, *1* (3), 204. https://doi.org/10.1038/s41928-018-0048-6.

(13) Xie, J.; Lu, Y. C. A Retrospective on Lithium-Ion Batteries. *Nat. Commun.* **2020**, *11* (1), 9–12. https://doi.org/10.1038/s41467-020-16259-9.

(14) Broussely, M.; Biensan, P.; Bonhomme, F.; Blanchard, P.; Herreyre, S.; Nechev, K.; Staniewicz, R. J. Main Aging Mechanisms in Li Ion Batteries. *J. Power Sources* **2005**, *146* (1–2), 90–96. https://doi.org/10.1016/j.jpowsour.2005.03.172.

(15) Xu, K. Nonaqueous Liquid Electrolytes for Lithium-Based Rechargeable Batteries. *Chem. Rev.* **2004**, *104* (10), 4303–4417. https://doi.org/10.1021/cr030203g.

(16) Liu, X.; Yin, L.; Ren, D.; Wang, L.; Ren, Y.; Xu, W.; Lapidus, S.; Wang, H.; He, X.; Chen, Z.; et al. In Situ Observation of Thermal-Driven Degradation and Safety Concerns of Lithiated Graphite Anode. *Nat. Commun.* **2021**, *12* (1). https://doi.org/10.1038/s41467-021-24404-1.

(17) Ulvestad, A. A Brief Review of Current Lithium Ion Battery Technology and Potential Solid State Battery Technologies. **2018**. https://doi.org/https://arxiv.org/abs/1803.04317.

(18) Placke, T.; Kloepsch, R.; Dühnen, S.; Winter, M. Lithium Ion, Lithium Metal, and Alternative Rechargeable Battery Technologies: The Odyssey for High Energy Density. *J. Solid State Electrochem.* **2017**, *21* (7), 1939–1964. https://doi.org/10.1007/s10008-017-3610-7.

(19) Cheng, X. B.; Zhang, R.; Zhao, C. Z.; Zhang, Q. Toward Safe Lithium Metal Anode in Rechargeable Batteries: A Review. *Chem. Rev.* **2017**, *117* (15), 10403–10473. https://doi.org/10.1021/acs.chemrev.7b00115.

(20) Blomgren, G. E. The Development and Future of Lithium Ion Batteries. *J. Electrochem. Soc.* **2017**, *164* (1), A5019–A5025. https://doi.org/10.1149/2.0251701jes.

(21) Jeong, S. K.; Seo, H. Y.; Kim, D. H.; Han, H. K.; Kim, J. G.; Lee, Y. B.; Iriyama, Y.; Abe, T.; Ogumi, Z. Suppression of Dendritic Lithium Formation by Using Concentrated Electrolyte Solutions. *Electrochem. commun.* **2008**, *10* (4), 635–638. https://doi.org/10.1016/j.elecom.2008.02.006.

(22) Camacho-Forero, L. E.; Smith, T. W.; Balbuena, P. B. Effects of High and Low Salt Concentration in Electrolytes at Lithium-Metal Anode Surfaces. *J. Phys. Chem. C* **2017**, *121* (1), 182–194. https://doi.org/10.1021/acs.jpcc.6b10774.

(23) Yoon, H.; Howlett, P. C.; Best, A. S.; Forsyth, M.; MacFarlane, D. R. Fast Charge/Discharge of Li Metal Batteries Using an Ionic Liquid Electrolyte. *J. Electrochem. Soc.* **2013**, *160* (10), A1629–A1637. https://doi.org/10.1149/2.022310jes.

(24) Togasaki, N.; Momma, T.; Osaka, T. Enhanced Cycling Performance of a Li Metal Anode in a Dimethylsulfoxide-Based Electrolyte Using Highly Concentrated Lithium Salt for a Lithium-Oxygen Battery. *J. Power Sources* **2016**, *307*, 98–104. https://doi.org/10.1016/j.jpowsour.2015.12.123.

(25) Gong, C.; Pu, S. D.; Gao, X.; Yang, S.; Liu, J.; Ning, Z.; Rees, G. J.; Capone, I.; Pi, L.; Liu, B.; et al. Revealing the Role of Fluoride-Rich Battery Electrode Interphases by Operando Transmission Electron Microscopy. *Adv. Energy Mater.* **2021**, *11* (10). https://doi.org/10.1002/aenm.202003118.

(26) Heine, J.; Hilbig, P.; Qi, X.; Niehoff, P.; Winter, M.; Bieker, P. Fluoroethylene Carbonate as Electrolyte Additive in Tetraethylene Glycol Dimethyl Ether Based Electrolytes for Application in Lithium Ion and Lithium Metal Batteries. *J. Electrochem. Soc.* **2015**, *162* (6), A1094–A1101. https://doi.org/10.1149/2.0011507jes.

(27) Sano, H.; Sakaebe, H.; Matsumoto, H. Observation of Electrodeposited Lithium by Optical Microscope in Room Temperature Ionic Liquid-Based Electrolyte. *J. Power Sources* **2011**, *196* (16), 6663–6669. https://doi.org/10.1016/j.jpowsour.2010.12.023.

(28) Guo, J.; Wen, Z.; Wu, M.; Jin, J.; Liu, Y. Vinylene Carbonate-$LiNO_3$: A Hybrid Additive in Carbonic Ester Electrolytes for SEI Modification on Li Metal Anode. *Electrochem. commun.* **2015**, *51*, 59–63. https://doi.org/10.1016/j.elecom.2014.12.008.

(29) Janek, J.; Zeier, W. G. A Solid Future for Battery Development. *Nat. Energy* **2016**, *1* (9), 16141. https://doi.org/10.1038/nenergy.2016.141.

(30) Xiao, Y.; Wang, Y.; Bo, S. H.; Kim, J. C.; Miara, L. J.; Ceder, G. Understanding Interface Stability in Solid-State Batteries. *Nat. Rev. Mater.* **2020**, *5* (2), 105–126. https://doi.org/10.1038/s41578-019-0157-5.

(31) Famprikis, T.; Canepa, P.; Dawson, J. A.; Islam, M. S.; Masquelier, C. Fundamentals of Inorganic Solid State Electrolytes for Batteries. *Nat. Mater.* **2019**. https://doi.org/10.1038/s41563-019-0431-3.

(32) Pervez, S. A.; Cambaz, M. A.; Thangadurai, V.; Fichtner, M. Interface in Solid-State Lithium Battery: Challenges, Progress, and Outlook. *ACS Appl. Mater. Interfaces* **2019**. https://doi.org/10.1021/acsami.9b02675.

(33) Krauskopf, T.; Richter, F. H.; Zeier, W. G.; Janek, J. Physicochemical Concepts of the Lithium Metal Anode in Solid-State Batteries. *Chem. Rev.* **2020**. https://doi.org/10.1021/acs.chemrev.0c00431.

(34) Ye, L.; Li, X. A Dynamic Stability Design Strategy for Lithium Metal Solid State Batteries. *Nature* **2021**, *593* (7858), 218–222. https://doi.org/10.1038/s41586-021-03486-3.

(35) Balaish, M.; Gonzalez-Rosillo, J. C.; Kim, K. J.; Zhu, Y.; Hood, Z. D.; Rupp, J. L. M. Processing Thin but Robust Electrolytes for Solid-State Batteries. *Nat. Energy* **2021**, *6* (3), 227–239. https://doi.org/10.1038/s41560-020-00759-5.

(36) Huang, K. J.; Ceder, G.; Olivetti, E. A. Manufacturing Scalability Implications of Materials Choice in Inorganic Solid-State Batteries. *Joule* **2021**, *5* (3), 564–580.

https://doi.org/10.1016/j.joule.2020.12.001.

(37) Wang, M. J.; Kazyak, E.; Dasgupta, N. P.; Sakamoto, J. Transitioning Solid-State Batteries from Lab to Market: Linking Electro-Chemo-Mechanics with Practical Considerations. *Joule* **2021**, *5* (6), 1371–1390. https://doi.org/10.1016/j.joule.2021.04.001.

(38) Bielefeld, A.; Weber, D. A.; Janek, J. Microstructural Modeling of Composite Cathodes for All-Solid-State Batteries. *J. Phys. Chem. C* **2019**, *123* (3), 1626–1634. https://doi.org/10.1021/acs.jpcc.8b11043.

(39) Miara, L.; Windmüller, A.; Tsai, C. L.; Richards, W. D.; Ma, Q.; Uhlenbruck, S.; Guillon, O.; Ceder, G. About the Compatibility between High Voltage Spinel Cathode Materials and Solid Oxide Electrolytes as a Function of Temperature. *ACS Appl. Mater. Interfaces* **2016**, *8* (40), 26842–26850. https://doi.org/10.1021/acsami.6b09059.

(40) Dück, G.; Naqash, S.; Finsterbusch, M.; Breuer, U.; Guillon, O.; Fattakhova-Rohlfing, D. Co-Sintering Study of $Na_{0.67}[Ni_{0.1}Fe_{0.1}Mn_{0.8}]O_2$ and NaSICON Electrolyte–Paving the Way to High Energy Density All-Solid-State Batteries. *Front. Energy Res.* **2021**, *9* (June), 0–9. https://doi.org/10.3389/fenrg.2021.689416.

(41) Ihrig, M.; Finsterbusch, M.; Tsai, C. L.; Laptev, A. M.; Tu, C. hao; Bram, M.; Sohn, Y. J.; Ye, R.; Sevinc, S.; Lin, S. kang; et al. Low Temperature Sintering of Fully Inorganic All-Solid-State Batteries – Impact of Interfaces on Full Cell Performance. *J. Power Sources* **2021**, *482* (August 2020), 228905. https://doi.org/10.1016/j.jpowsour.2020.228905.

(42) Koerver, R.; Aygün, I.; Leichtweiß, T.; Dietrich, C.; Zhang, W.; Binder, J. O.; Hartmann, P.; Zeier, W. G.; Janek, J. Capacity Fade in Solid-State Batteries: Interphase Formation and Chemomechanical Processes in Nickel-Rich Layered Oxide Cathodes and Lithium Thiophosphate Solid Electrolytes. *Chem. Mater.* **2017**, *29* (13), 5574–5582. https://doi.org/10.1021/acs.chemmater.7b00931.

(43) Conforto, G.; Ruess, R.; Schröder, D.; Trevisanello, E.; Fantin, R.; Richter, F. H.; Janek, J. Quantification of the Impact of Chemo-Mechanical Degradation on the Performance and Cycling Stability of NCM-Based Cathodes in Solid-State Li-Ion Batteries. *J. Electrochem. Soc.* **2021**, *168* (7), 070546. https://doi.org/10.1149/1945-7111/ac13d2.

(44) Zheng, F.; Kotobuki, M.; Song, S.; Lai, M. O.; Lu, L. Review on Solid Electrolytes for All-Solid-State Lithium-Ion Batteries. *J. Power Sources* **2018**, *389* (April), 198–213. https://doi.org/10.1016/j.jpowsour.2018.04.022.

(45) Wu, Z.; Xie, Z.; Yoshida, A.; Wang, Z.; Hao, X.; Abudula, A.; Guan, G. Utmost Limits of Various Solid Electrolytes in All-Solid-State Lithium Batteries: A Critical Review. *Renew. Sustain. Energy Rev.* **2019**, *109* (April), 367–385. https://doi.org/10.1016/j.rser.2019.04.035.

(46) Bielefeld, A.; Weber, D. A.; Janek, J. Modeling Effective Ionic Conductivity and

Binder Influence in Composite Cathodes for All-Solid-State Batteries. *ACS Appl. Mater. Interfaces* **2020**, *12* (11), 12821–12833. https://doi.org/10.1021/acsami.9b22788.

(47) Minnmann, P.; Quillman, L.; Burkhardt, S.; Richter, F. H.; Janek, J. Quantifying the Impact of Charge Transport Bottlenecks in Composite Cathodes of All-Solid-State Batteries. *J. Electrochem. Soc.* **2021**, *168* (4), 040537. https://doi.org/10.1149/1945-7111/abf8d7.

(48) Richards, W. D.; Miara, L. J.; Wang, Y.; Kim, J. C.; Ceder, G. Interface Stability in Solid-State Batteries. *Chem. Mater.* **2015**, *28*, 266–273. https://doi.org/10.1021/acs.chemmater.5b04082.

(49) Wenzel, S.; Leichtweiss, T.; Krüger, D.; Sann, J.; Janek, J. Interphase Formation on Lithium Solid Electrolytes - An in Situ Approach to Study Interfacial Reactions by Photoelectron Spectroscopy. *Solid State Ionics* **2015**, *278*, 98–105. https://doi.org/10.1016/j.ssi.2015.06.001.

(50) Pasta, M.; Armstrong, D.; Brown, Z. L.; Bu, J.; Castell, M. R.; Chen, P.; Cocks, A.; Corr, S. A.; Cussen, E. J.; Darnbrough, E.; et al. 2020 Roadmap on Solid-State Batteries. *J. Phys. Energy* **2020**, *2*, 0–52.

(51) Raj, R.; Wolfenstine, J. Current Limit Diagrams for Dendrite Formation in Solid-State Electrolytes for Li-Ion Batteries. *J. Power Sources* **2017**, *343*, 119–126. https://doi.org/10.1016/j.jpowsour.2017.01.037.

(52) Kalnaus, S.; Westover, A. S.; Kornbluth, M.; Herbert, E.; Dudney, N. J. Resistance to Fracture in the Glassy Solid Electrolyte Lipon. *J. Mater. Res.* **2021**, *36* (4), 787–796. https://doi.org/10.1557/s43578-020-00098-x.

(53) Monroe, C.; Newman, J. The Impact of Elastic Deformation on Deposition Kinetics at Lithium/Polymer Interfaces. *J. Electrochem. Soc.* **2005**, *152* (2), A396. https://doi.org/10.1149/1.1850854.

(54) Monroe, C.; Newman, J. Dendrite Growth in Lithium/Polymer Systems. *J. Electrochem. Soc.* **2003**, *150* (10), A1377. https://doi.org/10.1149/1.1606686.

(55) Wang, C.; Fu, K.; Kammampata, S. P.; McOwen, D. W.; Samson, A. J.; Zhang, L.; Hitz, G. T.; Nolan, A. M.; Wachsman, E. D.; Mo, Y.; et al. Garnet-Type Solid-State Electrolytes: Materials, Interfaces, and Batteries. *Chem. Rev.* **2020**, *120* (10), 4257–4300. https://doi.org/10.1021/acs.chemrev.9b00427.

(56) Wolfenstine, J.; Allen, J. L.; Read, J.; Sakamoto, J. Chemical Stability of Cubic $Li_7La_3Zr_2O_{12}$ with Molten Lithium at Elevated Temperature. *J. Mater. Sci.* **2013**, *48* (17), 5846–5851. https://doi.org/10.1007/s10853-013-7380-z.

(57) Zhu, Y.; He, X.; Mo, Y. Origin of Outstanding Stability in the Lithium Solid Electrolyte Materials: Insights from Thermodynamic Analyses Based on First-Principles Calculations. *ACS Appl. Mater. Interfaces* **2015**, *7* (42), 23685–23693. https://doi.org/10.1021/acsami.5b07517.

(58) Zhu, Y.; He, X.; Mo, Y. First Principles Study on Electrochemical and Chemical Stability of Solid Electrolyte-Electrode Interfaces in All-Solid-State Li-Ion Batteries. *J. Mater. Chem. A* **2016**, *4* (9), 3253–3266. https://doi.org/10.1039/c5ta08574h.

(59) Connell, J. G.; Fuchs, T.; Hartmann, H.; Krauskopf, T.; Zhu, Y.; Sann, J.; Garcia-Mendez, R.; Sakamoto, J.; Tepavcevic, S.; Janek, J. Kinetic versus Thermodynamic Stability of LLZO in Contact with Lithium Metal. *Chem. Mater.* **2020**, *32* (23), 10207–10215. https://doi.org/10.1021/acs.chemmater.0c03869.

(60) Sharafi, A.; Yu, S.; Naguib, M.; Lee, M.; Ma, C.; Meyer, H. M.; Nanda, J.; Chi, M.; Siegel, D. J.; Sakamoto, J. Impact of Air Exposure and Surface Chemistry on Li-$Li_7La_3Zr_2O_{12}$ Interfacial Resistance. *J. Mater. Chem. A* **2017**, *5* (26), 13475–13487. https://doi.org/10.1039/c7ta03162a.

(61) Sharafi, A.; Kazyak, E.; Davis, A. L.; Yu, S.; Thompson, T.; Siegel, D. J.; Dasgupta, N. P.; Sakamoto, J. Surface Chemistry Mechanism of Ultra-Low Interfacial Resistance in the Solid-State Electrolyte $Li_7La_3Zr_2O_{12}$. *Chem. Mater.* **2017**, *29* (18), 7961–7968. https://doi.org/10.1021/acs.chemmater.7b03002.

(62) Xia, W.; Xu, B.; Duan, H.; Guo, Y.; Kang, H.; Li, H.; Liu, H. Ionic Conductivity and Air Stability of Al-Doped $Li_7La_3Zr_2O_{12}$ Sintered in Alumina and Pt Crucibles. *ACS Appl. Mater. Interfaces* **2016**, *8* (8), 5335–5342. https://doi.org/10.1021/acsami.5b12186.

(63) Kim, K. H.; Iriyama, Y.; Yamamoto, K.; Kumazaki, S.; Asaka, T.; Tanabe, K.; Fisher, C. A. J.; Hirayama, T.; Murugan, R.; Ogumi, Z. Characterization of the Interface between $LiCoO_2$ and $Li_7La_3Zr_2O_{12}$ in an All-Solid-State Rechargeable Lithium Battery. *J. Power Sources* **2011**, *196* (2), 764–767. https://doi.org/10.1016/j.jpowsour.2010.07.073.

(64) Vardar, G.; Bowman, W. J.; Lu, Q.; Wang, J.; Chater, R. J.; Aguadero, A.; Seibert, R.; Terry, J.; Hunt, A.; Waluyo, I.; et al. Structure, Chemistry, and Charge Transfer Resistance of the Interface between $Li_7La_3Zr_2O_{12}$ Electrolyte and $LiCoO_2$ Cathode. *Chem. Mater.* **2018**, *30* (18), 6259–6276. https://doi.org/10.1021/acs.chemmater.8b01713.

(65) Wolfenstine, J.; Allen, J. L.; Sakamoto, J.; Siegel, D. J.; Choe, H. Mechanical Behavior of Li-Ion-Conducting Crystalline Oxide-Based Solid Electrolytes: A Brief Review. *Ionics (Kiel).* **2018**, *24* (5), 1271–1276. https://doi.org/10.1007/s11581-017-2314-4.

(66) Kim, Y.; Jo, H.; Allen, J. L.; Choe, H.; Wolfenstine, J.; Sakamoto, J. The Effect of Relative Density on the Mechanical Properties of Hot-Pressed Cubic $Li_7La_3Zr_2O_{12}$. *J. Am. Ceram. Soc.* **2016**, *99* (4), 1367–1374. https://doi.org/10.1111/jace.14084.

(67) Wang, A. N.; Nonemacher, J. F.; Yan, G.; Finsterbusch, M.; Malzbender, J.; Krüger, M. Mechanical Properties of the Solid Electrolyte Al-Substituted $Li_7La_3Zr_2O_{12}$ (LLZO) by Utilizing Micro-Pillar Indentation Splitting Test. *J. Eur. Ceram. Soc.* **2018**, *38* (9), 3201–3209.

https://doi.org/10.1016/j.jeurceramsoc.2018.02.032.

(68) Ni, J. E.; Case, E. D.; Sakamoto, J. S.; Rangasamy, E.; Wolfenstine, J. B. Room Temperature Elastic Moduli and Vickers Hardness of Hot-Pressed LLZO Cubic Garnet. *J. Mater. Sci.* **2012**, *47* (23), 7978–7985. https://doi.org/10.1007/s10853-012-6687-5.

(69) Hartmann, P.; Leichtweiss, T.; Busche, M. R.; Schneider, M.; Reich, M.; Sann, J.; Adelhelm, P.; Janek, J. Degradation of NASICON-Type Materials in Contact with Lithium Metal: Formation of Mixed Conducting Interphases (MCI) on Solid Electrolytes. *J. Phys. Chem. C* **2013**, *117* (41), 21064–21074. https://doi.org/10.1021/jp4051275.

(70) He, L.; Sun, Q.; Chen, C.; Oh, J. A. S.; Sun, J.; Li, M.; Tu, W.; Zhou, H.; Zeng, K.; Lu, L. Failure Mechanism and Interface Engineering for NASICON-Structured All-Solid-State Lithium Metal Batteries. *ACS Appl. Mater. Interfaces* **2019**, *11* (23), 20895–20904. https://doi.org/10.1021/acsami.9b05516.

(71) Lewis, J. A.; Cortes, F. J. Q.; Boebinger, M. G.; Tippens, J.; Marchese, T. S.; Kondekar, N.; Liu, X.; Chi, M.; McDowell, M. T. Interphase Morphology between a Solid-State Electrolyte and Lithium Controls Cell Failure. *ACS Energy Lett.* **2019**, *4* (2), 591–599. https://doi.org/10.1021/acsenergylett.9b00093.

(72) Chen, C. H.; Amine, K. Ionic Conductivity, Lithium Insertion and Extraction of Lanthanum Lithium Titanate. *Solid State Ionics* **2001**, *144* (1–2), 51–57. https://doi.org/10.1016/S0167-2738(01)00884-0.

(73) Sun, Y.; Guan, P.; Liu, Y.; Xu, H.; Li, S.; Chu, D. Recent Progress in Lithium Lanthanum Titanate Electrolyte towards All Solid-State Lithium Ion Secondary Battery. *Crit. Rev. Solid State Mater. Sci.* **2019**, *44* (4), 265–282. https://doi.org/10.1080/10408436.2018.1485551.

(74) Bai, X.; Duan, Y.; Zhuang, W.; Yang, R.; Wang, J. Research Progress in Li-Argyrodite-Based Solid-State Electrolytes. *J. Mater. Chem. A* **2020**, *8* (48), 25663–25686. https://doi.org/10.1039/d0ta08472g.

(75) Deng, Z.; Wang, Z.; Chu, I.-H.; Luo, J.; Ong, S. P. Elastic Properties of Alkali Superionic Conductor Electrolytes from First Principles Calculations. *J. Electrochem. Soc.* **2016**, *163* (2), A67–A74. https://doi.org/10.1149/2.0061602jes.

(76) Kamaya, N.; Homma, K.; Yamakawa, Y.; Hirayama, M.; Kanno, R.; Yonemura, M.; Kamiyama, T.; Kato, Y.; Hama, S.; Kawamoto, K.; et al. A Lithium Superionic Conductor. *Nat. Mater.* **2011**, *10* (9), 682–686. https://doi.org/10.1038/nmat3066.

(77) Seino, Y.; Ota, T.; Takada, K.; Hayashi, A.; Tatsumisago, M. A Sulphide Lithium Super Ion Conductor Is Superior to Liquid Ion Conductors for Use in Rechargeable Batteries. *Energy Environ. Sci.* **2014**, *7* (2), 627–631. https://doi.org/10.1039/c3ee41655k.

(78) Richards, W. D.; Miara, L. J.; Wang, Y.; Kim, J. C.; Ceder, G. Interface Stability in Solid-State Batteries. *Chem. Mater.* **2016**, *28* (1), 266–273. https://doi.org/10.1021/acs.chemmater.5b04082.

(79) Wenzel, S.; Sedlmaier, S. J.; Dietrich, C.; Zeier, W. G.; Janek, J. Interfacial Reactivity and Interphase Growth of Argyrodite Solid Electrolytes at Lithium Metal Electrodes. *Solid State Ionics* **2018**, *318* (July 2017), 102–112. https://doi.org/10.1016/j.ssi.2017.07.005.

(80) Chu, I. H.; Nguyen, H.; Hy, S.; Lin, Y. C.; Wang, Z.; Xu, Z.; Deng, Z.; Meng, Y. S.; Ong, S. P. Insights into the Performance Limits of the $Li_7P_3S_{11}$ Superionic Conductor: A Combined First-Principles and Experimental Study. *ACS Appl. Mater. Interfaces* **2016**, *8* (12), 7843–7853. https://doi.org/10.1021/acsami.6b00833.

(81) Lepley, N. D.; Holzwarth, N. A. W. Modeling Interfaces between Solids: Application to Li Battery Materials. *Phys. Rev. B - Condens. Matter Mater. Phys.* **2015**, *92* (21), 1–15. https://doi.org/10.1103/PhysRevB.92.214201.

(82) Busche, M. R.; Drossel, T.; Leichtweiss, T.; Weber, D. A.; Falk, M.; Schneider, M.; Reich, M. L.; Sommer, H.; Adelhelm, P.; Janek, J. Dynamic Formation of a Solid-Liquid Electrolyte Interphase and Its Consequences for Hybrid-Battery Concepts. *Nat. Chem.* **2016**, *8* (5), 426–434. https://doi.org/10.1038/nchem.2470.

(83) Mo, Y.; Ong, S. P.; Ceder, G. First Principles Study of the $Li_{10}GeP_2S_{12}$ Lithium Super Ionic Conductor Material. *Chem. Mater.* **2012**, *24* (1), 15–17. https://doi.org/10.1021/cm203303y.

(84) Zhu, Y.; He, X.; Mo, Y. Origin of Outstanding Stability in the Lithium Solid Electrolyte Materials: Insights from Thermodynamic Analyses Based on First-Principles Calculations. *ACS Appl. Mater. Interfaces* **2015**, *7* (42), 23685–23693. https://doi.org/10.1021/acsami.5b07517.

(85) Chen, Z.; Qin, Y.; Amine, K.; Sun, Y. K. Role of Surface Coating on Cathode Materials for Lithium-Ion Batteries. *J. Mater. Chem.* **2010**, *20* (36), 7606–7612. https://doi.org/10.1039/c0jm00154f.

(86) Herzog, M. J.; Esken, D.; Janek, J. Improved Cycling Performance of High-Nickel NMC by Dry Powder Coating with Nanostructured Fumed Al_2O_3, TiO_2, and ZrO_2: A Comparison. *Batter. Supercaps* **2021**, *4* (6), 1003–1017. https://doi.org/10.1002/batt.202100016.

(87) Herzog, M. J.; Gauquelin, N.; Esken, D.; Verbeeck, J.; Janek, J. Increased Performance Improvement of Lithium-Ion Batteries by Dry Powder Coating of High-Nickel NMC with Nanostructured Fumed Ternary Lithium Metal Oxides. *ACS Appl. Energy Mater.* **2021**. https://doi.org/10.1021/acsaem.1c00939.

(88) Chen, H. M.; Maohua, C.; Adams, S. Stability and Ionic Mobility in Argyrodite-Related Lithium-Ion Solid Electrolytes. *Phys. Chem. Chem. Phys.* **2015**, *17* (25), 16494–16506. https://doi.org/10.1039/c5cp01841b.

(89) Lee, H.; Oh, P.; Kim, J.; Cha, H.; Chae, S.; Lee, S.; Cho, J. Advances and Prospects of Sulfide All-Solid-State Lithium Batteries via One-to-One Comparison with Conventional Liquid Lithium Ion Batteries. *Adv. Mater.* **2019**, *31* (29), 1–26. https://doi.org/10.1002/adma.201900376.

(90) Bell, M. F.; Breitschwerdt, A. The Effect of Hydrogen on the Ionic Conductivity in Lithium Nitride. *Mat. Res. Bull.* **1981**, *16*, 267–272. https://doi.org/10.1016/0167-2738(91)90228-4.

(91) Rea, J. R.; Foster, D. L.; Mallory, P. R.; Co. Inc. High Ionic Conductivity in Densified Polycrystalline Lithium Nitride. *Mater. Res. Bull.* **1979**, *14* (6), 841–846. https://doi.org/10.1016/0025-5408(79)90146-6.

(92) Kim, S.; Oguchi, H.; Toyama, N.; Sato, T.; Takagi, S.; Otomo, T.; Arunkumar, D.; Kuwata, N.; Kawamura, J.; Orimo, S. ichi. A Complex Hydride Lithium Superionic Conductor for High-Energy-Density All-Solid-State Lithium Metal Batteries. *Nat. Commun.* **2019**, *10* (1). https://doi.org/10.1038/s41467-019-09061-9.

(93) Tang, W. S.; Yoshida, K.; Soloninin, A. V.; Skoryunov, R. V.; Babanova, O. A.; Skripov, A. V.; Dimitrievska, M.; Stavila, V.; Orimo, S. I.; Udovic, T. J. Stabilizing Superionic-Conducting Structures via Mixed-Anion Solid Solutions of Monocarba-Closo-Borate Salts. *ACS Energy Lett.* **2016**, *1* (4), 659–664. https://doi.org/10.1021/acsenergylett.6b00310.

(94) Tang, W. S.; Matsuo, M.; Wu, H.; Stavila, V.; Unemoto, A.; Orimo, S. I.; Udovic, T. J. Stabilizing Lithium and Sodium Fast-Ion Conduction in Solid Polyhedral-Borate Salts at Device-Relevant Temperatures. *Energy Storage Mater.* **2016**, *4*, 79–83. https://doi.org/10.1016/j.ensm.2016.03.004.

(95) Matsuo, M.; Nakamori, Y.; Orimo, S. I.; Maekawa, H.; Takamura, H. Lithium Superionic Conduction in Lithium Borohydride Accompanied by Structural Transition. *Appl. Phys. Lett.* **2007**, *91* (22), 1–4. https://doi.org/10.1063/1.2817934.

(96) Duchêne, L.; Remhof, A.; Hagemann, H.; Battaglia, C. Status and Prospects of Hydroborate Electrolytes for All-Solid-State Batteries. *Energy Storage Mater.* **2020**, *25* (May 2019), 782–794. https://doi.org/10.1016/j.ensm.2019.08.032.

(97) Asakura, R.; Duchêne, L.; Kühnel, R. S.; Remhof, A.; Hagemann, H.; Battaglia, C. Electrochemical Oxidative Stability of Hydroborate-Based Solid-State Electrolytes. *ACS Appl. Energy Mater.* **2019**, *2* (9), 6924–6930. https://doi.org/10.1021/acsaem.9b01487.

(98) Asano, T.; Sakai, A.; Ouchi, S.; Sakaida, M.; Miyazaki, A.; Hasegawa, S. Solid Halide Electrolytes with High Lithium-Ion Conductivity for Application in 4 V Class Bulk-Type All-Solid-State Batteries. *Adv. Mater.* **2018**, *30* (44), 1–7. https://doi.org/10.1002/adma.201803075.

(99) Wang, C.; Liang, J.; Jiang, M.; Li, X.; Mukherjee, S.; Adair, K.; Zheng, M.; Zhao, Y.; Zhao, F.; Zhang, S.; et al. Interface-Assisted in-Situ Growth of Halide

Electrolytes Eliminating Interfacial Challenges of All-Inorganic Solid-State Batteries. *Nano Energy* **2020**, *76* (May), 105015. https://doi.org/10.1016/j.nanoen.2020.105015.

(100) Muy, S.; Voss, J.; Schlem, R.; Koerver, R.; Sedlmaier, S. J.; Maglia, F.; Lamp, P.; Zeier, W. G.; Shao-Horn, Y. High-Throughput Screening of Solid-State Li-Ion Conductors Using Lattice-Dynamics Descriptors. *iScience* **2019**, *16*, 270–282. https://doi.org/10.1016/j.isci.2019.05.036.

(101) Wang, S.; Bai, Q.; Nolan, A. M.; Liu, Y.; Gong, S.; Sun, Q.; Mo, Y. Lithium Chlorides and Bromides as Promising Solid-State Chemistries for Fast Ion Conductors with Good Electrochemical Stability. *Angew. Chemie* **2019**, *131* (24), 8123–8127. https://doi.org/10.1002/ange.201901938.

(102) Park, K. H.; Kaup, K.; Assoud, A.; Zhang, Q.; Wu, X.; Nazar, L. F. High-Voltage Superionic Halide Solid Electrolytes for All-Solid-State Li-Ion Batteries. *ACS Energy Lett.* **2020**, 533–539. https://doi.org/10.1021/acsenergylett.9b02599.

(103) Riegger, L. M.; Schlem, R.; Sann, J.; Zeier, W. G.; Janek, J. Lithium-Metal Anode Instability of the Superionic Halide Solid Electrolytes and the Implications for Solid-State Batteries. *Angew. Chemie* **2021**, *133* (12), 6792–6797. https://doi.org/10.1002/ange.202015238.

(104) Bolloré Group. LMP®: cutting-edge, effective and safe technology https://blue-storage.com/en/our-technology/.

(105) Arya, A.; Sharma, A. L. *Polymer Electrolytes for Lithium Ion Batteries: A Critical Study*; Ionics, 2017; Vol. 23. https://doi.org/10.1007/s11581-016-1908-6.

(106) Dias, F. B.; Plomp, L.; Veldhuis, J. B. J. Trends in Polymer Electrolytes for Secondary Lithium Batteries. *J. Power Sources* **2000**, *88* (2), 169–191. https://doi.org/10.1016/S0378-7753(99)00529-7.

(107) Ramesh, S.; Winie, T.; Arof, A. K. Investigation of Mechanical Properties of Polyvinyl Chloride-Polyethylene Oxide (PVC-PEO) Based Polymer Electrolytes for Lithium Polymer Cells. *Eur. Polym. J.* **2007**, *43* (5), 1963–1968. https://doi.org/10.1016/j.eurpolymj.2007.02.006.

(108) Wu, F.; Zhang, K.; Liu, Y.; Gao, H.; Bai, Y.; Wang, X.; Wu, C. Polymer Electrolytes and Interfaces toward Solid-State Batteries: Recent Advances and Prospects. *Energy Storage Mater.* **2020**, *33* (July), 26–54. https://doi.org/10.1016/j.ensm.2020.08.002.

(109) Fauteax, D.; Massucco, A.; McLin, M.; van Buren, M.; Shi, J. Lithium-Polymer Electrolyte Rechargeable Batteries. *Electrochim. Acta* **1995**, *40* (13 14), 2185–2190. https://doi.org/10.1109/BCAA.2000.838389.

(110) Barai, P.; Higa, K.; Srinivasan, V. Lithium Dendrite Growth Mechanisms in Polymer Electrolytes and Prevention Strategies. *Phys. Chem. Chem. Phys.* **2017**, *19* (31), 20493–20505. https://doi.org/10.1039/c7cp03304d.

(111) Zhao, Q.; Liu, X.; Stalin, S.; Khan, K.; Archer, L. A. Solid-State Polymer Electrolytes with in-Built Fast Interfacial Transport for Secondary Lithium Batteries. *Nat. Energy* **2019**, *4* (5), 365–373. https://doi.org/10.1038/s41560-019-0349-7.

(112) Yu, X.; Manthiram, A. A Review of Composite Polymer-Ceramic Electrolytes for Lithium Batteries. *Energy Storage Mater.* **2021**, *34* (July 2020), 282–300. https://doi.org/10.1016/j.ensm.2020.10.006.

(113) Wang, Y.; Song, S.; Xu, C.; Hu, N.; Molenda, J.; Lu, L. Development of Solid-State Electrolytes for Sodium-Ion Battery - A Short Review. *Elements* **2021**, *1* (2), 91–100. https://doi.org/10.1016/j.nanoms.2019.02.007.

(114) Li, Z.; Liu, P.; Zhu, K.; Zhang, Z.; Si, Y.; Wang, Y.; Jiao, L. Solid-State Electrolytes for Sodium Metal Batteries. *Energy and Fuels* **2021**, *35* (11), 9063–9079. https://doi.org/10.1021/acs.energyfuels.1c00347.

(115) Morgan, B. J. Mechanistic Origin of Superionic Lithium Diffusion in Anion-Disordered Li_6PS_5X Argyrodites. *Chem. Mater.* **2021**, *33* (6), 2004–2018. https://doi.org/10.1021/acs.chemmater.0c03738.

(116) Yu, C.; Zhao, F.; Luo, J.; Zhang, L.; Sun, X. Recent Development of Lithium Argyrodite Solid-State Electrolytes for Solid-State Batteries: Synthesis, Structure, Stability and Dynamics. *Nano Energy* **2021**, *83* (February), 105858. https://doi.org/10.1016/j.nanoen.2021.105858.

(117) Boulineau, S.; Courty, M.; Tarascon, J. M.; Viallet, V. Mechanochemical Synthesis of Li-Argyrodite Li_6PS_5X(X = Cl, Br, I) as Sulfur-Based Solid Electrolytes for All Solid State Batteries Application. *Solid State Ionics* **2012**, *221*, 1–5. https://doi.org/10.1016/j.ssi.2012.06.008.

(118) Auvergniot, J.; Cassel, A.; Ledeuil, J. B.; Viallet, V.; Seznec, V.; Dedryvère, R. Interface Stability of Argyrodite Li_6PS_5Cl toward $LiCoO_2$, $LiNi_{1/3}Co_{1/3}Mn_{1/3}O_2$, and $LiMn_2O_4$ in Bulk All-Solid-State Batteries. *Chem. Mater.* **2017**, *29* (9), 3883–3890. https://doi.org/10.1021/acs.chemmater.6b04990.

(119) Zhou, Y.; Doerrer, C.; Kasemchainan, J.; Bruce, P. G.; Pasta, M.; Hardwick, L. Observation of Interfacial Degradation of Li_6PS_5Cl against Lithium Metal and $LiCoO_2$ via In Situ Electrochemical Raman Microscopy. *Batter. Supercaps* **2020**, 1–7. https://doi.org/10.1002/batt.201900218.

(120) Kasemchainan, J.; Zekoll, S.; Spencer Jolly, D.; Ning, Z.; Hartley, G. O.; Marrow, J.; Bruce, P. G. Critical Stripping Current Leads to Dendrite Formation on Plating in Lithium Anode Solid Electrolyte Cells. *Nat. Mater.* **2019**, *18*, 1105–1111. https://doi.org/10.1038/s41563-019-0438-9.

(121) Chen, B.; Xu, C.; Wang, H.; Zhou, J. Insights into Interfacial Stability of Li_6PS_5Cl Solid Electrolytes with Buffer Layers. *Curr. Appl. Phys.* **2019**, *19* (2), 149–154. https://doi.org/10.1016/j.cap.2018.12.003.

(122) Lee, D. H.; Lee, S. T.; Kim, J. S.; Lim, S. K. Analysis of Properties of Partially Stabilized Zirconia-Doped Na^+-Beta-Alumina Prepared by Calcining-Cum-Sintering Process. *Mater. Res. Bull.* **2017**, *96*, 143–148. https://doi.org/10.1016/j.materresbull.2017.05.003.

(123) Engstrom, H.; Bates, J. B.; Brundage, W. E.; Wang, J. C. Ionic Conductivity of Sodium Beta″-Alumina. *Solid State Ionics* **1981**, *2* (4), 265–276. https://doi.org/10.1016/0167-2738(81)90027-8.

(124) Wolf, D. On the Mechanism of Diffusion in Sodium Beta Alumina. *J. Phys. Chem. Solids* **1979**, *40* (10), 757–773. https://doi.org/10.1016/0022-3697(79)90158-6.

(125) Kim, K. K.; Mundy, J. N.; Chen, W. K. Diffusion and Ionic Conductivity in Sodium Beta-Alumina. *Solid State Commun.* **1979**, *30* (12), i. https://doi.org/10.1016/0038-1098(79)90058-9.

(126) Wenzel, S.; Leichtweiss, T.; Weber, D. A.; Sann, J.; Zeier, W. G.; Janek, J. Interfacial Reactivity Benchmarking of the Sodium Ion Conductors Na_3PS_4 and Sodium β-Alumina for Protected Sodium Metal Anodes and Sodium All-Solid-State Batteries. *ACS Appl. Mater. Interfaces* **2016**, *8* (41), 28216–28224. https://doi.org/10.1021/acsami.6b10119.

(127) Armstrong, R. D.; Dickinson, T.; Turner, J. The Breakdown of β-Alumina Ceramic Electrolyte. *Electrochim. Acta* **1974**, *19* (5), 187–192. https://doi.org/10.1016/0013-4686(74)85065-6.

(128) Richman, R. H.; Tennenhouse, G. J. A Model for Degradation of Ceramic Electrolytes in Na-S Batteries. *J. Am. Ceram. Soc.* **1975**, *58* (1–2), 63–67. https://doi.org/10.1111/j.1151-2916.1975.tb18986.x.

(129) Virkar, A. V.; Miller, G. R.; Gordon, R. S. Comment on "the Failure of Beta Alumina Electrolyte by a Dendritic Penetration Mechanism." *Electrochim. Acta* **1981**, *26* (8), 1023–1027. https://doi.org/10.1016/0013-4686(81)85071-2.

(130) Hull, A. W. A New Method of X-Ray Crystal Analysis. *Phys. Rev.* **1917**, *10* (6), 661–696. https://doi.org/10.1017/S0885715600016018.

(131) Markowitz, M. M.; Boryta, D. A. Lithium Metal-Gas Reactions. Interaction of Lithium Metal with Air and Its Component Gases. *J. Chem. Eng. Data* **1962**, *7* (4), 586–591. https://doi.org/10.1021/je60015a047.

(132) Li, Y.; Li, Y.; Sun, Y.; Butz, B.; Yan, K.; Koh, A. L.; Zhao, J.; Pei, A.; Cui, Y. Revealing Nanoscale Passivation and Corrosion Mechanisms of Reactive Battery Materials in Gas Environments. *Nano Lett.* **2017**, *17* (8), 5171–5178. https://doi.org/10.1021/acs.nanolett.7b02630.

(133) Otto, S. K.; Moryson, Y.; Krauskopf, T.; Peppler, K.; Sann, J.; Janek, J.; Henss, A. In-Depth Characterization of Lithium-Metal Surfaces with XPS and ToF-SIMS: Toward Better Understanding of the Passivation Layer. *Chem. Mater.* **2021**, *33* (3), 859–867. https://doi.org/10.1021/acs.chemmater.0c03518.

(134) Lide, D. R. *CRC Handbook of Chemistry and Physics*; Lide, D. R., Ed.; CRC Press, 2004. https://doi.org/10.1002/jctb.280500215.

(135) Heitjans, P.; Korblein, A.; Ackermann, H.; Dubbers, D.; Fujara, F.; Stockmann, H.-J. Self-Diffusion in Solid Lithium Probed by Spin-Lattice Relaxation of ^{8}Li Nuclei. *J. Phys. F Met. Phys.* **1985**, *15*, 41–54.

(136) Messer, R.; Noack, F. Nuclear Magnetic Relaxation by Self-Diffusion in Solid Lithium: T_1-Frequency Dependence. *Appl. Phys.* **1975**, *6* (1), 79–88. https://doi.org/10.1007/BF00883553.

(137) Masias, A.; Felten, N.; Garcia-mendez, R.; Wolfenstine, J.; Sakamoto, J. Elastic, Plastic, and Creep Mechanical Properties of Lithium Metal. *J. Mater. Sci.* **2019**, *54* (3), 2585–2600. https://doi.org/10.1007/s10853-018-2971-3.

(138) Fincher, C. D.; Ojeda, D.; Zhang, Y.; Pharr, G. M.; Pharr, M. Mechanical Properties of Metallic Lithium: From Nano to Bulk Scales. *Acta Mater.* **2020**, *186* (December 2019), 215–222. https://doi.org/10.1016/j.actamat.2019.12.036.

(139) Bedford, A.; Liechti, K. M. *Mechanics of Materials*, Second Edi.; Cham, Switzerland : Springer, 2020. https://doi.org/10.1007/978-3-030-22082-2: 10.1007/978-3-030-22.

(140) LePage, W. S.; Chen, Y.; Kazyak, E.; Chen, K.-H.; Sanchez, A. J.; Poli, A.; Arruda, E. M.; Thouless, M. D.; Dasgupta, N. P. Lithium Mechanics: Roles of Strain Rate and Temperature and Implications for Lithium Metal Batteries. *J. Electrochem. Soc.* **2019**, *166* (2), A89–A97. https://doi.org/10.1149/2.0221902jes.

(141) Xu, C.; Ahmad, Z.; Aryanfar, A.; Viswanathan, V.; Greer, J. R. Enhanced Strength and Temperature Dependence of Mechanical Properties of Li at Small Scales and Its Implications for Li Metal Anodes. *Proc. Natl. Acad. Sci. U. S. A.* **2017**, *114* (1), 57–61. https://doi.org/10.1073/pnas.1615733114.

(142) Bridgman, P. W. *The Effect of Tension on the Electrical Resistance of Certain Abnormal Metals*, 2013th ed.; Harvard University Press, 1922.

(143) Tariq, S.; Ammigan, K.; Hurh, P.; Schultz, R.; Liu, P.; Shang, J. Li Material Testing - Fermilab Antiproton Source Lithium Collection Lens. *Proc. 2003 Part. Accel. Conf.* **2003**, 1452–1454.

(144) Schultz, R. P. *Lithium: Measurement of Young's Modulus and Yield Strength*; 2002.

(145) Robertson, W. M.; Montgomery, D. J. Elastic Modulus of Isotoyically-Concentrated Lithium. *Phys. Rev.* **1960**, *117* (2), 440–442.

(146) Fincher, C. D.; Ojeda, D.; Zhang, Y.; Pharr, G. M.; Pharr, M. Mechanical Properties of Metallic Lithium: From Nano to Bulk Scales. *Acta Mater.* **2020**, *186*, 215–222. https://doi.org/10.1016/j.actamat.2019.12.036.

(147) Hull, D.; Rosenberg, H. M. The Deformation of Lithium, Sodium and Potassium at Low Temperatures: Tensile and Resistivity Experiments. *Philos. Mag.* **1959**, *4* (39), 303–315. https://doi.org/10.1080/14786435908233342.

(148) Nachtrieb, N. H.; Catalano, E.; Weil, J. A. Self-Diffusion in Solid Sodium. I. *J. Chem. Phys.* **1952**, *20* (8), 1185–1188.

(149) Wang, M. J.; Chang, J. Y.; Wolfenstine, J. B.; Sakamoto, J. Analysis of Elastic, Plastic, and Creep Properties of Sodium Metal and Implications for Solid-State Batteries. *Materialia* **2020**, *12* (5), 28. https://doi.org/10.1016/j.mtla.2020.100792.

(150) Fincher, C. D.; Zhang, Y.; Pharr, G. M.; Pharr, M. Elastic and Plastic Characteristics of Sodium Metal. *ACS Appl. Energy Mater.* **2020**. https://doi.org/10.1021/acsaem.9b02225.

(151) Spencer Jolly, D.; Ning, Z.; Darnbrough, J. E.; Kasemchainan, J.; Hartley, G. O.; Adamson, P.; Armstrong, D. E. J.; Marrow, J.; Bruce, P. G. Sodium/Na B″ Alumina Interface: Effect of Pressure on Voids. *ACS Appl. Mater. Interfaces* **2020**, *12* (1), 678–685. https://doi.org/10.1021/acsami.9b17786.

(152) Bay, M.; Wang, M.; Grissa, R.; Heinz, M. V. F.; Sakamoto, J.; Battaglia, C. Sodium Plating from Na-β″-Alumina Ceramics at Room Temperature, Paving the Way for Fast-Charging All-Solid-State Batteries. *Adv. Energy Mater.* **2020**, *10* (3), 1902899. https://doi.org/10.1002/aenm.201902899.

(153) Park, R. J. Y.; Eschler, C. M.; Fincher, C. D.; Badel, A. F.; Guan, P.; Pharr, M.; Sheldon, B. W.; Carter, W. C.; Viswanathan, V.; Chiang, Y. M. Semi-Solid Alkali Metal Electrodes Enabling High Critical Current Densities in Solid Electrolyte Batteries. *Nat. Energy* **2021**, *6* (3), 314–322. https://doi.org/10.1038/s41560-021-00786-w.

(154) Han, S. Y.; Lee, C.; Lewis, J. A.; Yeh, D.; Liu, Y.; Lee, H.; Mcdowell, M. T. Stress Evolution during Cycling of Alloy-Anode Solid-State Batteries of Alloy-Anode Solid-State Batteries. *Joule* **2021**, 1–16. https://doi.org/10.1016/j.joule.2021.07.002.

(155) Liang, X.; Pang, Q.; Kochetkov, I. R.; Sempere, M. S.; Huang, H.; Sun, X.; Nazar, L. F. A Facile Surface Chemistry Route to a Stabilized Lithium Metal Anode. *Nat. Energy* **2017**, *2* (July), 1–7. https://doi.org/10.1038/nenergy.2017.119.

(156) Krauskopf, T.; Mogwitz, B.; Rosenbach, C.; Zeier, W. G.; Janek, J. Diffusion Limitation of Lithium Metal and Li–Mg Alloy Anodes on LLZO Type Solid Electrolytes as a Function of Temperature and Pressure. *Adv. Energy Mater.* **2019**, *9* (44). https://doi.org/10.1002/aenm.201902568.

(157) Gu, J.; Shen, C.; Fang, Z.; Yu, J.; Zheng, Y.; Tian, Z.; Shao, L.; Li, X.; Xie, K. Toward High-Performance Li Metal Anode via Difunctional Protecting Layer. *Front. Chem.* **2019**, *7* (August), 1–9. https://doi.org/10.3389/fchem.2019.00572.

(158) Shi, Z.; Liu, M.; Gole, J. L. Electrochemical Properties of Li-Zn Alloy Electrodes

Prepared by Kinetically Controlled Vapor Deposition for Lithium Batteries. *Electrochem. Solid-State Lett.* **2000**, *3* (7), 312–315. https://doi.org/10.1149/1.1391133.

(159) Hiratani, M.; Miyauchi, K.; Ito, Y.; Kanehori, K.; Kirino, F.; Kudo, T. Solid State Lithium Battery. 4,645,726, 1987.

(160) Hiratani, M.; Miyauchi, K.; Kudo, T. Effect of a Lithium Alloy Layer Inserted between a Lithium Anode and a Solid Electrolyte. *Solid State Ionics* **1988**, *28–30* (PART 2), 1406–1410. https://doi.org/10.1016/0167-2738(88)90394-3.

(161) Michel, F.; Becker, M.; Janek, J.; Polity, A. Investigations of the Solid Electrolyte Interphase Using X-Ray Photoelectron Spectroscopy In Situ Experiment on the Lithium-Based Solid Electrolyte LiPSON. *Phys. Status Solidi Basic Res.* **2020**, *257* (3). https://doi.org/10.1002/pssb.201900336.

(162) Jow, T. R.; Liang, C. C. Interface Between Solid Electrode and Solid Electrolyte - A Study of the Li/LiI(AI_2O_3) Solid-Electrolyte System. *J. Electrochem. Soc.* **1983**, *130* (4), 737–740.

(163) Jow, T. R.; Liang, C. C. Interface between Solid Anode and Solid Electrolyte - Effect of Pressure on Li/LiI(Al_2O_3) Interface. *Solid State Ionics* **1983**, No. 9 & 10, 695–698.

(164) Koshikawa, H.; Matsuda, S.; Kamiya, K.; Miyayama, M.; Kubo, Y.; Uosaki, K.; Hashimoto, K.; Nakanishi, S. Dynamic Changes in Charge-Transfer Resistance at Li Metal/$Li_7La_3Zr_2O_{12}$ Interfaces during Electrochemical Li Dissolution/Deposition Cycles. *J. Power Sources* **2018**, *376*, 147–151. https://doi.org/10.1016/j.jpowsour.2017.11.082.

(165) Meyer, M.; Rickert, H.; Schwaitzer, U. Investigations on the Kinetics of the Anodic Dissolution of Lithium at the Interface Li/Li_3N. *Solid State Ionics* **1983**, *9–10* (PART 1), 689–693. https://doi.org/10.1016/0167-2738(83)90315-6.

(166) Krauskopf, T.; Hartmann, H.; Zeier, W. G.; Janek, J. Toward a Fundamental Understanding of the Lithium Metal Anode in Solid-State Batteries - An Electrochemo-Mechanical Study on the Garnet-Type Solid Electrolyte $Li_{6.25}Al_{0.25}La_3Zr_2O_{12}$. *Appl. Interfaces Mater.* **2019**, No. 11, 14463–14477. https://doi.org/10.1021/acsami.9b02537.

(167) Lewis, J.; Cortes, F. J. Q.; Liu, Y.; Miers, J.; Verma, A.; Vishnugopi, B.; Tippens, J.; Prakash, D.; Marchese, T.; Han, S. Y.; et al. Linking Void and Interphase Evolution to Electrochemistry in Solid-State Batteries Using Operando X-Ray Tomography. **2020**, No. 2. https://doi.org/10.26434/chemrxiv.12468170.

(168) Dixit, M. B.; Verma, A.; Zaman, W.; Zhong, X.; Kenesei, P.; Park, J. S.; Almer, J.; Mukherjee, P. P.; Hatzell, K. B. Synchrotron Imaging of Pore Formation in Li Metal Solid-State Batteries Aided by Machine Learning. *ACS Appl. Energy Mater.* **2020**, *3* (10), 9534–9542. https://doi.org/10.1021/acsaem.0c02053.

(169) Seymour, I. D.; Aguadero, A. Suppressing Void Formation in All-Solid-State Batteries: The Role of Interfacial Adhesion on Alkali Metal Vacancy Transport. *J. Mater. Chem. A* **2021**. https://doi.org/10.1039/d1ta03254b.

(170) Shishvan, S. S.; Fleck, N. A.; Deshpande, V. S. The Initiation of Void Growth during Stripping of Li Electrodes in Solid Electrolyte Cells. *J. Power Sources* **2021**, *488*, 229437.

(171) Yang, M.; Liu, Y.; Nolan, A. M.; Mo, Y. Interfacial Atomistic Mechanisms of Lithium Metal Stripping and Plating in Solid-State Batteries. *Adv. Mater.* **2021**, *33* (11), 1–12. https://doi.org/10.1002/adma.202008081.

(172) Wang, M. J.; Choudhury, R.; Sakamoto, J. Characterizing the Li-Solid-Electrolyte Interface Dynamics as a Function of Stack Pressure and Current Density. *Joule* **2019**, 1–14. https://doi.org/10.1016/j.joule.2019.06.017.

(173) Zhang, X.; Wang, Q. J.; Harrison, K. L.; Roberts, S. A.; Harris, S. J. Pressure-Driven Interface Evolution in Solid-State Lithium Metal Batteries. *Cell Reports Phys. Sci.* **2020**, *1* (2), 100012. https://doi.org/10.1016/j.xcrp.2019.100012.

(174) Sakamoto, J. More Pressure Needed. *Nat. Energy* **2019**, *4* (10), 827–828. https://doi.org/10.1038/s41560-019-0478-z.

(175) Spencer Jolly, D.; Ning, Z.; Hartley, G. O.; Liu, B.; Melvin, D. L. R.; Adamson, P.; Marrow, J.; Bruce, P. G. Temperature Dependence of Lithium Anode Voiding in Argyrodite Solid-State Batteries. *ACS Appl. Mater. Interfaces* **2021**, *13* (19), 22708–22716. https://doi.org/10.1021/acsami.1c06706.

(176) Tarascon, J. M.; Armand, M. Issues and Challenges Facing Rechargeable Lithium Batteries. *Nature* **2001**, *414* (6861), 359–367. https://doi.org/10.1038/35104644.

(177) Bai, P.; Li, J.; Brushett, F. R.; Bazant, M. Z. Transition of Lithium Growth Mechanisms in Liquid Electrolytes. *Energy Environ. Sci.* **2016**, *9* (10), 3221–3229. https://doi.org/10.1039/c6ee01674j.

(178) Lin, D.; Liu, Y.; Cui, Y. Reviving the Lithium Metal Anode for High-Energy Batteries. *Nat. Publ. Gr.* **2017**, *12*. https://doi.org/10.1038/NNANO.2017.16.

(179) Han, F.; Westover, A. S.; Yue, J.; Fan, X.; Wang, F.; Chi, M.; Leonard, D. N.; Dudney, N. J.; Wang, H.; Wang, C. High Electronic Conductivity as the Origin of Lithium Dendrite Formation within Solid Electrolytes. *Nat. Energy* **2019**. https://doi.org/10.1038/s41560-018-0312-z.

(180) Lu, Y.; Zhao, C. Z.; Yuan, H.; Cheng, X. B.; Huang, J. Q.; Zhang, Q. Critical Current Density in Solid-State Lithium Metal Batteries: Mechanism, Influences, and Strategies. *Adv. Funct. Mater.* **2021**, *2009925*, 1–33. https://doi.org/10.1002/adfm.202009925.

(181) Shen, F.; Dixit, M. B.; Xiao, X.; Hatzell, K. B. Effect of Pore Connectivity on Li Dendrite Propagation within LLZO Electrolytes Observed with Synchrotron X-

Ray Tomography. *ACS Energy Lett.* **2018**, *3* (4), 1056–1061. https://doi.org/10.1021/acsenergylett.8b00249.

(182) Kazyak, E.; Garcia-Mendez, R.; LePage, W. S.; Sharafi, A.; Davis, A. L.; Sanchez, A. J.; Chen, K. H.; Haslam, C.; Sakamoto, J.; Dasgupta, N. P. Li Penetration in Ceramic Solid Electrolytes: Operando Microscopy Analysis of Morphology, Propagation, and Reversibility. *Matter* **2020**, *2* (4), 1025–1048. https://doi.org/10.1016/j.matt.2020.02.008.

(183) Feldman, L. A.; De Jonghe, L. C. Initiation of Mode I Degradation in Sodium-Beta Alumina Electrolytes. *J. Mater. Sci.* **1982**, *17* (2), 517–524. https://doi.org/10.1007/BF00591486.

(184) Porz, L.; Swamy, T.; Sheldon, B. W.; Rettenwander, D.; Frömling, T.; Thaman, H. L.; Berendts, S.; Uecker, R.; Carter, W. C.; Chiang, Y. M. Mechanism of Lithium Metal Penetration through Inorganic Solid Electrolytes. *Adv. Energy Mater.* **2017**, *7* (20), 1–12. https://doi.org/10.1002/aenm.201701003.

(185) Klinsmann, M.; Hildebrand, F. E.; Ganser, M.; McMeeking, R. M. Dendritic Cracking in Solid Electrolytes Driven by Lithium Insertion. *J. Power Sources* **2019**, *442* (May), 227226. https://doi.org/10.1016/j.jpowsour.2019.227226.

(186) Shishvan, S. S.; Fleck, N. A.; McMeeking, R. M.; Deshpande, V. S. Dendrites as Climbing Dislocations in Ceramic Electrolytes: Initiation of Growth. *J. Power Sources* **2020**, *456* (February), 227989. https://doi.org/10.1016/j.jpowsour.2020.227989.

(187) Cao, D.; Sun, X.; Li, Q.; Natan, A.; Xiang, P.; Zhu, H. Lithium Dendrite in All-Solid-State Batteries: Growth Mechanisms, Suppression Strategies, and Characterizations. *Matter* **2020**, *3* (1), 57–94. https://doi.org/10.1016/j.matt.2020.03.015.

(188) Li, Y.; Zhou, W.; Chen, X.; Lü, X.; Cui, Z.; Xin, S.; Xue, L.; Jia, Q.; Goodenough, J. B. Mastering the Interface for Advanced All-Solid-State Lithium Rechargeable Batteries. *Proc. Natl. Acad. Sci. U. S. A.* **2016**, *113* (47), 13313–13317. https://doi.org/10.1073/pnas.1615912113.

(189) Cheng, E. J.; Sharafi, A.; Sakamoto, J. Intergranular Li Metal Propagation through Polycrystalline $Li_{6.25}Al_{0.25}La_3Zr_2O_{12}$ Ceramic Electrolyte. *Electrochim. Acta* **2017**, *223*, 85–91. https://doi.org/10.1016/j.electacta.2016.12.018.

(190) Krauskopf, T.; Dippel, R.; Hartmann, H.; Peppler, K.; Mogwitz, B.; Richter, F. H.; Zeier, W. G.; Janek, J. Lithium-Metal Growth Kinetics on LLZO Garnet-Type Solid Electrolytes. *Joule* **2019**, *3* (8), 2030–2049. https://doi.org/10.1016/j.joule.2019.06.013.

(191) Ning, Z.; Jolly, D. S.; Li, G.; De Meyere, R.; Pu, S. D.; Chen, Y.; Kasemchainan, J.; Ihli, J.; Gong, C.; Liu, B.; et al. Visualizing Plating-Induced Cracking in Lithium-Anode Solid-Electrolyte Cells. *Nat. Mater.* **2021**, *20* (August), 1121–1130. https://doi.org/10.1038/s41563-021-00967-8.

(192) De Jonghe, C.; Feldman, L.; Buechele, A. Failure Modes of Na-Beta Alumina. *Solid State Ionics* **1981**, *5*, 267–270.

(193) Song, Y.; Yang, L.; Zhao, W.; Wang, Z.; Zhao, Y.; Wang, Z.; Zhao, Q.; Liu, H.; Pan, F. Revealing the Short-Circuiting Mechanism of Garnet-Based Solid-State Electrolyte. *Adv. Energy Mater.* **2019**, *9* (21), 1–6. https://doi.org/10.1002/aenm.201900671.

(194) Aguesse, F.; Manalastas, W.; Buannic, L.; Del Amo, J. M. L.; Singh, G.; Llordés, A.; Kilner, J. Investigating the Dendritic Growth during Full Cell Cycling of Garnet Electrolyte in Direct Contact with Li Metal. *ACS Appl. Mater. Interfaces* **2017**, *9* (4), 3808–3816. https://doi.org/10.1021/acsami.6b13925.

(195) Liu, X.; Garcia-Mendez, R.; Lupini, A. R.; Cheng, Y.; Hood, Z. D.; Han, F.; Sharafi, A.; Idrobo, J. C.; Dudney, N. J.; Wang, C.; et al. Local Electronic Structure Variation Resulting in Li 'Filament' Formation within Solid Electrolytes. *Nat. Mater.* **2021**. https://doi.org/10.1038/s41563-021-01019-x.

(196) Viswanathan, L.; Ikuma, Y.; Virkar, A. V. Transfomation Toughening of B″-Alumina by Incorporation of Zirconia. *J. Mater. Sci.* **1983**, *18* (1), 109–113. https://doi.org/10.1007/BF00543815.

(197) Binner, J. G. P.; Stevens, R.; Tan, S. R. Toughening of Hot Pressed Beta-alumina Using Zirconia Additions Prepared from Zirconate, Tartrate and Carbonate Precursor Materials. *J. Microsc.* **1985**, *140* (2), 183–194. https://doi.org/10.1111/j.1365-2818.1985.tb02674.x.

(198) Lange, F. F.; Miller, K. T. *Improved Beta"-Alumina Oxide Electrolytes Through Transformation Toughening*; 1986.

(199) Lee, Y. G.; Fujiki, S.; Jung, C.; Suzuki, N.; Yashiro, N.; Omoda, R.; Ko, D. S.; Shiratsuchi, T.; Sugimoto, T.; Ryu, S.; et al. High-Energy Long-Cycling All-Solid-State Lithium Metal Batteries Enabled by Silver–Carbon Composite Anodes. *Nat. Energy* **2020**, *5* (APril), 299–308. https://doi.org/10.1038/s41560-020-0575-z.

(200) Hippauf, F.; Schumm, B.; Doerfler, S.; Althues, H.; Fujiki, S.; Shiratsushi, T.; Tsujimura, T.; Aihara, Y.; Kaskel, S. Overcoming Binder Limitations of Sheet-Type Solid-State Cathodes Using a Solvent-Free Dry-Film Approach. *Energy Storage Mater.* **2019**, *21* (February), 390–398. https://doi.org/10.1016/j.ensm.2019.05.033.

(201) Inada, T.; Takada, K.; Kajiyama, A.; Kouguchi, M.; Sasaki, H.; Kondo, S.; Watanabe, M.; Murayama, M.; Kanno, R. Fabrications and Properties of Composite Solid-State Electrolytes. *Solid State Ionics* **2003**, *158* (3–4), 275–280. https://doi.org/10.1016/S0167-2738(02)00889-5.

(202) Nam, Y. J.; Oh, D. Y.; Jung, S. H.; Jung, Y. S. Toward Practical All-Solid-State Lithium-Ion Batteries with High Energy Density and Safety: Comparative Study for Electrodes Fabricated by Dry- and Slurry-Mixing Processes. *J. Power Sources* **2018**, *375* (September 2017), 93–101.

https://doi.org/10.1016/j.jpowsour.2017.11.031.

(203) Yersak, T.; Salvador, J. R.; Schmidt, R. D.; Cai, M. Hot Pressed, Fiber-Reinforced $(Li_2S)_{70}(P_2S_5)_{30}$ Solid-State Electrolyte Separators for Li Metal Batteries. *ACS Appl. Energy Mater.* **2019**, *2* (5), 3523–3531. https://doi.org/10.1021/acsaem.9b00290.

(204) Yang, C.; Zhang, L.; Liu, B.; Xu, S.; Hamann, T.; McOwen, D.; Dai, J.; Luo, W.; Gong, Y.; Wachsman, E. D.; et al. Continuous Plating/Stripping Behavior of Solid-State Lithium Metal Anode in a 3D Ion-Conductive Framework. *Proc. Natl. Acad. Sci. U. S. A.* **2018**, *115* (15), 3770–3775. https://doi.org/10.1073/pnas.1719758115.

(205) Xu, S.; Hu, L. Towards a High-Performance Garnet-Based Solid-State Li Metal Battery: A Perspective on Recent Advances. *J. Power Sources* **2020**, *472* (July), 228571. https://doi.org/10.1016/j.jpowsour.2020.228571.

(206) Xu, S.; McOwen, D. W.; Zhang, L.; Hitz, G. T.; Wang, C.; Ma, Z.; Chen, C.; Luo, W.; Dai, J.; Kuang, Y.; et al. All-in-One Lithium-Sulfur Battery Enabled by a Porous-Dense-Porous Garnet Architecture. *Energy Storage Mater.* **2018**, *15* (August), 458–464. https://doi.org/10.1016/j.ensm.2018.08.009.

(207) Liu, B.; Zhang, L.; Xu, S.; McOwen, D. W.; Gong, Y.; Yang, C.; Pastel, G. R.; Xie, H.; Fu, K.; Dai, J.; et al. 3D Lithium Metal Anodes Hosted in Asymmetric Garnet Frameworks toward High Energy Density Batteries. *Energy Storage Mater.* **2018**, *14* (April), 376–382. https://doi.org/10.1016/j.ensm.2018.04.015.

(208) Fu, K.; Gong, Y.; Hitz, G. T.; McOwen, D. W.; Li, Y.; Xu, S.; Wen, Y.; Zhang, L.; Wang, C.; Pastel, G.; et al. Three-Dimensional Bilayer Garnet Solid Electrolyte Based High Energy Density Lithium Metal-Sulfur Batteries. *Energy Environ. Sci.* **2017**, *10* (7), 1568–1575. https://doi.org/10.1039/c7ee01004d.

(209) Xu, S.; McOwen, D. W.; Wang, C.; Zhang, L.; Luo, W.; Chen, C.; Li, Y.; Gong, Y.; Dai, J.; Kuang, Y.; et al. Three-Dimensional, Solid-State Mixed Electron-Ion Conductive Framework for Lithium Metal Anode. *Nano Lett.* **2018**, *18* (6), 3926–3933. https://doi.org/10.1021/acs.nanolett.8b01295.

(210) Kim, S.; Jung, C.; Kim, H.; Thomas-Alyea, K. E.; Yoon, G.; Kim, B.; Badding, M. E.; Song, Z.; Chang, J. M.; Kim, J.; et al. The Role of Interlayer Chemistry in Li-Metal Growth through a Garnet-Type Solid Electrolyte. *Adv. Energy Mater.* **2020**, *10* (12), 1–11. https://doi.org/10.1002/aenm.201903993.

(211) Taylor, N. J.; Stangeland-Molo, S.; Haslam, C. G.; Sharafi, A.; Thompson, T.; Wang, M.; Garcia-Mendez, R.; Sakamoto, J. Demonstration of High Current Densities and Extended Cycling in the Garnet Li7La3Zr2O12 Solid Electrolyte. *J. Power Sources* **2018**, *396* (April), 314–318. https://doi.org/10.1016/j.jpowsour.2018.06.055.

(212) Wakasugi, J.; Munakata, H.; Kanamura, K. Effect of Gold Layer on Interface Resistance between Lithium Metal Anode and $Li_{6.25}Al_{0.25}La_3Zr_2O_{12}$ Solid Electrolyte. *J. Electrochem. Soc.* **2017**, *164* (6), A1022–A1025.

https://doi.org/10.1149/2.0471706jes.

(213) Tsai, C. L.; Roddatis, V.; Chandran, C. V.; Ma, Q.; Uhlenbruck, S.; Bram, M.; Heitjans, P.; Guillon, O. $Li_7La_3Zr_2O_{12}$ Interface Modification for Li Dendrite Prevention. *ACS Appl. Mater. Interfaces* **2016**, *8* (16), 10617–10626. https://doi.org/10.1021/acsami.6b00831.

(214) Dubey, R.; Sastre, J.; Cancellieri, C.; Okur, F.; Forster, A.; Pompizii, L.; Priebe, A.; Romanyuk, Y. E.; Jeurgens, L. P. H.; Kovalenko, M. V; et al. Building a Better Li-Garnet Solid Electrolyte/Metallic Li Interface with Antimony. *Adv. Energy Mater.* **2021**, 2102086. https://doi.org/10.1002/aenm.202102086.

(215) Fu, K. K.; Gong, Y.; Fu, Z.; Xie, H.; Yao, Y.; Liu, B.; Carter, M.; Wachsman, E.; Hu, L. Transient Behavior of the Metal Interface in Lithium Metal–Garnet Batteries. *Angew. Chemie - Int. Ed.* **2017**, *56* (47), 14942–14947. https://doi.org/10.1002/anie.201708637.

(216) Lu, Y.; Huang, X.; Ruan, Y.; Wang, Q.; Kun, R.; Yang, J.; Wen, Z. An in Situ Element Permeation Constructed High Endurance Li-LLZO Interface at High Current Densities. *J. Mater. Chem. A* **2018**, *6* (39), 18853–18858. https://doi.org/10.1039/c8ta07241h.

(217) Luo, W.; Gong, Y.; Zhu, Y.; Fu, K. K.; Dai, J.; Lacey, S. D.; Wang, C.; Liu, B.; Han, X.; Mo, Y.; et al. Transition from Superlithiophobicity to Superlithiophilicity of Garnet Solid-State Electrolyte. *J. Am. Chem. Soc.* **2016**, *138* (37), 12258–12262. https://doi.org/10.1021/jacs.6b06777.

(218) Zhao, N.; Fang, R.; He, M. H.; Chen, C.; Li, Y. Q.; Bi, Z. J.; Guo, X. X. Cycle Stability of Lithium/Garnet/Lithium Cells with Different Intermediate Layers. *Rare Met.* **2018**, *37* (6), 473–479. https://doi.org/10.1007/s12598-018-1057-3.

(219) Luo, W.; Gong, Y.; Zhu, Y.; Li, Y.; Yao, Y.; Zhang, Y.; Fu, K. K.; Pastel, G.; Lin, C. F.; Mo, Y.; et al. Reducing Interfacial Resistance between Garnet-Structured Solid-State Electrolyte and Li-Metal Anode by a Germanium Layer. *Adv. Mater.* **2017**, *29* (22), 1–7. https://doi.org/10.1002/adma.201606042.

(220) Feng, W.; Dong, X.; Li, P.; Wang, Y.; Xia, Y. Interfacial Modification of Li/Garnet Electrolyte by a Lithiophilic and Breathing Interlayer. *J. Power Sources* **2019**, *419* (January), 91–98. https://doi.org/10.1016/j.jpowsour.2019.02.066.

(221) He, M.; Cui, Z.; Chen, C.; Li, Y.; Guo, X. Formation of Self-Limited, Stable and Conductive Interfaces between Garnet Electrolytes and Lithium Anodes for Reversible Lithium Cycling in Solid-State Batteries. *J. Mater. Chem. A* **2018**, *6* (24), 11463–11470. https://doi.org/10.1039/c8ta02276c.

(222) Su, Y.; Ye, L.; Fitzhugh, W.; Wang, Y.; Gil-González, E.; Kim, I.; Li, X. A More Stable Lithium Anode by Mechanical Constriction for Solid State Batteries. *Energy Environ. Sci.* **2020**, *13* (3), 908–916. https://doi.org/10.1039/c9ee04007b.

(223) Clegg, W. *X-Ray Crystallography*, Second Edi.; New York : Oxford University

Press, 2015.

(224) West, A. R. *Solid State Chemistry and Its Applications*, Second Edi.; John Wiley & Sons, 2014.

(225) Rigaku. Operando Measurement of Li Ion Battery Positive Electrode in Charge/Discharge Process by X-Ray Diffraction. *Appl. Noteb.* **2018**, *33* (3), 49.

(226) Shigemasa, S.; Akira, S.; Christian, T. *Photoelectron Spectroscopy*, Second Edi.; Springer, 2021.

(227) Greczynski, G.; Hultman, L. Towards Reliable X-Ray Photoelectron Spectroscopy: Sputter-Damage Effects in Transition Metal Borides, Carbides, Nitrides, and Oxides. *Appl. Surf. Sci.* **2021**, *542*. https://doi.org/10.1016/j.apsusc.2020.148599.

(228) Woicik, J. C. *Hard X-Ray Photoelectron Spectroscopy (HAXPES)*; Springer, 2016.

(229) Ul-Hamid, A. *A Beginners' Guide to Scanning Electron Microscopy*; Springer, 2018. https://doi.org/10.1007/978-3-319-98482-7.

(230) Wells, O. C.; Boyde, A.; Lifshin, E.; Rezanowich, A. *Scanning Electron Microscopy*; McGraw-Hill, New York, 1974.

(231) Lee, J. Z.; Wynn, T. A.; Schroeder, M. A.; Alvarado, J.; Wang, X.; Xu, K.; Meng, Y. S. Cryogenic Focused Ion Beam Characterization of Lithium Metal Anodes. *ACS Energy Lett.* **2019**, *4* (2), 489–493. https://doi.org/10.1021/acsenergylett.8b02381.

(232) Microscopy Australia. EDS https://myscope.training/legacy/analysis/eds/ (accessed Aug 17, 2021).

(233) Pietsch, P.; Wood, V. X-Ray Tomography for Lithium Ion Battery Research: A Practical Guide. *Annu. Rev. Mater. Res.* **2017**, *47*, 451–479. https://doi.org/10.1146/annurev-matsci-070616-123957.

(234) Eastwood, D. S.; Bradley, R. S.; Tariq, F.; Cooper, S. J.; Taiwo, O. O.; Gelb, J.; Merkle, A.; Brett, D. J. L.; Brandon, N. P.; Withers, P. J.; et al. The Application of Phase Contrast X-Ray Techniques for Imaging Li-Ion Battery Electrodes. *Nucl. Instruments Methods Phys. Res. Sect. B Beam Interact. with Mater. Atoms* **2014**, *324*, 118–123. https://doi.org/10.1016/j.nimb.2013.08.066.

(235) Eastwood, D. S.; Bayley, P. M.; Chang, H. J.; Taiwo, O. O.; Vila-Comamala, J.; Brett, D. J. L.; Rau, C.; Withers, P. J.; Shearing, P. R.; Grey, C. P.; et al. Three-Dimensional Characterization of Electrodeposited Lithium Microstructures Using Synchrotron X-Ray Phase Contrast Imaging. *Chem. Commun.* **2015**, *51* (2), 266–268. https://doi.org/10.1039/c4cc03187c.

(236) Gamry Instruments. Basics of Electrochemical Impedance Spectroscopy (Application Note) https://www.gamry.com/application-notes/EIS/basics-of-electrochemical-impedance-spectroscopy/ (accessed Aug 17, 2021).

(237) Vadhva, P.; Hu, J.; Johnson, M. J.; Stocker, R.; Braglia, M.; Brett, D. J. L.; Rettie, A. J. E. Electrochemical Impedance Spectroscopy for All-Solid-State Batteries: Theory, Methods and Future Outlook. *ChemElectroChem* **2021**, *8* (11), 1930–1947. https://doi.org/10.1002/celc.202100108.

(238) Von Hauff, E. Impedance Spectroscopy for Emerging Photovoltaics. *J. Phys. Chem. C* **2019**, *123* (18), 11329–11346. https://doi.org/10.1021/acs.jpcc.9b00892.

(239) Gamry Instruments. Measuring Batteries using the Right Setup (Application Note) https://www.gamry.com/application-notes/battery-research/four-terminal-eis-of-batteries/ (accessed Sep 17, 2021).

(240) Su, J.; Huang, X.; Song, Z.; Xiu, T.; Badding, M. E.; Jin, J.; Wen, Z. Overcoming the Abnormal Grain Growth in Ga-Doped $Li_7La_3Zr_2O_{12}$ to Enhance the Electrochemical Stability against Li Metal. *Ceram. Int.* **2019**, *45* (12), 14991–14996. https://doi.org/10.1016/j.ceramint.2019.04.236.

(241) Mo, F.; Ruan, J.; Sun, S.; Lian, Z.; Yang, S.; Yue, X.; Song, Y.; Zhou, Y. N.; Fang, F.; Sun, G.; et al. Inside or Outside: Origin of Lithium Dendrite Formation of All Solid-State Electrolytes. *Adv. Energy Mater.* **2019**, *9* (40), 1–10. https://doi.org/10.1002/aenm.201902123.

(242) Linden, E.; Reddy, T. B. *Handbook of Batteries*; McGraw-Hill, New York, 2001.

(243) Wu, T.; Wen, Z.; Sun, C.; Wu, X.; Zhang, S.; Yang, J. Disordered Carbon Tubes Based on Cotton Cloth for Modulating Interface Impedance in Beta''-Al_2O_3-Based Solid-State Sodium Metal Batteries. *J. Mater. Chem.. A* **2018**, No. 6, 12623–12629. https://doi.org/10.1039/c8ta01883a.

(244) Lacivita, V.; Wang, Y.; Bo, S. H.; Ceder, G. Ab Initio Investigation of the Stability of Electrolyte/Electrode Interfaces in All-Solid-State Na Batteries. *J. Mater. Chem. A* **2019**, *7* (14), 8144–8155. https://doi.org/10.1039/c8ta10498k.

(245) De Jonghe, L. C.; Feldman, L.; Beuchele, A. Slow Degradation and Electron Conduction in Sodium/Beta-Aluminas. *J. Mater. Sci.* **1981**, *16* (3), 780–786. https://doi.org/10.1007/BF00552217.

(246) Hueso, K. B.; Armand, M.; Rojo, T. High Temperature Sodium Batteries: Status, Challenges and Future Trends. *Energy Environ. Sci.* **2013**, *6* (3), 734. https://doi.org/10.1039/c3ee24086j.

(247) Zhao, C.; Liu, L.; Qi, X.; Lu, Y.; Wu, F.; Zhao, J.; Yu, Y.; Hu, Y. S.; Chen, L. Solid-State Sodium Batteries. *Adv. Energy Mater.* **2018**, *8* (17), 14–16. https://doi.org/10.1002/aenm.201703012.

(248) Lu, X.; Xia, G.; Lemmon, J. P.; Yang, Z. Advanced Materials for Sodium- Beta Alumina Batteries: Status, Challenges and Perspectives. *J. Power Sources* **2010**, *195* (9), 2431–2442. https://doi.org/10.1016/j.jpowsour.2009.11.120.

(249) Oh, J. A. S.; He, L.; Chua, B.; Zeng, K.; Lu, L. Inorganic Sodium Solid-State

Electrolyte and Interface with Sodium Metal for Room-Temperature Metal Solid-State Batteries. *Energy Storage Mater.* **2021**, *34* (September 2020), 28–44. https://doi.org/10.1016/j.ensm.2020.08.037.

(250) Hou, W.; Guo, X.; Shen, X.; Amine, K.; Yu, H.; Lu, J. Solid Electrolytes and Interfaces in All-Solid-State Sodium Batteries: Progress and Perspective. *Nano Energy* **2018**, *52* (June), 279–291. https://doi.org/10.1016/j.nanoen.2018.07.036.

(251) Whalen, T. J.; Tennenhouse, G. J.; Meyer, C. Relation of Properties to Microstructure in Beta"-Alumina Ceramic. *J. Am. Ceram. Soc.* **1974**, *57* (11), 497–498. https://doi.org/10.1111/j.1151-2916.1974.tb11401.x.

(252) Doux, J. M.; Nguyen, H.; Tan, D. H. S.; Banerjee, A.; Wang, X.; Wu, E. A.; Jo, C.; Yang, H.; Meng, Y. S. Stack Pressure Considerations for Room-Temperature All-Solid-State Lithium Metal Batteries. *Adv. Energy Mater.* **2020**, *10* (1), 1–6. https://doi.org/10.1002/aenm.201903253.

(253) Irvine, J. T. S.; Sinclair, D. C.; West, A. R. Electroceramics Characterized by Impedance Spectroscopy. *Adv. Mater.* **1990**, *2* (3), 132–138. https://doi.org/10.1002/adma.19900020304.

(254) Wang, M.; Sakamoto, J. Correlating the Interface Resistance and Surface Adhesion of the Li Metal-Solid Electrolyte Interface. *J. Power Sources* **2018**, *377*, 7–11. https://doi.org/10.1016/j.jpowsour.2017.11.078.

(255) Han, X.; Gong, Y.; Fu, K.; He, X.; Hitz, G. T.; Dai, J.; Pearse, A.; Liu, B.; Wang, H.; Rubloff, G.; et al. Negating Interfacial Impedance in Garnet-Based Solid-State Li Metal Batteries. *Nat. Mater.* **2017**, *16* (5), 572–579. https://doi.org/10.1038/nmat4821.

(256) Youngblood, G. E.; Miller, G. R.; Gordon, R. S. Relative Effects of Phase Conversion and Grain Size on Sodium Ion Conduction in Polycrystalline, Lithia-Stabilized Beta”-Alumina. *J. Am. Ceram. Soc.* **1978**, *61* (1), 86–87.

(257) Virkar, A. V; Miller, G. R.; Gordon, R. S. Resistivity-Microstructure Relations in Lithia-Stabilized Polycrystalline Beta”- Alumina. *J. Am. Ceram. Soc.* **1978**, No. 1, 250–252.

(258) Swift, P. Adventitious Carbon—the Panacea for Energy Referencing? *Surf. Interface Anal.* **1982**, *4* (2), 47–51. https://doi.org/10.1002/sia.740040204.

(259) Barr, T. L.; Seal, S. Nature of the Use of Adventitious Carbon as a Binding Energy Standard. *J. Vac. Sci. Technol. A Vacuum, Surfaces, Film.* **1995**, *13* (3), 1239–1246. https://doi.org/10.1116/1.579868.

(260) Fang, D.; He, F.; Xie, J.; Xue, L. Calibration of Binding Energy Positions with C1s for XPS Results. *J. Wuhan Univ. Technol. Mater. Sci. Ed.* **2020**, *35* (4), 711–718. https://doi.org/10.1007/s11595-020-2312-7.

(261) Thanh, D. N. H.; Prasath, V. B. S.; Hieu, L. M. A Review on CT and X-Ray

Images Denoising Methods. *Informatica* **2019**, *43* (2), 151–159. https://doi.org/10.31449/inf.v43i2.2179.

(262) Kraft, M. A.; Culver, S. P.; Calderon, M.; Böcher, F.; Krauskopf, T.; Senyshyn, A.; Dietrich, C.; Zevalkink, A.; Janek, J.; Zeier, W. G. Influence of Lattice Polarizability on the Ionic Conductivity in the Lithium Superionic Argyrodites Li_6PS_5X (X = Cl, Br, I). *J. Am. Chem. Soc.* **2017**, *139* (31), 10909–10918. https://doi.org/10.1021/jacs.7b06327.

(263) Randrema, X.; Barcha, C.; Chakir, M.; Viallet, V.; Morcrette, M. A Detailed Characterisation Study of Li6PS5Cl Ionic Conductors from Several Synthetic Routes. *Solid State Sci.* **2021**, *118* (April). https://doi.org/10.1016/j.solidstatesciences.2021.106681.

(264) Yu, C.; van Eijck, L.; Ganapathy, S.; Wagemaker, M. Synthesis, Structure and Electrochemical Performance of the Argyrodite Li_6PS_5Cl Solid Electrolyte for Li-Ion Solid State Batteries. *Electrochim. Acta* **2016**, *215*, 93–99. https://doi.org/10.1016/j.electacta.2016.08.081.

(265) Zhang, Z.; Zhang, L.; Liu, Y.; Yu, C.; Yan, X.; Xu, B.; Wang, L. min. Synthesis and Characterization of Argyrodite Solid Electrolytes for All-Solid-State Li-Ion Batteries. *J. Alloys Compd.* **2018**, *747*, 227–235. https://doi.org/10.1016/j.jallcom.2018.03.027.

(266) Ayu, N. I. P.; Kartini, E.; Prayogi, L. D.; Faisal, M.; Supardi. Crystal Structure Analysis of Li_3PO_4 Powder Prepared by Wet Chemical Reaction and Solid-State Reaction by Using X-Ray Diffraction (XRD). *Ionics (Kiel).* **2016**, *22* (7), 1051–1057. https://doi.org/10.1007/s11581-016-1643-z.

(267) Auvergniot, J.; Cassel, A.; Foix, D.; Viallet, V.; Seznec, V.; Dedryvère, R. Redox Activity of Argyrodite Li_6PS_5Cl Electrolyte in All-Solid-State Li-Ion Battery: An XPS Study. *Solid State Ionics* **2017**, *300*, 78–85. https://doi.org/10.1016/j.ssi.2016.11.029.

(268) Adeli, P.; Bazak, J. D.; Park, K. H.; Kochetkov, I.; Huq, A.; Goward, G. R.; Nazar, L. F. Boosting Solid-State Diffusivity and Conductivity in Lithium Superionic Argyrodites by Halide Substitution. *Angew. Chemie - Int. Ed.* **2019**, *58* (26), 8681–8686. https://doi.org/10.1002/anie.201814222.

(269) Yu, C.; Ganapathy, S.; De Klerk, N. J. J.; Roslon, I.; Van Eck, E. R. H.; Kentgens, A. P. M.; Wagemaker, M. Unravelling Li-Ion Transport from Picoseconds to Seconds: Bulk versus Interfaces in an Argyrodite Li_6PS_5Cl-Li_2S All-Solid-State Li-Ion Battery. *J. Am. Chem. Soc.* **2016**, *138* (35), 11192–11201. https://doi.org/10.1021/jacs.6b05066.

(270) Rao, R. P.; Adams, S. Studies of Lithium Argyrodite Solid Electrolytes for All-Solid-State Batteries. *Phys. Status Solidi Appl. Mater. Sci.* **2011**, *208* (8), 1804–1807. https://doi.org/10.1002/pssa.201001117.

(271) Deiseroth, H. J.; Maier, J.; Weichert, K.; Nickel, V.; Kong, S. T.; Reiner, C. Li_7PS_6

and Li_6PS_5X (X: Cl, Br, I): Possible Three-Dimensional Diffusion Pathways for Lithium Ions and Temperature Dependence of the Ionic Conductivity by Impedance Measurements. *Zeitschrift fur Anorg. und Allg. Chemie* **2011**, *637* (10), 1287–1294. https://doi.org/10.1002/zaac.201100158.

(272) Randau, S.; Weber, D. A.; Kötz, O.; Koerver, R.; Braun, P.; Weber, A.; Ivers-Tiffée, E.; Adermann, T.; Kulisch, J.; Zeier, W. G.; et al. Benchmarking the Performance of All-Solid-State Lithium Batteries. *Nat. Energy* **2020**, *5* (3), 259–270. https://doi.org/10.1038/s41560-020-0565-1.

(273) Ma, J.; Chen, B.; Wang, L.; Cui, G. Progress and Prospect on Failure Mechanisms of Solid-State Lithium Batteries. *J. Power Sources* **2018**, *392* (189), 94–115. https://doi.org/10.1016/j.jpowsour.2018.04.055.

(274) Kerman, K.; Luntz, A.; Viswanathan, V.; Chiang, Y.-M.; Chen, Z. Review - Practical Challenges Hindering the Development of Solid State Li Ion Batteries. *J. Electrochem. Soc.* **2017**, *164* (7), A1731–A1744. https://doi.org/10.1149/2.1571707jes.

(275) Schmuch, R.; Wagner, R.; Hörpel, G.; Placke, T.; Winter, M. Performance and Cost of Materials for Lithium-Based Rechargeable Automotive Batteries. *Nat. Energy* **2018**, *3* (4), 267–278. https://doi.org/10.1038/s41560-018-0107-2.

(276) Sanyo Energy. Panasonic NCR18650B. *Panasonic 18650B Specification*. 2012.

(277) Wang, M. J.; Carmona, E.; Gupta, A.; Albertus, P.; Sakamoto, J. Enabling "Lithium-Free" Manufacturing of Pure Lithium Metal Solid-State Batteries through in Situ Plating. *Nat. Commun.* **2020**, *11* (1), 1–9. https://doi.org/10.1038/s41467-020-19004-4.

(278) Weber, R.; Genovese, M.; Louli, A. J.; Hames, S.; Martin, C.; Hill, I. G.; Dahn, J. R. Long Cycle Life and Dendrite-Free Lithium Morphology in Anode-Free Lithium Pouch Cells Enabled by a Dual-Salt Liquid Electrolyte. *Nat. Energy* **2019**, *4* (8), 683–689. https://doi.org/10.1038/s41560-019-0428-9.

(279) Assegie, A. A.; Cheng, J. H.; Kuo, L. M.; Su, W. N.; Hwang, B. J. Polyethylene Oxide Film Coating Enhances Lithium Cycling Efficiency of an Anode-Free Lithium-Metal Battery. *Nanoscale* **2018**, *10* (13), 6125–6138. https://doi.org/10.1039/c7nr09058g.

(280) Qian, J.; Adams, B. D.; Zheng, J.; Xu, W.; Henderson, W. A.; Wang, J.; Bowden, M. E.; Xu, S.; Hu, J.; Zhang, J. G. Anode-Free Rechargeable Lithium Metal Batteries. *Adv. Funct. Mater.* **2016**, *26* (39), 7094–7102. https://doi.org/10.1002/adfm.201602353.

(281) Xie, H.; Yang, C.; Ren, Y.; Xu, S.; Hamann, T. R.; Mcowen, D. W.; Wachsman, E. D.; Hu, L. Amorphous-Carbon-Coated 3D Solid Electrolyte for an Electro-Chemomechanically Stable Lithium Metal Anode in Solid-State Batteries. *Nano Lett.* **2021**. https://doi.org/10.1021/acs.nanolett.1c01748.

(282) Huang, C.; Grobert, N.; Watt, A. A. R.; Johnston, C.; Crossley, A.; Young, N. P.; Grant, P. S. Layer-by-Layer Spray Deposition and Unzipping of Single-Wall Carbon Nanotube-Based Thin Film Electrodes for Electrochemical Capacitors. *Carbon N. Y.* **2013**, *61*, 525–536. https://doi.org/10.1016/j.carbon.2013.04.107.

(283) Huang, C.; Young, N. P.; Zhang, J.; Snaith, H. J.; Grant, P. S. A Two Layer Electrode Structure for Improved Li Ion Diffusion and Volumetric Capacity in Li Ion Batteries. *Nano Energy* **2017**, *31* (November 2016), 377–385. https://doi.org/10.1016/j.nanoen.2016.11.043.

(284) Allart, D.; Montaru, M.; Gualous, H. Model of Lithium Intercalation into Graphite by Potentiometric Analysis with Equilibrium and Entropy Change Curves of Graphite Electrode. *J. Electrochem. Soc.* **2018**, *165* (2), A380–A387. https://doi.org/10.1149/2.1251802jes.

(285) Höltschi, L.; Borca, C. N.; Huthwelker, T.; Marone, F.; Schlepütz, C. M.; Pelé, V.; Jordy, C.; Villevieille, C.; Kazzi, M. El; Novák, P. Performance-Limiting Factors of Graphite in Sulfide-Based All-Solid-State Lithium-Ion Batteries. *Electrochim. Acta* **2021**, *389*, 138735. https://doi.org/10.1016/j.electacta.2021.138735.

(286) Jeon, Y.; Noh, H. K.; Song, H. K. A Lithium-Ion Battery Using Partially Lithiated Graphite Anode and Amphi-Redox $LiMn_2O_4$ Cathode. *Sci. Rep.* **2017**, *7* (1), 1–9. https://doi.org/10.1038/s41598-017-14741-x.

(287) Missyul, A.; Bolshakov, I.; Shpanchenko, R. XRD Study of Phase Transformations in Lithiated Graphite Anodes by Rietveld Method. *Powder Diffr.* **2017**, *32* (S1), S56–S62. https://doi.org/10.1017/S0885715617000458.

(288) Schweidler, S.; De Biasi, L.; Schiele, A.; Hartmann, P.; Brezesinski, T.; Janek, J. Volume Changes of Graphite Anodes Revisited: A Combined Operando X-Ray Diffraction and in Situ Pressure Analysis Study. *J. Phys. Chem. C* **2018**, *122* (16), 8829–8835. https://doi.org/10.1021/acs.jpcc.8b01873.

(289) Boulet-Roblin, L.; Borel, P.; Sheptyakov, D.; Tessier, C.; Novák, P.; Villevieille, C. Operando Neutron Powder Diffraction Using Cylindrical Cell Design: The Case of $LiNi_{0.5}Mn_{1.5}O_4$ vs Graphite. *J. Phys. Chem. C* **2016**, *120* (31), 17268–17273. https://doi.org/10.1021/acs.jpcc.6b05777.

(290) Sheptyakov, D.; Boulet-Roblin, L.; Pomjakushin, V.; Borel, P.; Tessier, C.; Villevieille, C. Stroboscopic Neutron Diffraction Applied to Fast Time-Resolved: Operando Studies on Li-Ion Batteries (d-$LiNi_{0.5}Mn_{1.5}O_4$ vs. Graphite). *J. Mater. Chem. A* **2020**, *8* (3), 1288–1297. https://doi.org/10.1039/c9ta11826h.

(291) Taminato, S.; Yonemura, M.; Shiotani, S.; Kamiyama, T.; Torii, S.; Nagao, M.; Ishikawa, Y.; Mori, K.; Fukunaga, T.; Onodera, Y.; et al. Real-Time Observations of Lithium Battery Reactions - Operando Neutron Diffraction Analysis during Practical Operation. *Sci. Rep.* **2016**, *6* (February), 1–12. https://doi.org/10.1038/srep28843.

(292) Dahn, J. R. Phase Diagram of Li_xC_6. *Phys. Rev. B* **1991**, *44* (17), 9170–9177.

(293) Heß, M.; Novák, P. Shrinking Annuli Mechanism and Stage-Dependent Rate Capability of Thin-Layer Graphite Electrodes for Lithium-Ion Batteries. *Electrochim. Acta* **2013**, *106*, 149–158. https://doi.org/10.1016/j.electacta.2013.05.056.

(294) Kim, S. W.; Seo, D. H.; Ma, X.; Ceder, G.; Kang, K. Electrode Materials for Rechargeable Sodium-Ion Batteries: Potential Alternatives to Current Lithium-Ion Batteries. *Adv. Energy Mater.* **2012**, *2* (7), 710–721. https://doi.org/10.1002/aenm.201200026.

(295) Perlitz, H.; Aruja, E. A Redetermination of the Crystal Structure of Lithium. *London, Edinburgh, Dublin Philos. Mag. J. Sci.* **1940**, *30* (198), 55–63. https://doi.org/10.1080/14786444008520697.

(296) Wang, J.; Wang, H.; Xie, J.; Yang, A.; Pei, A.; Wu, C. L.; Shi, F.; Liu, Y.; Lin, D.; Gong, Y.; et al. Fundamental Study on the Wetting Property of Liquid Lithium. *Energy Storage Mater.* **2018**, *14* (March), 345–350. https://doi.org/10.1016/j.ensm.2018.05.021.

(297) Wang, S. H.; Yue, J.; Dong, W.; Zuo, T. T.; Li, J. Y.; Liu, X.; Zhang, X. D.; Liu, L.; Shi, J. L.; Yin, Y. X.; et al. Tuning Wettability of Molten Lithium via a Chemical Strategy for Lithium Metal Anodes. *Nat. Commun.* **2019**, *10* (1), 1–8. https://doi.org/10.1038/s41467-019-12938-4.

(298) Vegard, L. IX. The Structure of Silver Crystals . *London, Edinburgh, Dublin Philos. Mag. J. Sci.* **1916**, *31* (181), 83–87. https://doi.org/10.1080/14786440108635473.

(299) Freeth, W. E.; Raynor, G. V. The Constitution of the System Silver-Lithium. *J. Inst. Met.* **1953**, *82*, 569–574.

(300) Taillades, G.; Sarradin, J. Silver: High Performance Anode for Thin Film Lithium Ion Batteries. *J. Power Sources* **2004**, *125* (2), 199–205. https://doi.org/10.1016/j.jpowsour.2003.07.004.

(301) Arnberg, L.; Westman, S. Note on the Structure of the Gamma Brass Like Gamma-3 Phase in the Silver Lithium System. *Acta Chem. Scand.* **1972**, *26*, 1748–1750. https://doi.org/10.3891/acta.chem.scand.26-1748.

(302) Jin, S.; Ye, Y.; Niu, Y.; Xu, Y.; Jin, H.; Wang, J.; Sun, Z.; Cao, A.; Wu, X.; Luo, Y.; et al. Solid-Solution-Based Metal Alloy Phase for Highly Reversible Lithium Metal Anode. *J. Am. Chem. Soc.* **2020**, *142* (19), 8818–8826. https://doi.org/10.1021/jacs.0c01811.

(303) Persson, K.; Sethuraman, V. A.; Hardwick, L. J.; Hinuma, Y.; Meng, Y. S.; Van Der Ven, A.; Srinivasan, V.; Kostecki, R.; Ceder, G. Lithium Diffusion in Graphitic Carbon. *J. Phys. Chem. Lett.* **2010**, *1* (8), 1176–1180. https://doi.org/10.1021/jz100188d.

(304) Xie, J.; Imanishi, N.; Hirano, A.; Takeda, Y.; Yamamoto, O.; Zhao, X. B.; Cao, G.

S. Electrochemical Kinetics of Nanosized Ag and Ag_2O Thin Films Prepared by Radio Frequency Magnetron Sputtering. *J. Solid State Electrochem.* **2011**, *15* (9), 2031–2039. https://doi.org/10.1007/s10008-010-1228-0.

(305) Kim, S. Y.; Li, J. Porous Mixed Ionic Electronic Conductor Interlayers for Solid-State Batteries. *Energy Mater. Adv.* **2021**, *2021*, 1–15. https://doi.org/10.34133/2021/1519569.

(306) Chen, K. H.; Goel, V.; Namkoong, M. J.; Wied, M.; Müller, S.; Wood, V.; Sakamoto, J.; Thornton, K.; Dasgupta, N. P. Enabling 6C Fast Charging of Li-Ion Batteries with Graphite/Hard Carbon Hybrid Anodes. *Adv. Energy Mater.* **2021**, *11* (5). https://doi.org/10.1002/aenm.202003336.

(307) Obrovac, M. N.; Chevrier, V. L. Alloy Negative Electrodes for Li-Ion Batteries. *Chem. Rev.* **2014**, *114* (23), 11444–11502. https://doi.org/10.1021/cr500207g.

(308) Zhang, W. J. A Review of the Electrochemical Performance of Alloy Anodes for Lithium-Ion Batteries. *J. Power Sources* **2011**, *196* (1), 13–24. https://doi.org/10.1016/j.jpowsour.2010.07.020.

(309) Wu, X.; Billaud, J.; Jerjen, I.; Marone, F.; Ishihara, Y.; Adachi, M.; Adachi, Y.; Villevieille, C.; Kato, Y. Operando Visualization of Morphological Dynamics in All-Solid-State Batteries. *Adv. Energy Mater.* **2019**, *9* (34). https://doi.org/10.1002/aenm.201901547.

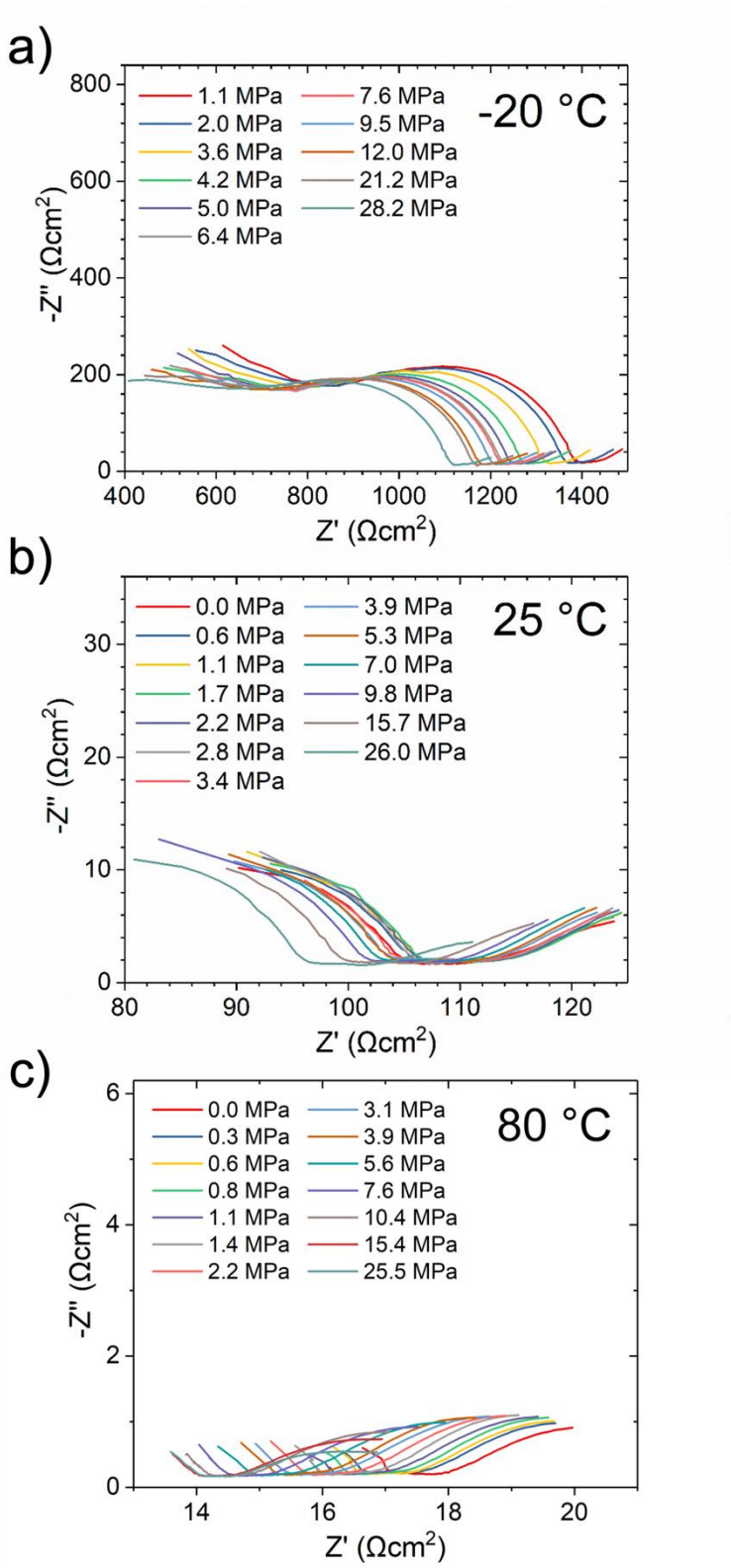
(310) Wang, J.; Fan, F.; Liu, Y.; Jungjohann, K. L.; Lee, S. W.; Mao, S. X.; Liu, X.; Zhu, T. Structural Evolution and Pulverization of Tin Nanoparticles during Lithiation-Delithiation Cycling. *J. Electrochem. Soc.* **2014**, *161* (11), F3019–F3024. https://doi.org/10.1149/2.0041411jes.

(311) Song, X. Y.; Kinoshita, K.; Tran, T. D. Microstructural Characterization of Lithiated Graphite. *J. Electrochem. Soc.* **1996**, *143* (6), L120–L123. https://doi.org/10.1149/1.1836896.

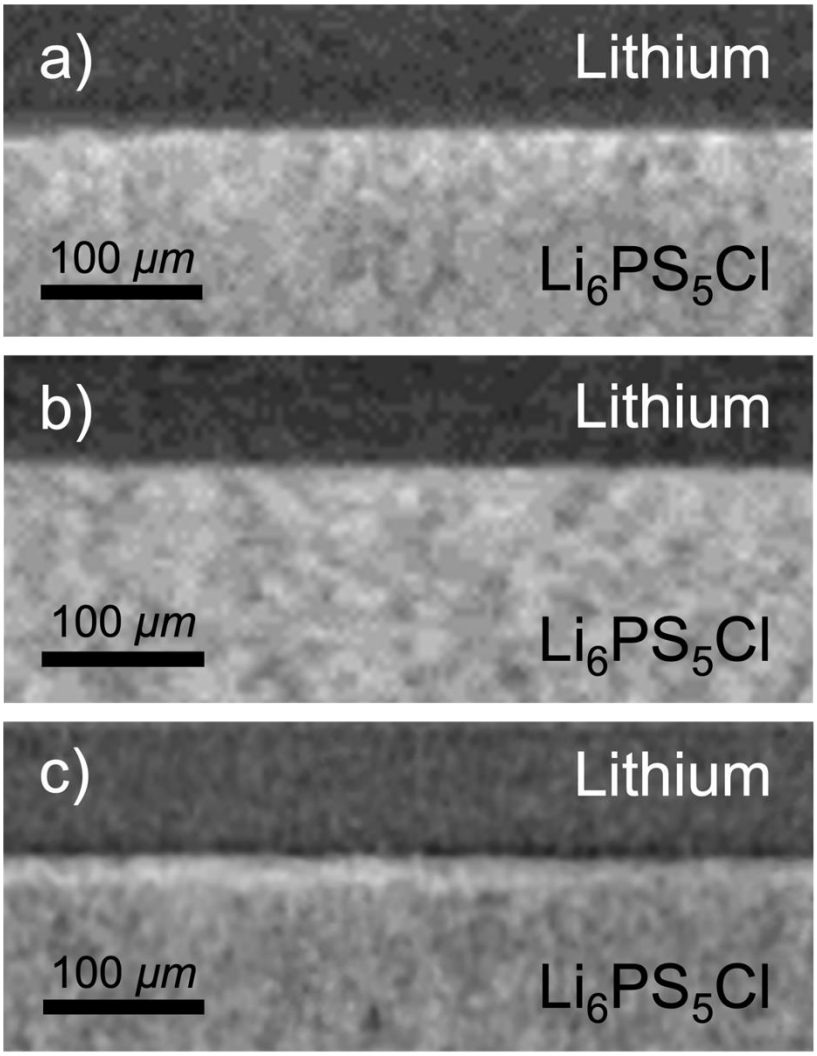
(312) Qi, W.; Shapter, J. G.; Wu, Q.; Yin, T.; Gao, G.; Cui, D. Nanostructured Anode Materials for Lithium-Ion Batteries: Principle, Recent Progress and Future Perspectives. *J. Mater. Chem. A* **2017**, *5* (37), 19521–19540. https://doi.org/10.1039/c7ta05283a.

(313) Obrovac, M. N.; Christensen, L.; Le, D. B.; Dahn, J. R. Alloy Design for Lithium-Ion Battery Anodes. *J. Electrochem. Soc.* **2007**, *154* (9), A849. https://doi.org/10.1149/1.2752985.

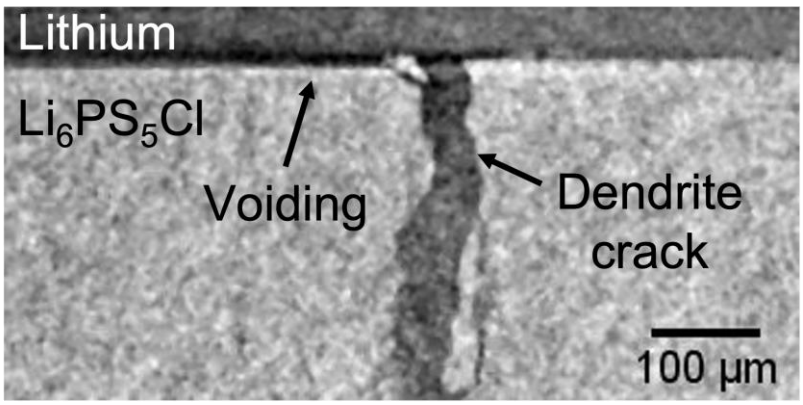
8 Appendices



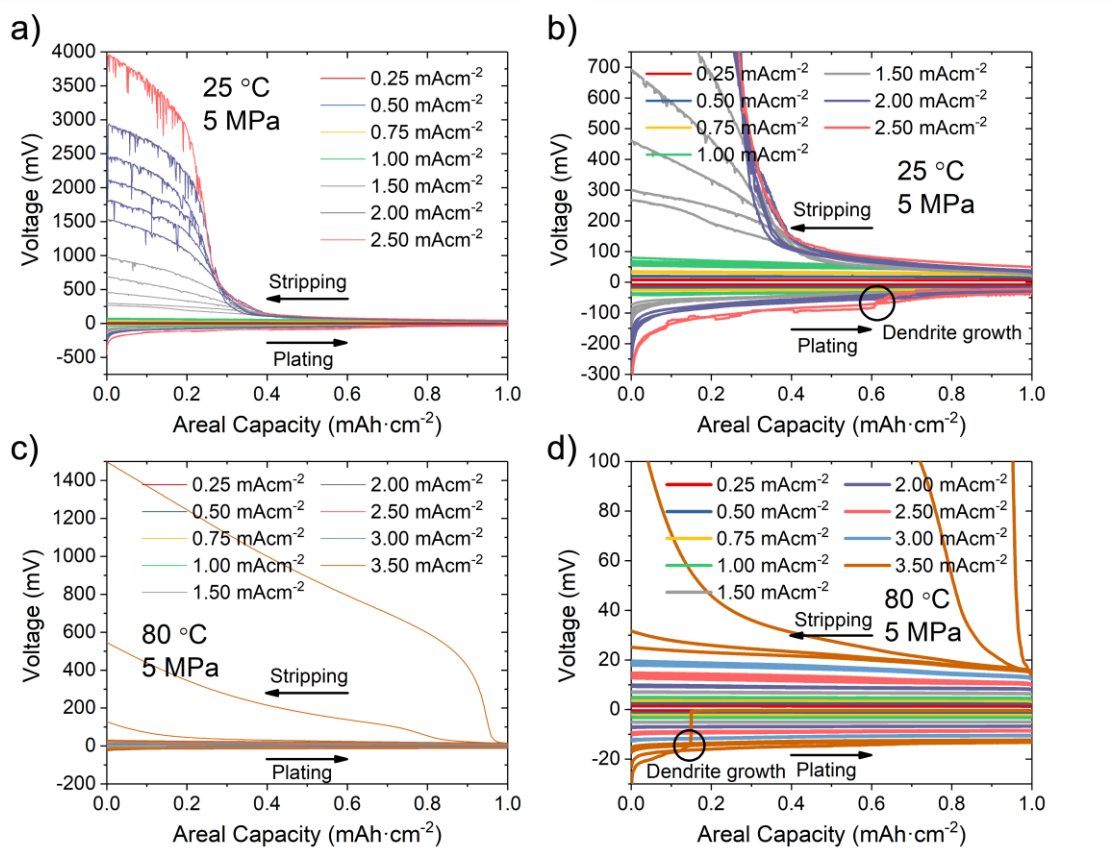
Appendix Figure 4.1: Nyquist plots showing the pressure dependence of cell impedance at a) -20 °C, b) 25 °C and c) 80 °C. Cells were placed under a formation pressure of approximately 25 MPa for 12 hours prior to the measurements. PEIS was carried out using a voltage perturbation of 5 mV in a frequency range of 0.4 MHz to 0.04 Hz, collecting 10 points per decade.



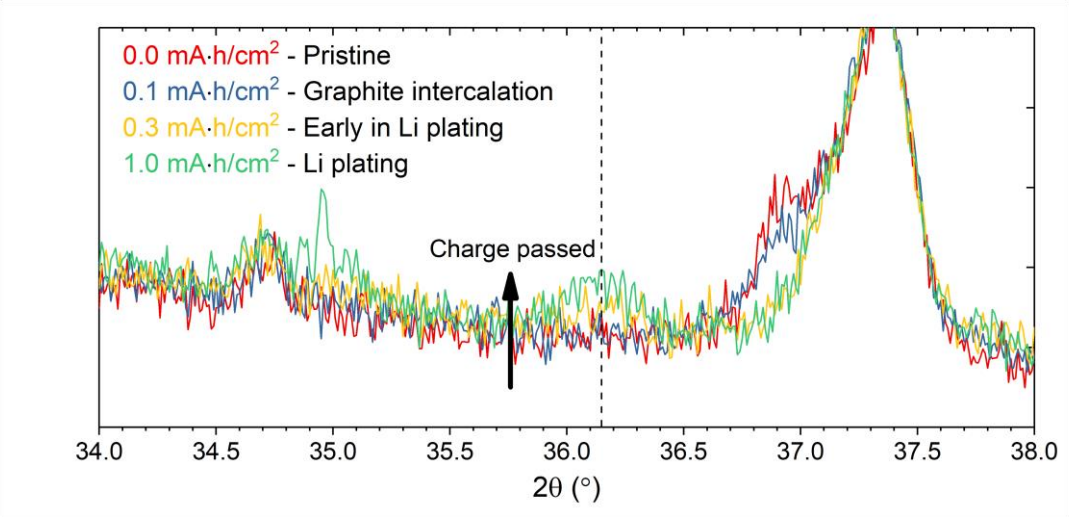
Appendix Figure 4.2: Unsegmented X-ray tomography cross-sectional images of the Li/Li_6PS_5Cl interface for a) a pristine cell and after cycling under 1 MPa stack-pressure at b) 0.5 mA/cm^2 and c) 0.75 mA/cm^2.



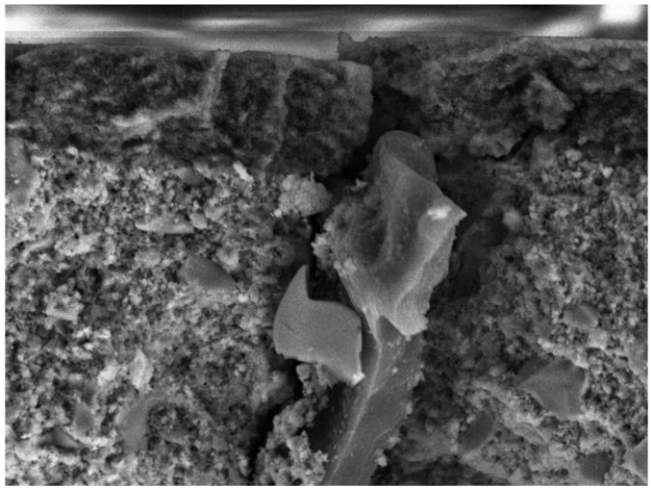
Appendix Figure 4.3: Unsegmented X-ray tomography cross-sectional images of Li dendrite penetration into Li/Li_6PS_5Cl after cycling under 1 MPa stack-pressure at 0.75 mA/cm^2.



Appendix Figure 4.4: 3-electrode cycling under 5 MPa pressure moving 1 mA·h/cm^2 capacity at 25 °C a) full data and b) expanded, and at 80 °C c) full data and d) expanded.



Appendix Figure 5.1: Figure showing Li deposition on the current collector after lithiation of the graphite phase. The dashed line shows a reflection indicative of Li metal which only appears and increases in intensity after the graphite phase becomes fully lithiated.



Appendix Figure 5.2: SEM showing Li dendrite penetration into the Li_6PS_5Cl ceramic electrolyte following nucleation beneath the carbon black interlayer.